

25th Anniversary Conference on
Numerical Simulation of
Optoelectronic Devices

BOOK OF ABSTRACTS

14–18 September 2025, Łódź, Poland

25th Anniversary Conference on

**Numerical Simulation
of Optoelectronic Devices**

14 – 18 September 2025
Łódź, Poland

Editors / Chairs:
Paolo Bardella and Maciej Dems

Organizers



Lodz University of Technology
Institute of Physics



**Politecnico
di Torino**

Sponsors



Ministry of Science and Higher Education
Republic of Poland

25 Years of NUSOD

Welcome to the 25th NUSOD Conference!

This year, we look back at a quarter century of the annual NUSOD conference, which started in 2001 at the University of California in Santa Barbara (UCSB). The first meeting emerged from the urgent need for a better connection between theory and practice in optoelectronics. On the theoretical side, we could find a number of highly developed mathematical models. On the practical side, there was strong interest in novel devices, for instance vertical cavity lasers and GaN-based light emitters, which require a deeper understanding of internal physics. Numerical simulation offers a much-needed bridge between both sides. At that time, advanced software packages became available on personal computers, but still exhibited a number of shortcomings.

Thus, the first NUSOD meeting was originally supposed to establish a networking platform for users of commercial laser simulation packages made by Crosslight Software in Canada. However, very few users responded to the invitation to talk about their work, probably due to company secrecy. Therefore, we decided to open the meeting to all researchers working in this field and invited some of the leading scientists. This generated 22 presentations and we expected a total of 30–40 participants. UCSB provided free access to conference facilities and Crosslight provided financial support. To our great surprise, long lines formed at the registration table and we ended up with more than 70 participants, mainly from US companies. The telecom boom was still ongoing in 2001 and many companies probably needed some simulated predictions to keep investors happy. This success generated the idea to start an annual conference. In fact, participants from Switzerland immediately volunteered to organize the 2002 meeting. In order to reach a worldwide audience, the conference was then scheduled to travel around the globe, following the example of the IEEE semiconductor laser conference.

Subsequent NUSOD conferences were held in more than 15 countries on 4 continents. However, unlike other conferences, we established a two-tier organizational structure, consisting of a more permanent position of program chair and annually appointed local chair, depending on availability. The former organizes reoccurring pre-conference tasks, such as website, advertisement, paper submission and review, as well as program development. After that, the local chair manages registration and payment, facilities, catering, and excursion. Free university and online services allow us to keep the registration fee relatively low, so that those students and engineers can participate who often do the actual simulation work. The broad spectrum of participants underscores the continuing need for worldwide exchange and collaboration in our diverse field.

During the pandemic years, Politecnico di Torino hosted three virtual NUSOD conferences offering free registration, which generated record attendances. Pre-recorded presentations were constantly accessible, thereby eliminating the time zone problem. The ability to rerun video segments also improved the educational value. Hundreds of written comments, questions, and answers were generated, with some detailed debates continuing for several days. However, nothing beats the personal contact at onsite meetings for forming or maintaining fruitful collaborations.

The NUSOD conference is now regarded as one of the key conference fixtures in optoelectronics to network and discuss the latest developments and challenges in device modelling, simulation, analysis, and design. As we celebrate 25 years of NUSOD, we look forward to continuing this tradition of bridging theory and practice, exploring emerging technologies, and establishing new collaborations.

We wish you an enjoyable and stimulating conference!

Joachim Piprek & Paolo Bardella

Welcome to the Lodz University of Technology

This year, the great honor of hosting the 25th anniversary NUSOD conference comes to the Lodz University of Technology, located in the very center of the European continent. Established in 1945, it is one of the largest and most prestigious technical universities in Poland, educating over 11,000 students each year. The university is structured into nine faculties, covering a wide range of disciplines including electrical, electronic, computer, and information technologies; chemistry; biotechnology and food sciences; mechanical, civil, and environmental engineering; as well as management and innovation studies.

Research at the Lodz University of Technology is strongly interdisciplinary, spanning advanced materials, photonics, nanotechnology, telecommunications, information systems, sustainable energy, and biomedical engineering. Many projects are carried out in close collaboration with industry, ensuring both practical applications and high impact. The university actively participates in international programs and research networks, contributing to scientific progress in areas at the forefront of modern technology.

Its modern campus combines historic post-industrial architecture with state-of-the-art laboratories, fostering innovation across engineering, science, and technology. Set in the heart of Łódź, the campus reflects the city's unique character, where 19th-century factory buildings have been transformed into dynamic academic spaces. This blend of tradition and modernity creates a stimulating environment for both study and research, making the Lodz University of Technology an inspiring setting for the NUSOD 25th anniversary conference.

We are proud to welcome around 70 participants from all over the world to Łódź for four days of inspiring exchange. The conference program features a diverse range of presentations, highlighting the latest advances in theory, simulation, and applications of nanoscale optoelectronic devices. Through plenary lectures, invited talks, contributed presentations, and poster sessions, participants will have the opportunity to share knowledge, engage in fruitful discussions, and explore new directions in research. This rich scientific program, combined with the collaborative spirit of the NUSOD community, promises a memorable and productive meeting.

Maciej Dems
Local NUSOD 2025 Chair

Chairs and Committees

NUSOD 2025 Chairs

Program Chair: Paolo Bardella, *Politecnico di Torino, Italy*

Local Chair: Maciej Dems, *Lodz University of Technology, Poland*

NUSOD 2025 Program Committee

Urs Aeberhard, *Fluxim AG, Switzerland*

Matthias Auf der Maur, *University of Rome "Tor Vergata", Italy*

Uwe Bandelow, *Weierstrass Institute, Germany*

Prasanta Basu, *University of Calcutta, India*

Rikmantra Basu, *National Institute of Technology Delhi, India*

Chris Broderick, *University of California at Santa Barbara, USA*

Pierluigi Debernardi, *CNR-IEIT, Italy*

Alexandra Djuricic, *Hong Kong University, China*

Silvano Donati, *University of Pavia, Italy*

Kankat Ghosh, *Indian Institute of Technology Jammu, India*

Niels Gregersen, *Technical University of Denmark, Denmark*

Christian Jirauschek, *Technical University of Munich, Germany*

Sergey Karpov, *STR-Soft, Russia*

Tsong-Sheng Lay, *National Chung Hsing University, Taiwan*

Nicolai Matuschek, *Exalos AG, Switzerland*

Grzegorz Muziol, *Institute of High Pressure Physics, Poland*

Wei-Choon Ng, *Hisilicon, China*

Salah Obayya, *Zewail City of Science and Technology, Egypt*

Stefan Schulz, *Tyndall National Institute, Ireland*

Slawek Sujecki, *Wroclaw University of Science and Technology, Poland*

Xie Zhang, *Beijing Computational Science Research Center, China*

NUSOD Steering Committee

Aldo Di Carlo, *University of Rome "Tor Vergata", Italy*

Martijn de Sterke, *University of Sydney, Australia*

Thomas Koprucki, *Weierstrass Institute, Germany*

Giovanni Ghione, *Politecnico di Torino, Italy*

Eric Larkins, *University of Nottingham, UK*

Wei Lu, *Shanghai Institute of Technical Physics, China*

Joachim Piprek, *USA*

Berthold Schmidt, *Trumpf, Germany*

Bernd Witzigmann, *University of Erlangen-Nurnberg, Germany*

Keynote Speakers



Andrea Alù

CUNY Advanced Science Research Center, USA

Extreme light control with structured nanophotonics [MA01]



Franco Prati

Universit'a Dell'Insubria, Italy

Dynamics of passive mode-locking in class-B lasers with a saturable absorber [TuB01]



Karin Hinzer

University of Ottawa, Canada

Machine learning enhanced design optimization and knowledge discovery for multi-junction photonic power converters [WA01]



Hans Wenzel

Ferdinand-Braun-Institut, Germany

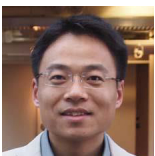
Trying to understand semiconductor lasers for 40 years [WB01]



Philippe Lalanne

Laboratoire de Photonique, Numérique et Nanoscience, France

A few elementary studies on electromagnetic resonances [WC01]



Ling Lu

Institute of Physics, Chinese Academy of Sciences, China

Topological-cavity surface-emitting laser [ThB01]



Joachim Piprek

USA

Lessons learned in 25 years of NUSOD conferences [ThE]

Invited Speakers

Nicola Vukovic, *School of Electrical Engineering, University of Belgrade, Serbia*, Numerical Simulations of Terahertz Quantum Cascade Laser Electronic Structure and Dynamics [MA02]

Lucio Andreani, *University of Pavia, Italy*, Bound States in the Continuum Empowering Maximum Chirality and Strong Coupling Regime in Plasmonic Metasurfaces [MB01]

Kamil Postava, *Technical University of Ostrava, Czech Republic*, Coherent and incoherent phenomena in anisotropic periodic gratings [TuA01]

David Childs, *Huawei R&D UK Ltd, Ipswich, UK*, Sooner and Better, Perfection in Compromise and Getting it Right First Time: Some Hopes and Realities of Simulation in Industry [TuA02]

Michał Matuszewski, *Institute of Physics Polish Academy of Sciences, Poland*, Strong light-matter coupling in nanostructures and quantum neural networks [TuA03]

Christian Jirauschek, *Technical University of Munich, Germany*, Density Matrix Simulations of Quantum Cascade Lasers: Optical and Microwave Dynamics [WB02]

Runzhang Xie, *Shanghai Institute of Technical Physics, Chinese Academy of Sciences, China*, Renormalization Theory and Monte Carlo Simulation of HgCdTe Single Carrier Avalanche Process [ThA01]

Lilli Kuen, *Weierstrass Institute, Germany*, Numerical study of spatio-temporal dynamics in all semiconductor PCSELs [ThB02]

Lin Zschiedrich, *JCMwave GmbH, Germany*, Efficient Photonic Component Analysis via AAA Rational Approximation [ThC01]

Thomas Christensen, *Technical University of Denmark, Denmark*, Tight-binding models for 3D photonic crystals [ThC02]

Social Events

We are pleased to offer a number of social events that will allow you to relax after the scientifically intensive sessions and provide excellent opportunities for networking and building informal contacts.

Welcome Reception

Upon your arrival in Łódź, we invite you to join us for a warm welcome with a glass of prosecco or wine, accompanied by a selection of hot and cold snacks.

Sunday, 14 September, 18:00

Conference venue — Lodz University of Technology, Institute of Physics, *Wólczańska 217/221*, Building B14

Poster Session

The poster session will provide an excellent opportunity to present and discuss research in an informal and engaging atmosphere. Light snacks and beer will be served to encourage lively discussions and networking among participants.

Monday, 15 September, 17:00–18:30

Conference venue

City Tour

Łódź is a unique city where 19th-century industrial architecture blends with a lively artistic atmosphere, featuring revitalized factories, creative courtyards, and impressive murals. During the excursion, we will discover some of the city's top landmarks, including a stop at the world-renowned Łódź Film School, alma mater of Roman Polański, Andrzej Wajda, and Krzysztof Kieślowski.

Tuesday, 16 September, 15:00–19:00

Tour begins at the conference venue

Informal Beer

Right after the city tour, we will enjoy an informal beer at Browar Warkot, a lively brewpub near Piotrkowska Street, offering house-made craft beers in a warm, industrial-chic atmosphere. The tour will conclude at this location, but you are also welcome to join us directly on the spot.

Tuesday, 16 September, from 19:00

Browar Warkot, *Narutowicza 7/9*

Social Dinner

The official conference dinner will feature a festive atmosphere and delicious cuisine, providing an excellent opportunity to connect with fellow participants. During this special evening, we will also celebrate the **25th anniversary of NUSOD**.

Wednesday, 17 September, 18:00

Three Chimneys Restaurant, *Piotrkowska 295*



Conference Venue

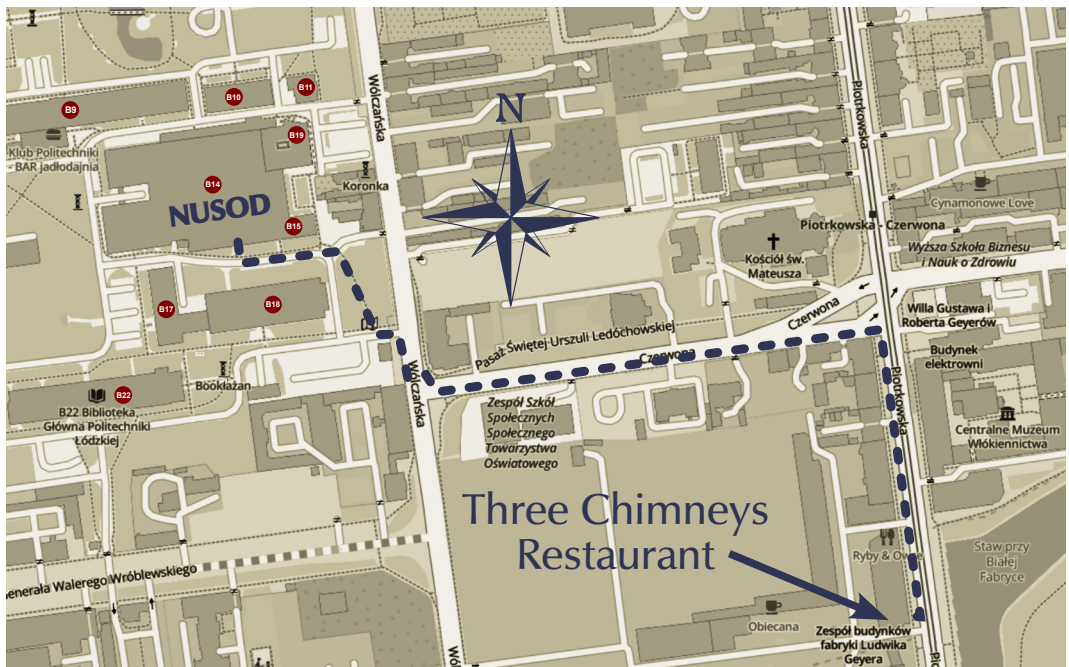
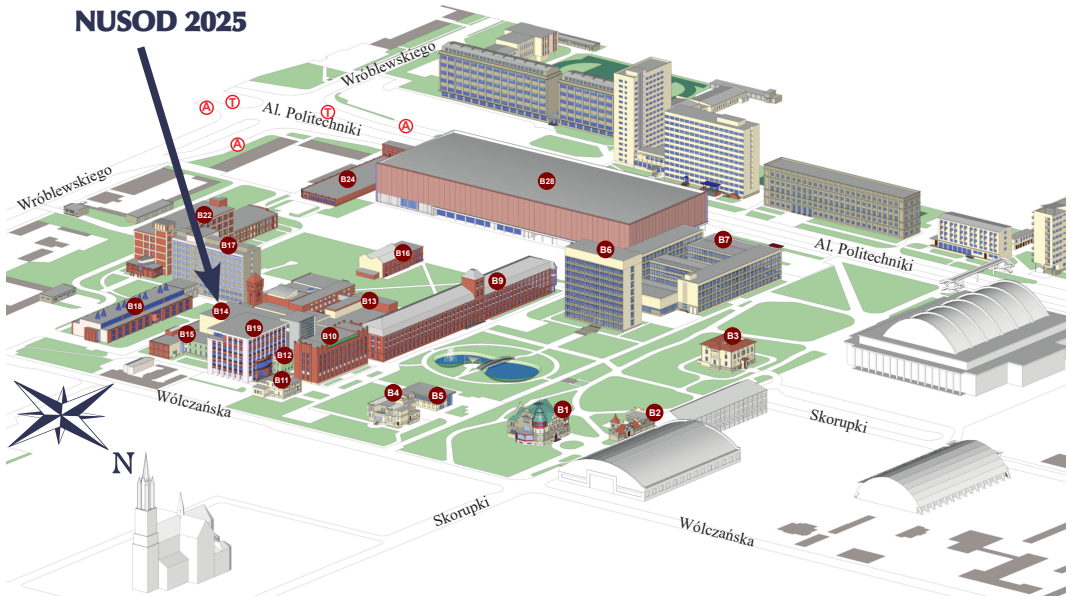


Informal Beer



Social Dinner

NUSOD 2025



Conference Program

Program Overview

Sunday	Monday	Tuesday	Wednesday	Thursday
	8:00–8:30 Registration	8:00–8:30 Morning coffee	8:30–9:00 Morning coffee	8:15–8:45 Morning coffee
	8:30–8:45 Opening	8:30–10:25 Photonics II	9:00–10:45 Solar Cells and Photovoltaics	8:45–10:25 Detectors
	8:45–10:35 Novel Materials and Devices I			
	10:35–11:05 Coffee break	10:25–10:55 Coffee break	10:45–11:15 Coffee break	10:25–10:55 Coffee break
	11:05–13:10 Photonics I	10:55–13:00 Novel Materials and Devices II	11:15–13:05 Laser Diodes I	10:55–13:05 Laser Diodes II
	13:10–14:10 Lunch	13:00–14:00 Lunch	13:05–14:05 Lunch	13:00–14:00 Lunch
	14:10–15:50 Light-Emitting Diodes		14:05–16:10 Photonics III	14:00–15:50 Mathematical Methods
	15:50–16:20 Coffee break	15:00–19:00 City Tour		15:50–16:20 Coffee break
17:30–18:00 Registration	16:20–17:00 Poster Preview	from 19:00 Informal Beer	from 18:00 Social Dinner	16:20–17:40 VCSELs
18:00–19:30 Welcome Reception	17:00–18:30 Poster Session			17:40–18:40 25 Years of NUSOD

Monday, 15

Novel Materials and Devices I

8:45–10:35

chair: Prof. Franco Prati

- MA01** Extreme light control with structured nanophotonics; A. Alù; Advanced Science Research Center, City University of New York (USA) – **(KEYNOTE)**
- MA02** Numerical Simulations of Terahertz Quantum Cascade Laser Electronic Structure and Dynamics; N. Vukovic (1), M. Ignjatovic (1), N. Stanojevic (1),(2), A. Demic (3), M. Stojkovic (1), F. Perisic (1), D. Indjin (3), J. Radovanovic (1); (1) School of Electrical Engineering, University of Belgrade (SRB); (2) Vlatacom Institute of High Technologies, Belgrade (SRB); (3) School of Electronic and Electrical Engineering, University of Leeds (UK) – **(INVITED)**
- MA03** Solution-Processed Heterojunction Oxide Thin-Film Transistors for Displays; W. Cai; Chongqing University (CHN)
- MA04** Solvent-free Synthesis of Hybrid Copper Halides for High-performance White Emission and X-ray Imaging; S. Zhao; Chongqing University (CHN)

Photonics I

11:05–13:10

chair: Prof. Andrea Alù

- MB01** Bound States in the Continuum Empowering Maximum Chirality and Strong Coupling Regime in Plasmonic Metasurfaces; L. Andreani (1), H. Ali (1), G. Pellegrini (1), E. Petronijevic (2); (1) University of Pavia (ITA); (2) Sapienza University of Rome (ITA) – **(INVITED)**
- MB02** Investigation on digital twin model of 3×3 Mach-Zehnder Interferometer mesh; T. Ma (1), A. Marchisio (1), F. Da Ros (2), V. Curri (1), A. Carena (1), P. Bardella (1); (1) Politecnico di Torino (ITA); (2) Danmarks Tekniske Universitet (DEN)
- MB03** Novel Variable Confinement SOAs Modelling; C. Cruz (1), C. Calò (1), H. Carrere (2); (1) III-V Lab, a joint laboratory between Nokia Bell Labs, Thales Research & Technology and CEA-LETI, Palaiseau (FRA); (2) Laboratoire de Physique et Chimie des Nano-Objets, Université de Toulouse, Toulouse (FRA)
- MB04** On-chip Rewritable Phase-change Metasurfaces for Programmable Optical Routing; S. Zarei; Department of Electrical Engineering, Sharif University of Technology, Tehran, Iran
- MB05** Graphics Processor Unit Accelerated Design of Multimode Interference Reflectors; G. M. Jandu, P. M. Smowton; The school of physics and astronomy, Cardiff University, Cardiff (UK)
- MB06** A Tunable MOEMS Open Microring Resonator for the Detection of Water Concentration in Ethanol Solutions; N. Hanine (1), A. Buzzin (1), L. Giannini (1), A. Alaeddini (1), N. P. Belfiore (2), R. Asquini (1); (1) Sapienza University of Rome (ITA); (2) Roma Tre University (ITA)

chair: Prof. Kamil Postava

- MC01** Multi-scale hybrid band simulation of (Al,Ga)N UV-C light emitting diodes; R. Finn (1), P. Farrell (2), T. Streckenbach (2), J. Moatti (3), S. Schulz (1,4), T. Koprucki (2), M. O'Donovan (2); (1) Tyndall National Institute, University College Cork, Cork (IRL); (2) Weierstrass Institute (WIAS), Berlin (GER); (3) Univ. Bordeaux, CNRS, Bordeaux INP, Talence (FRA); (4) School of Physics, University College Cork, Cork (IRL) – **(TOP 10%)**
- MC02** Modelling Electron Beam Induced Current in III-Nitride Light Emitting Diodes.; B. Utsch (1), F. Roemer (1), S. Faber (1), F. Bertram (2), G. Schmidt (2), P. Veit (2), C. Berger (2), A. Dadgar (2), A. Strittmatter (2), J. Christen (2), B. Witzigmann (1); (1) Friedrich-Alexander-Universität Erlangen-Nürnberg (GER); (2) Otto-von-Guericke-Universität Magdeburg (GER) – **(TOP 10%)**
- MC04** Estimation of light extraction efficiency in GaN-based light emitting diodes via ray-tracing modeling; S. Lach, M. Hajdel, G. Muziol; Institute of High Pressure Physics PAS (POL)
- MC05** Superluminescent Light-Emitting Diodes (SLEDs) Operating at Ultra-High Ambient Temperatures; N. Matuschek, M. Duelk; Exalos AG (indie Switzerland) Wagistrasse 21 CH-8952 Schlieren (CH)
- MC06** Mg–Si Doped Barriers for Polarization Field Screening in High-Power InGaN/GaN Green LEDs; C. P. Singh, K. Ghosh; Department of Electrical Engineering, Indian Institute of Technology Jammu, Jammu (IND)

Poster Session 16:20–17:00 (*preview in the main room*) 17:00–18:30 (*discussion in the patio*)

- MP01** Simulations and Theoretical Background: Quantum Entanglement in Photonic Quantum Computing and Cryptography; M. Nadir; Tampere University (FIN)
- MP02** High-Efficiency Nanoplasmonic Dual-Band Band-Stop Filters Using Step Impedance Resonators; K. Thirupathaiah (1), M. Qasymeh (2); (1) Koneru Lakshmaiah Education Foundation, Hyderabad, Telangana (IND); (2) Abu Dhabi University, Abu Dhabi (UAE)
- MP03** All-Optical 2R Regeneration Based on Similariton Generation in HNL-PCF for High Bit Rate Networks; L. Cherbi, H. Azza; Laboratory of instrumentation (LINS), Faculty of Electrical Engineering University of Sciences and Technology Houari Boumediene (USTHB) Algiers, Algeria
- MP04** Simulations of light emission at reverse voltage of wide-well InGaN light-emitting diodes; K. Sakowski, A. Bercha, G. Muziol, M. Hajdel, W. Trzeciakowski; Institute of High Pressure Physics, Polish Academy of Sciences (POL)
- MP06** Inverse-Designed Ultra-Compact Polarization Demultiplexer; P. Kumar (1), T. Srivas (2), E.S. Shivaleela (3); Indian Institute of Science, Bengaluru (IND)
- MP07** DFB-LD connected in series to DBR with optical gain; M. Ueno and T. Numai; Ritsumeikan University (JPN)
- MP08** Self-Powered High Performance AlGaIn-Based Solar Blind UV MSM Photodetector; B. Choubey, A. Ahmad Bhat, K. Ghosh; Department of Electrical Engineering, Indian Institute of Technology Jammu, Jammu-181221 (IND)

- MP09** Design of Polarization Maintaining Fiber Based on Polyethylene Terephthalat Polymer for Sensing Application; L. Cherbi, M. Benlachheb; Laboratory of instrumentation (LINS), Faculty of Electrical Engineering University of Sciences and Technology Houari Boumediene (USTHB) Algiers (ALG)
- MP10** Numerical models for the analysis of thermal phenomena in nitride edge-emitting lasers and their one-dimensional arrays; D. Dąbrowka, R.P. Sarzała; Institute of Physics, Lodz University of Technology (POL)
- MP12** Light Interference Fringe Detection with DBSCAN for Integrated Mirrors; V. Voskerchyan, N.X. Xu Bonnie, L. Chang, S. Garcia-Blanco; University of Twente (NLD)
- MP13** Legume: A guided-mode expansion method for photonic crystal slabs for inverse design and light-matter interaction; S. Zanotti (1), M. Minkov (2), D. Nigro (1), D. Gerace (1), S. Fan (3), L.C. Andreani (1); (1) University of Pavia (ITA); (2) Flexcompute (USA); (3) Stanford University (USA)
- MP14** Inaccuracy Amplified: Compressed Sensing Under Experimental Misalignment; B. Ersöz, P. Chaudhary, P. Bardella, M. Dabbicco, L. Columbo, M. Brambilla; (1) Politecnico di Torino (ITA); (2) Università di Bari Aldo Moro (ITA); (3) Politecnico di Bari (ITA)
- MP15** Modeling Gaussian Beam Propagation in Micro-Droplets with Ray Optics; R.H. Klenk (1), S. Abdani (1), W. Vogel (1), M. Berroth (1), M. Heymann (2), G. Rademacher (1); (1) Institute of Electrical and Optical Communications, University of Stuttgart (GER); (2) Institute of Biomaterials and Biomolecular Systems, University of Stuttgart (GER)
- MP16** Signatures of non-classical light emission from semiconductor lasers; D. Nello (1), L. Columbo(1); Politecnico di Torino, Department of Electronics and Telecommunications (ITA)

Tuesday, 16

Photonics II

8:30–10:25

chair: Prof. Philippe Lalanne

- TuA01** Coherent and incoherent phenomena in anisotropic periodic gratings; K. Postava, T. Fordos, T. Kohut, L. Halagacka; VSB – Technical University of Ostrava Faculty of Materials Science and Technology and Nanotechnology Center, Poruba (CZE) – **(INVITED)**
- TuA02** Sooner and Better, Perfection in Compromise and Getting it Right First Time: Some Hopes and Realities of Simulation in Industry; D. Childs; Ipswich Research Centre, Huawei R&D UK Ltd, Ipswich (UK) – **(INVITED)**
- TuA03** Strong light-matter coupling in nanostructures and quantum neural networks; Michał Matuszewski (1), Amir Rahmani (1), Andrzej Opala (2), Dogyun Ko (2), Maciej Dems (3); (1) Institute of Physics Polish Academy of Sciences (POL); (2) Faculty of Physics University of Warsaw (POL); (3) Institute of Physics, Łódź University of Technology (POL) – **(INVITED)**
- TuA04** Dielectric Dipole Nanoantenna Design for highly Directional Emission from SiV Color Centers; M.A. Ahamad, F.A. Inam; Aligarh Muslim University (IND)
- TuA05** Dependence of optical modes in hyperbolic metamaterials on surrounding medium; O. A. Kochanowska, T. J. Antosiewicz; Faculty of Physics, University of Warsaw (POL)

Novel Materials and Devices II

10:55–13:00

- TuB01** Dynamics of passive mode-locking in class-B lasers with a saturable absorber; F. Prati; Insubria University, Como (ITA) – **(KEYNOTE)**
- TuB03** Theoretical investigation of optical polarisation in alloy disordered (Al,Ga)N quantum well systems; R. Finn, M. O'Donovan, T. Koprucki and S. Schulz; (1) Tyndall National Institute, University College Cork, Cork (IRL); (2) Weierstrass Institute (WIAS), Berlin (GER); (3) School of Physics, University College Cork, Cork (IRL)
- TuB04** Numerical and experimental investigation of erbium (III) ion doped fluoride glass fiber laser operation at threshold; S. Sujecki (1), L. Sojka (2), L. Pajewski (2), S. Lamrini (3), M. Farries (4), A. Seddon (4), D. Furniss (4), E. Barney (4), S. Phang (4); (1) Military University of Technology Warsaw (POL); (2) Wroclaw University of Science and Technology Wroclaw (POL); (3) LIMA Photonics GmbH Goettingen (D), (4) Nottingham University Nottingham (UK)
- TuB05** Simulating a High Extinction Ratio Interferometric Electroabsorption-Modulated Laser Transmitter; R. Spalding, D. Moodie, R. Cronin, N. Hattasan, J. Griffiths, D. Childs; Huawei IRC, Ipswich (UK) – **(TOP 10%)**
- TuB06** Development of 2D carrier transport model for random dopant effect and exciton coupling model; M.-H. Chang, L.-A. Huang, Y.-R. Wu; National Taiwan University (TWN)

Wednesday, 17

Solar Cells and Photovoltaics

9:00–10:45

chair: Prof. Michal Matuszewski

- WA01** Machine learning enhanced design optimization and knowledge discovery for multi-junction photonic power converters; K. Hinzer (1), R.F.H. Hunter (1), G.P. Forcade (1), Y. Grinberg (2), D. Paige Wilson (1), M. N. Beattie (1), C.E. Valdivia (1), M. de Lafontaine (1), L.-P. St-Arnaud (1), O. Höhn (3), D. Lackner (3), C. Pellegrino (3), J.J. Krich (1), A. Walker (4), H. Helmers (3); (1) SUNLAB, University of Ottawa, Ottawa (CAN); (2) Digital Technologies Research Centre, National Research Council Canada, Ottawa (CAN); (3) Fraunhofer Institute for Solar Energy Systems, Freiburg (GER); (4) Quantum and Nanotechnologies Research Centre, National Research Council Canada, Ottawa (CAN) – **(KEYNOTE)**
- WA02** Degradation Lifetime Modeling for Perovskite Photovoltaic Modules; M. Auf der Maur, P. Amiri; University of Rome Tor Vergata, Rome (ITA) – **(TOP 10%)**
- WA03** Optimal bandgap of GaInAsN for integration in a space four-junction photovoltaic cell; A. Fees (1,2), J. Mekki (3), T. Nuns (2), G. Almuneau (1); (1) LAAS-CNRS, CNRS, Université de Toulouse (FRA); (2) Office National d'études et de recherches Aérospatiales (Onera), Toulouse (FRA); (3) Centre National d'Études Spatiales (CNES), Toulouse (FRA) – **(TOP 10%)**
- WA04** Tight-binding model for mixed perovskites; A. Di Vito (1), A.L. Phan (1), D. Soccodato (1), A. Pecchia (2), M. Auf der Maur (1), A. Di Carlo (3); (1) University of Rome Tor Vergata, Rome (ITA); (2) CNR-ISMN, Monterotondo (Rome) (ITA); (3) CNR-ISM, Frascati (Rome) (ITA)

Laser Diodes I

11:15–13:05

chair: Prof. Ling Lu

- WB01** Trying to understand semiconductor lasers for 40 years; H. Wenzel; Ferdinand-Braun-Institut, Humboldt-Universität, Berlin (GER) – **(KEYNOTE)**
- WB02** Density Matrix Simulations of Quantum Cascade Lasers: Optical and Microwave Dynamics; C. Jirauschek; Technical University of Munich – TUM (GER) – **(INVITED)**
- WB03** Computational Techniques for Optimization and Design of InGaAlAs MQW Lasers; D. Paige Wilson (1), M. Mohsin (2), Y. Grinberg (3), B. Paquette (4), M. Rahim (2), K. Hinzer (5); (1) SUNLAB, School of Electrical Engineering and Computer Sciences, University of Ottawa (CAN); (2) Quantum and Nanotechnologies Research Centre, National Research Council of Canada (CAN); (3) Digital Technologies Research Centre, National Research Council of Canada (CAN); (4) Canadian Photonics Fabrication Centre, National Research Council of Canada (CAN); (5) SUNLAB, School of Electrical Engineering and Computer Sciences, Department of Physics, University of Ottawa (CAN)
- WB04** Asymmetric Electron-Hole Model for Gain-Switched InAs/InP Quantum Dot Laser; N. Dogru, I. Akkaya; Gaziantep University, Gaziantep (TUR)

chair: Prof. Lucio Andreani

- WC01** A few elementary studies on electromagnetic resonances; P. Lalanne; Laboratoire de photonique, numérique et nanoscience, Bordeaux (FRA) – **(KEYNOTE)**
- WC02** Intermediate Value Wavefront Matching Method for InP Waveguide Design; A. Schindler (1, 2), P. Runge (2), M. Schell (1, 2); (1) Technical University Berlin (GER); (2) Fraunhofer Heinrich Hertz Institute (GER) – **(TOP 10%)**
- WC03** Exciton Dynamics and Charge Carrier Transport in SiGeSn based MQW devices; A. Abdi, T. Alexewicz, D. Schulz; TU Dortmund University, Dortmund (GER)
- WC04** Ultrafast grating-based spin VCSELs; O.J. Hejtman (1), T. Fördös (1), M. Dems (2); (1) Faculty of Materials Science and Technology, VSB-Technical University of Ostrava (CZE); (2) Institute of Physics, Lodz University of Technology (POL)
- WC05** Controlling Spontaneous Emission in SiC Pillar Metasurface with Color Centers; M.A. Ahamad, F.A. Inam; Aligarh Muslim University (IND)

Thursday, 18

Detectors

8:45–10:25

chair: Prof. Karin Hinzer

- ThA01** Renormalization Theory and Monte Carlo Simulation of HgCdTe Single Carrier Avalanche Process; R. Xie; Shanghai Institute of Technical Physics, Chinese Academy of Sciences (CHN) – **(INVITED)**
- ThA03** Numerical Analysis of Different Impact Ionization Models in Single-Photon Avalanche Diodes; Li-An Huang (1), Jau-Yang Wu (2), and Yuh-Renn Wu (1); (1) National Taiwan University (TWN); (2) National Taiwan University of Science and Technology (TWN)
- ThA04** Triple-mesa InGaAs/InP SPAD for heterogenous integration with InP waveguides; D. Orlandelli, S. Sorrentino, L. Finazzi, F. Telesca, A. Tosi; Dipartimento di Elettronica, Informazione e Bioingegneria, Politecnico di Milano (ITA)
- ThA05** Small-signal compact modeling and TCAD validation of ultra-fast lateral Ge-on-Si waveguide photodetectors; M.G.C. Alasio(1), G. Divincenzo(1), A. Mudanò(1), G. Ghione(1), M. Vallone(1), M. Goano(1,2); (1) Department of Electronics and Telecommunications, Politecnico di Torino, Torino (ITA); (2) IEIIT-CNR, Torino (ITA)
- ThA06PD** Study of Hexagonal Photo-diode for Efficient Side-coupling to Silicon Wave-guide; S. Sant (1,2); (1) SemiVi LLC (CH); (2) Integrated Systems Laboratory, ETH Zurich (CH) – (Post-deadline)

Laser Diodes II

10:55–13:05

chair: Prof. Hans Wenzel

- ThB01** Topological-cavity surface-emitting laser; L. Lu; Institute of Physics, Chinese Academy of Sciences (CN) – **(KEYNOTE)**
- ThB02** Numerical study of spatio-temporal dynamics in all semiconductor PCSELs; L. Kuen (1), Eduard Kuhn (1), H. Wenzel (2), P. Crump (2), M. Radziunas (1); (1) Weierstrass Institute (WIAS), Berlin (GER); (2) Ferdinand-Braun-Institut (FBH), Berlin (GER) – **(INVITED)**
- ThB03** Simulation and Design of InGaAlAs O Band PCSELs; K. Boylan (1), D. Moodie (1), R. Spalding (1), S. Rihani (1), N. Hattasan (1), M. Silva (1), D. Childs (1), G. Berry (1), Jixiaochen (1), B. Lang (2), P. Sewell (2), A. Vukovic (2); (1) Huawei IRC, B83 Adastral Park, Martlesham Heath, Ipswich, IP5 3RE (UK); (2) School of Electrical and Electronic Engineering, University of Nottingham, Nottingham, NG7 2RD (UK)
- ThB04** Simulation of Finite-Size Photonic Crystal Surface Emitting Lasers with Efficient Eigenmode Solver; Y.-C. Han, G. Lin; National Yang Ming Chiao Tung University (TWN)
- ThB05PD** Experimental and theoretical study of frequency combs in hybrid lasers with a narrow-band mirror.; S. Cucco (1), A. Memon (2), C. Rimoldi (3), M. Novarese (2), L. L. Columbo (1), K. J. Boller (2), and M. Gioannini (1); (1) Department of Electronic and Telecommunication, Politecnico di Torino, Torino (ITA); (2) Department of Science and Technology, University of Twente, Enschede (NL); (3) Istituto Nazionale di Ottica (CNR-INO), Firenze (ITA) – (Post-deadline)

- ThC01** Efficient Photonic Component Analysis via AAA Rational Approximation; L. Zschiedrich (1), F. Betz (2), F. Binkowski (1,2), L. Kuen (3), M. Hammerschmidt (1), S. Burger (1, 2); (1) JCMwave GmbH, Berlin (GER); (2) Zuse Institute Berlin (GER); (3) Weierstrass Institute Berlin (GER) – **(INVITED)**
- ThC02** Tight-binding models for 3D photonic crystals; T. Christensen; Technical University of Denmark (DEN) – **(INVITED)**
- ThC03** A New Analytical Model of Gain in Highly-Saturated SOAs; P. Morel (1), B. Dumas Feris (2,1), T. Rampone (1), J. Ramadan (1), A. Sharaiha (1); (1) Bretagne INP, ENIB, Lab-STICC, CNRS, Brest (FRA) (2) School of Electrical Engineering, Pontificia Universidad Catolica de Valparaíso (PUCV), Valparaíso (CL)
- ThC04** Realization of high-speed 3D waveguide analysis model via transfer learning based on 2D-FDTD simulation; G. Ichisawa (1), S. Okada (2), and T. Amemiya (1); (1) Institute of Science Tokyo (JP); (2) National Institute of Information and Communications Technology (JP)
- ThC05** Instabilities in Pulse Propagation described by Generalized Nonlinear Schrödinger Equations; Shalva Amiranashvili (1), Uwe Bandelow (1), Raimondas Čiegis (2); (1) WIAS Berlin (GER); (2) Vilnius Gediminas Technical University (LTU)

VCSELs*16:20–17:40*

chair: Prof. Maciej Dems

- ThD02** Modelling coherent emission in transverse coupled cavity VCSELs; M. D'Alessandro (1), V. Torrelli (1), P. Debernardi (2), A. Gullino (2), K. Azimi Asrari (3), M. Lindemann (4), T. de Adelsburg Ettmayer (4), G. Giuliani (3-5), A. Tibaldi (1); (1) Politecnico di Torino (ITA); (2) CNR-IEIT Torino (ITA); (3) University of Pavia (ITA); (4) Ruhr-Universität Bochum (GER); (5) Julight Srl (ITA) – **(TOP 10 %)**
- ThD03** 1D vectorial simulations of anisotropic VCSELs; V. Torrelli (1,2), M. D'Alessandro (1,2), P. Debernardi (2); (1) Politecnico di Torino (ITA); (2) CNR-IEIT (ITA)
- ThD04** VCSEL thermal sources: a physics-based simulation approach; A. Gullino (1), M. D'Alessandro (1,2), V. Torrelli (1,2), A. Tibaldi (1,2), F. Bertazzi (1,2), P. Debernardi (1); (1) Consiglio Nazionale delle Ricerche, CNR (ITA); (2) Politecnico di Torino (ITA)
- ThD05** Comparative Study of Nano-Cylindrical Waveguide and Buried-SiO₂ Apertures in Blue InGaN VCSELs; L. Sharma, L. Persson, J. Ciers, and Å. Haglund; Chalmers University of Technology, Gothenburg (SWE)

NUSOD: A Journey Through 25 Years*17:40–18:40*

- ThE** Lessons learned in 25 years of NUSOD conferences; J. Piprek (USA) – **(KEYNOTE)**
- Closing Ceremony and awards

Abstracts

Numerical Simulations of Terahertz Quantum Cascade Laser Electronic Structure and Dynamics

Nikola Vuković
School of Electrical Engineering
University of Belgrade
Belgrade, Serbia
nvukovic@etf.bg.ac.rs

Milan Ignjatović
School of Electrical Engineering
University of Belgrade
Belgrade, Serbia
ignjatovic@etf.bg.ac.rs

Novak Stanojević
School of Electrical Engineering
University of Belgrade
Vlatom Institute of High Technologies
Belgrade, Serbia
novak.stanojevic@vlatom.com

Aleksandar Demić
School of Electronic and Electrical
Engineering
University of Leeds
Leeds, United Kingdom
A.Demic@leeds.ac.uk

Mihailo Stojković
School of Electrical Engineering
University of Belgrade
Belgrade, Serbia
sm180469d@student.etf.bg.ac.rs

Filip Perišić
School of Electrical Engineering
University of Belgrade
Belgrade, Serbia
fperisic12@gmail.com

Dragan Indjin
School of Electronic and Electrical
Engineering
University of Leeds
Leeds, United Kingdom
D.Indjin@leeds.ac.uk

Jelena Radovanović
School of Electrical Engineering
University of Belgrade
Belgrade, Serbia
radovanovic@etf.bg.ac.rs

Abstract—In this work, we present our recent numerical modelling results of the terahertz frequency quantum cascade laser active region. Electronic structure calculations are performed using the derivative transfer matrix method, while dynamics simulations are based on the Maxwell-Bloch formalism in various QCL configurations and model complexities.

Keywords— terahertz quantum cascade laser, transfer matrix method, density matrix, Maxwell-Bloch equations, passive mode-locking

I. INTRODUCTION

Terahertz quantum cascade lasers (THz QCLs) [1], [2] applications span from local oscillators for heterodyne spectroscopy in astronomy, to real-time THz imaging, biomedical imaging, dual-comb spectroscopy with QCL frequency combs, [3], etc. Recent thermoelectric cooling [4] and remarkable bandwidth coverage will drive this technology to new fields of research. In this contribution, we present our recent numerical modelling results of these devices in a Fabry–Perot (FP) configuration. In particular, the electronic structure is obtained using the derivative transfer matrix method, while the laser dynamics is modelled using macroscopic Maxwell–Bloch (MB) equations, owing to their intuitiveness, flexibility, and numerical efficiency. One of the major disadvantages of transfer matrix approaches is the necessity of sweeping parameters in a shooting-like manner, which results in lower precision in comparison to

finite difference methods (FDM). The recently developed machine precision derivative transfer matrix method [5] outperforms FDM by handling higher spatial resolution and having better time performance while computing eigenvalues with high precision and linear numerical complexity. The main idea of the derivative transfer matrix method (dTMM) is solving the eigenvalue problem by numerically finding the zeroes of the analytically calculated first derivative of the transfer matrix using numerically efficient zero finding algorithms, instead of using the numerically complex minima finding algorithms, as in the standard TMM.

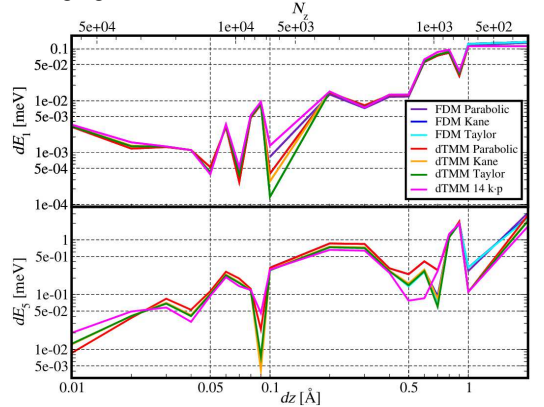


Fig. 1. Convergence of calculated first and fifth energy states vs spatial step size (bottom x-axis) and spatial resolution (top x-axis) for two-well record high-temperature THz QCL from [4]. The convergence is calculated as the energy difference between consecutive solutions as the spatial resolution is varied. The range of spatial step size was an array between 0.01 and 2 Å.

Fig. 1 shows dTMM versus FDM tested on the standard Schrödinger equation under effective mass approximation

This work was financially supported by the Science Fund of the Republic of Serbia, Grant No. 10504, "Ultra-short pulsations from TERAHERTZ quantum cascade laser using passive mode-LOCKing with graphene saturable absorber"-TERALOCK, Vlatom Institute of High Technologies under project 178, the Ministry of Science, Technological Development and Innovation of the Republic of Serbia under contract number: 451-03-65/2024-03/200103, European Cooperation in Science and Technology (COST) Action CA21159 PhoBioS.

with parabolic subbands, on two-band Kane nonparabolicity model and its Taylor approximation, and finally on a 4th-order Schrödinger equation that accounts for nonparabolic subbands using the 14-band $\mathbf{k}\cdot\mathbf{p}$ approach, which takes into account the interaction of the lowest conduction band with the light-hole and heavy-hole valence bands, split-off band, and three higher conduction bands.

Investigation of light-matter interactions with applications in metrology and ultrahigh-speed communications requires ultrashort terahertz pulses with large intensities, only recently achieved using passively mode-locked bound-to-continuum THz QCL [6]. Mode-locking operation with 4-ps-long pulses was realized using graphene-based saturable absorber (SA) stripes distributed along the laser cavity. Here, we perform self-consistent carrier transport density matrix simulations [7] of the QCL active region and extract the eigenenergies, optical dipole moments, scattering and dephasing rates, material gain, current density, and frequency using laser parameters from [8] for the structure operating at 3 THz. The active region dynamics is modelled using MB equations, with and without graphene saturable absorber, using full-wave treatment and also employing rotating wave approximation (RWA) and slowly varying envelope approximation (SVEA) to reduce the numerical load. We try a two-level model for mode-locking described in [9], but we are also interested in simulations with an arbitrary number of laser levels [10], [11]. Interesting dynamics arise when effective semiconductor MB equations are applied in modelling QCL in a self-mixing configuration, which was investigated in [12].

II. RESULTS AND DISCUSSION

Time evolution and spatial distribution of the electric field inside the resonator of length 2.37 mm are calculated by solving MB equations and adopting SVEA and RWA. Nine quantized levels per period in the active region were considered. Fig. 2 shows the electric field waveform on the right mirror without a saturable absorber. The electric field oscillates rapidly and the dominant frequency is around 3 THz. The simulation takes into account the attenuation at the mirrors, GVD and charge carrier diffusion.

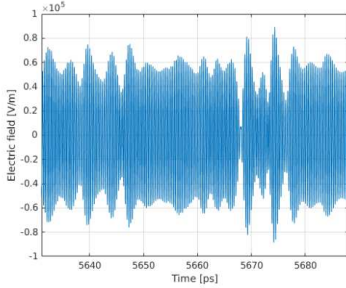


Fig. 2. Electric field waveform at the right mirror for the duration of one roundtrip without SA.

Simulation results when the effect of the SA is taken into account using the equation for slow absorber are shown in Fig. 3, where pulses with distinct intensity peaks can be seen occurring at time intervals of one roundtrip. Intensity waveform on the right mirror is a consequence of the movement of the pulse inside the resonator, where it is reflected alternately between the left and right mirrors.

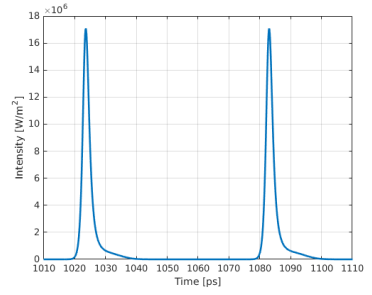


Fig. 3. The intensity at the right mirror when graphene SA is included.

III. CONCLUSION

In this paper, we present the results of our numerical simulations of the THz QCL active region, where we use a novel numerical method for electronic structure calculation and Maxwell-Bloch equations for modelling dynamics.

REFERENCES

- [1] J. Faist, F. Capasso, D. L. Sivco, C. Sirtori, A. L. Hutchinson, and A. Y. Cho, "Quantum Cascade Laser," *Science* (1979), vol. 264, no. 5158, pp. 553–556, Apr. 1994, doi: 10.1126/science.264.5158.553.
- [2] R. Köhler *et al.*, "Terahertz semiconductor-heterostructure laser," *Nature*, vol. 417, no. 6885, pp. 156–159, May 2002, doi: 10.1038/417156a.
- [3] G. Scalari and J. Faist, "30 years of the quantum cascade laser," *Commun. Phys.*, vol. 7, no. 1, p. 394, Dec. 2024, doi: 10.1038/s42005-024-01888-z.
- [4] A. Khalatpour, M. C. Tam, S. J. Addamane, J. Reno, Z. Wasilewski, and Q. Hu, "Enhanced operating temperature in terahertz quantum cascade lasers based on direct phonon depopulation," *Appl. Phys. Lett.*, vol. 122, no. 16, Apr. 2023, doi: 10.1063/5.0144705.
- [5] N. Stanojević *et al.*, "Derivative transfer matrix method: Machine precision calculation of electron structure and interface phonon dispersion in semiconductor heterostructures," *Comput. Phys. Commun.*, vol. 311, p. 109573, Jun. 2025, doi: 10.1016/j.cpc.2025.109573.
- [6] E. Riccardi *et al.*, "Short pulse generation from a graphene-coupled passively mode-locked terahertz laser," *Nat. Photonics*, Apr. 2023, doi: 10.1038/s41566-023-01195-z.
- [7] A. Demic *et al.*, "Infinite-Period Density-Matrix Model for Terahertz-Frequency Quantum Cascade Lasers," *IEEE Trans. Terahertz Sci. Technol.*, vol. 7, no. 4, pp. 368–377, Jul. 2017, doi: 10.1109/TTHZ.2017.2705481.
- [8] L. H. Li *et al.*, "Broadband heterogeneous terahertz frequency quantum cascade laser," *Electron. Lett.*, vol. 54, no. 21, pp. 1229–1231, Oct. 2018, doi: 10.1049/el.2018.6062.
- [9] L. Seitner, J. Popp, M. Haider, S. S. Dhillon, M. S. Vitiello, and C. Jirauschek, "Theoretical model of passive mode-locking in terahertz quantum cascade lasers with distributed saturable absorbers," *Nanophotonics*, vol. 13, no. 10, pp. 1823–1834, Apr. 2024, doi: 10.1515/nanoph-2023-0657.
- [10] C. Jirauschek, "Theory of Hybrid Microwave-Photonic Quantum Devices," *Laser Photon. Rev.*, vol. 17, no. 12, Dec. 2023, doi: 10.1002/lpor.202300461.
- [11] C. Jirauschek, M. Riesch, and P. Tzenov, "Optoelectronic Device Simulations Based on Macroscopic Maxwell-Bloch Equations," *Adv. Theory Simul.*, vol. 2, no. 8, Aug. 2019, doi: 10.1002/adts.201900018.
- [12] C. Silvestri, X. Qi, T. Taimre, and A. D. Rakić, "Frequency combs induced by optical feedback and harmonic order tunability in quantum cascade lasers," *APL Photonics*, vol. 8, no. 11, Nov. 2023, doi: 10.1063/5.0164597.

Solution-Processed Heterojunction Oxide Thin-Film Transistors for Displays

Wensi Cai

Key Laboratory of Optoelectronic
Technology & Systems (Ministry of
Education)

Chongqing University
Chongqing, China
wensi.cai@cqu.edu.cn

Abstract—In this study, we investigate the effect of channel layer thickness on the performance of InZnO/AlInZnO (IZO/AIZO) heterojunction thin-film transistors (TFTs) fabricated using a solution-based method. The conduction band offset at the heterointerface significantly influences the operating characteristics of TFTs, which can be modulated by adjusting the layer thickness, as confirmed through both experimental and computational analysis. Due to the formation of a quasi-two-dimensional electron gas system at the IZO/AIZO interface, optimized TFTs show a high mobility of $\sim 18 \text{ cm}^2/\text{Vs}$, a near-zero turn-on voltage and a current on/off ratio approaching 10^8 . The work offers valuable insights into the operating principles of oxide-based heterojunction TFTs and highlights their potential for next-generation printable displays.

Keywords—oxide semiconductors, thin-film transistors, solution-processed, displays

I. INTRODUCTION

Amorphous oxide semiconductor based thin-film transistors (TFTs) fabricated by sputtering have been commercialized as backplane drivers for flat panel displays due to their superior electrical characteristics [1]. However, sputtering is not compatible with next-generation printable electronics. TFTs prepared by solution-based methods are thus desirable, but it is still quite challenging for them to achieve a mobility greater than $10 \text{ cm}^2/\text{Vs}$. In addition, residue organic species can lead to serious stability issues. As a result, solution-processed oxide TFTs reported to date still far short of the performance requirements for next-generation high-resolution displays.

Recently, we demonstrated that by adjusting the annealing temperature and/or doping the film with slight metal cations, the mobility and stability of solution-processed TFTs can be improved [2-5]. However, the mobility and current on/off ratio achieved so far remain insufficient. One promising approach to further improve device performance is to stack oxide semiconductors with different mobilities and carrier concentrations, as this can induce the formation of a quasi-two-dimensional electron gas (q2DEG) system at the heterointerface. However, such bilayer TFTs often suffer from various drawbacks, including negative turn-on and threshold voltages, and instability under negative bias illumination stress (NBIS). For displays, achieving stable operation under bias conditions and a near-zero turn-on voltage is essential.

In this work, we report IZO/AIZO heterojunction TFTs fabricated via a solution-based method. The influence of channel layer thickness on electron distribution and resulting device performance is systematically investigated. Through a combination of experimental measurements and simulations,

we demonstrate optimized IZO/AIZO TFTs with a mobility of $17.6 \text{ cm}^2/\text{Vs}$ and a good stability. The underlying mechanisms of thickness-dependent performance are thoroughly analyzed. This study provides useful insights for the further development of heterojunction transistor architectures and shows potential for applications in next-generation displays.

II. EXPERIMENTAL PROCEDURES

A schematic of the prepared oxide TFT is shown in Fig. 1(a). The deposition process is similar to our previous work [6]. In this study, the AIZO layer (Al:In:Zn = 1:49.5:49.5 by volume) was fixed as 5.6 nm. Single channel IZO (In:Zn = 6:4 by volume) TFTs has a channel thickness of 7.2 nm. In the case of heterojunction TFTs, the IZO thickness was varied to 5, 7.2 and 10 nm, corresponding to devices labeled IZO-1/AIZO, IZO-2/AIZO and IZO-3/AIZO, respectively. Device simulations were performed using TCAD tools.

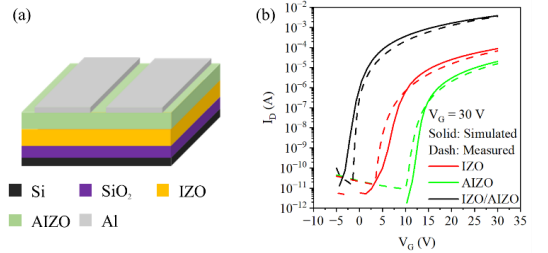


Fig. 1. (a) A schematic diagram showing the device structure. (b) Transfer characteristics of both simulated and measured device performance.

III. RESULTS AND DISCUSSIONS

The transfer characteristics of IZO and AIZO TFTs are shown in Fig. 1(b), along with simulated transfer curves generated using TCAD based on the respective band structures of IZO and AIZO. In both devices, electrons are primarily located at the dielectric/channel interface, as expected, and the simulated characteristics closely match the experimental results.

The combination of IZO and AIZO in a heterojunction structure leads to a substantially enhanced mobility - from $0.2 \text{ cm}^2/\text{Vs}$ (AIZO) and $0.6 \text{ cm}^2/\text{Vs}$ (IZO) to $17.6 \text{ cm}^2/\text{Vs}$ (IZO/AIZO). Additionally, the current on/off ratio is improved by approximately twofold, as shown in Fig. 1(b).

To investigate the conduction mechanism, TCAD simulations were carried out under both off- and on-states, as shown in Fig. 2. In the off and turn-on states, a potential well with a depth of $\sim 300 \text{ meV}$ forms near the IZO/AIZO heterointerface. However, under a large positive gate bias (on-state) the potential barrier is significantly reduced, and no potential well is observed. This suggests that free electrons

The work was financially supported by the National Natural Science Foundation of China (No. 62204027).

migrate from the heterointerface into the IZO channel near the IZO/SiO₂ interface. In single channel TFTs, electron accumulation occurs only at the channel/SiO₂ interface, while the heterojunction TFTs exhibit electrons accumulation at both the IZO/AIZO and the IZO/SiO₂ interface, indicating the formation of a quasi-2DEG system. This dual-interface electron accumulation enhances the total electron density in the channel and is considered the primary factor responsible for the enhanced device performance.

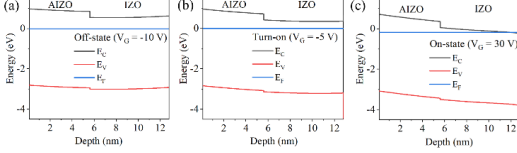


Fig. 2. TCAD simulation of band alignment in the (a) off-state, (b) turn-on state and (c) on-state.

To investigate the correlation between IZO thickness and the device performance, we conducted both TCAD simulations and experimental measurements, as shown in Fig. 3. A left shift of the transfer characteristics was observed with the increase of IZO thickness. This shift is attributed to the shift of CBM toward the Fermi level, leading to a greater energy band bending in thicker IZO cases and enhanced electron accumulation in the channel. However, excessive electron accumulation can make it difficult to turn off the TFT within the applied gate voltage range (IZO-3/AIZO), resulting in a reduced current on/off ratio. Additionally, the experimental data reveal that the mobility of IZO-3/AIZO TFT is slightly lower than that of the IZO-2/AIZO TFT. The reduction in mobility may be related to the limited Debye length, increased impurity scattering, or charge trapping induced by the defects in the thicker IZO layer.

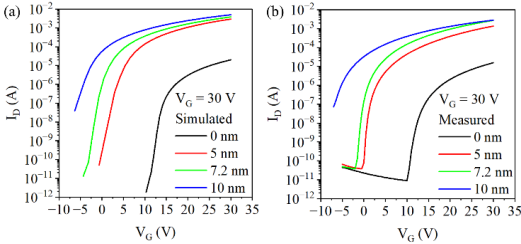


Fig. 3. Transfer characteristics of (a) simulated and (b) measured IZO/AIZO TFTs with a different IZO thickness.

The optimized device performance is achieved in TFTs featuring a 7.2 nm IZO/5.6 nm AIZO heterojunction channel, exhibiting a mobility of 17.6 cm²/Vs and a current on/off ratio

of $\sim 10^8$. To evaluate the suitability of these devices for displays, both positive bias stress (PBS, $V_G = +30$ V) and NBIS ($V_G = -30$ V, under WLED illumination) tests were conducted, as shown in Fig. 4. The TFTs demonstrate a good stability, with threshold voltage shifts of +1.4 V and -2.47 V after 1800 s of PBS and NBIS, respectively. These results represent significant improvements compared to single channel TFTs, and might be further improved by passivating the top channel surface to minimize the effects of ambient air exposure.

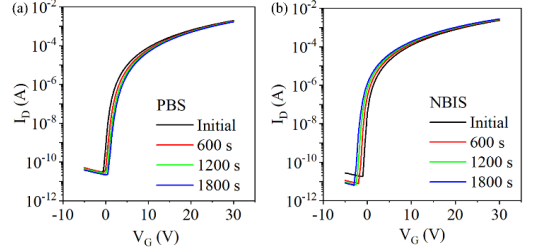


Fig. 4. Transfer characteristics of IZO/AIZO TFTs under (a) PBS and (b) NBIS conditions.

In summary, we investigated the effects of channel layer thickness on the performance of solution-processed heterojunction oxide TFTs through both computational simulations and experimental measurements. This work provides valuable insights into the design of high-performance oxide electronics and may contribute to the development of next-generation high-resolution, printable display technologies.

REFERENCES

- [1] J. Wager, "Oxide TFTs: A Progress Report," *Inf. Disp.*, vol. 32, no. 1, pp. 16-21, 2016.
- [2] W. Cai, H. Li, and Z. Zang, "One-Volt, Solution-Processed InZnO Thin-Film Transistors," *IEEE Electron Device Lett.*, vol. 42, no. 4, pp. 525-528, 2021.
- [3] W. Cai, M. Li, H. Li, Q. Qian, and Z. Zang, "Significant performance and stability improvement of low-voltage InZnO thin-film transistors by slight La doping," *Appl. Phys. Lett.*, vol. 121, no. 6, p. 062108, 2022.
- [4] W. Cai, H. Li, M. Li, and Z. Zang, "Performance enhancement of solution-processed InZnO thin-film transistors by Al doping and surface passivation," *J. Semicond.*, vol. 43, no. 3, p. 034101, 2022.
- [5] Y. Zheng, Z. Wu, H. Tong, Z. Zang, and W. Cai, "Effects of La Doping on Persistent Photoconductivity of Solution-Processed InZnO Thin-Film Transistors," *IEEE Trans. Electron Devices*, vol. 71, no. 10, pp. 6061-6066, 2024.
- [6] W. Cai, M. Li, S. Lu, Q. Qian, and Z. Zang, "Heterojunction Channel Engineering in Performance Enhancement of Solution-Processed Oxide Thin-Film Transistors," *IEEE Trans. Electron Devices*, vol. 70, no. 6, pp. 3085-3091, 2023.

Solvent-free Synthesis of Hybrid Copper Halides for High-performance White Emission and X-ray Imaging

Shuangyi Zhao, Zhigang Zang*

Key Laboratory of Optoelectronic Technology & Systems (Ministry of Education)

Chongqing University

Chongqing, China

shyzhao@cqu.edu.cn; zangzg@cqu.edu.cn

Abstract—Lead-free metal halides have received significant research interest due to their non-toxicity, cost-effectiveness, and remarkable stability coupled with superior optoelectronic characteristics. Nevertheless, conventional synthesis approaches for such materials predominantly rely on high-temperature solution processing in toxic solvents, characterized by prolonged reaction durations, which may hinder practical implementation. This work demonstrates a solvent-free strategy for room-temperature synthesis of hybrid copper halides ((TOA)CuBr₂, TOA: tetrabutylammonium) exhibiting bright green luminescence and exceptional stability. Because of these advantages, (TOA)CuBr₂ powders are successfully implemented as emitters and scintillators in white light-emitting diodes (WLEDs) and X-ray imaging systems. The WLEDs achieve a high color rendering index of 93 and a correlated color temperature of 5150 K. Furthermore, flexible scintillator films fabricated from these powders demonstrate high-performance X-ray detection performance, facilitating three-dimensional imaging via a space-reconfiguration method.

Keywords—Solvent-free synthesis, copper halides, white emission, X-ray imaging

I. INTRODUCTION

The rapid advancement of sustainable and interconnected societal development underscores the critical urgency to prioritize healthy living environments, safety assurance, and efficient display. Notably, white emission and X-ray scintillation imaging have emerged as pivotal technologies, with white light-emitting diodes (WLEDs) being extensively deployed for display and X-ray scintillation imaging serving essential roles in medical diagnostics and security screening applications. Current research reveals that the performance of both WLEDs and X-ray scintillation systems exhibits fundamental dependence on the optoelectronic characteristics and operational stability of materials. However, conventional implementations face inherent limitations: WLEDs (e.g., GaN-based semiconductors and rare-earth phosphors) suffer from prohibitive fabrication costs and chemical instability, while commercial scintillators (e.g., CsI:TI, Lu_{1.8}Y_{0.2}SiO₅:Ce, and CdWO₄) present challenges including toxicity and restricted radiation hardness.

Herein, a simple and green-chemistry mechanochemical strategy was proposed to synthesize hybrid copper halide

((TOA)CuBr₂, TOA: tetrabutylammonium) powders on a large scale at room temperature. As-prepared powders exhibited acceptable crystallinity and purity. The utilization of a simple and low-cost procedure, high reproduction, and avoidance of toxic solvents make this method ideal for commercialization of copper halides. Electronic structures and excited carrier distribution of (TOA)CuBr₂ were calculated and simulated, their emission is attributed to self-trapped excitons (STEs) in low-dimensional configuration. The efficient green emission of (TOA)CuBr₂ powders enable their promising potentials in WLEDs and X-ray scintillators. Remarkably, WLEDs involving (TOA)CuBr₂ powders, which were fabricated by depositing powders and red ceramics phosphors on optical chips, showed high color rendering index of 93 and a correlated color temperature of 5150 K, implying its potential feasibility for lighting and displaying. Furthermore, flexible X-ray films were achieved by mixing (TOA)CuBr₂ powders with polymethylmethacrylate (PMMA). Benefiting from a high light yield of fabricated scintillation films, they exhibited excellent imaging performance for complex and irregular objects. With the assistance of space reconfiguration, three-dimensional imaging results can be demonstrated.

II. EXPERIMENTAL SECTION

A. First-principle calculation

The electronic band structures are studied by density-functional theory (DFT), as implemented in Vienna ab initio simulation package (VASP). Electronic properties were calculated at the theory level of Perdew-Burke-Ernzerhof - HSE06 hybrid functional, projector augmented-wave and norm-conserving pseudopotential were employed to calculate the electronic band structure and density of states, respectively.

B. Preparation of lead-free powders, as well as fabrication of WLEDs and X-ray scintillators

CuBr and (TOA)Br at a stoichiometric molar ratio of 1:1 were mixed in a mortar and grinded for 15 min at atmosphere. Afterward, prepared powders were washed with isopropanol for two times and then transferred in an oven to vacuum for 1 h to evaporate the residual isopropanol at room temperature. Fabrication of WLEDs and X-ray scintillation screens has been reported by our previous works.

The authors extend their appreciation to National Natural Science Foundation of China (Nos. 11974063); Young Elite Scientists Sponsorship Program by CAST (2022QNR001), and Natural Science Foundation of Chongqing (No. CSTB2024NSCQ-MSX0507).

III. RESULTS AND DISCUSSION

With the assistance of crystal analysis, the crystal structure of (TOA)CuBr₂ is shown in Fig. 1a, indicating its zero-dimensional (0D) configuration with isolated [CuBr₂]⁻ clusters and organic molecules. Moreover, the carrier distribution for LUMO and HOMO states is simulated and exhibited in Fig. 1b, suggestion most of excited electrons and holes locate near Br and Cu atoms. As a result, the [CuBr₂]⁻ clusters are regarded as emissive centers.

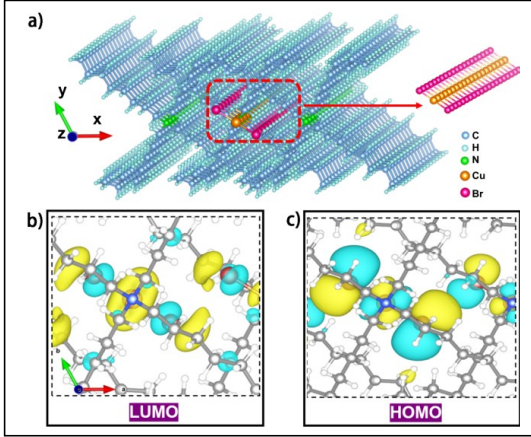


Fig. 1. a) Structure diagram of (TOA)CuBr₂. Electron wavefunctions of b) LUMO and c) HOMO of (TOA)CuBr₂.

Fig. 2a and b exhibit steady-state and transient photoluminescence (PL) spectra of as-prepared (TOA)CuBr₂ powders, respectively, which PL peak centered at 528 nm and PL lifetime is 53.2 μ s. The luminescent features are attributed to formation of self-trapped excitons (STEs) in low-dimension structures of (TOA)CuBr₂ with significant structural distortion when it is excited.

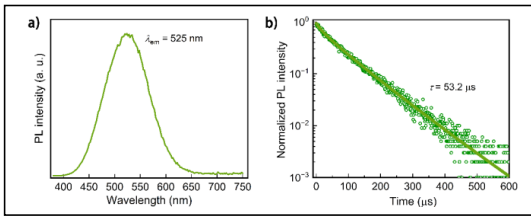


Fig. 2. a) Steady-state and b) transient PL spectra of (TOA)CuBr₂ powders at atmosphere.

Because of high-efficient and broadband green emission, well as and large-scale preparation of (TOA)CuBr₂ powders, they can be employed as emitters in WLEDs. The WLEDs were fabricated by coating mix of (TOA)CuBr₂ powders and red phosphors onto blue chips. Fig. 3a displays a series of electroluminescence (EL) spectra of fabricated WLEDs. As increase of driving voltages, EL intensity enhance gradually. Besides, the WLEDs demonstrate attractive performance, including a CIE color coordinate of (0.3418, 0.3612), a high CRI

of 93, and a CCT of 5150 K (Fig. 3b). The WLEDs were operated continuously at 6.5 V for 720 h, exhibiting excellent operating stability, as shown in Fig. 3c and d.

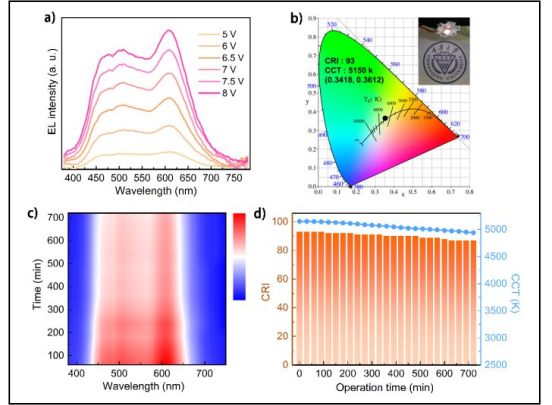


Fig. 3. a) Variety of WLEDs with increase of operating voltages. b) CIE chromaticity of the WLEDs. c) Pseudocolor image of EL and d) variety of CRI and CCT of WLEDs during the prolonged operation.

Moreover, flexible scintillation screens are fabricated and utilized in the X-ray imaging application. Due to the high emission efficiency of the (TOA)CuBr₂ powders, the clear X-ray imaging with 3D-reconfiguration of a spring pen is obtained and provided in Figure 4, confirming the prominent potential of the flexible screens in high-performance X-ray imaging.

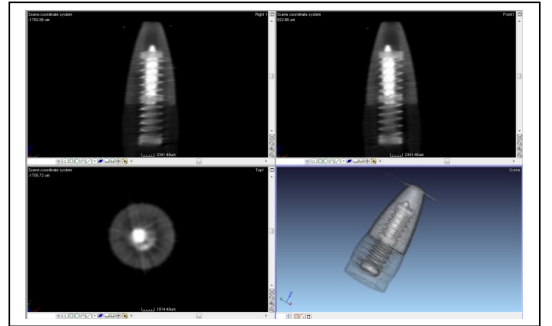


Fig. 4. 3D-reconfiguration of X-ray imaging for a spring pen with the (TOA)CuBr₂ screens.

References

- [1] S. Zhao, J. Zhao, S. M. H. Qaid, D. Liang, K. An, W. Cai, Q. Qian, Z. Zang, "White emission metal halides for flexible and transparent x-ray scintillators," *Appl. Phys. Rev.*, 2024, vol. 11, pp. 011408.
- [2] S. Zhao, Z. Jia, Y. Huang, Q. Qian, Q. Lin, Z. Zang, "Solvent-Free Synthesis of Inorganic Rubidium Copper Halides for Efficient Wireless Light Communication and X-Ray Imaging," *Adv. Funct. Mater.*, 2023, vol. 33, pp. 2305858.
- [3] S. Zhao, C. Chen, W. Cai, R. Li, H. Li, S. Jiang, M. Liu, Z. Zang, "Efficiently Luminescent and Stable Lead-free Cs₃Cu₂Cl₅@Silica Nanocrystals for White Light-Emitting Diodes and Communication," *Adv. Optical Mater.*, 2021, pp. 210030.

Bound States in the Continuum Empowering Maximum Chirality and Strong Coupling Regime in Plasmonic Metasurfaces

Lucio Andreani
Physics Department “A. Volta”
University of Pavia
27100 Pavia, Italy
lucio.andreani@unipv.it

Hanan Ali
Physics Department “A. Volta”
University of Pavia
27100 Pavia, Italy
hanan.ali01@universitadipavia.it

Giovanni Pellegrini
Physics Department “A. Volta”
University of Pavia
27100 Pavia, Italy
giovanni.pellegrini@unipv.it

Emilija Petronijevic
Department S.B.A.I.
Sapienza University of Rome
00161 Rome, Italy
emilija.petronijevic@uniroma1.it

Abstract— We theoretically demonstrate that Bound States in the Continuum (BICs) can appear in plasmonic metasurfaces, specifically in a metal nanohole array with broken symmetry, and can be exploited to yield a strong chiral response with high Q-factor and local field enhancement. When the nanoholes are filled with a medium supporting a Lorentz-like resonance, the interaction between the quasi-BIC and the active medium can give rise to strongly coupled hybrid modes, which represent chiral polariton BICs in the plasmonic system.

Keywords—Plasmonic metasurfaces, bound states in the continuum, chirality, strong-coupling regime

I. INTRODUCTION

Maximizing the chiral response in photonic and plasmonic systems is a key goal in current nanophotonics research. Bound states in a continuum (BIC) in dielectric metasurfaces are known to yield ultra-narrow resonances, with low radiative losses and enhanced radiation-matter interaction [1]. They give rise to topological singularities that split into circularly polarized states (CPS) with maximum chirality upon symmetry breaking [2,3]. In this work, we demonstrate that BICs can also appear in plasmonic metasurfaces and can be exploited to yield a strong chiral response.

II. CHIRAL BOUND STATES IN THE CONTINUUM IN A PLASMONIC NANOHOLE ARRAY

We consider a metasurface consisting of a gold layer on glass, which is etched with a square lattice of nanoholes (Fig. 1a), whose shape is deformed from circular to oval (Fig. 1b). The symmetry breaking is such that $r_2 + r_3 = 2r_1$, i.e., it maintains the area of the circular nanoholes.

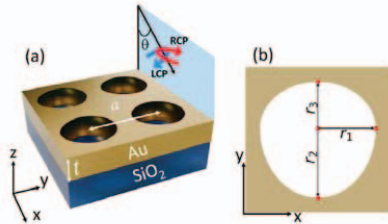


Fig. 1 (a), (b): Sketch of the metasurface with broken-symmetry holes studied in this work, with Au thickness $t = 100$ nm. Light is incident from the air along the xz orientation.

Upon symmetry breaking, a quasi-BIC appears in absorption spectra at the low-energy side of the surface-plasmon polariton (SPP) peak. The Q-factor of the q-BIC is much larger compared to the Q-factor of the SPP resonance. At a finite angle of incidence along the xz orientation, all mirror symmetries are broken and the system acquires extrinsic chirality. The BIC has a strongly chiral optical response with nearly unit circular dichroism (CD), see Fig. 2 – again in contrast with the SPP, which is very weakly chiral. The maximum CD defined as $CD = (A_{lcp} - A_{rcp}) / (A_{lcp} + A_{rcp})$ is nearly independent of the deformation, thus the chiroptical response is robust with respect to structure parameters. This is a definite advantage of the design. Analysis of the symmetry properties and of the local field profiles confirms that the resonance is indeed a symmetry-protected BIC, with strong enhancement of the local electric field [4]. Maximum CD is also found in calculated emission spectra.

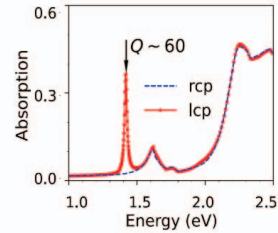


Fig. 2 Absorption spectra for a metasurface with lattice constant $a = 500$ nm, $r_1 = 200$ nm, $r_2 = 240$ nm, $r_3 = 160$ nm, at $\theta = 4^\circ$ for right and left circular polarizations (rcp, lcp), showing a BIC resonance with chiral response.

Next, we include an active medium at the bottom of the nanoholes (which can consist, e.g., in colloidal quantum dots) and consider the interaction of the BIC with a Lorentz-like resonance of the active medium. On increasing the oscillator strength of the resonance, the interaction between the BIC and the active medium gives rise to two absorption peaks that show a vacuum Rabi splitting, typical of the strong coupling regime. For oval holes at finite incidence angle, as shown in Fig. 3, the strongly coupled quasiparticles are chiral with polaritons being formed only for left circular polarization and with nearly maximum CD.

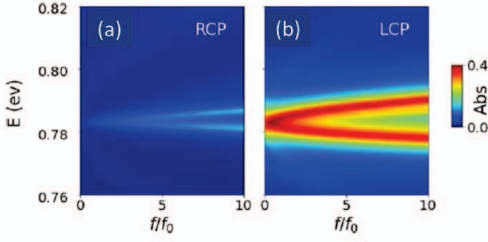


Fig. 3 Absorption for a metasurface with $a = 1000$ nm, $r_1 = 400$ nm, $r_2 = 480$ nm, $r_3 = 320$ nm, at $\theta = 3^\circ$ for rcp (a) and lcp (b). The metasurface contains a resonant medium at the bottom of the nanoholes, in a ring of 50 nm width and 10 nm height, with a linewidth $\gamma = 0.002$ eV. The absorption map is shown as a function of the oscillator strength of the active medium, in units of f_0 where $f_0/V = 10^{24}$ m $^{-3}$.

Absorption maps as a function of the angle of incidence show the typical anticrossing behaviour of the strong coupling regime [5]. Thus, the present metasurface with active medium supports the formation of chiral hybrid polariton BICs, which are the analog of polaritons in microcavities [6] or in photonic crystal slabs [7-9].

III. CONCLUSIONS

The results of the present work may prove useful in order to maximize the chiral response of plasmonic metasurfaces by means of a simple design concept, which is based on BICs with symmetry breaking. The results can also be used in order to demonstrate strong light-matter coupling with hybrid

chiral polariton BICs in plasmonic metasurfaces, possibly leading to quantum and nonlinear phenomena related to polariton interactions.

- [1] C. W. Hsu, B. Zhen, A. D. Stone, J. D. Joannopoulos, M. Soljacic, "Bound states in the continuum," *Nat. Rev. Mater.* 1, 16048 (2016).
- [2] W. Liu, B. Wang, Y. Zhang, J. Wang, M. Zhao, F. Guan, X. Liu, L. Shi, and J. Zi, "Circularly polarized states spawning from bound states in the continuum," *Phys. Rev. Lett.* 123, 116104 (2019).
- [3] L. Zagaglia, S. Zanotti, M. Minkov, M. Liscidini, D. Gerace, and L.C. Andreani, "Polarization states and far-field optical properties in dielectric photonic crystal slabs," *Opt. Lett.* 48, 5017 (2023).
- [4] H. Ali, S. Zanotti, G. Pellegrini, E. Petronijevic, and L.C. Andreani, "Maximum Chirality Empowered by a Bound State in a Continuum in a Plasmonic Metasurface," *ACS Appl. Opt. Mat.* 2, 825 (2024).
- [5] H. Ali, G. Pellegrini, E. Petronijevic, and L.C. Andreani, "Strong coupling regime of a quasi-bound state in a continuum in a plasmonic nanohole array with broken symmetry," *Optics Express* 33, 554841, pp. 19700-19714 (2025).
- [6] C. Weisbuch, M. Nishioka, A. Ishikawa, Y. Arakawa, "Observation of the coupled exciton-photon mode splitting in a semiconductor quantum microcavity," *Phys. Rev. Lett.* 69, 23 (1992).
- [7] D. Gerace and L.C. Andreani, "Quantum theory of exciton-photon coupling in photonic crystal slabs with embedded quantum wells," *Phys. Rev. B* 75, 235325 (2007).
- [8] D. Bajoni, D. Gerace, M. Galli, J. Bloch, R. Braive, I. Sagnes, A. Miard, A. Lemaître, M. Patrini, and L.C. Andreani, "Exciton polaritons in two-dimensional photonic crystals," *Phys. Rev. B* 80, 201308(R) (2009).
- [9] Simone Zanotti, Hai Son Nguyen, Momchil Minkov, Lucio C. Andreani, and Dario Gerace, "Theory of photonic crystal polaritons in periodically patterned multilayer waveguides," *Phys. Rev. B* 106, 115424 (12 pp) (2022)

Investigation on digital twin model of 3x3 Mach-Zehnder Interferometer mesh

Teng Ma
Politecnico di Torino
Torino, Italy
teng.ma@polito.it

Andrea Marchisio
Politecnico di Torino
Torino, Italy
andrea_marchisio@polito.it

Francesco Da Ros
Technical University of Denmark
Lyngby, Denmark
fdro@dtu.dk

Vittorio Curri
Politecnico di Torino
Torino, Italy
vittorio.curri@polito.it

Paolo Bardella
Politecnico di Torino
Torino, Italy
paolo.bardella@polito.it

Andrea Carena
Politecnico di Torino
Torino, Italy
andrea.carena@polito.it

Abstract—A physics-based digital twin model of a 3-by-3 Mach-Zehnder Interferometer (MZI) mesh is established by interpolating the experimental data with an accurate mathematical representation, then utilized to investigate the wideband capabilities of the device to implement programmable logic functions. Most of the evaluated functions perform correctly over a broad wavelength range (1524 nm – 1568 nm) under the voltage configuration determined at 1550 nm. The findings showcase the potential of digital twin model in Photonic Integrated Circuit (PIC) design, allowing novel designs in photonic computing and telecommunication applications.

Index Terms—Digital twin model, Mach-Zehnder Interferometers, Wideband capability.

I. INTRODUCTION

The digital twin, a concept first adopted in the aerospace industry, was defined as “an integrated multiphysics, multi-scale, probabilistic simulation of an as-built vehicle or system that uses the best available physical models, sensor updates, fleet history, etc., to mirror the life of its corresponding flying twin” [1]. Due to its capability to characterize and model electronic devices accurately and efficiently, the digital twin exhibits favorable prospects in the semiconductor industry [2].

Photonic Integrated Circuits (PICs) are an emerging technology that focuses on detection, generation, transmission, and manipulation of photons [3], commercially applied in several fields such as optic communication, biomedicine, and photonic computing, exploiting the physics of structures such as Mach-Zehnder Interferometer (MZI). The digital twin model introduced in [4] is adopted in this work to verify the capability of a thermally tuned 3-by-3 MZI mesh [5] to implement user-defined logic functions over a wide wavelength range. The results show that the fitted model can successfully perform wideband logic operations, implying promising potential for digital twin modeling of PIC.

II. DIGITAL TWIN MODEL

The reference device (Fig. 1) is a 3-by-3 MZI mesh realized on a Silicon-on-Insulator (SOI) platform, part of a C-band optical switch developed by the Technical University of Denmark (DTU) [6], where the input signals are linearly summed

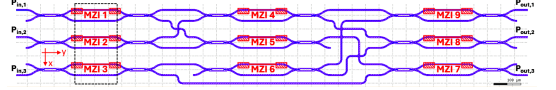


Fig. 1. Mask of the reference device. The Ti heaters are shown in red, the waveguides in blue. The black rectangle defines the area for thermal analysis.

at the three output ports by thermal tuning of the MZIs. The single MZI comprises two 2-by-2 Multi-Mode Interferometers (MMIs) and $\sim 267 \mu\text{m}$ long bent waveguides, while thermal tuning is regulated by a Thermo-Optic Phase Shifter (TOPS). A transmission matrix-based model is developed to accurately describe the single component [4]:

$$\bar{T}_{\text{MMI}_p} = \begin{bmatrix} \alpha_{\text{MMI}_p} \sqrt{\gamma_1} & j\alpha_{\text{MMI}_p} \sqrt{1-\gamma_2} \\ j\alpha_{\text{MMI}_p} \sqrt{1-\gamma_1} & \alpha_{\text{MMI}_p} \sqrt{\gamma_2} \end{bmatrix} \quad (1)$$

$$\bar{T}_p = \begin{bmatrix} e^{-\alpha_p L} e^{j(\kappa n_{\text{eff},1}(T)L + \delta\varphi)} & 0 \\ 0 & e^{-\alpha_p L} e^{j(\kappa n_{\text{eff},2}(T)L - \delta\varphi)} \end{bmatrix} \quad (2)$$

where α_{MMI_p} , $p = \{\text{in}, \text{out}\}$ are the insertion losses for input and output MMIs, γ_j are the corresponding splitting ratios, α_p are the propagation losses through the waveguide, L is the length of the MZI arms, $\kappa = \frac{2\pi}{\lambda}$ is the wavenumber at operating wavelength λ . The $\delta\varphi$ terms represent phase correction that can be adjusted with the optimization routine (e.g. particle swarm optimization (PSO) [7]) to fit experimental data. The two quantities $n_{\text{eff},1}(T)$ and $n_{\text{eff},2}(T)$ are the effective refractive indices of the MZI's waveguides. The Ti heater undergoes Ohmic heating when an external voltage is applied, resulting in modified optical properties of the waveguides. The dependency of n_{eff} on the temperature is expressed as a first-order Taylor expansion:

$$n_{\text{eff}}(T(V)) = n_{\text{eff}}(T_0) + \left. \frac{dn_{\text{eff}}}{dT} \right|_{T_0} (T(V) - T_0) \quad (3)$$

Thermal crosstalk can significantly affect the device behavior: in the area shown in the black rectangle in Fig. 1, the temperature variation caused by a single heater can perturb the temperature (and the corresponding effective index) of all the vertically stacked (x direction) waveguides. We assume, at

the same time, that this coupling effect is negligible in the y direction. The temperature distribution in the x direction can be established by summing the independent contributions from the three heaters, solving the 1D heat equation for each source individually, under the ideal adiabatic boundary conditions. The obtained results have been validated using a complete 3D thermal simulation, performed in COMSOL Multiphysics, of the heaters - waveguides system. Fig. 2 shows the spatial distribution of temperature variation when different voltages are applied to 3 heaters, indicating that the approximated 1D method accurately mimics COMSOL thermal simulations. From this example, it is immediately evident that thermal cross-talk affects the device, and is non-negligible not only between neighboring MZIs, but also between the two arms of the same MZI. The adopted numerical approach is convenient for its computational efficiency. Using the temperature varia-

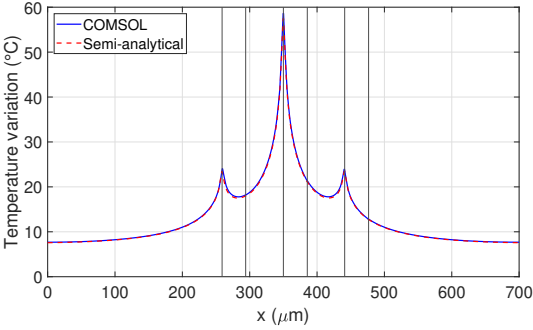


Fig. 2. Example of spatial distribution of temperature variation for $V_{in,1} = 1V$, $V_{in,2} = 2V$, and $V_{in,3} = 1V$ applied simultaneously to the three heaters, simulated in COMSOL Multiphysics (solid blue line) and restored using numerical method (dashed red line).

tions estimated with this method, we can compute $n_{eff}(T(V))$ in each waveguide, which can then be used in (2). The total transmission matrix can be then obtained by cascading the three constitutive elements of the MZI, which can be used to compute the output field at the two output ports of the MZI:

$$\bar{T} = \bar{T}_{MMI_{out}} \bar{T}_p \bar{T}_{MMI_{in}} \quad (4)$$

We fine-tuned the parameter $\delta\varphi$ in Eq. (2) by adopting the PSO algorithm, to precisely fit the experimental measurements executed to assess the behavior of the real device. The method successfully accounts for possible manufacturing imperfections, effectively implementing a well-established digital twin model of the reference device.

III. EVALUATION OF WIDEBAND PROGRAMMABILITY

The digital twin model was deployed in an initial assessment of the capabilities of the mesh as a programmable logic device [4]. A data set with 6 million entries was created with randomized values of the nine MZIs driving voltages, considering the $2^3 = 8$ possible permutations of the signals at the three input ports, assumed as Boolean signals with values 1 or 0. From the statistical analysis of the power

levels at the three output ports, we estimated three thresholds to convert the output levels into digital states. After this preliminary investigation, we then used the PSO method to find the best control voltages to implement a set of logic functions at the three output ports (such as AND of the three inputs at output port 1, XOR at output port 2, and OR at output port 3). We numerically verified that the device can be used to implement a vast number of logical functions, from the simplest ones (NAND, NOR) to more complex ones (such as 2's complements of the 3 bit binary number at the input); it is also possible to obtain the AND or the OR of the optical signals at port 1 and port 2, depending on the value of the signal at port 3, thus implementing an optically-programmable gate. Although the first analysis was performed at 1550 nm, the device is subsequently simulated over a wider wavelength interval ranging from 1524 nm to 1568 nm. This operation required a proper evaluation, based on FDTD simulations performed in Synopsys RSoft™ of the dispersion of the effective index and the coupling coefficients. The digital twin exhibits the wideband programmability expected from the reference device, being able to consistently implement a plethora of programmable logic functions on the entire C-band, proving the potential of the model to explore the properties of PICs.

IV. CONCLUSIONS AND OUTLOOK

We developed a digital twin model of a 3x3 MZI mesh by calibrating the model parameters to fit the experimental data, thus describing crucial effects such as thermal crosstalk and tolerances in the production process. Applying the combination of driving voltages determined by the model at 1550 nm, we estimate the capability of the reference device to perform multiple programmable logic functions on the entire C-band.

REFERENCES

- [1] E. Glaesgen and D. Stargel, *The Digital Twin Paradigm for Future NASA and U.S. Air Force Vehicles*, p. 7. 2012.
- [2] S. Behrendt, T. Altenmüller, M. C. May, A. Kuhnle, and G. Lanza, "Real-to-sim: automatic simulation model generation for a digital twin in semiconductor manufacturing," *Journal of Intelligent Manufacturing*, 2025.
- [3] L. Coldren, S. Corzine, and M. Mashanovitch, *Diode Lasers and Photonic Integrated Circuits*. Wiley Series in Microwave and Optical Engineering, Wiley, 2012.
- [4] A. Marchisio, L. Tunesi, E. Ghillino, V. Curri, A. Carena, and P. Bardella, "Comprehensive thermal crosstalk model of meshed MZI topologies for neuromorphic computing," in *AI and Optical Data Sciences VI*, vol. 13375, p. 133750F, SPIE, 2025.
- [5] A. Marchisio, A. Cem, Y. Ding, V. Curri, A. Carena, F. Da Ros, and P. Bardella, "Optimization of 3x3 neuromorphic photonic network for programmable Boolean operations," in *SPIE Photonic West: Physics and Simulation of Optoelectronic Devices XXXII*, vol. 12880, pp. 191104-8, 2024.
- [6] Y. Ding, V. Kamchevska, K. Dalgaard, F. Ye, R. Asif, S. Gross, M. J. Withford, M. Galili, T. Morioka, and L. K. Oxenløwe, "Reconfigurable SDM switching using novel silicon photonic integrated circuit," *Scientific Reports*, vol. 6, no. 1, p. 39058, 2016.
- [7] A. Marchisio, E. Ghillino, V. Curri, A. Carena, and P. Bardella, "Particle swarm optimization-assisted approach for the extraction of VCSEL model parameters," *Opt. Lett.*, vol. 49, pp. 125-128, 1 2024.

Novel Variable Confinement SOAs Modelling

Célia Cruz
Processing Team
III-V Lab
Palaiseau, France
celia.cruz@3-5lab.fr

Cosimo Calò
Processing Team
III-V Lab
Palaiseau, France
cosimo.calo@3-5lab.fr

Hélène Carrere
LPCNO - INSA
Université de Toulouse
Toulouse, France
carrere@insa-toulouse.fr

Abstract - We have developed a numerical model for variable-confinement semiconductor optical amplifier (VC-SOA) operation which takes into account carrier recombination and loss mechanisms. It provides simulations of gain, noise figure and power saturation effects across different designs, serving as a valuable tool for device optimization.

Keywords – VC-SOAs, design, material engineering, simulation

I. INTRODUCTION

To meet the ever-growing demand for higher capacity in optical telecommunication networks, semiconductor optical amplifiers (SOAs) are promising due to their broadband optical gain. However, to achieve optimal performance, they require careful engineering of the active material and device design. In this context, novel variable confinement SOA architectures have been developed to locally adjust the active area to optical confinement ratio, enabling more efficient simultaneous optimization of gain, saturation output power (P_{sat}), and noise figure (NF) [1]. The numerical model presented enables accurate performance prediction and is validated against experimental data, positioning it as a reliable tool for the design of high-performance SOAs.

II. VARIABLE CONFINEMENT SOA MODELLING

The model we developed is based on M. J. Connelly's work [2] with appropriate modifications to tailor new multi-quantum wells (MQWs) slab-coupled optical waveguide (SCOW) [3]. The energy levels are computed by solving the Schrödinger equation for a finite square potential well along the growth direction, assuming parabolic band dispersion in the in-plane direction for both conduction and valence bands [4]. The bandgap energy is derived from the active zone composition, taking into account strain and bandgap shrinkage effects. Subsequently, the carrier density, quasi-Fermi levels, Fermi-Dirac distribution functions, and the material gain coefficient are numerically calculated for MQWs structures. The travelling-wave equations are solved for the SOA discretized into spatial slices, taking into account the non-uniform carrier density distribution. Thus, amplified spontaneous emission (ASE) powers, gain, noise figure and saturation output power are extracted under steady-state condition. For further details on the model, refer to [4] and herein references.

The novel variable confinement structures are 4-mm long and feature an active layer of thickness d composed of four compressively-strained $\text{Ga}_{0.19}\text{In}_{0.804}\text{As}_{0.784}\text{P}_{0.216}$ QWs grown by gas source molecular beam epitaxy, engineered to emit across the C+L band. The design enables to bind multiple electron and hole energy levels and supports broadband emission in the Transverse Electric (TE) polarization mode. This TE dominance arises from strong electron-to-heavy-hole transitions and is further enhanced by the asymmetric cladding of SCOW structures [3]. To this architecture, we add a high-confinement (HC) region thanks to a p-doped high-

index upper layer, which pulls the optical mode towards the quantum wells, enhancing optical confinement Γ in the active area. This layer is etched in tapers at the edges to gradually reduce the optical confinement, thereby forming the low-confinement (LC) regions (Fig. 1). The waveguide width w is also increased at the ends, enabling a transition from a low $d.w/\Gamma$ ratio in HC regions to a high ratio in LC regions.

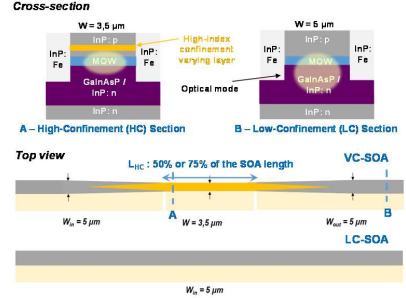


Fig. 1. Variable confinement SOA and investigated design variants.

The model has been adjusted to account for optical confinement, waveguide width and loss coefficient α variations along the simulated devices. The designs are simulated using the Fimmprop software (PhotonDesign) to extract the optical confinement along the SOA. Variations in waveguide width are implemented into the model and tailored to each specific simulated structure. Finally, intrinsic losses, approximated by fitting to the experimental data, are assumed to vary with Γ because the optical mode is shifted away from the lossy upper p-cladding in LC sections. Nevertheless, intrinsic losses remain one of the most uncertain parameters in the model, though it still allows meaningful trend analysis. According to the literature, Γ/α_0 remains nearly constant along the structure - a condition that was applied in this work [1].

III. VARIABLE CONFINEMENT SOA DESIGN STUDY

As depicted in Fig. 1, the fabricated structures feature a 3.5- μm -wide waveguide, flared to 5 μm at both ends. The high-index upper layer extends over 50% or 75% of the SOA length and is positioned centrally. We first measure and simulate the gain spectra and NF of the 75% (green) and 50% HC (orange) regions designs at 700 mA, along with a reference SOA with a constant 5- μm wide waveguide and without HC region - referred to as the LC SOA (blue). Both experimental and calculated results are reported in Fig. 2.

The model accurately predicts the gain trend of these variable confinement designs, with the highest measured on-chip gain (33 dB) obtained for the 75% HC design at 1580 nm - 10 dB higher than the standard LC design gain. However, the measured gain spectra of both HC designs are narrower than simulated, likely due to thermal effects arising from device heating at high gain levels. This discrepancy is particularly pronounced in the 75% HC design.

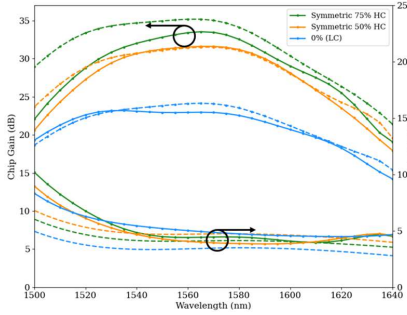


Fig. 2. Measured (solid line) and calculated (dashed line) small-signal chip gain and NF of the 3 designs biased at 700 mA.

Furthermore, the simulated and experimental NF values are in fairly good agreement. But, it is more challenging to accurately simulate the NF given the various influencing factors, especially propagation losses, and differential gain. The measured NF of the LC SOA (blue line) appears higher despite its lower I , which should typically reduce losses by reducing the optical mode confinement in the lossy p-doped cladding. This is likely due to the lower gain level. On the other hand, the model predicts that the 75% HC design should exhibit a lower NF than the 50% HC design due to its longer HC section enhancing the material gain when the measurements show no significant differences. This discrepancy could be due to an underestimation of losses – potentially higher than simulated in the HC regions due to the upper p-doped layer – and/or the lower measured gain compared to simulations, due to heating effects. Moreover, under the same operating conditions, the simulated P_{sat} has been confronted with experimental results as reported in Fig. 3. The simulated data are in very good agreement with the measured results. The P_{sat} of the 50% HC design is slightly higher than the one of the 75% HC design, consistent with the model's prediction at 700 mA and 1580 nm. Additionally, the LC SOA P_{sat} was measured to be 18.5 dBm, near the simulated value of 19 dBm, which is higher than that of both VC-SOAs designs, as expected due to its higher active area to optical confinement ratio ($d.w/I$).

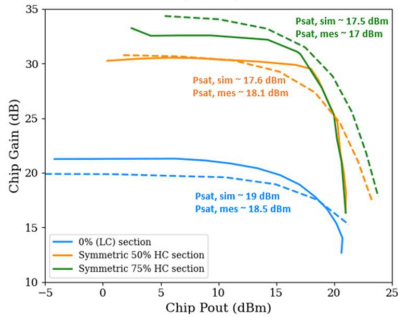


Fig. 3. Measured (solid line) and calculated (dashed line) chip gain and NF of the 3 designs at 1580 nm and 700 mA.

For a standard SOA, I can be adjusted through material engineering to achieve a given chip gain, and corresponding P_{sat} and NF. In fact, the $d.w/I$ ratio is minimized for a HC-type SOA with a constant A-cross-section and maximized for

a LC-type SOA with an B-cross-section (Fig. 1). Both exhibiting its own specific performance characteristics. However, in a complete VC-SOA structure with both HC and LC-type cross-sections, predicting performances becomes more complex and can be assisted by modeling. In Fig. 4.a. simulations using the developed model indicate that varying the ratio of the HC section length results in very little P_{sat} and NF variations at a given current (700 mA), with only a slight P_{sat} increase observed when the HC section length is reduced, but leading to gain degradation (Fig. 4.b).

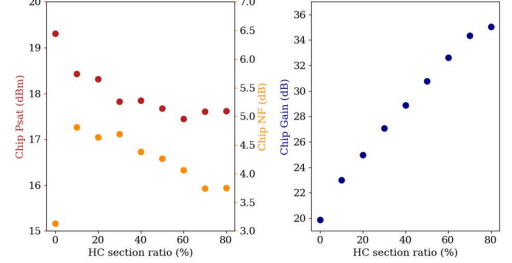


Fig. 4. Chip P_{sat} , NF (a) and gain (b) vs. HC ratio of a symmetric VC-SOA.

The VC-SOA design will therefore require LC sections to improve P_{sat} compared to the HC SOA exhibiting lower values compared to the LC SOA, combined with a HC section to improve chip gain level and NF. Thus, the HC section must therefore be long enough to obtain the desired level of gain at a given current (700 mA in Fig. 4) and can be easily chosen since both P_{sat} and NF value vary only slightly with HC section length for this design. The goal is to achieve the needed gain level at a reasonable injection current to reduce power consumption. In this respect, the model proves to be very useful for VC-SOA design, as it allows simulation of both material and geometric parameters along the device. Further work will consider asymmetric designs where the HC section is shifted toward the SOA input facet to evaluate its impact on the overall NF. Indeed, this positioning can be critical, as noise generated near the input is further amplified along the device.

IV. CONCLUSION

In this work, we presented a numerical model for gain, NF and P_{sat} operation of novel VC-SOA architectures. The model developed accurately reproduces key performance trends, making it a valid tool to assist future SOAs design.

ACKNOWLEDGMENT

The author thanks N. Vaissière, A. Wilk, O. Delorme, C. Fortin, I. Mijovic, K. Mekhazni for their contribution.

REFERENCES

- [1] S. Yu, A. Gallet, I. Demitzioglou, S. Azouigui, N. El Dahdah, R. Brenot, "New SOA design with large gain, small noise figure, and high saturation output power level", *J. Quant. Electron.*, vol. 60, no. 2, 2024.
- [2] M. J. Connelly, *Semiconductor optical amplifiers*. Springer NY, 2002.
- [3] P. Juodawlkis, J. Plant, W. Loh, L. Missaggia, F. O'Donnell, D. Oakley and *al.*, "High-power, low-noise 1.5- μ m slab-coupled optical waveguide (SCOW) emitters physics, devices, and applications", *J. Quant. Electron.*, vol. 17, no. 6, 2011.
- [4] C. Cruz, C. Calo, F. Pommereau, A. Wilk, O. Delorme, N. Vaissiere, J. Decobert and H. Carrere, "Versatile global model for semiconductor optical amplifier design", *ICTON*, 2024.

On-chip Rewritable Phase-change Metasurfaces for Programmable Optical Routing

Sanaz Zarei
Department of Electrical Engineering
Sharif University of Technology
Tehran, Iran
szarei@sharif.edu

Abstract—Phase-change materials offer a promising solution to implement programmable photonics. In this work, an on-chip programmable optical router based on rewritable phase-change metasurfaces is inverse-designed and Genetic-algorithmically optimized. The presented router can be created by employing the technique of direct laser writing on a Sb_2Se_3 thin film. The rewritable, nonvolatile, and ultra-compact optical router operates at the wavelength of $1.55\mu\text{m}$.

Keywords—programmable optical router, phase-change metasurface, Sb_2Se_3 , direct laser writing

I. INTRODUCTION

Integration of low-loss Sb_2Se_3 phase change material with a multi-mode interference device has been accomplished in previous works to realize programmable photonics [1-3]. Delany et al. demonstrated a programmable router based on patterns of weakly scattering perturbations induced by switching of the Sb_2Se_3 [1]. The pixel perturbation pattern was optimized using an iterative scheme [1]. How the performance of the presented programmable router is dependent on the Sb_2Se_3 layer thickness is also investigated by the same group in [2]. Wu et al. presented a programmable multifunctional device capable of both wavelength division multiplexing and mode division multiplexing [3]. The device's function is modified by transferring the inverse-designed phase pattern to the Sb_2Se_3 thin film [3]. Direct laser writing technique is employed in all these proposals to create the desired patterns [4]. Compared to programmable mesh structures that require a constant power supply to operate, these multi-mode interference devices are of interest because of their nonvolatile nature and small footprint.

In the presented study, an ultra-compact programmable router is realized based on the concept of wavefront shaping using a system of cascaded on-chip phase-change metasurfaces. The waveguides, router region, and metasurfaces are directly laser-written on a thin Sb_2Se_3 film. A high level of control over the flow of light can be achieved by metasurfaces design and optimization [5]. The metasurfaces are primarily inverse-designed [6-7] and thereafter optimized by a Genetic algorithm [5].

II. ROUTER DESIGN

The programmable router is designed to perform 1×2 beam splitting. The device footprint is $8.2\mu\text{m} \times 18.5\mu\text{m}$, and it is composed of five one-dimensional (1D) metasurfaces (metalines), each of which consists of 20 meta-atoms (please see Fig. 1(a)). The distance between the adjacent metasurfaces, as well as the distance between the last metasurface and the output line (conjoint with two output waveguides), is $3.5\mu\text{m}$. The distance between the input line (conjoint with an input waveguide) and the first metasurface is $1\mu\text{m}$. The waveguides are $0.8\mu\text{m}$ wide, and the output waveguides centers are $3.2\mu\text{m}$ distant.

The Sb_2Se_3 film is 30nm thick and is coated with a 200nm -thick SiO_2 layer. The SiO_2 topcoat is aimed for the protection and oxidation inhibition of Sb_2Se_3 . There is a 330nm -thick Si_3N_4 layer beneath the Sb_2Se_3 film, which lays on a standard oxidized substrate. The router region and waveguides are made of crystalline Sb_2Se_3 (c Sb_2Se_3), and the metasurfaces are composed of amorphous Sb_2Se_3 (a Sb_2Se_3) rods through a c Sb_2Se_3 substrate. Like previous studies [1-4], all these components are created by direct laser writing on Sb_2Se_3 .

III. METAS-ATOM DESIGN

The phase-change metasurface is a one-dimensional array of amorphous Sb_2Se_3 (a Sb_2Se_3) rods in the crystalline Sb_2Se_3 (c Sb_2Se_3) thin substrate with the lattice constant of 400nm . Each meta-atom consists of a single (a Sb_2Se_3) rod. By adjusting the dimensions of the (a Sb_2Se_3) rod, the

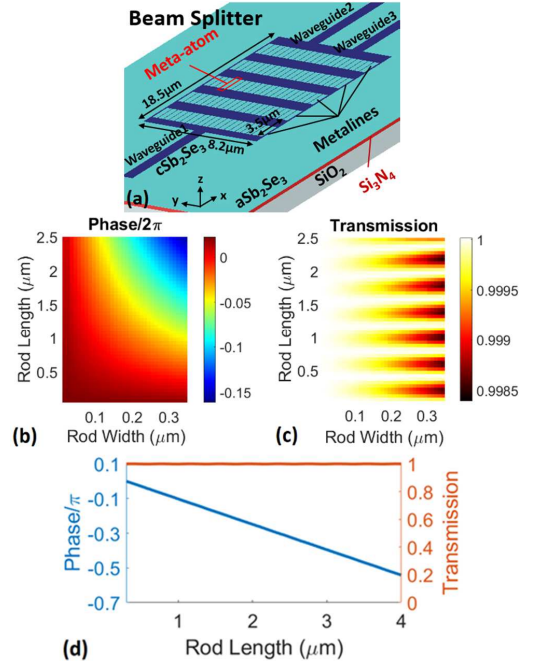


Fig. 1. (a) The schematic of the programmable router implemented in the Sb_2Se_3 thin film using direct laser writing. The electric field transmission phase (b) and amplitude (c) of a meta-atom of the constituent metasurfaces for TE-polarized guided waves versus (a Sb_2Se_3) rod's length and width. (c) The transmission amplitude and phase of a meta-atom versus the (a Sb_2Se_3) rod's length when the (a Sb_2Se_3) rod's width is fixed at 350nm . The diagrams in (b), (c), and (d) are generated using the Lumerical FDTD commercial software package at the wavelength of $1.55\mu\text{m}$.

TABLE I. THE UTILIZED HYPER-PARAMETERS IN THE GENETIC ALGORITHM OPTIMIZATIONS.

Split Ratio	Population Size	Selection Rate	Mutation Rate	Cross-over Rate	Reinitialization Rate [5]	Number of Generations in an Optimization [5]	Total Number of Generations	Initial Perturbation Range [5]
50-50	30	20%	20%	40%	20%	20	180	$\{\Delta RL \in [-400nm, 400nm]\}$
100-0	30	20%	20%	40%	20%	20	240	$\{\Delta RL \in [-400nm, 400nm]\}$

transmission amplitude and phase of a meta-atom for TE-polarized guided wave can be acquired. Figures 1(b) and 1(c) depict the transmission phase and amplitude of a meta-atom, respectively, versus the (aSb₂Se₃) rod length and width. If the rod width is fixed to 350nm and the rod length is swept between 300nm and 4μm, the transmission phase changes more than $\pi/2$, with the transmission amplitude very close to 1 (Fig. 1(d)). The simulation results of Fig. 1 are calculated using the Lumerical FDTD commercial software package at the wavelength of 1.55μm, setting the fundamental TE mode for excitation and the x-axis for the injection axis.

IV. RESULTS

The 1×2 programmable router is designed for two target split ratios of 50-50 and 100-0 while keeping the total device transmission as near as possible to 0dB. The system of cascaded metasurfaces is primarily designed using the inverse design method presented in [6-7]. Thereafter, the designed metasystems are further optimized using a Genetic algorithm [5], the hyper-parameters of which are summarized in Table I. In the Genetic algorithm optimizations, the 2.5D variational FDTD solver of the Lumerical Mode Solution is exploited for structural modeling. The variable parameters in the design and optimization are (aSb₂Se₃) rod lengths (RL), which are restricted to be in the range of $300nm \leq RL \leq 3.4\mu m$. There are 50 variable parameters for the router with the 50-50 split ratio (due to the equivalence of the outputs and the resulting symmetry with respect to $y=0$) and 100 variable parameters for the router with the 100-0 split ratio that need to be adjusted. Figure 2 illustrates the finally optimized devices and the x-y view of the electric field distribution at the midplane of the Sb₂Se₃ film through these devices. For the router of figures 2(a) and 2(c), the transmission of output waveguides, normalized to a reference straight waveguide, is -4.2dB at the wavelength of 1.55μm, while for the router of figures 2(b) and 2(d), the normalized transmissions of output waveguides are -0.44dB (bottom) and -16.5dB (top).

The cascaded on-chip phase-change metasurfaces provide an alternative means for on-chip wavefront shaping and programmable optical flow control to the ones presented in [1-3]. Compared to the multimode interference devices integrated with Sb₂Se₃ in [1-3], the presented router has a smaller footprint. The presented scheme for realizing programmable photonics takes advantage of the ultralow-loss Sb₂Se₃, ultra-compact footprint, and nonvolatility, which is beneficial compared to programmable mesh structures. Interferometer meshes that are based on thermo-optic effect or electro-optic effect, although underpin many new technologies for fully programmable optical circuits, suffer from large programming energy, large footprint, and volatile nature. Furthermore, the function of the proposed device can be easily changed by erasing and rewriting.

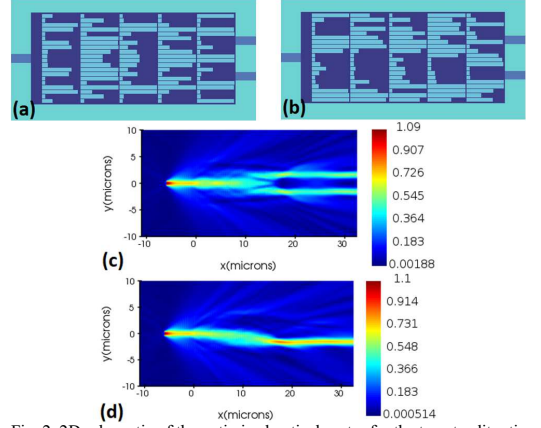


Fig. 2. 2D schematic of the optimized optical router for the target split ratio of 50-50 (a) and 100-0 (b). The x-y view of the electric field distribution at the midplane of the Sb₂Se₃ film through the router designed for 50-50 (c) and 100-0 (d) split ratios.

V. CONCLUSIONS

In summary, an ultra-compact scheme for programmable optical routing with a footprint of $8.2\mu m \times 18.5\mu m$ is presented. The proposed scheme can be realized by direct laser writing on a Sb₂Se₃ phase-change film. Therefore, it is non-volatile and rewritable, with easy correction of the writing errors by locally erasing and restoring. Inverse design combined with a Genetic algorithm optimization is utilized for the design of a 1×2 beam splitter with different split ratios. This scheme can be used in a variety of applications, such as optical routing, analog computing, and artificial intelligence.

REFERENCES

- [1] M. Delaney et al. "Nonvolatile programmable silicon photonics using an ultralow-loss Sb₂Se₃ phase change material," *Sci. Adv.*, vol. 7, p. eabg3500, June 2021.
- [2] S. Blundell et al. "Ultracompact programmable silicon photonics using layers of low-loss phase-change material Sb₂Se₃ of increasing thickness," *ACS Photonics*, vol. 12, no. 3, pp. 1382–1391, March 2025.
- [3] C. Wu et al. "Reconfigurable inverse designed phase-change photonics," *APL Photonics*, vol. 10, p. 016113, Jan. 2025.
- [4] C. Wu et al. "Freeform direct-write and rewritable photonic integrated circuits in phase-change thin films," *Sci. Adv.*, vol. 10, p. eadk1361, Jan. 2024.
- [5] S. Zarei, "On-chip programmable optical routing using nonvolatile Sb₂Se₃ phase-change metasurfaces," 2024, [Online]. Available: <https://doi.org/10.21203/rs.3.rs-3958831/v1>.
- [6] A. S. Backer, "Computational inverse design for cascaded systems of metasurface optics," *Opt. Express*, vol. 27, pp. 30308–30331, Oct. 2019.
- [7] S. Zarei and A. Khavasi, "Computational inverse design for cascaded systems of metasurface optics: comment," *Opt. Express*, vol. 30, pp. 36996–37005, Sept. 2022.

Graphics Processor Unit Accelerated Design of Multimode Interference Reflectors

George M. Jandu
School of Physics and Astronomy
Cardiff University
Cardiff, UK
JanduGM@cardiff.ac.uk

Peter M. Smowton
School of Physics and Astronomy
Cardiff University
Cardiff, UK
SmowtonPM@cardiff.ac.uk

Abstract—A modified three-part algorithm based on extracting effective scattering matrix parameters is presented for the design of multimode interference reflectors. In contrast to previous work, each stage of the suggested simulation strategy is completed in the frequency domain. We demonstrate that this new approach is able to calculate the reflectivity of a multimode interference reflector across a 2D parameter space 7.2 times faster than a standard GPU accelerated three-part simulation and over 68 times faster than a typical CPU implementation.

Index Terms—FDFD, MMIR, GPU acceleration

I. INTRODUCTION

With applications as broadband reflectors, power splitters [1] and temperature insensitive laser devices [2], multimode interference reflectors (MMIRs) are versatile components. The design of MMIR devices is complicated by the omni-directional propagation of light between the angled mirrors (see Fig. 1b), which renders the fast uni- and bi-directional methods typically employed in photonic simulations unsuitable. Omni-directional solvers are computationally intensive, constraining the practicality of running full device simulations on personal computers. First introduced by Kleijn et al. in 2013, two classes of approach have previously been used to circumvent these issues: the equivalent geometry approach (EGA) and three-part simulations [3]. In their original formulation, neither approach is conducive to efficient parameter sweeps and, therefore, efficient device optimisation. The EGA is inherently flawed in several ways. The method neglects mirror losses and reflection induced phase shifts, and the equivalent geometry prevents the investigation of mirror defects.

The focus of the present work is the efficient implementation of a three-part simulation enabling the practical design of MMIRs on personal computers. The use of graphics processor units (GPUs) in photonic simulations can reduce run times by factors as large as 20 [4]. Combining GPU acceleration with an effective scattering matrix technique, we reduce the time taken to span a two-dimensional parameter space by a factor of 68, compared to traditional CPU simulations.

This work was funded by the EPSRC CDT in compound semiconductor manufacturing, EP/S024441/1

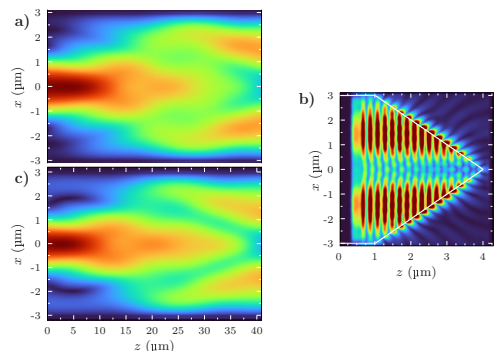


Fig. 1. The absolute magnitude of E_x at each stage of a three-part simulation of an MMIR. a) The input fields propagated through the straight waveguide sections with EME. b) An FDFD simulation inbetween the angled mirrors. c) The reflected waves from b) propagated back through the straight waveguide sections using EME.

II. SIMULATION

A. Three-part simulations in three dimensions

Typically, the three-dimensional simulation of an MMIR has three stages. First, the input field is propagated through the straight waveguide sections using a fast uni- or bi-directional technique. The field at the end of the straight waveguide section can then be loaded into an omni-directional solver to propagate the fields through the angled mirrors. The reflected waves can then be quickly propagated back through the straight waveguides.

Previously, the finite-difference time domain (FDTD) method has been used in the second part of the simulation. However, information about the fields at intermediate time steps is not required to calculate the reflectivity. The finite-difference frequency domain (FDFD) method provides a natural way to compute the steady state fields directly. When discretised according to Yee's scheme [5], using Maxwell's equations to calculate the steady state solution to a frequency domain scattering problem reduces to solving an equation of the form:

$$f = A^{-1}b. \quad (1)$$

Here f is a column vector containing the steady state field components at each point on the grid, b is a column vector containing the source field calculated at each point on the grid in the absence of the device, and A is a large sparse matrix [6].

In three dimensions, the size of A usually prohibits direct matrix division, but the use of stretched coordinate perfectly matched layers (SCPMLs) allows (1) to be solved iteratively. When using MATLAB, (1) can be solved on the GPU by simply passing f , A and b to the GPU using the `gpuArray()` function, without the need for low-level CUDA programming [7]. The field profile through an example MMIR calculated using a three-part simulation based on the eigenmode expansion (EME) and FDFD techniques is shown in Fig. 1.

B. Computationally efficient parameter sweeps

Two common parameter sweeps in the design of MMIRs are device length and the wavelength of the input field. In the standard three-part (ST) model, the entire simulation must be repeated at each point in the 2D parameter space. However, if we make the approximation that there is no coupling between the modes as a result of the mirrors, then we can extract effective scattering matrix parameters from a single FDFD simulation, and use this to calculate the reflectivity at other lengths, following the improved-scattering matrix formalism [8]. Using this effective three-part (ET) model, only one FDFD simulation is required per wavelength, significantly reducing run times without any major alterations to the algorithm. The no-coupling approximation is expected to hold best near the optimum device length, so the FDFD simulation should be performed here. As the value of the optimum length is not known in advance, we perform the simulation at the value predicted by the beat length in the multimode section (which neglects mirror phase shifts and the non-quadratic mode spacing in real devices) [3].

III. RESULTS AND DISCUSSION

A. GPU acceleration

We simulated a typical AlGaAs MMIR structure with an input width of $3\mu\text{m}$, mirror width of $6\mu\text{m}$ and total multimode length of $44\mu\text{m}$, under the injection of the fundamental mode with wavelength $1.36\mu\text{m}$. We found that when solving (1) on an NVIDIA GeForce RTX4090 GPU the simulation took on average 140 s, whereas when solving on an intel Core i9 14900HX processor with 64 GB of RAM the total run time was 1340 s. In this case, GPU acceleration reduces the run time by a factor of 9.6 without any other alterations to the algorithm.

B. Effective scattering parameters

The ST and ET models were used to perform length scans on the device described in the previous section for several input wavelengths. Fig. 2 shows that the agreement between the two approaches is excellent near the optimum lengths, with only minor discrepancies towards the ends of the scans where the no-coupling approximation is less valid.

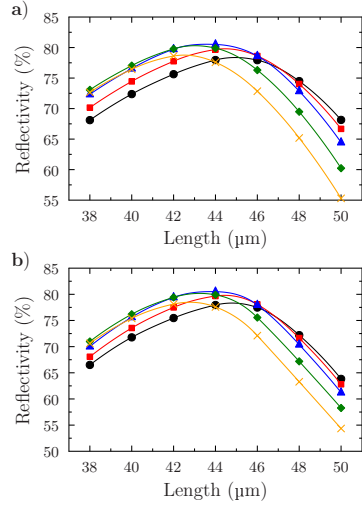


Fig. 2. The reflectivity of a multimode interference reflector as a function of length at wavelengths of $1.32\mu\text{m}$ (circles), $1.34\mu\text{m}$ (squares), $1.36\mu\text{m}$ (triangles), $1.38\mu\text{m}$ (diamonds), and $1.4\mu\text{m}$ (crosses). a) The standard three-part method. b) The effective scattering matrix three-part method.

However, there is a significant difference in the total run times, with the ST method on the GPU requiring 5389 s and the ET method on the GPU requiring only 747 s. The ET method is 7.2 times faster than the ST method, meaning that in total GPU acceleration in combination with the effective scattering matrix algorithm spans the parameter space over 68 times faster than standard three-part simulations on the CPU.

REFERENCES

- [1] P. Lourenço, M. Véstias, A. Fantoni, and M. Vieira, "Multimode interference reflectors and output tuning using neural networks," in *Physics and Simulation of Optoelectronic Devices XXXII* (B. Witzigmann, M. Osinski, and Y. Arakawa, eds.), vol. 12880, p. 128800K, International Society for Optics and Photonics, SPIE, 2024.
- [2] F. T. Albeladi, S. Gillgrass, J. Nabialek, P. Mishra, R. Forrest, T. R. Albiladi, S. Shutts, M. Tang, H.-Y. Liu, and P. M. Smowton, "Multi-mode Interference Reflector based InAs-QD Laser," in *2022 28th International Semiconductor Laser Conference (ISLC)*, pp. 1–2, 2022.
- [3] E. Kleijn, M. K. Smit, and X. J. M. Leijtens, "Multimode interference reflectors: A new class of components for photonic integrated circuits," *Journal of Lightwave Technology*, vol. 31, no. 18, pp. 3055–3063, 2013.
- [4] "Graphics processor unit (gpu) acceleration of finite-difference frequency-domain (fdtd) method," *Progress In Electromagnetics Research M*, vol. 23, pp. 29–51, 2012.
- [5] K. Yee, "Numerical solution of initial boundary value problems involving maxwell's equations in isotropic media," *IEEE Transactions on Antennas and Propagation*, vol. 14, no. 3, pp. 302–307, 1966.
- [6] A. Ivinskaya, *Finite-Difference Frequency-Domain Method in Nanophotonics*. PhD thesis, 2011.
- [7] D. De Donno, A. Esposito, L. Tarricone, and L. Catarinucci, "Introduction to gpu computing and cuda programming: A case study on fdtd [em programmer's notebook]," *IEEE Antennas and Propagation Magazine*, vol. 52, no. 3, pp. 116–122, 2010.
- [8] R. Rumpf, "Improved formulation of scattering matrices for semi-analytical methods that is consistent with convention," *Progress In Electromagnetics Research B*, vol. 35, pp. 241–261, 08 2011.

A Tunable MOEMS Open Microring Resonator for the Detection of Water Concentration in Ethanol Solutions

Nicolas Hanine

*Department of Information Engineering,
Electronics and Telecommunications,
Sapienza University of Rome
Rome, Italy
nicolas.hanine@uniroma1.it*

Alessio Buzzin

*Department of Information Engineering,
Electronics and Telecommunications,
Sapienza University of Rome
Rome, Italy
alessio.buzzin@uniroma1.it*

Lorenzo Giannini

*Department of Information Engineering,
Electronics and Telecommunications,
Sapienza University of Rome
Rome, Italy
lorenzo.giannini@uniroma1.it*

Ahmadreza Alaeddini

*Department of Information Engineering,
Electronics and Telecommunications,
Sapienza University of Rome
Rome, Italy
ahmadreza.alaeddini@uniroma1.it*

Nicola Pio Belfiore

*Department of Industrial, Electronic
and Mechanical Engineering
Roma Tre University
Rome, Italy
nicolapio.belfiore@uniroma3.it*

Rita Asquini

*Department of Information Engineering,
Electronics and Telecommunications,
Sapienza University of Rome
Rome, Italy
rita.asquini@uniroma1.it*

Abstract—In this work, we present a micro-opto-electro-mechanical system (MOEMS) designed as a tunable microring resonator with a novel open-ring configuration. The device incorporates a low-voltage rotary electrostatic actuator to mechanically tune the overlapping region of the open ring, thereby adjusting the resonant frequency and eliminating the need for costly tunable laser sources. The behaviour and performance of the structure are assessed by employing it as an ethanol purity sensor through electromechanical and optical simulations. Results demonstrate the overall feasibility of the device, highlighting its mechanical stability and its ability to detect ethanol concentration changes via shifts in the resonant frequency.

Index Terms—optical ring resonators, Micro-electro-mechanical systems, ethanol purity, microsensors

INTRODUCTION

Ethanol has a central role in a wide range of industrial applications, including chemical synthesis, pharmaceuticals, food preservation, and sustainable fuel production [1], [2]. However, despite the improvement of the process, water is frequently present in the final stages of production and must be subject to regular monitoring to ensure the maintenance of the required ethanol/water ratio [3]. The necessity of ensuring the purity of ethanol has led to the development of cost-effective, efficient, simple, and reliable methods to quantify the water content in ethanol [4]–[7]. The most common

approach to measure the resonance shift is to use a tunable laser source or a broad-band optical source as input, and a spectrometer as output [8]. Despite their efficacy, the use of these methods gives rise to a number of issues, including increased complexity, cost, and portability.

In this work, a novel micro opto-electromechanical system (MOEMS) structure is studied for the determination of the water content of ethanol solutions. The microring's resonant frequency can be shifted to change the input wavelength through a small voltage, enabling single-laser scanning and avoiding expensive input sources.

I. WORKING PRINCIPLE

The proposed device, schematically illustrated in Fig. 1, consists of a mechanically tunable ring resonator deliberately designed with an open-loop configuration. This includes a dedicated coupling region between its two ends, where a tailored overlap section facilitates controlled optical coupling. The ring is mechanically linked to a rotary comb-drive actuator which, upon voltage application, generates a controlled in-plane rotational displacement. This mechanical actuation modifies the optical path length, thereby shifting the resonant frequency. When the microring is exposed to a fluid mixture, the refractive index of the surrounding medium changes depending on the composition, resulting in a shift in the resonance condition. Instead of sweeping the input wavelength, the device operates with a fixed-wavelength laser: the applied voltage is varied to shift the microring's resonance until it aligns with the laser. When resonance occurs, a transmission peak is observed, and the corresponding voltage provides a direct indication of the ethanol-water concentration.

This work was partially supported by the European Union under the Italian National Recovery and Resilience Plan (NRRP) of Next Generation EU, partnership on "Telecommunications of the Future" (PE00000001—Program "RESTART"), by the European Union under the Italian National Recovery and Resilience Plan (NRRP) of Next Generation EU, PNRR MUR project PE00000023-NQSTI (the National Quantum Science and Technology Institute, and by the Sapienza University Major Project RG12419112B8DBA3 "Water Cookie".

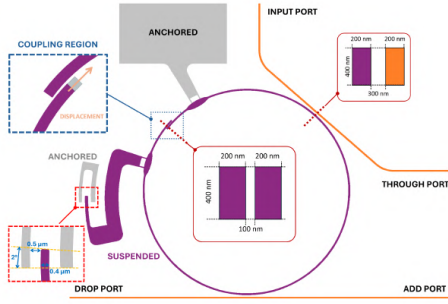


Fig. 1. Schematic representation of the MOEMS-based microring resonator sensor.

II. RESULTS

The device was analyzed using Ansys Lumerical FDTD simulations with a 1550–1555 nm light source to observe resonance shifts. Mechanical and electrostatic analyses were performed in COMSOL Multiphysics to evaluate the device's deformation under voltages ranging from 0 to 0.5 V. The refractive index increases with the water content, ranging from 1.361876 at 1.09 mol% to 1.362936 at 9.05 mol% [9]. Fig. 2a presents the transmission spectra of the microring resonator for different ethanol-water mixtures used as cladding. As the water concentration increases, a red-shift of the resonance wavelength is observed. The shift is approximately 4 pm for the lowest concentrations, up to approximately 170 pm for the highest concentrations with a quadratic trend, as shown in Fig. 2b. A voltage ranging from 0 to 0.5 V, in steps of 0.1 V, was applied to the MEMS actuator to induce a controlled mechanical deformation of the resonator. Fig. 2c illustrates the simulated transmission spectra of the microring resonator at different applied voltages, showing a clear and progressive blue-shift of the resonance peak; as shown in Fig. 2d, the resonance shifts from 8.2 pm at 0.1 V up to 204 pm at 0.5 V. The data presents a quadratic dependence in agreement with the expected behaviour of an electrostatically actuated MEMS structure, where displacement scales with the square of the applied voltage.

III. CONCLUSIONS

In this work, we have presented and analyzed a MOEMS-based microring resonator designed for sensing the concentration of water in ethanol-water solutions. The key operating principle relies on the shift of the resonance wavelength caused by changes in the cladding refractive index and by mechanical deformation of the resonator induced through electrostatic actuation. We demonstrated that by applying a variable voltage, it is possible to effectively control the resonance condition, enabling a voltage-based interrogation scheme at a single fixed laser wavelength. This approach eliminates the need for an expensive tunable laser source, as only a simple fixed-wavelength laser is required.

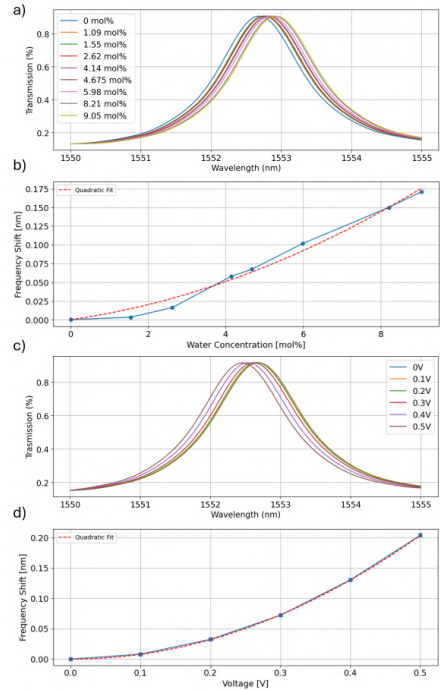


Fig. 2. (a) Simulated transmission spectra of the microring resonator for increasing water concentrations in ethanol. (b) Quadratic fit of resonance frequency shift as a function of water concentration. (c) Transmission spectra at different applied voltages. (d) Quadratic fit of resonance frequency shift as a function of applied voltage.

REFERENCES

- [1] B. Le Dare et al., "Therapeutic applications of ethanol: a review," *Journal of Pharmacy and Pharmaceutical Sciences*, vol. 22, pp. 525–535, 2019.
- [2] K. Osmolak et al., "Efficient production of fuel ethanol via the simultaneous use of distillery stillage biomass and beet molasses," *Energies*, vol. 18, no. 2, p. 312, 2025.
- [3] H. Idris et al., "The use of some mixtures of medicinal plant ethanol extracts as an antifungal in the control of peanut stem rot diseases," *Results in Engineering*, vol. 25, p. 103669, 2025.
- [4] M. Bianchetti et al., "A fabry-pérot sensing setup based on a coreless fiber for the measurement of ethanol concentration in water-based solutions," *Sensors and Materials*, vol. 37, no. 1, pp. 13–22, 2025.
- [5] R. M. Shedam et al., "Ethanol sensor based on nano crystalline Nd³⁺ substituted in Mg-Cd ferrite thick film," *Sensors and Actuators B: Chemical*, vol. 426, p. 137128, 2025.
- [6] A. Umar et al., "Indium oxide nanocubes for enhanced ethanol gas sensing and photocatalytic applications," *Ceramics International*, 2025.
- [7] V. Fallahi et al., "A solution for detection of ethanol and methanol with overlapping refractive indexes based on photonic crystal ring resonator optical sensors," *IEEE Sensors Journal*, vol. 23, no. 7, pp. 6791–6798, 2023.
- [8] E. Luan et al., "Silicon photonic biosensors using label-free detection," *Sensors*, vol. 18, no. 10, p. 3519, 2018.
- [9] R. J. Jiménez Riobó et al., "Concentration and temperature dependence of the refractive index of ethanol-water mixtures: Influence of intermolecular interactions," *The European Physical Journal E*, vol. 30, pp. 19–26, 2009.

Multi-scale hybrid band simulation of (Al,Ga)N UV-C light emitting diodes

Robert Finn[†], Patricio Farrell*, Timo Streckenbach*, Julien Moatti[‡],
Stefan Schulz^{†,§}, Thomas Koprucki*, Michael O'Donovan*,

[†]Tyndall National Institute, University College Cork, Cork, T12 R5CP, Ireland

*Weierstrass Institute (WIAS), Mohrenstr. 39, 10117 Berlin, Germany

[‡]Univ. Bordeaux, CNRS, Bordeaux INP, IMB, UMR 5251, Talence F-33400, France

[§]School of Physics, University College Cork, Cork, T12 YN60, Ireland

Email: odonovan@wias-berlin.de

Abstract—Aluminium gallium nitride alloys are used for developing light emitting diodes operating in the UV part of the electromagnetic spectrum. These devices suffer from a low efficiency. To gain insight to this question we develop a 3-D modified drift-diffusion model which takes into account both alloy disorder effects and valence band mixing, and investigate the device efficiency. Results show that the current injection efficiency is strongly influenced by the chosen doping profile.

Index Terms—UV-C emitters, electronic structure, drift-diffusion, disordered energy landscape, carrier transport

I. INTRODUCTION

Due to its wide tunable direct bandgap which can span from visible ($E_G^{GaN} \approx 3.45$ eV) to UV-C wavelengths ($E_G^{AlN} \approx 6.00$ eV), the semiconductor alloy aluminium gallium nitride (Al,Ga)N is of particular interest for light-emitting devices operating in the UV part of the electromagnetic spectrum [1]. At high AlN contents (UV-C, emission wavelength < 280 nm) devices suffer from a low quantum efficiency [1]. Simulation tools play an important role for understanding the origin of this decrease, and engineering device design to improve efficiency. For this, modeling frameworks should capture the relevant physical effects which impact device characteristics.

The valence states of (Al,Ga)N alloys require particular attention. Firstly, alloy disorder leads to carrier localization which modifies the density of states and the carrier density distribution in a quantum well (QW) [2]. The in-plane distribution of a hole ground state of a *c*-plane QW, computed using tight binding (TB) in the presence of alloy disorder, is shown in Fig. 1 (top right). The state is localized in a small region of space due to alloy fluctuations – without alloy disorder the wavefunction would be homogeneously distributed across the shown area. Modifications of the wavefunctions will impact recombination processes in a device [3]. Additionally, perturbations of the electronic structure also impacts carrier transport, where alloy disorder introduces low-energy pathways which enable percolation currents in a device [3]. Thus alloy effects impact both the transport and recombination properties.

This work received funding from the Leibniz Competition 2022 (UVSimTec, K415/2021), the Sustainable Energy Authority of Ireland and Taighde Éireann – Research Ireland (17/CDA/4789, 12/RC/2276 P2 and 21/FFP-A/9014), and the Leibniz competition 2020 (NUMSEMIC, J89/2019).

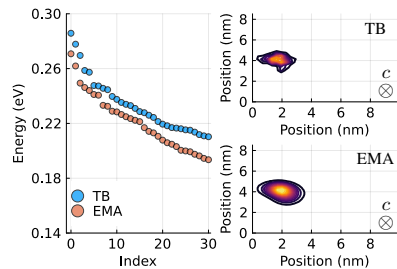


Fig. 1. Left: Hole energies of the first 30 states calculated from tight binding (TB) (blue) and a hybrid single band effective mass approximation (EMA) (orange) for a 2 nm $Al_{0.75}Ga_{0.25}N$ quantum well including alloy disorder. Right: 2-D slice of the TB (top) and EMA (bottom) ground state charge density for the chosen configuration within the quantum well.

Secondly, wavefunctions which contribute to emission can be constructed from states which facilitate emission of transverse electric (TE) or transverse magnetic (TM) light [2]. Unstrained bulk AlN emits primarily TM polarized photons, whereas bulk GaN emits mainly TE polarized photons. In (Al,Ga)N-based heterostructures the relative contribution of each depends on (among other factors) alloy composition, heterostructure properties (e.g. QW width) and carrier density.

To account for alloy disorder in a 3-D drift-diffusion (DD) device simulation the atomistic TB Schrödinger equation can in principle be coupled with the DD equations. This, however, is numerically prohibitive, as it requires solving a (large) eigenvalue problem self-consistently with the DD equations. Instead, we develop a framework which accounts for mixing between TE and TM emitting states in an approximation of a single band model, while also including alloy disorder. To further reduce the numerical demand, the atomistically treated QWs are embedded in a sparse mesh which describes regions where alloy disorder is of secondary importance.

II. THEORETICAL FRAMEWORK

To consider alloy disorder effects in DD, an energy landscape is extracted from TB via a local diagonalization of the TB Hamiltonian [4]. The energy landscape thus includes local

variations in composition, strain and polarization potential on an atomistic scale. The energy landscape is mapped onto a finite volume mesh which contains a node for every atom in the system, and is then embedded in a sparse mesh. Quantum corrections are included via localization landscape theory which approximates the single band effective mass approximation (EMA) of the Schrödinger equation [5].

As previously mentioned, the valence states of (Al,Ga)N alloys can be comprised of either TE or TM emitting states. This in principle requires a multi-band model, however to treat this with an EMA we construct a hybrid effective mass which is informed by the fraction of TE or TM emission:

$$\frac{1}{m_d(x_{\text{AlN}}, P_{\text{TE}})} = \frac{P_{\text{TE}}}{m_d^{\text{HH}}(x_{\text{AlN}})} + \frac{1 - P_{\text{TE}}}{m_d^{\text{CH}}(x_{\text{AlN}})} \quad (1)$$

Here m_d is the hybrid effective masses in the direction d (in- or out-of-plane), x_{AlN} is the AlN composition of the quantum well and P_{TE} is the fraction of TE emission which is computed from TB calculations [2]. m_d^{B} is the effective mass of the band B for the TE emitting band (B = HH) or TM emitting band (B = CH), which are a harmonic average of the AlN and GaN bands weighted by the alloy composition.

The model has been calibrated against TB. The separation between energy eigenvalues is similar in the EMA and TB. As this energetic separation depends on the inverse effective mass, this indicates the choice of mass is suitable (Fig. 1 left). The band offset within the QW was adjusted by a constant to ensure that absolute scale of the electronic structure is well represented. The position of the ground state is also in good agreement (c.f. Fig. 1 right, top and bottom) however we note that the EMA predicts a weaker localization compared to atomistic TB.

We apply this advanced framework to a UV-C emitting LED which contains five ≈ 2 nm $\text{Al}_{0.75}\text{Ga}_{0.25}\text{N}$ QWs separated by ≈ 7 nm $\text{Al}_{0.85}\text{Ga}_{0.15}\text{N}$ barriers. Recombination is treated using an ABC model which includes non-radiative Shockley-Read-Hall (R^{SRH}) and Auger-Meitner (R^{AM}) recombination as well as radiative recombination (R^{Rad}). An AlN electron blocking layer and p-GaN cap are included to prevent electron overshoot and aid hole injection into the QW regions. These are Mg-doped with a density of 10^{19} cm^{-3} . The software `ddfermi` is used to model the device using DD [6], and `AMGCL` is used to solve the system of equations [7].

III. RESULTS

The band edge diagram of the structure (including quantum corrections as an effective confining potential from LLT) is shown in Fig. 2 (left). Alloy disorder impacts the energy landscape used in the DD calculations. This is shown in an in-plane slice through the QW closest to the p-side (Fig. 2 (right)). The fluctuations impact the carrier density, recombination and current density, and thus also the device efficiency. The efficiency is studied in terms of the carrier injections efficiency η^{CIE} (probability of injected carriers recombining within QWs) and radiative recombination efficiency η^{RRE} (probability that a recombination in the QWs will emit a photon); the internal

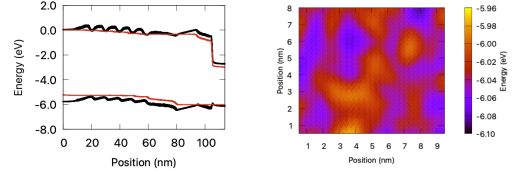


Fig. 2. Left: Band edge diagram of the LED structure studied in this work under bias. Right: In-plane valence band edge energy showing the impact of alloy disorder: The valence band energy varies by over 100 meV in the $10 \times 9 \text{ nm}^2$ area. The data is shown for a slice through the right-most quantum well of the stack (on the p-side).

quantum efficiency is thus $\eta^{\text{IQE}} = \eta^{\text{CIE}} \times \eta^{\text{RRE}}$. Our results show that η^{CIE} is strongly influenced by the doping profile, and the chosen doping activation energy. Without a suitable doping profile the electrons overshoot the active region leading to a lower internal quantum efficiency.

IV. CONCLUSION

In this work we present a framework to study device characteristics of (Al,Ga)N-based UV-C emitting LEDs. Optical polarization and disorder effects are considered. The framework builds on a hybrid band electronic structure model which is benchmarked against TB. Our results show that the doping profile is an important aspect for engineering higher device efficiencies in (Al,Ga)N-based UV-C LEDs.

REFERENCES

- [1] H. Amano, R. Collazo, C. D. Santi, S. Einfeldt, M. Funato, J. Glaab, S. Hagedorn, A. Hirano, H. Hirayama, R. Ishii, Y. Kashima, Y. Kawakami, R. Kirste, M. Kneissl, R. Martin, F. Mehnke, M. Meneghini, A. Ougazaden, P. J. Parbrook, S. Rajan, P. Reddy, F. Römer, J. Ruschel, B. Sarkar, F. Scholz, L. J. Schowalter, P. Shields, Z. Sitar, L. Sulmoni, T. Wang, T. Wernicke, M. Weyers, B. Witzigmann, Y.-R. Wu, T. Wunderer, and Y. Zhang, “The 2020 UV emitter roadmap,” *Journal of Physics D: Applied Physics*, vol. 53, p. 503001, sep 2020.
- [2] R. Finn, M. O’Donovan, T. Koprucki, and S. Schulz, “Theoretical study of the impact of carrier density screening on Urbach tail energies and optical polarization in (Al,Ga)N quantum well systems,” *Preprint at 10.48550/arXiv.2501.16808*, 2025.
- [3] R. Finn, M. O’Donovan, P. Farrell, J. Moatti, T. Streckenbach, T. Koprucki, and S. Schulz, “Theoretical study of the impact of alloy disorder on carrier transport and recombination processes in deep UV (Al,Ga)N light emitters,” *Applied Physics Letters*, vol. 122, p. 241104, 06 2023.
- [4] M. O’Donovan, D. Chaudhuri, T. Streckenbach, P. Farrell, S. Schulz, and T. Koprucki, “From atomistic tight-binding theory to macroscale drift-diffusion: Multiscale modeling and numerical simulation of unipolar charge transport in (In,Ga)N devices with random fluctuations,” *Journal of Applied Physics*, vol. 130, no. 6, p. 065702, 2021.
- [5] C.-K. Li, M. Piccardo, L.-S. Lu, S. Mayboroda, L. Martinelli, J. Peretti, J. S. Speck, C. Weisbuch, M. Filoche, and Y.-R. Wu, “Localization landscape theory of disorder in semiconductors. III. Application to carrier transport and recombination in light emitting diodes,” *Phys. Rev. B*, vol. 95, no. 14, p. 144206, 2017.
- [6] D. H. Doan, P. Farrell, J. Fuhrmann, M. Kantner, T. Koprucki, and N. Rundo, “ddfermi – a drift-diffusion simulation tool,” tech. rep., Weierstrass Institute (WIAS), doi: <http://doi.org/10.20347/WIAS.SOFTWARE.DDFERMI>, 2020.
- [7] D. Demidov, “AMGCL: An Efficient, Flexible, and Extensible Algebraic Multigrid Implementation,” *Lobachevskii Journal of Mathematics*, vol. 40, no. 5, pp. 535–546, 2019.

Modelling Electron Beam Induced Current in III-Nitride Light Emitting Diodes.

B. Utsch[†], F. Römer^{†*}, S. Faber[†], F. Bertram[‡], G. Schmidt[‡], P. Veit[‡], C. Berger[‡], A. Dadgar[‡], A. Strittmatter[‡], J. Christen[‡], and B. Witzigmann[†]

[†] Lehrstuhl für Optoelektronik, Department EEI, Friedrich-Alexander-Universität Erlangen-Nürnberg
Konrad-Zuse-Str. 3/5, D-91052 Erlangen, Germany

[‡] Otto-von-Guericke-Universität Magdeburg, Universitätsplatz 2, D-39106 Magdeburg, Germany

* Email: friedhard.roemer@fau.de

Abstract—Electron beam induced current (EBIC) has been used as a tool in semiconductor analytics to determine the diffusion length of minority carriers in pn-junctions. Recent progress in controlling the electron beam and penetration has enabled the resolution of much finer structures, including the active region of multi quantum well (MQW) optoelectronic devices. The interpretation of the measured EBIC profiles is not straight forward, though. In this context we have devised and implemented an EBIC model and have simulated the EBIC in an indium gallium nitride (InGaN) MQW light emitting diode. The simulations demonstrate a combined effect of doping, band edges, and the polarization field on the EBIC. The simulations facilitate an isolation of these effects and therefore support the interpretation of the measured EBIC profiles. We demonstrate that the joint experimental and numerical EBIC analysis has the potential to reveal the structure of the III-nitride MQW active region.

I. INTRODUCTION

The optimization of III-nitride multi quantum well (MQW) light emitting diodes and lasers is often impaired by the vague structural data of realized devices. Analytical methods to reveal the structure such as secondary ion mass spectroscopy are expensive, destructive, and have a limited spatial resolution. Electron microscopy methods show the structure on the atomic scale but do not give account of the doping concentration and the composition of the material. For semiconductor junctions the electron beam induced current (EBIC) can be investigated in a scanning electron microscope in addition. The electron beam sweeping the device locally generates secondary electron hole pairs resulting in a short circuit current which varies with the beam target. In a pn-homojunction the current profile reflects the diffusion of minority electrons and holes in the quasi neutral regions giving rise to the diffusion length as well as the position and size of the space charge region (SCR) [1].

Recent advances in controlling the electron beam size and penetration enable the resolution of features in the MQW active region of III-nitride light emitters [2], [3]. However, in contrast to a simple pn-junction the EBIC profile of the targeted InGaN MQW light emitting diode (LED) with electron blocking layer (EBL) cannot be interpreted immediately because of the interplay of the hetero junction band offsets, the polarization charge, and the doping profile in the active region. This obstacle gives rise to the EBIC modelling reported in the work. We have been simulating the short circuit current in the

MQW LED with Synopsys Sentaurus using the physical model interface of Sentaurus Device to implement the electron beam induced generation. Thus, a complete EBIC profile is generated in one quasistationary sweep. Subsequently, we identify the effect of the polarization charge and the EBL doping on the current providing guidelines for the interpretation of the EBIC characterization.

II. EBIC SIMULATION

For EBIC the electron beam penetrates the epitaxial stack parallel to the layers. The secondary electron hole pair generation profile is defined by the beam axis and entrance position. Generation is described by a Gaussian distribution perpendicular to the beam axis and by a Poisson distribution parallel to the axis [4]. The resulting generation profile is illustrated in Fig. 1 for an electron beam directed to the n-side of the MQW. Primary electrons typically generate a few hundred secondary electron hole pairs but do not contribute to the short circuit current to comply with charge neutrality and continuity. The secondary electron generation is considered like optical generation.

In short circuit the generation presents a local perturbation of the thermal equilibrium of electrons and holes. A short circuit current evolves only if electrons and holes are separated by a drift or diffusion force. In the MQW active region of a III-nitride light emitting diode the EBIC profile is less intuitive because of the interaction of doping, heterojunctions, and the polarization charge. The GaN/InGaN MQW LED under investigation has five quantum wells. The AlGaIn EBL has an acceptor doping $N_A = 4 \cdot 10^{18} \text{ cm}^{-3}$. The p-side barrier has an acceptor doping as well. We consider a polarization charge screening about 50% [5] and complete ionization. The band structure in Fig. 2 illustrates that the SCR extends across the EBL because of the polarization charge.

The SCR is reflected in the EBIC profile in Fig. 3, simulated at the temperature $T = 184 \text{ K}$. In the quasi neutral n-region the EBIC reflects the hole diffusion as in a homojunction pn-diode. The low hole diffusion length $l_p \approx 60 \text{ nm}$ can be attributed to the low hole mobility in doped GaN. The EBIC shows a strong decrease on the p-side of the diode which can be attributed to the EBL. The band diagram Fig. 2 shows that

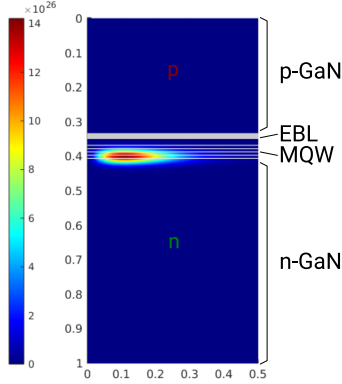


Fig. 1. Generation rate in $\text{cm}^{-3} \text{s}^{-1}$ for an electron beam hitting the layer stack near the n-side of the MQW. Coordinates are in μm . The grey overlay illustrates the position of the EBL and the MQW.

electrons are subject to a $\Delta E_C \approx 0.5 \text{ eV}$ barrier from the p-side. Thus, electrons generated at the p-side are captured and recombine there rather than contributing to the short circuit current. Though polarization fields mitigate the barrier the screening by ionized dopants enhances it again. Therefore, the EBIC on the p-side reduces with the EBL acceptor doping.

The EBL polarization field and the global SCR field have the same sign but the built in voltage is determined by the contact quasi Fermi levels. Therefore, the doping related screening of the polarization field in the EBL enhances the global field in the MQW region. This supports the separation of electrons and holes which competes with the strong recombination in the quantum wells. Thus, the EBIC increases in the MQW with the EBL acceptor doping as shown in the inset of Fig. 3.

III. CONCLUSION

The EBIC characterization establishes a valuable tool in semiconductor analytics but in contrast to a pn-homojunction its interpretation for a III-nitride LED active region is more involved. Thus, we propose to complement experiments with EBIC simulation including drift-diffusion. The aspect discussed in this study, the EBL doping, already demonstrates the complexity of its effect on the EBIC signal but also that the modelling supports the interpretation of EBIC experiments. In an outlook we are going to analyze the influence of other design parameters, for instance the composition of the EBL and compare the simulation results to experimental EBIC data. It is planned to expand the model to full three dimensions.

ACKNOWLEDGMENT

This work has been supported in part by the Deutsche Forschungsgemeinschaft priority programme 2312 GaNius (energy efficient power electronics).

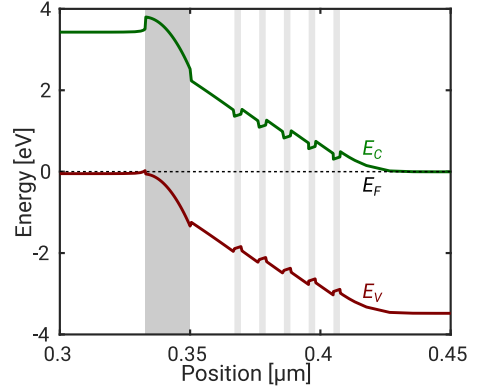


Fig. 2. Band structure of the MQW active region for $N_{A,EBL} = 4 \cdot 10^{18} \text{ cm}^{-3}$ in thermal equilibrium. The grey areas illustrate the EBL and the MQW.

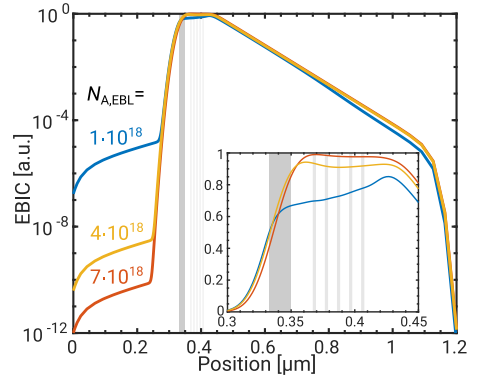


Fig. 3. Variation of the EBIC profiles with the EBL acceptor doping $N_{A,EBL}$. The inset shows a magnification of the EBIC in the active region.

REFERENCES

- [1] D. Abou-Ras and T. Kirchartz, "Electron-Beam-Induced Current Measurements of Thin-Film Solar Cells," *ACS Appl. Energy Mater.*, vol. 2, no. 9, pp. 6127–6139, 2019.
- [2] K. Wein, F. Bertram, G. Schmidt, P. Veit, J. Christen, S. Faber, B. Witzigmann, M. Heuken, T. Zweipfenning, H. Kalisch, A. Vescan, and A. Debal, "Nano-characterization of a space-charge region in a pn-diode with long drift layer: detailed cathodoluminescence and EBIC correlation," in *Gallium Nitride Materials and Devices XVIII*, vol. PC12421. SPIE, 2023.
- [3] H. Eisele, K. Wein, F. Bertram, G. Schmidt, J. Christen, A. Dadgar, C. Berger, A. Strittmatter, A. Debal, M. Heuken, T. Zweipfenning, H. Kalisch, A. Vescan, S. Faber, and B. Witzigmann, "(Late news) characterization of the space-charge region of a GaN pn-junction and pin-drift-diode using EBIC and CL," in *65th Electronic Materials Conference, Santa Barbara*, no. W04, 2023, pp. 116–117.
- [4] J.-M. Bonard and J.-D. Ganière, "Quantitative analysis of electron-beam-induced current profiles across *p-n* junctions in GaAs/Al_{0.4}Ga_{0.6}As heterostructures," *J. Appl. Phys.*, vol. 79, no. 9, pp. 6987–6994, 1996.
- [5] F. Römer and B. Witzigmann, "Effect of Auger recombination and leakage on the droop in InGa_{0.5}GaN quantum well LEDs," *Opt. Express*, vol. 22, no. S6, p. A1440, 2014.

Estimation of light extraction efficiency in GaN-based light emitting diodes via ray-tracing modeling

1st Szymon Lach

MBE Laboratory

Institute of High Pressure Physics PAS
Warsaw, Poland

szymon.lach@unipress.waw.pl

2nd Mateusz Hajdel

MBE Laboratory

Institute of High Pressure Physics PAS
Warsaw, Poland

hajdel@unipress.waw.pl

3rd Grzegorz Muziol

MBE Laboratory

Institute of High Pressure Physics PAS
Warsaw, Poland

gmuziol@unipress.waw.pl

Abstract—Simple ray-tracing model was created to estimate the dependence of light extraction efficiency (LEE) on the shape of the light emitting diodes (LEDs). It is shown that triangularly shaped LEDs have a much greater LEE than standard rectangular devices. Furthermore, the model is used to determine the internal quantum efficiency of InGaN LEDs grown by plasma-assisted molecular beam epitaxy.

Index Terms—LED, tri-LED, numerical simulation, ray-tracing, InGaN.

I. INTRODUCTION

Efficient light extraction from LEDs is a heavily researched topic, because external quantum efficiency (EQE), which is measurement of how efficient a LED is, strongly depends on the portion of photons emitted from the device. There are many ways to increase light extraction efficiency (LEE), for example: encapsulation in medium with light refraction index (n) value in between that of the LED and air, structurization of external surface of the device or simply using different than usual geometry of the device. This paper discuss the last approach, due to its less post-processing effort in comparison to other methods.

II. THEORETICAL BACKGROUND

A. Reflectance

Photons generated inside a LED are moving freely, until they come across one of the borders of the LED. At the air-LED interface they have a chance of escaping, determined by angle of incidence - Θ_i , refractive indices, n_1 - for the device and n_2 - for surrounding medium, to pass through or reflect back inside the crystal. Reflectance, depends on polarization and for s-polarized light (often named TE), and equals [1]:

$$R_s = \frac{\left| n_1 \cos \Theta_i - n_2 \sqrt{1 - \left(\frac{n_1}{n_2} \sin \Theta_i\right)^2} \right|^2}{\left| n_1 \cos \Theta_i + n_2 \sqrt{1 - \left(\frac{n_1}{n_2} \sin \Theta_i\right)^2} \right|^2}. \quad (1)$$

Work partially financed from project "Monolithic integration of multi-color arrays of micro- and nano-LEDs" project carried out within the First Team program of the Foundation for Polish Science co-financed by the European Union under the European Funds for Smart Economy 2021-2027 (FENG)

Similarly, for p-polarized (TM) light reflectance equals:

$$R_p = \frac{\left| n_1 \sqrt{1 - \left(\frac{n_1}{n_2} \sin \Theta_i\right)^2} - n_2 \cos \Theta_i \right|^2}{\left| n_1 \sqrt{1 - \left(\frac{n_1}{n_2} \sin \Theta_i\right)^2} + n_2 \cos \Theta_i \right|^2}. \quad (2)$$

For non-polarized light reflectance equals to the average of these two values.

B. Importance of the device geometry

Since most LEDs are made from materials with a high refractive index, photons with an incidence angle above the critical angle are totally reflected back inside the LED. This means that only part of the light generated inside the LED is able to exit the crystal on the first contact with the air-LED interface. External quantum efficiency, defined as:

$$EQE = \eta \cdot LEE \cdot IQE, \quad (3)$$

where: η - carrier injection efficiency and IQE- internal quantum efficiency, is limited with LEE, and in order to increase EQE one need to maximize both LEE and IQE.

To better understand how LEE changes with different LED base geometries, polar graphs of transmittance were made. Few simplifications were made, such as: all photons are emitted from the geometric center of base figure, sides are perfectly smooth, and there is no light absorption. For InGaN LED, emitting light of wavelength 430 (nm), transmittance graphs are shown on Fig. 1. Transmittance for photons on the first and the second contact with the interface is plotted.

From Fig. 1 one can say that triangular base shape provides better light extraction efficiency than the square shape. This is because after reflection from one side of the triangle the incident angle of the second contact increases by $\frac{\pi}{3}$.

With square geometry, incidence angle after reflection is increased by $\frac{\pi}{2}$. This specific value changes nothing in the calculated reflectance since the existence of the reduction formulas. One can see this effect as totally overlapped patterned and colored sections on the bottom of Fig. 1. Reference [2] was the first to come up with a design utilizing a triangular shape and flip-chip mounting, and named it tri-LED.

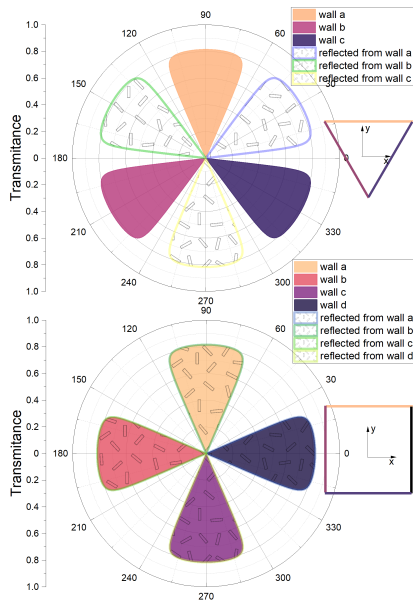


Fig. 1. Polar plots of transmittance made for two different base geometries: equilateral triangle and square. On the right from graph are color-coded sides of the base shapes.

III. NUMERICAL MODEL

Three dimensional numerical model of photons moving inside the LED was created to better approximate the real behavior. Basic assumptions made to simplify simulation were: no volumetric absorption or scattering, perfectly smooth external surface of the LED, and metallization with a reflectance of 0.9 on the bottom surface of the devices. Inside the simulated LED, photon packets were ray traced from their origin, set in 3 (nm) high bottom layer, until they reached maximum number of collisions, ranging from 0 (no internal reflections) to 250. With each collision, the angle of incidence was used to calculate how much of the packet intensity was able to escape and how much was reflected. Finally these values were used to calculate LEEs, which are shown on Fig. 2.

IV. DEVICE MEASUREMENTS

To confirm that in fact triangular shaped devices have greater LEE than square shaped, electroluminescence measurements of LEDs grown by us using plasma-assisted MBE were conducted. The LEDs were mounted in flip-chip manner, with Ni/Ag/Ni/Au metallization on the bottom. EQE values obtained from these measurements are shown on Fig. 3. It is important to mention that usually MBE-grown LEDs have EQE reaching nearly 1.7% [3], and by using only tri-LED design ours LEDs reached EQE of 22%.

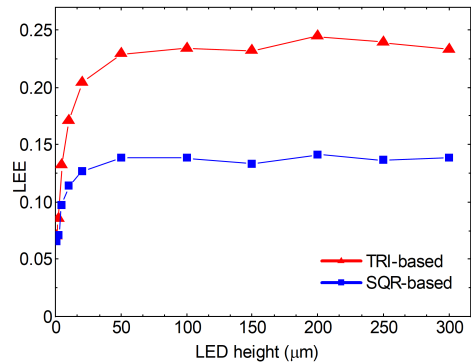


Fig. 2. Obtained from the numerical simulation LEE values for two base geometries: square and equilateral triangle.

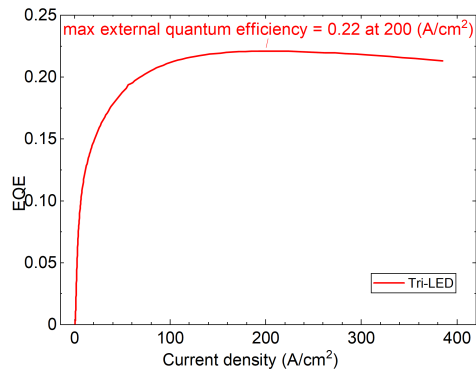


Fig. 3. EQE of InGaIn tri-LED, grown by plasma-assisted MBE.

V. CONCLUSION

Such high EQE is a direct effect of utilizing tri-LED design, as well as very high IQE of measured device. Further improvements to simulation model, inter alia implementation of surface scattering, refraction between layers and volumetric absorption are planned to better fit model behavior to experimental data. The main reason behind creating this model was to numerically confirm that devices with a triangular base shape would have higher light extraction efficiency than square-based ones, which was confirmed.

REFERENCES

- [1] E. Hecht and A. Zajac, *Optics*. Addison-Wesley world student series, Addison-Wesley Publishing Company, 1987.
- [2] M. J. Cich, R. I. Aldaz, A. Chakraborty, A. David, M. J. Grundmann, A. Tyagi, M. Zhang, F. M. Steranka, and M. R. Krames, "Bulk gan based violet light-emitting diodes with high efficiency at very high current density," *Applied Physics Letters*, vol. 101, p. 223509, 11 2012.
- [3] D. J. Myers, A. C. Espenlaub, K. Gelzinyte, E. C. Young, L. Martinelli, J. Peretti, C. Weisbuch, and J. S. Speck, "Evidence for trap-assisted auger recombination in mbe grown ingan quantum wells by electron emission spectroscopy," *Applied Physics Letters*, vol. 116, p. 091102, 03 2020.

Superluminescent Light-Emitting Diodes (SLEDs) Operating at Ultra-High Ambient Temperatures

Nicolai Matuschek and Marcus Duelk

EXALOS AG (indie Switzerland), Wagistrasse 21, CH-8952 Schlieren, Switzerland
Tel.: +41-43-444 60 90, Fax: +41-43-444 60 99, E-mail: matuschek@exalos.com

Abstract – SLEDs are attractive light sources for various applications in the visible and near-infrared spectral region. Some applications require operation at ultra-high ambient temperatures of up to 150°C. We show that the electro-optical device performance at such challenging conditions is limited by the thermal degradation of the material gain and by the non-radiative Auger recombination processes that are strongly increasing with temperature. Still, with proper design choices, several milliwatts of optical output power can be generated at ultra-high chip temperatures.

I. INTRODUCTION

Superluminescent light emitting diodes (SLEDs) are efficient light sources that emit broadband light with several tens of milliwatts of output power into single-mode fibers. SLEDs typically operate at wavelengths from 400 nm to 1700 nm with broadband emission of 5-150 nm FWHM. The electro-optical performance is based on amplifying spontaneous emission (ASE) through stimulated emission along an optical waveguide [1]. These characteristics make them attractive light sources for various applications, including biomedical imaging, fiber optic gyroscopes or fiber sensing. Typical temperature ranges of operation cover -40°C to +85°C, but there has been also some recent interest in SLEDs operating at ultra-high ambient temperatures of up to 150°C even.

In this presentation, we discuss the electro-optical performance of SLED devices with an emission wavelength of 800-900 nm operating at ultra-high ambient temperatures beyond 100°C. Under these conditions, the main limitation for the achievable output power is given by the thermal degradation of the material gain and, even more so, by the strongly increasing non-radiative Auger recombination processes. Consequently, ex-facet output power levels of more than 1 mW can be hardly achieved with standard SLEDs operating at 110°C or higher. This limitation can be overcome by using reflective SLEDs (R-SLEDs) [1] with optimized epitaxial layer structures. These devices can generate decent output powers of several milliwatts at ambient temperatures up to 140°C and with Gaussian-shaped ASE spectra having a bandwidth of 10-20 nm FWHM.

II. EPITAXIAL LAYER DESIGN AND MATERIAL GAIN

The epitaxial layer structure of SLEDs operating in the near-infrared wavelength range from 800 nm to 900 nm relies on (Al)GaInAs active-region layers grown on a GaAs substrate. The SLEDs under consideration consist of compressively strained quantum-well (QW) layers. Quantum barrier layers with relatively high bandgap energy are used to provide deep

quantum wells. This should keep the carriers (particularly electrons) well confined in the active layer and lower the effect of thermionic emission of carriers out of the QWs, which would reduce the SLED's efficiency at high-temperature operation.

SLEDs operate in the so-called ASE regime below lasing threshold. As a result, the carrier density in the active-region layer(s) is not clamped so that, for a fixed junction temperature, the output power is basically determined by the material gain for a given pump level or a given carrier density. On the other hand, it is well known that, for a fixed pump level, the material peak gain degrades severely with increasing junction temperature. Fig. 1 shows that the peak material at a junction temperature of 120°C is approximately only half of the peak gain at 20°C. Moreover, the peak gain, and thus the ASE spectrum may shift by more than 30 nm to longer wavelengths over the large temperature range. This wavelength shift must be considered when designing the ASE spectrum for the correct wavelength position at the foreseen high-temperature operating condition.

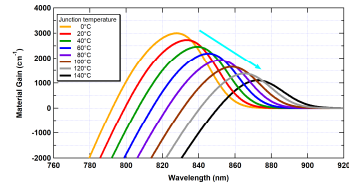


Fig. 1. Spectral dependence of the TE material gain for one quantum well with a fixed carrier density of $5 \cdot 10^{24} \text{ m}^{-3}$ at various junction temperatures.

III. AUGER RECOMBINATION

The efficiency of SLEDs suffers severely from non-radiative Auger recombination losses, as has been already pointed out by Piprek because of its generally higher and non-clamped carrier concentration compared to laser diodes [2]. Moreover, the Auger losses increase with increasing junction temperature. The temperature dependence of the Auger coefficient can be well described by an Arrhenius-type equation of the form

$$C_n = C_p \equiv C(T_j) = C_0 \cdot \exp\left(E_a / k_B \cdot (1/T_0 - 1/T_j)\right), \quad (1)$$

assuming same Auger coefficients for electrons (C_n) and holes (C_p) [3]. In (1), C_0 is the Auger coefficient at room temperature $T_0 = 298 \text{ K}$, E_a the activation energy, and T_j the actual junction temperature. For high activation energies, the Auger coefficient increases enormously with increasing junction temperature, as shown in Fig. 2. For an activation energy of 250 meV, the Auger coefficient is a factor of ten higher at a junction temperature of 120°C compared to room temperature.

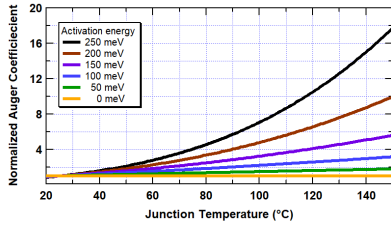


Fig. 2. Normalized Auger coefficient C/C_0 as function of the junction temperature for various activation energies from 0 up to 250 meV.

IV. FULL 3D DEVICE SIMULATION AND DEVICE OPTIMIZATION

The electro-optical performance of the SLED chips has been simulated using a full 3D simulation software tool. The simulator has been calibrated using measurement results, obtained from fabricated modules, over the temperature range from 20°C to 120°C. The Auger coefficient C_0 and the activation energy E_a have been used as open parameters for fitting the measured $L-I$ characteristics. The fiber-coupled output power values of the modules have been multiplied by factors of 2.2 assuming a realistic fiber coupling efficiency of 45%. This allows a direct comparison with the simulated ex-facet output power from the SLED chip. From our simulations, as shown in Fig. 3, we find that the best agreement with measured $L-I$ characteristics is achieved using an activation energy of 250 meV and a room temperature Auger coefficient of $2.4 \times 10^{-42} \text{ m}^6/\text{s}$.

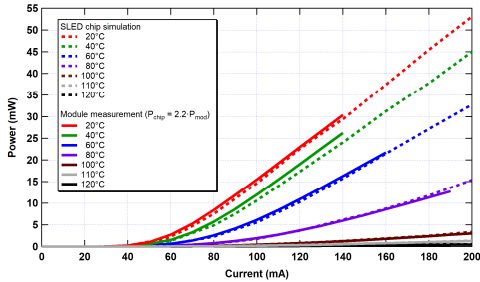


Fig. 3. Comparison of measured (solid lines) with simulated (dashed lines) $L-I$ characteristics for various heatsink temperatures from 20°C up to 120°C.

With standard SLED design rules, it appears to be very challenging to achieve an output power of more than 1 mW for heatsink temperatures of 110°C or above. This is mainly due to the Auger loss coefficient that is strongly increased at high ambient temperatures and for high activation energies (see Fig. 2). However, with a continuous reduction of the activation energy from 250 meV (black curve) to 0 meV (orange curve), the $L-I$ characteristics can be significantly improved, as shown in Fig. 4, even at high junction temperatures. Having zero activation energy means that the temperature dependence of the Auger coefficient is switched off, resulting in device operation with a constant Auger coefficient C_0 . Consequently, the remaining difference between the orange curve (120°C) and the red curve (25°C) is caused by the reduction in material gain and by thermionic loss of carriers from the QWs.

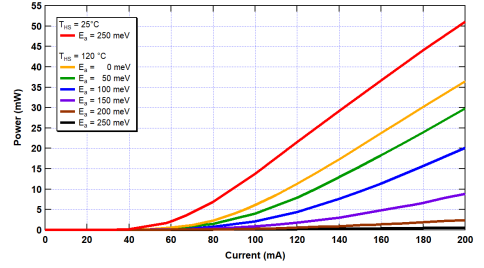


Fig. 4. $L-I$ characteristics simulated for various activation energies at a heatsink temperature of 120 °C. The red curve shows is for room temperature (25°C).

A significant improvement for high-temperature operation can be achieved with R-SLED devices [1] with a double-pass amplification process, which results in a significant boost in output power. After additional epitaxial design optimization, optical output power levels of more than 20 mW at 130°C, around 6 mW at 140°C and even 1 mW at 150°C are obtained with low injection currents of 200 mA only, as shown in Fig. 5.

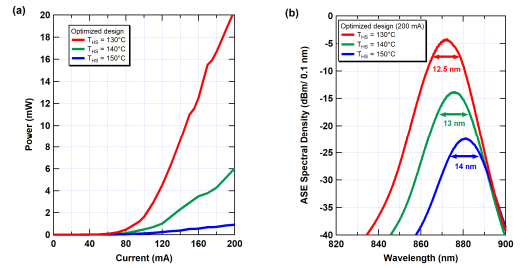


Fig. 5. (a) Simulated $L-I$ characteristics for an optimized R-SLED structure for heatsink temperatures of 130°C, 140°C, and 150°C. (b) Gaussian-shaped ASE spectra obtained at an injection current of 200 mA.

V. SUMMARY

We have shown that the electro-optical performance of GaAs-based SLED devices, operating at 800-900 nm and at ultra-high ambient temperatures, is mainly limited by the strong temperature-dependence of the Auger coefficient for high activation energies and, secondly, by the thermal degeneration of the material gain. Consequently, R-SLED designs seem superior in generating several milliwatts of output power at chip temperatures beyond 100°C compared to standard SLED designs.

REFERENCES

- [1] N. Matuschek and M. Duelk, "Superluminescent light-emitting diodes," in *Handbook of Optoelectronic Device Modeling & Simulation*, ed. J. Piprek, ch. 19, CRC Press, 2019.
- [2] J. Piprek, "What limits the efficiency of GaN-based superluminescent light-emitting diodes (SLEDs)," *Optical and Quantum Electron.*, 51(12), DOI: 10.1007/s11082-019-2106-3, 2019.
- [3] J. Piprek, *Semiconductor Optoelectronic Devices: Introduction to Physics and Simulation*, Academic Press, 2003.

Mg-Si Doped Barriers For Polarization Field Screening in High-Power InGaN/GaN Green LEDs

Chandra Prakash Singh
Department of Electrical Engineering
Indian Institute of Technology Jammu
Jammu, India
2020ree2054@iitjammu.ac.in

Kankat Ghosh
Department of Electrical Engineering
Indian Institute of Technology Jammu
Jammu, India
kankat.ghosh@iitjammu.ac.in

Abstract— We present numerical simulations demonstrating that polarization-induced electric fields in c-plane InGaN/GaN quantum wells (QWs) can be effectively neutralized by introducing asymmetrically doped barrier layers sandwiching a 3 nm-thick $\text{In}_{0.3}\text{Ga}_{0.7}\text{N}$ QW. Specifically, a 6 nm-thick n-GaN layer doped with Si ($1 \times 10^{19} \text{ cm}^{-3}$) and a 1 nm-thick p-GaN layer doped with Mg ($2 \times 10^{19} \text{ cm}^{-3}$) are employed as barriers to form the sandwich structure named Mg-QW-Si. Based on this design, we propose a green LED that achieves a peak internal quantum efficiency of 87%, exhibits only 32% droop at 500 A/cm², and a 32% reduction in operating voltages. These results demonstrate a viable pathway for realizing high-efficiency in long-wavelength III-nitride LEDs for high-power applications.

Keywords—III-Nitride, efficiency droop, green-gap, polarization field screening.

I. INTRODUCTION

InGaN-based light-emitting diodes (LEDs) have achieved widespread adoption, but their efficiency at high injection currents is limited by a phenomenon known as efficiency droop, a non-thermal decline in internal quantum efficiency (IQE) at elevated current densities [1]. This phenomenon restricts high-power LEDs to operate at lower current densities, where peak efficiency is typically achieved. In conventional c-plane LEDs, strong polarization-induced electric fields in strained InGaN/GaN quantum wells (QWs) aggravate this issue by spatially separating the electron and hole wavefunctions, thereby reducing their overlap and the associated oscillator strength. The suppressed radiative recombination rate leads to an elevated carrier concentration (n) in the active region at a given injection current density (J), which in turn accelerates the onset of droop, primarily due to Auger recombination that dominates at high n [2]. Furthermore, these polarization fields give rise to the quantum-confined Stark effect (QCSE), a well-known phenomenon responsible for the green-gap, which refers to the significant efficiency degradation observed in long-wavelength III-nitride QWs [3]. Consequently, neutralizing the internal electric field within QWs presents a promising strategy to mitigate both efficiency droop and green-gap.

While non-polar and semipolar orientations help reduce internal electric fields and suppress the QCSE, their dependence on expensive substrates limits widespread adoption. Alternatively, reducing polarization fields in c-plane structures through QW design and polarization screening methods such as doping offers a scalable and cost-effective solution. In this work, we explore such doping-based strategies to enable high-efficiency, low-droop LEDs on large-area c-plane substrates.

II. DEVICE STRUCTURE

The reference structure of the Ga-polar c-plane InGaN/GaN LED with p-side-up geometry is shown in Fig. 1.

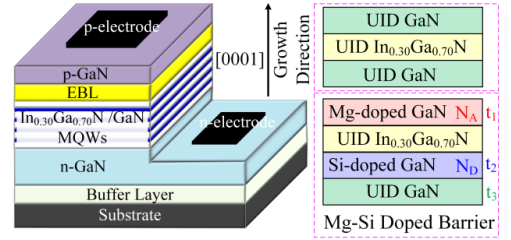


Fig. 1. Schematic of reference device structure with UID GaN barriers and engineered Mg-QW-Si architecture.

It consists of a 200 nm-thick n-GaN layer ($\text{Si}: 5 \times 10^{18} \text{ cm}^{-3}$) followed by a multi-quantum-well (MQW) active region, a 15 nm-thick $\text{p-Al}_{0.15}\text{Ga}_{0.85}\text{N}$ electron blocking layer (EBL), and a 180 nm-thick p-GaN layer ($\text{Mg}: 2 \times 10^{19} \text{ cm}^{-3}$). The active region comprises five unintentionally doped (UID) 3 nm-thick $\text{In}_{0.3}\text{Ga}_{0.7}\text{N}$ QW, each separated by 18 nm UID GaN barriers with a background doping of $1 \times 10^{16} \text{ cm}^{-3}$. Numerical simulations were performed using a one-dimensional drift-diffusion charge control solver that self-consistently resolves energy band diagrams and current density-voltage (J - V) characteristics. Further details on the simulation methodology with experimental validation are provided in [4].

III. RESULTS AND DISCUSSION

In c-plane InGaN/GaN QWs, the polarization-induced internal electric field (E_{pol}), resulting from spontaneous and piezoelectric polarization, can reach several MV/cm and typically points toward the $[000\bar{1}]$ substrate direction. Its magnitude is inherently linked to the In-content in the InGaN QWs, making independent tuning difficult without affecting the emission wavelength. To counteract E_{pol} and suppress the QCSE, we introduce an asymmetric doping scheme within the GaN barriers, specifically using Si-donors (N_D) on the n-side and Mg-acceptors (N_A) on the p-side, as illustrated in Fig. 2. This configuration establishes a built-in electric field (E_{pm}) oriented opposite to E_{pol} , effectively reducing the net electric field in the QW (E_{QW}). Unlike the fixed nature of E_{pol} , the compensating field E_{pm} is tunable by adjusting the dopant concentrations (N_A , N_D) and the spatial widths of the doped regions (t_1 , t_2), along with an UID intermediate layer (t_3).

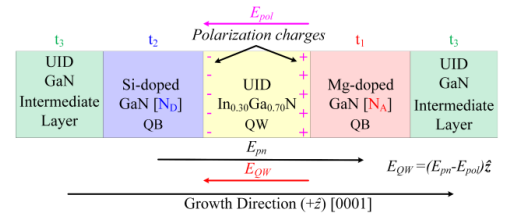


Fig. 2. Conceptual illustration of polarization field cancellation.

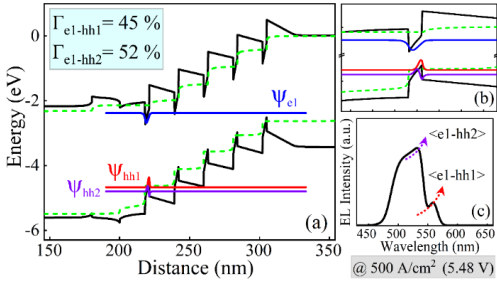


Fig. 3. (a) Energy band diagram with localized wavefunctions, (b) magnified last QW, and (c) EL spectrum with dual peaks at 532 nm and 560 nm for the LED with UID-QWs structure.

Moreover, E_{pm} aligns co-directionally with the forward bias-induced electric field (E_{FB}), enhancing polarization field screening and facilitating more efficient carrier injection. To identify the optimal doping profiles and layer thicknesses for the Mg-Si sandwich QW architecture, a series of numerical simulations were performed. The final structure comprises 3 nm-thick $\text{In}_{0.3}\text{Ga}_{0.7}\text{N}$ QW asymmetrically enclosed by a 1 nm thick (ti) p-GaN ($N_A = 2 \times 10^{19} \text{ cm}^{-3}$) and a 6 nm thick (tz) n-GaN ($N_D = 1 \times 10^{19} \text{ cm}^{-3}$), forming the Mg-QW-Si configuration. To prevent the formation of a direct p-n junction, which could introduce abrupt band bending and localized electric field discontinuities, a 4 nm thick (ts) UID GaN intermediate layer is inserted between the doped barriers. This design ensures a smooth potential profile and uniform electric field distribution across the active region.

As illustrated in Fig. 3 (a), the energy band diagram and corresponding localized wavefunctions are plotted for the last QW of the LED structure employing undoped sandwich QWs (UID-QWs) under an injection current density of 500 A/cm^2 . As expected, the UID-QW structure exhibits a substantial E_{pol} , resulting in strong band bending across the QW region. This effect is clearly depicted in the magnified view in Fig. 3 (b), where the internal field reduces the spatial overlap between the ground-state electron (e1) and heavy-hole (hh1 and hh2) wavefunctions. The close proximity of these overlap values indicates that both transitions contribute notably to radiative recombination. As a result, the electroluminescence (EL) spectrum, as shown in Fig. 3 (c), exhibits a characteristic head-and-shoulder profile, with two peaks located at 532 nm and 560 nm. This spectral broadening reflects reduced color selectivity, attributed to the simultaneous contribution of multiple recombination pathways within the MQWs induced by the strong QCSE.

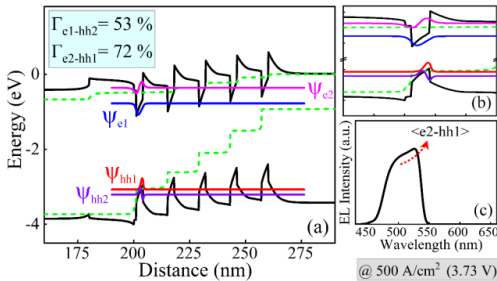


Fig. 4. (a) Energy band diagram with localized wavefunctions, (b) magnified last QW, and (c) EL spectrum with single peaks at 525 nm for the LED with Mg-Si sandwich QW.

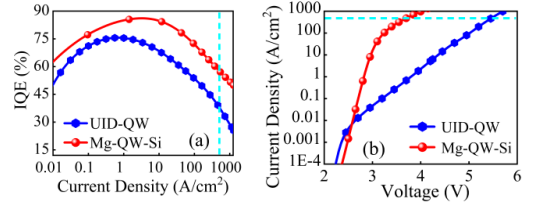


Fig. 5. (a) IQE-J, and (b) J-V characteristics for injection currents density ranging from 0 to 1000 A/cm^2 .

In contrast, the Mg-QW-Si structure exhibits distinctly improved electrostatic and optical behaviour. Optimised asymmetrically doped GaN barriers generates a compensating field E_{pm} that neutralizes E_{pol} , resulting in a flattened band profile across the QW at 500 A/cm^2 , as shown in Fig. 4 (a) and (b), confirming effective field compensation. This enhances the wavefunction overlaps to 53% for the $\langle e1-hh2 \rangle$ transition and a significantly higher 72% for the $\langle e2-hh1 \rangle$ transition. This significant difference in the improved overlap leads to a single dominant EL peak at 525 nm, as illustrated in Fig. 4 (c). The observed blue shift of the emission peak relative to the 532 nm peak in the undoped structure further validates the suppression of QCSE. The enhanced spatial overlap directly improves radiative recombination efficiency. As a result, the Mg-QW-Si structure achieves a peak IQE of 87% at low injection levels ($< 20 \text{ A/cm}^2$), outperforming the UID-QW structure, which reaches a maximum of 75%, as shown in Fig. 5 (a). More importantly, the Mg-Si design maintains superior performance at high injection levels, sustaining an IQE of 58% at 500 A/cm^2 , compared to only 35% for the UID-QW. Furthermore, as shown in Fig. 5 (b), the Mg-QW-Si LED yields a 32% reduction in forward operating voltage at 500 A/cm^2 , which directly contributes to improved wall-plug efficiency and enhanced overall performance under high-power operating conditions.

IV. CONCLUSION

The proposed Mg-QW-Si architecture offers an effective and scalable approach for polarization field compensation in high-power c-plane InGaN/GaN LEDs. The design enables significant improvement in wavefunction overlap, spectral purity, and voltage performance, achieving 72% overlap, 32% lower operating voltage, and 58% IQE at 500 A/cm^2 . These findings confirm the effectiveness of field-neutralization in high-In-content QWs for overcoming efficiency droop and the green-gap problem in long-wavelength III-nitride optoelectronic devices.

REFERENCES

- [1] L. Wang, Z.-H. Zhang and N. Wang, "Current Crowding Phenomenon: Theoretical and Direct Correlation With the Efficiency Droop of Light Emitting Diodes by a Modified ABC Model," in *IEEE Journal of Quantum Electronics*, vol. 51, no. 5, pp. 1-9, Art no. 3200109, May 2015.
- [2] Y. Kang et al., "Efficiency droop suppression and light output power enhancement of deep ultraviolet light-emitting diode by incorporating inverted-V-shaped quantum barriers," in *IEEE Trans. Electron Devices*, vol. 67, no. 11, pp. 4958-4962, Nov. 2020.
- [3] S. Lai, et al., "Green InGaN/GaN multiple-quantum-wells with pre-layer for high-efficiency mini-LEDs," in *IEEE Electron Device Letters*, vol. 44, no. 6, pp. 907-910, 2023.
- [4] C. P. Singh and K. Ghosh, "Enhancing the yellow-LED performance with improvised pre-stress alleviation layer: a theoretical and numerical analysis," in *Journal of Physics D: Applied Physics*, vol. 58, no. 1, Art. no. 015113, Oct. 2024.

Simulations and Theoretical Background: Quantum Entanglement in Photonic Quantum Computing and Cryptography

Mohammed Nadir

Faculty of Engineering and Natural Sciences, Tampere University, Finland
email:mohammed.nadir.fi@ieee.org

Abstract—Quantum entanglement is a cornerstone of quantum mechanics and has profound implications for quantum computing and cryptography. This article explores the theoretical underpinnings of quantum entanglement in photonic systems, its application in quantum computing with qubits, and its role in quantum cryptography. We present the mathematical models and verification through simulations, including Bell test experiments and Quantum Key Distribution (QKD) protocols. The results show the feasibility of photonic qubits in secure communication and highlight future prospects for practical applications.

I. INTRODUCTION

Quantum entanglement, a phenomenon where particles exhibit correlated behaviors regardless of distance, has revolutionized our understanding of quantum mechanics. Photonic qubits, due to their robustness against decoherence and ease of manipulation, serve as an ideal platform for implementing quantum computing and cryptographic protocols [1]. This paper delves into the theoretical background of quantum entanglement, demonstrates key experiments using simulations, and discusses the implications for future technologies [2].

II. MATHEMATICAL BACKGROUND

Quantum entanglement can be mathematically represented through entangled states, such as Bell states. These states form a basis for two-qubit systems and are crucial for understanding quantum correlations [3].

A. Two-Qubit Systems and Bell States

In quantum mechanics, a qubit is the basic unit of quantum information, analogous to a bit in classical information theory. A single qubit can be in a superposition of the states $|0\rangle$ and $|1\rangle$, which are typically represented as:

$$|0\rangle = \begin{pmatrix} 1 \\ 0 \end{pmatrix}, \quad |1\rangle = \begin{pmatrix} 0 \\ 1 \end{pmatrix}$$

A two-qubit system consists of two such qubits, and its state can be represented in the combined basis $\{|00\rangle, |01\rangle, |10\rangle, |11\rangle\}$. The state of a two-qubit system can thus be written as:

$$|\psi\rangle = \alpha|00\rangle + \beta|01\rangle + \gamma|10\rangle + \delta|11\rangle$$

where $\alpha, \beta, \gamma, \delta$ are complex coefficients that satisfy the normalization condition $|\alpha|^2 + |\beta|^2 + |\gamma|^2 + |\delta|^2 = 1$.

Bell states are a specific set of maximally entangled quantum states of two qubits. They are named after physicist John Bell, who formulated Bell's theorem. The four Bell states are:

$$\begin{aligned} |\Phi^+\rangle &= \frac{1}{\sqrt{2}}(|00\rangle + |11\rangle), \\ |\Phi^-\rangle &= \frac{1}{\sqrt{2}}(|00\rangle - |11\rangle), \\ |\Psi^+\rangle &= \frac{1}{\sqrt{2}}(|01\rangle + |10\rangle), \\ |\Psi^-\rangle &= \frac{1}{\sqrt{2}}(|01\rangle - |10\rangle). \end{aligned} \tag{1}$$

These states form an orthonormal basis for the space of two qubits and are used to demonstrate quantum entanglement. Each Bell state represents a situation where the measurement outcomes of the two qubits are perfectly correlated or anti-correlated [7].

Entanglement is a quantum phenomenon where the quantum states of two or more objects are interconnected, such that the state of one object cannot be described independently of the state of the other(s). This leads to correlations between the measurement outcomes of entangled particles that are stronger than those predicted by classical physics [4].

For instance, if we measure both qubits of the $|\Phi^+\rangle$ state along the same axis, we always find them in the same state (both 0 or both 1), showing perfect correlation. Similarly, in the $|\Psi^+\rangle$ state, measurements along the same axis will always yield opposite outcomes (one 0 and one 1), showing perfect anti-correlation [8].

B. Spontaneous Parametric Down-Conversion (SPDC)

SPDC is a nonlinear optical process in which a photon (the pump photon) passing through a nonlinear crystal is converted into two lower-energy photons (signal and idler photons). This process is probabilistic and is widely used to generate entangled photon pairs. The generated photon pairs can exhibit quantum entanglement, making SPDC a fundamental process in experimental quantum optics [6].

Mathematically, the state of the entangled photon pair generated by SPDC can be written as:

$$|\psi\rangle = \frac{1}{\sqrt{2}}(|H\rangle_s |H\rangle_i + |V\rangle_s |V\rangle_i), \tag{2}$$

where $|H\rangle$ and $|V\rangle$ represent horizontal and vertical polarizations, respectively, and the subscripts s and i refer to the signal and idler photons [4].

C. Quantum Key Distribution (QKD)

QKD is a secure communication method that uses quantum mechanics to allow two parties to produce a shared random secret key, which can then be used to encrypt and decrypt messages. The security of QKD is based on the principles of quantum mechanics, particularly the no-cloning theorem and the detection of eavesdropping attempts [5], [9].

The BB84 protocol, developed by Charles Bennett and Gilles Brassard in 1984, is one of the most well-known QKD protocols. It involves the transmission of qubits in one of four possible states, chosen at random. The key steps of the BB84 protocol are as follows: 1. *Preparation*: Alice randomly prepares qubits in one of four states (e.g., horizontal, vertical, diagonal, anti-diagonal). 2. *Transmission*: Alice sends the qubits to Bob over a quantum channel. 3. *Measurement*: Bob randomly chooses one of two bases to measure each qubit. 4. *Sifting*: Alice and Bob publicly compare their basis choices and keep only the results where their bases match. 5. *Key Distillation*: Alice and Bob apply error correction and privacy amplification to produce a shared secret key [4].

III. VERIFICATION BY SIMULATIONS AND EXPERIMENTS

A. Bell Test Experiment

The Bell test experiment verifies quantum entanglement by comparing measurement results of entangled photons against classical predictions. A violation of Bell's inequality indicates quantum correlations [2].

B. Explanation of Bell's Inequality and Violation

Bell's inequality provides a way to test the predictions of quantum mechanics against those of classical physics. In a classical, local hidden variable theory, the Bell parameter S must satisfy the inequality $S \leq 2$.

In the context of the Bell test, the Bell parameter S is calculated using correlations between measurement outcomes of entangled particles. For example, consider a scenario where Alice and Bob each measure one of the entangled particles in different bases (e.g., horizontal, vertical, diagonal, anti-diagonal). The correlations between their measurement outcomes are used to compute S .

Quantum mechanics predicts that for certain entangled states and measurement settings, the value of S can exceed 2. Specifically, for maximally entangled Bell states and appropriately chosen measurement bases, quantum mechanics predicts that S can reach a value as high as $2\sqrt{2}$ (approximately 2.828). This violation of Bell's inequality ($S > 2$) is a direct indication of quantum entanglement and cannot be explained by any classical local hidden variable theory [7].

The key to observing a violation of Bell's inequality lies in the correct preparation of the entangled state, the choice of measurement bases, and the accurate calculation of correlations between measurement outcomes. When these conditions are met, the experimentally measured value of

S will demonstrate the non-classical nature of quantum entanglement [6].

C. Quantum Key Distribution (QKD) Simulation

QKD ensures secure communication by exploiting quantum entanglement. The BB84 protocol, demonstrated through simulations, illustrates how keys can be securely shared [9].

1) *Results and Justification*: The QKD simulation using the BB84 protocol resulted in the generation of secure keys for Alice and Bob. The keys were generated only where their measurement bases matched. Sample keys generated were:

- Alice's key: [1, 0, 1, 1, 0, ...]
- Bob's key: [1, 0, 1, 1, 0, ...]

The matching keys indicate that the QKD protocol successfully established a secure communication channel, ensuring that any eavesdropping attempt would be detectable. This demonstrates the practical feasibility of using photonic qubits for secure communication [8].

IV. CONCLUSION AND FUTURE PROSPECTS

Quantum entanglement in photonic systems offers a robust foundation for quantum computing and cryptography. The simulations utilize the theoretical models and demonstrate the feasibility of practical applications, such as secure communication through QKD. Future research will focus on scaling these technologies for widespread use, exploring advanced quantum algorithms, and enhancing the robustness of quantum networks.

Acknowledgement: Thanks to Tampere University.

REFERENCES

- [1] Aspect, A., Dalibard, J., & Roger, G. (1982). Experimental test of Bell's inequalities using time-varying analyzers. *Physical Review Letters*, 49(25), 1804.
- [2] Hensen, B., Bernien, H., Dréau, A. E., Reiserer, A., Kalb, N., Blok, M. S., ... & Hanson, R. (2015). Loophole-free Bell inequality violation using electron spins separated by 1.3 kilometres. *Nature*, 526(7575), 682-686.
- [3] Tegmark, M. (1998). The interpretation of quantum mechanics: Many worlds or many words?. *Fortschritte der Physik: Progress of Physics*, 46(6-8), 855-862.
- [4] Pan, J.-W., Chen, Z.-B., Lu, C.-Y., Weinfurter, H., Zeilinger, A., & Zukowski, M. (2012). Multiphoton entanglement and interferometry. *Reviews of Modern Physics*, 84(2), 777.
- [5] Bennett, C. H., & Brassard, G. (1984). Quantum cryptography: Public key distribution and coin tossing. *Proceedings of IEEE International Conference on Computers, Systems and Signal Processing*, 175-179.
- [6] Ursin, R., Tiefenbacher, F., Schmitt-Manderbach, T., Weier, H., Scheidl, T., Lindenthal, M., ... & Zeilinger, A. (2007). Entanglement-based quantum communication over 144 km. *Nature Physics*, 3(7), 481-486.
- [7] Bell, J. S. (1964). On the Einstein Podolsky Rosen paradox. *Physica Physique Fizika*, 1(3), 195-200.
- [8] Bennett, C. H., Brassard, G., Crépeau, C., Jozsa, R., Peres, A., & Wootters, W. K. (1993). Teleporting an unknown quantum state via dual classical and Einstein-Podolsky-Rosen channels. *Physical Review Letters*, 70(13), 1895.
- [9] Ekert, A. K. (1991). Quantum cryptography based on Bell's theorem. *Physical Review Letters*, 67(6), 661.

High-Efficiency Nanoplasmonic Dual-Band Band-Stop Filters Using Step Impedance Resonators

^{1,2} Kola Thirupathaiah, ² Montasir Qasymeh

¹Department of Electronics and Communication Engineering, Koneru Lakshmaiah Education Foundation, Hyderabad-500075, India

² Department of Electrical Engineering, Abu Dhabi University, Abu Dhabi, UAE
kola.jntu@gmail.com, montasir.qasymeh@adu.ac.ae

Abstract—This article presents dual-band stop filters using quarter-wavelength step-impedance resonators (SIRs) in subwavelength MIM structures, operating at 186.67 THz and 227.63 THz. Full-wave simulations analyze variations in transmission and reflection coefficients to validate concurrent filtering performance at the targeted optical frequency bands.

Index Terms—Nanoplasmonic, SIRs, Band-Stop, PICs

I. INTRODUCTION

Surface plasmon polaritons (SPPs) are electromagnetic waves confined to metal-dielectric interfaces, arising from the interaction between incident photons and oscillations of conduction electrons. These waves exhibit exponential field decay perpendicular to the interface and enable subwavelength confinement beyond the diffraction limit. Unlike conventional optical waveguides that carry only photonic signals, SPPs support the propagation of both optical and electronic signals, making them well-suited for nanoscale integration and high-density photonic integrated circuits (PICs). The slow-wave nature of SPPs leads to shorter wavelengths, reduced phase velocity, and higher surface impedance compared to waves in equivalent dielectric media. These characteristics allow SPP-guiding structures to be effectively modeled using transverse electromagnetic (TEM) equivalent transmission line theory.

Various nanoplasmonic waveguiding structures, such as insulator-metal-insulator (IMI), MIM waveguides, and nanowires, have been explored for PICs. Among them, MIM structures offer superior subwavelength confinement and light localization. Numerous SPP-based MIM devices, including filters [1] and diplexers [2], have been demonstrated. However, these components typically operate within a dual frequency band, primarily exhibiting band-pass characteristics.

Recently, bandpass filters operating under odd-mode conditions ($R_Z = Z_2/Z_1 < 1$), along with a diplexer designed for PICs, have been reported in [3] and [4]. This work presents the design of a concurrent dual-band bandstop filter based on even-mode conditions ($R_Z = Z_2/Z_1 > 1$), where the field distribution exhibits even-mode symmetry. The proposed filters are implemented using planar plasmonic MIM waveguides. The transmission line characteristics, dual-band filtering response, and band-stop behavior of SIRs are analyzed. Full-wave simulations using CST Microwave Studio validate the proposed design.

II. DESIGN AND ANALYSIS OF BAND STOP FILTERS

Fig.1 illustrates the SIR and its equivalent circuit, implemented using a plasmonic MIM waveguide with a single centrally position slit. Fig.2 shows the geometry of the proposed band-stop filter. Silica (SiO_2) is used as the dielectric medium with a relative permittivity of $\epsilon_r = 2.50$, while the frequency-dependent permittivity of silver follows the Drude model [5]. The narrow waveguide supports the fundamental transverse magnetic (TM) mode due to its subwavelength width. SPPs entering the input port are partially reflected and coupled into the resonant cavity, where they propagate along the metal-dielectric interfaces and form standing waves that couple to the output port. The resonance conditions for the fundamental and spurious frequencies are detailed in [6].

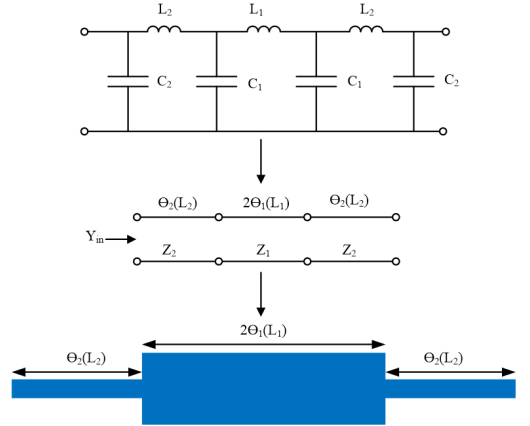


Fig. 1. Geometry of the quarter-wavelength SIR and its equivalent circuit.

In each plasmonic SIR, resonance occurs in either the even or odd mode. The odd mode represents the fundamental resonance, whereas the even mode supports the first and higher-order resonances. The resonance conditions are given by:

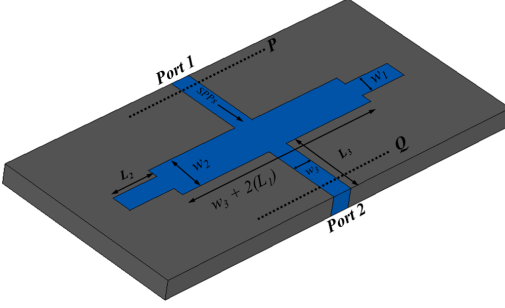


Fig. 2. Schematic of the plasmonic Band Stop Filter

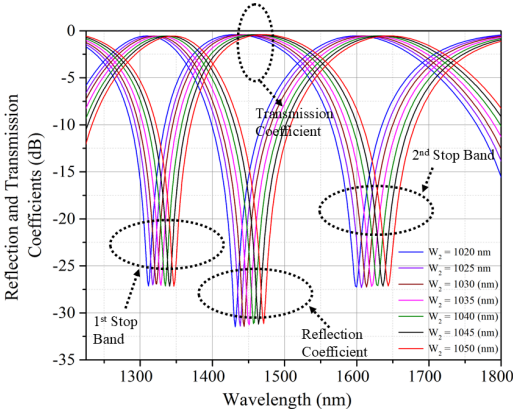


Fig. 3. Transmission and reflection coefficients of the band stop filter

$$\tan \theta_1 = R_Z \cot \theta_2 \quad (\text{odd-mode}) \quad (1)$$

$$\tan \theta_2 = -R_Z \tan \theta_1 \quad (\text{even-mode}) \quad (2)$$

$$R_Z = \frac{Z_2}{Z_1} = \tan \theta_1 \tan \theta_2 \quad (\text{impedance ratio}) \quad (3)$$

The relationship between fundamental and spurious resonance frequencies for the special case $\theta_1 = \theta_3 = \theta_0$ is given in [1]. In the simulation, power monitors P and Q are placed equidistant from the center of the MIM SIR to measure the input and output power levels. A grid size of $5 \text{ nm} \times 5 \text{ nm}$ is used along the x and y directions. The fundamental TM mode is excited from the left, propagating rightward. Only the fundamental TM mode can propagate, as the waveguide width is subwavelength.

$$\lambda \frac{f_{S1}}{f_0} = \frac{\pi}{2 \tan^{-1} \sqrt{R_Z}} \quad (4)$$

$$\lambda \frac{f_{S3}}{f_0} = \frac{\pi}{\tan^{-1} \sqrt{R_Z}} \quad (5)$$

where f_0 , f_{S1} , and f_{S3} represent the center, first spurious, and second spurious frequencies, respectively.

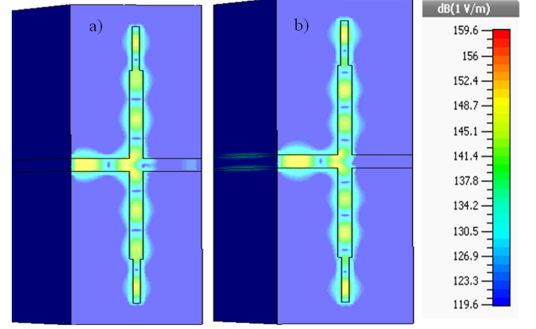


Fig. 4. Field distribution at wavelengths: (a) 1606 nm and (b) 1317 nm.

The dual-band filter is designed and simulated with fixed dimensions: $w_1 = 62 \text{ nm}$, $w_2 = 100 \text{ nm}$, $w_3 = 30 \text{ nm}$, satisfying the condition $w_3 + 2L_1 = 2250 \text{ nm}$, and lengths $L_1 = 1050 \text{ nm}$, $L_2 = 525 \text{ nm}$, and $L_3 = 500 \text{ nm}$. The transmission coefficients of the proposed band-stop filter are shown in Fig. 3. Based on Eq. (1), resonance occurs at $R_Z = 5.9$. The first stopband peak appears at the fundamental frequency $f_0 = 186.67 \text{ THz}$ (1607 nm), while the second peak occurs at the first spurious frequency $f_{S1} = 227.63 \text{ THz}$ (1317 nm) for $\theta_1 = \theta_2 = \theta_0$. However, due to unequal electrical lengths θ_1 and θ_2 , the second peak shifts slightly to 1320 nm, as shown in Fig.3. The parametric analysis demonstrates that varying L_1 has a more pronounced effect on transmission than changes in w_2 , indicating its greater influence on the resonance behavior. Fig. 4 shows the field distribution at 1606 nm and 1317 nm wavelengths.

CONCLUSION

Dual-band band-stop filters have been designed and analyzed using SIR structures based on MIM waveguide structures. The proposed filters operate efficiently at optical frequencies of 186.67 THz and 227.63 THz, achieving suppression levels greater than 30 dB. These findings support advanced design approaches for nanoscale PICs based on SPPs.

REFERENCES

- [1] K. Thirupathiah, N. P. Pathak, and V. Rastogi, "Concurrent dual band filters using plasmonic slotwaveguide," *IEEE Photon. Techn. Lett.*, vol. 25, no. 22, pp. 2217–2220, Nov. 2013.
- [2] K. Thirupathiah, B. Iyer, N. P. Pathak, and V. Rastogi, "Concurrent dualband diplexer for nanoscale wireless links," *IEEE Photon. Technol. Lett.*, vol. 26, no. 18, pp. 1832–1835, Sep. 2014.
- [3] S. Mokkapati, D. Saxena, N. Jiang, H. H. Tan, and C. Jagadish, "Plasmonic cavities for increasing the radiative efficiency of GaAs nanowires," in *Proc. Optoelectron. Microelectron. Mater. Devices Conf. (COMMAD)*, vol. 1, pp. 244–245, Dec. 2014.
- [4] J. Qi *et al.*, "Independently tunable double Fano resonances in asymmetric MIM waveguide structure," *Opt. Express*, vol. 22, no. 12, pp. 14688–14695, Jun. 2014.
- [5] K. R. Hiremath, L. Zschiedrich, and F. Schmidt, "Numerical solution of nonlocal hydrodynamic Drude model for arbitrary shaped nanoplasmonic structures using Nédélec finite elements," *J. Comput. Phys.*, vol. 231, no. 17, pp. 5890–5896, May 2012.

All-Optical 2R Regeneration Based on Similariton Generation in HNL-PCF for High Bit Rate Networks

Lynda Cherbi

Laboratory of instrumentation (LINS)
Faculty of Electrical Engineering
University of Sciences and Technology
Houari Boumediene (USTHB)
Algiers, Algeria
molvrs24@gmail.com

Hafida Azza

Laboratory of instrumentation (LINS)
Faculty of Electrical Engineering
University of Sciences and Technology
Houari Boumediene (USTHB)
Algiers, Algeria
hafidaazza3@gmail.com

Abstract— This paper presents an advanced all-optical 2R regenerator based on optical similariton generation in a custom-designed highly nonlinear photonic crystal fiber (HNL-PCF) amplifier. The HNL-PCF is optimized for high nonlinearity and low dispersion, enabling efficient similariton formation. The proposed scheme suppresses ASE noise and restores signal integrity across data rates from 40 Gb/s to 160 Gb/s. Compared to recent 2R regenerators based on self-phase modulation (SPM), our system demonstrates superior performance, offering enhanced noise suppression and signal quality. Integrated into a high-speed optical link, it significantly improves signal quality, highlighting its potential for next-generation optical networks.

Keywords—All-optical 2R regenerator, Raman amplification, optical similariton, high-capacity optical networks.

I. INTRODUCTION

The rising demand for high data rates in modern optical networks makes all-optical signal regeneration vital for maintaining transmission quality. Unlike electronic regeneration, which involves optical-electrical conversion, all-optical methods keep signals in the optical domain, offering higher bandwidth, lower latency, and better energy efficiency. Among these, 2R regeneration combining reamplification and reshaping offers a good trade-off between complexity and performance [1]. Self-phase modulation (SPM) is often used in such systems, with the Mamyshev regenerator standing out for its simplicity [2]. However, SPM-based methods encounter issues like spectral ripples and instability at high bit rates. This work presents a 2R regeneration approach based on optical similariton pulses, which exhibit smooth spectral broadening and linear chirp. These features improve amplitude noise suppression and reduce timing jitter. The method is implemented in a Raman-amplified highly nonlinear photonic crystal fiber (HNL-PCF) and evaluated at 40, 80, and 160 Gb/s. Results show superior performance over conventional SPM regenerators in terms of signal quality, jitter reduction, and transmission stability.

II. SIMULATION AND RESULTS

A. Generation of Optical Similariton Pulses

Figure 1 shows the simulation setup used to generate optical similariton pulses in a silica-based Raman amplifier HNL-

PCF, implemented using OptiSystem. Numerical modeling, carried out using the Finite Element Method (FEM) guided the optimization of parameters to achieve efficient pulse shaping and stable similariton formation [3]. The optimized configuration includes an input pulse power of 1 W, pulse duration of 0.2 ps, fiber dispersion of -1.53 ps/(nm.km), nonlinear coefficient $\gamma = 41$ W $^{-1}$.km $^{-1}$, and Raman gain coefficient $g_R = 7.6 \times 10^{-13}$ m/W.

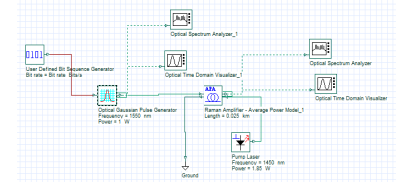


Fig. 1: Schematic of the setup for generating optical similariton pulses at 1550 nm in the modeled HNL-PCF (25 m). Simulation parameters: input power $P_0=1$ W, pulse duration $T_0 = 0.2$ ps, dispersion $D = -1.53$ ps/(nm.km), nonlinear coefficient $\gamma = 41$ W $^{-1}$.km $^{-1}$, and Raman gain coefficient $g_R = 7.6 \times 10^{-13}$ m/W.

Figure 2 shows that an input train of Gaussian pulses evolves into a train of optical similaritons after 25 meters of amplification. The resulting spectrum demonstrates excellent flatness, with minimal power variation across a 40 nm bandwidth effectively covering the C-band of the third optical telecommunications window. The output peak power reaches 104.6 W, reflecting strong pulse shaping and efficient nonlinear interaction.

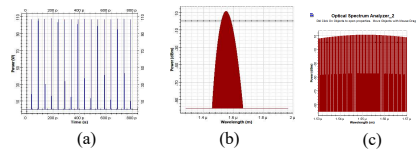


Fig. 2: Temporal (a) and Spectral (b) Profiles of Similariton Pulses generated in a Raman-Enhanced HNL-PCF ($L=25$ m, $P_0=1$ W, $T_0=0.2$ ps, $D=-1.53$ ps/(nm.km), $\gamma=41$ W $^{-1}$.km $^{-1}$, $g_R=7.6 \times 10^{-13}$ m/W at 1550 nm). (c) Zoomed-in view of the central part of the spectrum shown in (b)

B. Performance Analysis of High-Bit-Rate Optical Links Without Signal Regeneration

A 40 Gb/s optical transmission system over 50 km was simulated in OptiSystem 7.0, using 1 W input pulses to intentionally degrade the signal and demonstrate the effectiveness of the all-optical 2R regenerator. An EDFA (gain: 16.3 dB) compensates for attenuation, and a variable optical attenuator manages power levels. The transmission span consists of standard single-mode fiber (SMF) and

dispersion-compensating fiber (DCF), with parameters summarized below.

Figure 3 shows severe signal degradation in the transmission link without regeneration, as evidenced by a closed eye diagram and a low quality factor of $Q = 2$.

Table1: Transmission link parameters

Fiber	D (ps/(nm.km))	S_D (ps/(nm ² .km))	A_{eff} (μm^2)	α (dB/km)
SMF (G652)	16.75	0.075	80	0.2
DCF	-80	0.21	27	0.6

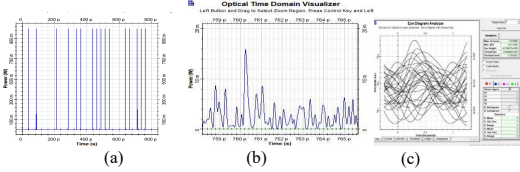


Fig. 3: (a) Input optical signal; (b) Signal shape at the output of a 400 km, 40 Gb/s transmission link without regeneration; (c) Eye diagram of the received signal.

C. Performance Analysis of 2R Regeneration with Similariton Pulses

Figure4 illustrates the simulation setup of the proposed 2R regenerator based on optical similariton pulses. The degraded signal from the 400 km link is first amplified using an optical amplifier with a gain of 18 dB to reach 1 W, then filtered with a 60 GHz Gaussian filter centered at 1550 nm, and further optimized using a 2.25 m SMF segment to reduce residual chirp.

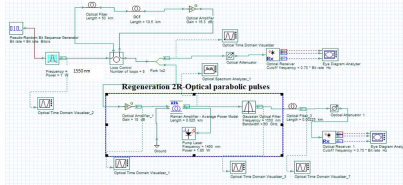


Fig. 4: 2R Optical Regeneration Setup using similariton pulse generation in a Raman- HNL-PCF amplifier

Figure 5 shows that after 2R regeneration using parabolic pulses at 40 Gb/s, the signal exhibits a fully open eye diagram with a quality factor improvement from $Q = 2$ to 81.85, highlighting effective noise suppression at the zero level and reduced intensity fluctuations in the "1" bit.

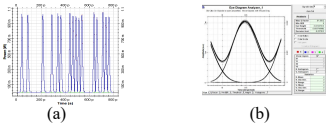


Fig. 5: (a) Temporal Profile and (b) Eye Diagram of the regenerated signal for a 40 Gb/s, 400 km link

D. Comparison Between SPM-Based Regeneration and 2R Optical similariton Pulse Regeneration

The SPM-based regenerator restores degraded signals by amplifying them to induce spectral broadening in a normal dispersion fiber. This process is followed by filtering out

ASE noise and injecting the signal into a band-pass filter, whose center frequency is calculated using the relation $\omega_f = \omega_0 + \Delta\omega_{spm}$ where $\Delta\omega_{spm} = \Delta\omega_0(2\pi/\lambda) n_2 I_p L$, ω_0 is input signal bandwidth, pulse intensity is denoted by I_p , n_2 is a nonlinear refractive index, λ is the wavelength and L is the length of nonlinear medium. [4]. The SPM regeneration process was simulated using OptiSystem,. If $\omega_{spm}/2 < \Delta\omega_{shift}$, the pulse is rejected by the optical filter, which occurs when the pulse intensity I_p is very small, representing noise in the "zero" state. If the pulse intensity is sufficiently high so that $\omega_{spm}/2 \geq \Delta\omega_{shift}$, the broadened pulse passes through the filter.

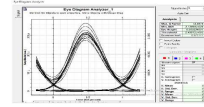


Fig. 6: Eye Diagram of the signal regenerated by the spm-based regenerator for a 40 Gb/s, 400 km Link

Figure 6 shows the regeneration of a degraded signal using the SPM-based regenerator, reducing noise but with some intensity fluctuations and temporal jitter, yielding a Q factor of 12.48 at 40 Gb/s much lower than the seven-fold improvement seen with optical parabolic pulse regeneration.

E. Impact of Bit Rate and Transmission Length on Optical Similariton Pulse Regeneration

Figure 7 illustrates the impact of bit rate and transmission distance on signal quality, showing how the quality factor (Q) decreases with increasing bit rate and distance due to nonlinear effects and chromatic dispersion.

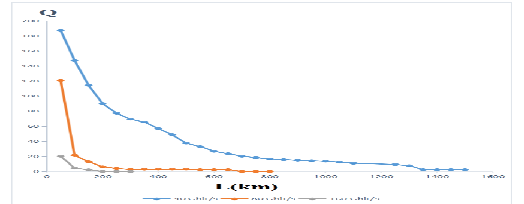


Fig. 7: Q-Factor vs. Distance – similariton 2R regenerator for (40Gbit/s-80Gbit/s-160Gbit/s).

III. CONCLUSION

An all-optical 2R regenerator based on similariton pulses was implemented using a Raman-enhanced HNL-PCF. It achieved a Q factor of 187.48 at 40 Gb/s and maintained Q greater than 6 up to 1300 km. These results confirm its strong potential, to be further highlighted through comparison with conventional SPM-based regeneration.

REFERENCES

- [1] Gay, Mathilde. Etude théorique et expérimentale de l'impact de la régénération 2R dans un système de transmission optique haut débit. Diss. INSA de Rennes, 2006.
- [2] Fabio B., et al. "All-Optical 2R Regenerator Non-Linear Optic Based on the Mamyshev Model." (2017).
- [3] Hafida Azza, Lynda Cherbi, "Self-Similar generation in ultra-flattened low dispersion microstructured fiber Raman Amplifier for Telecommunication applications" ADOP 2023.
- [4] TALUKDER, Hriteshwar, HUMAIRA, H., et REFAT, K. All optical 2R regeneration and optimization. *pulse*, 2016, vol. 2, no 3, p. 14-17.

Simulations of light emission at reverse voltage of wide-well InGaN light-emitting diodes

1st Konrad Sakowski

Institute of High Pressure Physics, PAS
Warsaw, Poland
0000-0003-1511-074X

2nd Artem Bercha

Institute of High Pressure Physics, PAS
Warsaw, Poland
0000-0002-7916-2744

3rd Grzegorz Muziol

Institute of High Pressure Physics, PAS
Warsaw, Poland
0000-0001-7430-3838

4th Mateusz Hajdel

Institute of High Pressure Physics, PAS
Warsaw, Poland
0000-0001-9732-6119

5th Witold Trzeciakowski

Institute of High Pressure Physics, PAS
Warsaw, Poland
0000-0002-4871-1069

GaN-based heterostructures are typically grown in the polar direction. Due to differences in polarization constants between layers of varying composition and the built-in strain, significant interfacial charges emerge. This phenomenon is particularly important for quantum wells (QWs), where the resulting built-in electric fields lead to the quantum-confined Stark effect (QCSE) and a spatial separation of electrons and holes. This separation significantly reduces the radiative recombination efficiency, especially in wider quantum wells where the increased distance between carriers is more detrimental to recombination.

Moreover, these interface polarization charges attract mobile carriers, which can partially screen these charges. While such mobile carriers are present in quantum wells, they do not significantly contribute to radiative recombination due to the spatial separation of electrons and holes, which tend to accumulate on opposite sides of the QWs.

Using drift-diffusion simulations of an InGaN LED, we have shown that this screening charge, or *dark charge*, can slowly accumulate under low forward voltages. These voltages, while insufficient to generate electroluminescence, allow to charge the quantum well by inducing an electron-hole buildup on opposite sides of the QW. We demonstrated that for a given forward bias, a sufficient time is required to charge the device with this screening dark charge and reach a stable concentration. This stable concentration, as well as the charging time, depends on the applied voltage; the dark charge concentration increases with the voltage, while the charging time decreases.

The presence of this dark charge was confirmed through both numerical simulations and physical experiments. The experimental confirmation relies on the application of short reverse-bias negative voltage pulses. These pulses alter the electric field distribution within the quantum well, affecting the distribution of charge carriers. Subsequently, some of the excess carriers recombine radiatively, leading to short pulses of light. The intensity of these light pulses depends on both the charging time and the applied forward voltage. The numerical simulations show qualitative agreement with the experimental

results.

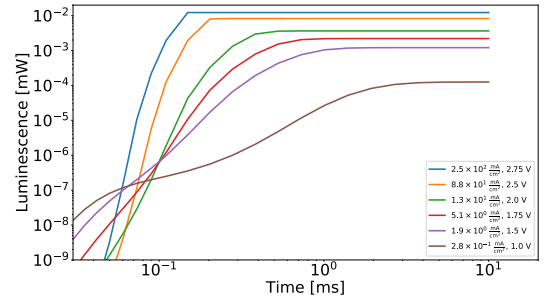


Fig. 1. Simulated intensity of the short pulses of light as a function of charging time for various forward biases and corresponding currents for an InGaN LED with 25 nm $\text{In}_{17\%}\text{Ga}_{83\%}\text{N}$ quantum well.

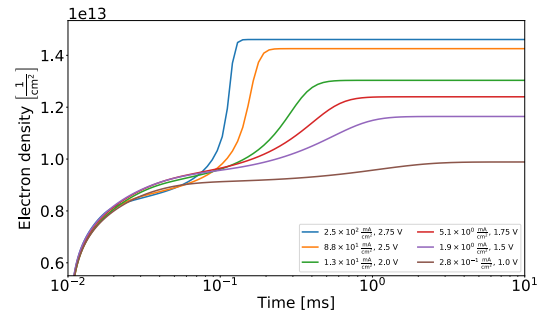


Fig. 2. Electron density in the quantum well vs charging time.

REFERENCES

- [1] A. Bercha, K. Sakowski, G. Muziol, M. Hajdel, and W. Trzeciakowski, "Light emission at reverse voltage in a wide-well (In,Ga)N/GaN light-emitting diode," *Physical Review Applied*, vol. 21, no. 5, p. 054030, 2024.
- [2] K. Sakowski, L. Marcinkowski, P. Strak, P. Kempisty, and S. Krukowski, "On the composite discontinuous Galerkin method for simulations of electric properties of semiconductor devices," *Electronic Transactions on Numerical Analysis*, vol. 51, pp. 75–98, 2019.

Inverse-Designed Ultra-Compact Polarization Demultiplexer

Preetam Kumar

Electrical Communication Engineering
Indian Institute of Science
Synopsys Inc.
Bangalore, India
ps1235711@gmail.com

E.S.Shivaleela

Electrical Communication Engineering
Indian Institute of Science
Bangalore, India
lila@iisc.ac.in

T.Srinivas

Electrical Communication Engineering
Indian Institute of Science
Bangalore, India
tsrinu@iisc.ac.in

Abstract—An ultracompact ($3 \times 3 \mu m^2$) silicon nitride-based 1x2 polarization demultiplexer for near-infrared (1400-1600nm) is designed by the inverse method. It achieves around 90% transmission, efficiently separating TE and TM polarization.

Index Terms—Inverse Design, Polarization Demultiplexer, SiN PICs

I. INTRODUCTION

Photonic Integrated Circuits (PICs) are vital for applications from optical communication to sensing. Within PICs, Polarization Demultiplexers (PDMs) are essential for separating orthogonal polarization states (TE and TM) into distinct paths, with their performance—low loss, high extinction, broad bandwidth, and compactness—critically impacting system efficiency and density.

The drive for higher integration necessitates ultra-compact components. Traditional PDM designs [1]–[4], while functional, often struggle to achieve optimal performance in minimal footprints and can involve extensive design iterations. Inverse design (ID) methodologies [5]–[10] offer a powerful alternative, algorithmically discovering non-intuitive nanostructures optimized for specific optical functions, often surpassing conventional designs in performance and compactness.

Silicon nitride (SiN) offers a low-loss, CMOS-compatible platform ideal for passive near-infrared (NIR) PICs, especially in the critical 1400-1600 nm telecom window. This work leverages inverse design to realize an ultra-compact SiN-based 1x2 PDM for this NIR range. We demonstrate a device with a minimal footprint that efficiently separates TE and TM polarizations to their respective output ports. This paper details the ID approach, simulation, and performance of the optimized PDM, highlighting the potential of ID for advanced photonic components.

II. DESIGN METHODOLOGY

The device is initialized as shown in Fig.1. We have assumed that the device is invariant in the z-direction and the propagation is confined only in the x and y direction. The design region is discretized by rectangular pixels with a size of $\delta x, \delta y = 100$ nm. Here, each pixel is classified as either SiN or Silica depending on optimization algorithm. The target

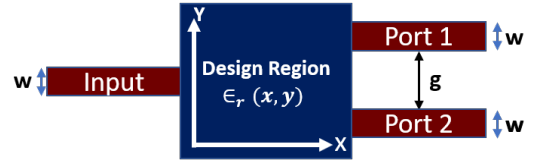


Fig. 1. shows the the block structure of the device. Design Region $\epsilon_r(x,y)$ has the size of $3\mu m \times 3\mu m$. Thickness of the device is 350 nm, width(w) of the input and the output waveguide is 550 nm and the gap(g) between the output ports is $1\mu m$.

port for the transmission of TE and TM mode is Port1 and Port 2 respectively.

This 2D approximation reduces computational complexity substantially. The core of the inverse design process is then formulated as an optimization problem. The objective is to maximize a defined Figure of Merit (FOM), which quantifies the device performance, by tailoring the permittivity distribution, $\epsilon(r)$ within the specified design region. This optimization problem can be expressed as:

$$\begin{aligned} & \underset{\epsilon}{\text{maximize}} \quad \text{FOM}(\{E_i(\epsilon)\}) \\ & \text{s.t.} \quad \nabla \times (\mu_0^{-1} \nabla \times \mathbf{E}_i) - \omega_i^2 \epsilon \mathbf{E}_i = -j\omega_i \mathbf{J}_i \end{aligned} \quad (1)$$

In Equation (1), the subscript 'i' denotes parameters corresponding to different discrete operating wavelengths within the target spectral range. ' E_i ' represents the complex electric field phasor at angular frequency ' ω_i '. $\epsilon = \epsilon(r)$ is the spatially varying permittivity distribution within the design region, which is the variable being optimized. ' μ_0 ' is the permeability of free space. J_i represents the source current density excitation at angular frequency ω_i .

III. RESULTS

The final optimized structure of the polarization demultiplexer, generated by the inverse design algorithm, is presented in Fig. 2. This figure illustrates the distribution of silicon nitride (shown in red) and air cladding (shown in blue) within

the design region. The algorithm has converged to a non-intuitive, freeform geometry that is tailored to achieve the desired functionality.

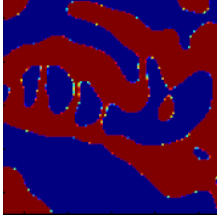


Fig. 2. shows the the final design of the structure. Red color shows the silicon nitride with blue color as the air cladd.

The simulated transmission characteristics of the optimized device for the TM and TE polarizations are shown in Fig. 3 and Fig. 4, respectively, across the near-infrared wavelength range of 1400 nm to 1600 nm.

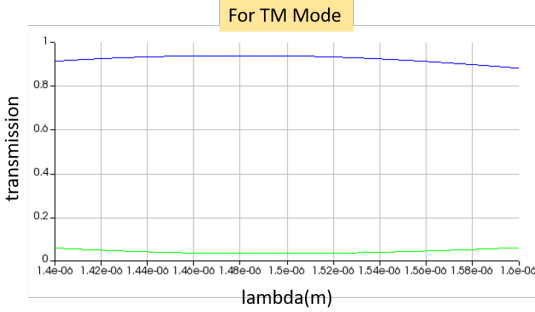


Fig. 3. shows the transmission of TM Mode. Blue color and the Green color shows the transmission at the Port 2 and Port 1 respectively.

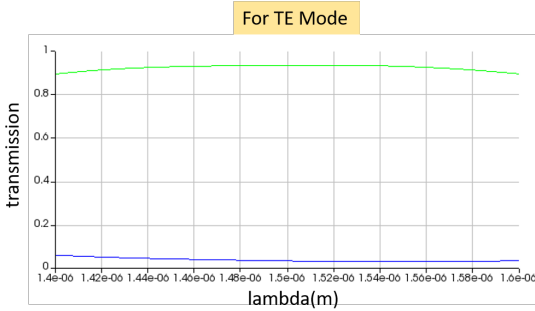


Fig. 4. shows the transmission of TE Mode. Blue color and the Green color shows the transmission at the Port 2 and Port 1 respectively.

As targeted, Fig.3 shows the TM mode predominantly routed to Port 2 (blue curve) with approximately 90% trans-

mission, while crosstalk to Port 1 (green curve) remains minimal (below 4%). Similarly, Fig.4 demonstrates efficient TE mode transmission (around 90%) to Port 1 (green curve), with suppressed crosstalk to Port 2 (blue curve, below 4%). These results collectively validate the successful functionality of the inverse-designed ultra-compact mode demultiplexer, achieving high transmission for both polarizations to their respective target ports over a 200 nm bandwidth within a footprint, underscoring the efficacy of inverse design for miniaturized, high-performance photonic components.

IV. CONCLUSION

We have successfully demonstrated an ultra-compact silicon nitride-based 1x2 mode demultiplexer for the near-infrared (1400-1600 nm) spectrum using an inverse design methodology. The optimized device exhibits high transmission efficiencies of approximately 90% for both TE and TM polarizations to their respective designated output ports over a 200 nm bandwidth, along with effective polarization separation and low crosstalk. These results validate the capability of inverse design to realize high-performance, miniaturized photonic components with non-intuitive geometries, paving the way for denser integration and enhanced functionalities in advanced photonic integrated circuits.

REFERENCES

- [1] D. Dai, Z. Wang and J. E. Bowers, "Considerations for the Design of Asymmetrical Mach-Zehnder Interferometers Used as Polarization Beam Splitters on a Submicrometer Silicon-On-Insulator Platform," in *Journal of Lightwave Technology*, vol. 29, no. 12, pp. 1808-1817, June 15, 2011, doi: 10.1109/JLT.2011.2142392.
- [2] Chenlei Li and Daoxin Dai, "Compact polarization beam splitter for silicon photonic integrated circuits with a 340-nm-thick silicon core layer," *Opt. Lett.* 42, 4243-4246 (2017).
- [3] José Manuel Luque-González, Alaine Herrero-Bermello, Alejandro Ortega-Moñux, Marina Sánchez-Rodríguez, Aitor V. Velasco, Jens H. Schmid, Pavel Cheben, Íñigo Molina-Fernández, and Robert Halir, "Polarization splitting directional coupler using tilted subwavelength gratings," *Opt. Lett.* 45, 3398-3401 (2020).
- [4] Sijie Dai and Jinbiao Xiao, "Compact and broadband silicon-based polarization beam splitter using asymmetric directional couplers embedded with subwavelength gratings and slots," *Appl. Opt.* 61, 126-134 (2022).
- [5] Lalau-Keraly, Christopher M., et al. "Adjoint shape optimization applied to electromagnetic design." *Optics express* 21.18 (2013): 21693-21701.
- [6] Piggott, Alexander Y., et al. "Fabrication-constrained nanophotonic inverse design." *Scientific reports* 7.1 (2017): 1786.
- [7] Molesky, Sean, et al. "Inverse design in nanophotonics." *Nature Photonics* 12.11 (2018): 659-670.
- [8] Kumar, Preetam, et al. "Polarization-independent dual-channel broadband wavelength demultiplexer design by inverse method." *Integrated Optics: Devices, Materials, and Technologies XXVII*. Vol. 12424. SPIE, 2023.
- [9] Kumar, Preetam, et al. "Inverse design of SiN based wavelength demultiplexer." *2023 International Conference for Advancement in Technology (ICONAT)*. IEEE, 2023.
- [10] Kumar, P., Mihret, F., Shivaleela, E. S., & Srinivas, T. (2023, September). A compact 1x4 wavelength demultiplexer by Inverse Design. In *2023 International Conference on Numerical Simulation of Optoelectronic Devices (NUSOD)* (pp. 45-46). IEEE.

DFB-LD connected in series to DBR with optical gain

Makio Ueno
Graduate School of Science and Engineering
Ritsumeikan University
Kusatsu, Japan
re0119kr@ed.ritsumeikai.ac.jp

Takahiro Numai
Graduate School of Science and Engineering
Ritsumeikan University
Kusatsu, Japan
numai@se.ritsumeikai.ac.jp

Abstract—This paper reports on a DFB-LD connected in series to a DBR with optical gain. This DFB-LD shows highly stable single longitudinal mode (SLM) operation with high external quantum efficiency more than 64% due to asymmetric facet light output. It is found that the main mode is determined by one of the resonance modes in the DFB-LD within high reflective wavelength region in the DBR. It is expected that the present DFB-LD shows SLM operation up to 600 mA.

Keywords—laser diode, grating, single longitudinal mode

I. INTRODUCTION

Because of dispersion in the optical fibers, single longitudinal mode (SLM) LDs have been utilized in long-haul, large capacity optical fiber communication systems. The most stable SLM LD is a phase-shifted DFB-LD which has been used in the trunk lines more than 30 years [1]. In the phase-shifted DFB-LD, front facet light output is almost the same as the rear facet light output. The front facet light output of 0 dBm is used as a signal and the rear facet light output is used as monitor light to suppress tracking errors. The rear facet light output of -20 dBm is enough as the monitor light. As a result, if we can obtain asymmetric light output between the front facet light output and the rear facet light output, we can expect improvement of external quantum efficiency and wall-plug efficiency of the DFB-LD. To achieve asymmetric light output between the front facet light output and the rear facet light output, slight transfer of the phase-shift position toward the front facet [2], introducing phase-shift at the boundary of uniform corrugations and chirped ones [3], DR-LDs [4], [5], and resonance-shifted DFB-LDs [6], [7] have been reported.

In this paper, a DFB-LD connected in series to a DBR with optical gain is studied. The external quantum efficiency more than 64% due to asymmetric facet light output is obtained. The oscillation mode is determined by one of the resonance modes in the DFB-LD within high reflective wavelength region in the DBR with SLM operation up to 600 mA.

II. STRUCTURE

Figure 1 shows a schematic cross-sectional view of the DFB-LD connected in series to a DBR with optical gain.

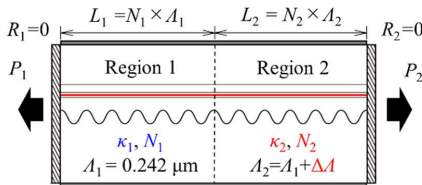


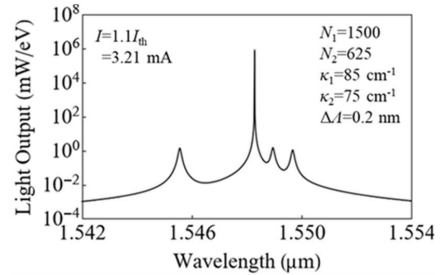
Fig. 1 Cross-sectional view cut along the longitudinal axis.

Region 1 with grating coupling constant κ_1 is connected to Region 2 with grating coupling constant κ_2 in series. The grating pitch A_1 in Region 1 is 0.242 μm ; the grating pitch A_2 in Region 2 is $A_1 + \Delta A$. The number of grating periods in Region 1 is N_1 ; the number of grating periods in Region 2 is N_2 . As a result, length of Region 1 is $L_1 = N_1 A_1$; length of Region 2 is $L_2 = N_2 A_2$.

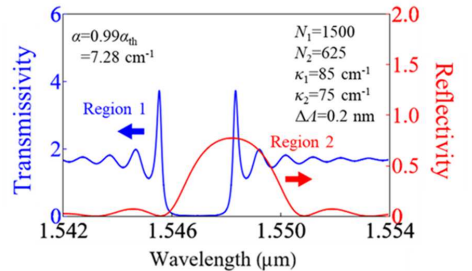
III. SIMULATED RESULTS AND DISCUSSION

Figure 2 (a) illustrates oscillation spectrum for $N_1 = 1500$, $N_2 = 625$, $\kappa_1 = 85 \text{ cm}^{-1}$, $\kappa_2 = 75 \text{ cm}^{-1}$, $\kappa_1 L_1 = 3.09$, $\kappa_2 L_2 = 1.14$, $\Delta A = 0.2 \text{ nm}$, injection current $I = 1.1 I_{\text{th}} = 3.21 \text{ mA}$ where I_{th} is threshold current.

Figure 2 (b) depicts transmission spectrum of Region 1 and reflection spectrum of Region 2 for amplitude optical gain $a = 0.99 a_{\text{th}} = 7.28 \text{ cm}^{-1}$ where a_{th} is threshold amplitude optical gain. The main mode is a resonance mode of Region 1, which is located in the wavelength region with high reflectance of Region 2. It should be noted that the main mode is not determined by resonance modes of the coupled cavity consisting of Region 1 and Region 2.



(a) Oscillation spectrum



(b) Transmission spectrum of Region 1 and reflection spectrum of Region 2

Fig. 2 Optical spectra.

Figure 3 shows maximum injection current I_{\max} for SLM operation as a function of relative grating coupling coefficient $\kappa_1 L_1$ of Region 1 and relative grating coupling coefficient $\kappa_2 L_2$ of Region 2. In Fig. 3 (a) κ_1 is 85 cm^{-1} ; in Fig. 3 (b) κ_1 is 75 cm^{-1} . In Fig. 3 (a) and (b) κ_2 is 75 cm^{-1} . We can expect highly stable SLM operation because I_{\max} exceeds 600 mA. The condition to obtain $I_{\max} \geq 600 \text{ mA}$ is to satisfy $\kappa_i L_i \leq 1.36$ and $\kappa_j L_j \geq 1.59$ simultaneously ($i, j = 1, 2$). It should be noted that a region with $\kappa_i L_i \leq 1.36$ functions as a DBR with optical gain; a region with $\kappa_j L_j \geq 1.59$ acts as a DFB-LD.

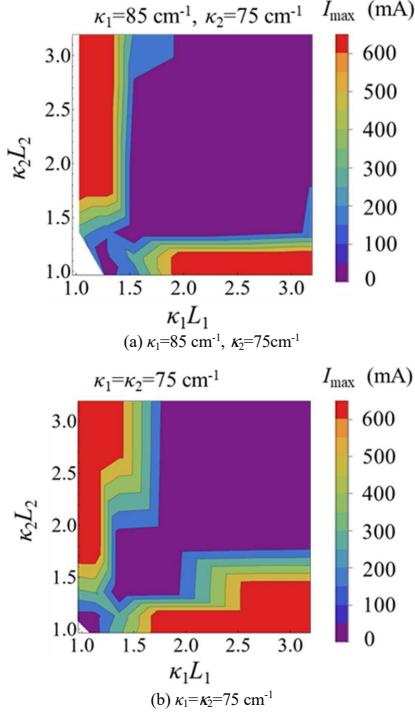


Fig. 3 Maximum injection current for SLM operation as a function of relative grating coupling coefficients of Region 1 and Region 2.

Figure 4 reveals wall-plug efficiency for the front facet light output as a function of relative grating coupling coefficient $\kappa_1 L_1$ of Region 1 and relative grating coupling coefficient $\kappa_2 L_2$ of Region 2. In Fig. 4 (a) κ_1 is 85 cm^{-1} and the front facet light output $P_f = 1 \text{ mW}$; in Fig. 4 (b) κ_1 is 75 cm^{-1} and the front facet light output $P_f = 10 \text{ mW}$. In Fig. 4 (a) and (b) κ_2 is 75 cm^{-1} .

The highest wall-plug efficiency for $P_f = 1 \text{ mW}$ is 23.1% when $N_1 = 1500$, $N_2 = 625$, $\kappa_1 = 85 \text{ cm}^{-1}$, $\kappa_2 = 75 \text{ cm}^{-1}$, $\kappa_1 L_1 = 3.09$, $\kappa_2 L_2 = 1.14$, and $\Delta l = 0.2 \text{ nm}$. In this condition the external quantum efficiency is 64% while the average external quantum efficiency for DR-LDs is 20% [5]. The highest wall-plug efficiency for $P_f = 10 \text{ mW}$ is 53.2% when $N_1 = 1500$, $N_2 = 750$, $\kappa_1 = \kappa_2 = 75 \text{ cm}^{-1}$, $\kappa_1 L_1 = 2.72$, $\kappa_2 L_2 = 1.36$, and $\Delta l = 0.3 \text{ nm}$. In this condition the external quantum efficiency is 74%. These external quantum efficiencies are the highest among SLM LDs with asymmetric light output from the front/rear facet to the authors' knowledge.

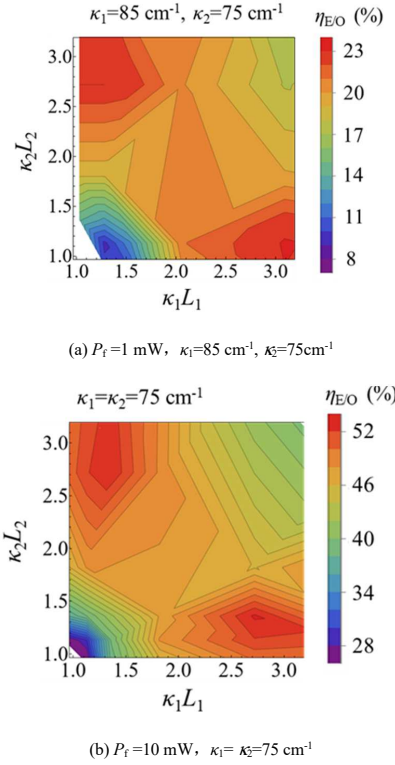


Fig.4 Wall-Plug efficiency for the front facet light output as a function of relative grating coupling coefficients of Region 1 and Region 2.

IV. CONCLUSIONS

A DFB-LD connected in series to a DBR with optical gain was studied. This DFB-LD showed highly stable single longitudinal mode operation with high external quantum efficiency more than 64% which exceeds 20% in DR-LDs [5] due to asymmetric facet light output. The main mode was determined by one of the resonance modes in the DFB-LD within high reflective wavelength region in the DBR with optical gain. We can expect that the present DFB-LD shows SLM operation up to 600 mA.

REFERENCES

- [1] T. Numai, "Fundamentals of Semiconductor Lasers," Second Edition, Chap. 4, pp.203-207, Springer, 2014.
- [2] M. Usami, S. Akiba, and K. Utaka, IEEE J. Quantum. Electron., Vol. QE-23, No. 6, pp.815-821, 1987.
- [3] K. Sato, Y. Muroya, and T. Okuda, IEICE Trans. Electron., Vol. E83-C, No. 6, pp. 855-859, 2000.
- [4] M. Aoki, K. Komori, Y. Miyamoto, S. Arai, and Y. Suematsu, Electron. Lett., Vol. 25, No. 24, pp.1650-1651, 1989.
- [5] I. Arima, J.-I. Shim, S. Arai, I. Morita, R. Somchai, and Y. Suematsu, IEEE Photon. Technol. Lett., 2, pp.385-387, 1990.
- [6] K. Ichikawa and T. Numai, Optik, Vol. 127, pp. 6253-6257, 2016.
- [7] K. Ichikawa, S. Ito, and T. Numai, Optik, Vol. 127, pp. 12078-12084, 2016.

Self-Powered High Performance AlGa_N-Based Solar Blind UV MSM Photodetector

Balkrishna Choubey
Dept. of Electrical Engineering
IIT Jammu
Jammu-181221, India
2019ree0018@iitjammu.ac.in

Aamir Ahmad Bhat
Dept. of Electrical Engineering
IIT Jammu
Jammu-181221, India
2024ree1051@iitjammu.ac.in

Kankat Ghosh
Dept. of Electrical Engineering
IIT Jammu
Jammu-181221, India
kankat.ghosh@iitjammu.ac.in

Abstract— In this research article, we attempt to show the performance of a self-powered Aluminum Gallium Nitride (AlGa_N)-based solar-blind ultraviolet (SBUV) metal-semiconductor-metal photodetector. The excellent crystalline quality of the AlGa_N film is evidenced by its low screw threading dislocation density ($\sim 10^8$), which suppresses the dark current in the order of pA (i.e., 1.02 pA) and enhances the photocurrent (4×10^{-10} A). The device achieves a sensitivity greater than 10^2 , a responsivity of 1.2 mA/W, and a detectivity of 2.42×10^8 Jones at 0 V bias. Hence, the device's low dark current, high sensitivity, excellent responsivity, and strong detection capability at zero bias establish AlGa_N as a highly promising material for self-powered SBUV detection applications.

Keywords—AlGa_N, Solar-Blind, Self-Powered, Dark Current, Responsivity.

I. INTRODUCTION

The Solar-blind ultraviolet (SBUV) photodetectors have attracted significant research interest due to their wide range of applications in fields such as space exploration, missile warning, flame detection, and biomedical imaging [1]. Among various semiconductor materials, the wide bandgap AlGa_N alloy [1-2] is particularly promising due to its tuneable bandgap, intrinsic solar-blind response, high thermal stability, and excellent chemical and physical robustness. Furthermore, the built-in polarization fields in AlGa_N can be leveraged to develop self-powered photodetectors, thereby minimizing the reliance on external power sources [3].

Thus, in this research article, we demonstrate a self-powered AlGa_N-based SBUV photodetector, utilizing the material's intrinsic polarization to achieve self-powered operation, thereby reducing dependence on external power sources.

II. DEVICE FABRICATION AND MATERIAL CHARACTERIZATION

The epilayers (AlN and Al_xGa_{1-x}N), as illustrated in the device schematic (Fig. 1a), were grown using plasma-assisted molecular beam epitaxy (PAMBE). Post-growth, the sample underwent sequential cleaning with trichloroethylene, acetone, isopropyl alcohol, and concentrated hydrochloric acid, followed by a rinse with deionized water. The standard photolithography was then used to define interdigitated electrode (IDT) patterns on the cleaned surface. A Ni/Au (40/120 nm) metal stack was used as the IDT structures, followed by an overnight lift-off process. The fabricated IDT patterns consist of fingers length (L) of 98 μ m, fingers width (W) of 5 μ m, and finger spacing (S) of 6 μ m, as shown in Fig. 1(b).

The quality of the grown epilayer was analysed using high-resolution x-ray diffraction (HR-XRD) and x-ray rocking curve (XRC) measurements around the characteristic peaks.

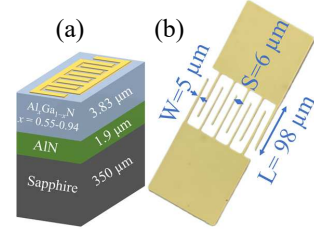


Fig. 1. Demonstrate the schematic of fabricated AlGa_N-based deep UV MSM photodetector. The grown sample consists of an Al_xGa_{1-x}N ($x = 0.55-0.94$) epilayer (3.83 μ m), AlN (1.9 μ m), and sapphire. The Ni/Au metal (40/120 nm) stack is deposited using standard photolithography process.

Additionally, atomic force microscopy (AFM) was used to evaluate the surface roughness of the film. A conventional characterization setup was utilized to measure the photoresponse and temporal response of the photodetector.

III. RESULTS AND DISCUSSIONS

Fig. 2(b) presents the HRXRD peak of the Al_{0.55}Ga_{0.45}N (0002) at 35.39° , with a full width at half maximum (FWHM) of approximately 0.07° , indicating excellent crystalline quality of the Al_{0.55}Ga_{0.45}N epilayer. The AlN (0002) peak, situated at 36.12° , confirms the successful growth of intermediate layers, which serve to alleviate the lattice mismatch between the active layer and the sapphire substrate. Additionally, the AFM image shows the rms roughness of 620 pm, indicated a smoothness of the grown film. It is well known that screw threading dislocations can provide additional conductive paths in a device, leading to increased leakage current. Therefore, the XRC scan (not shown) confirms a screw dislocation density (TDD) on the order of $\sim 10^8$ cm⁻², which is approximately two orders of magnitude lower than that reported in existing literature.

To characterize our device, we measured the photocurrent and dark current as a function of applied voltage, as shown in Fig. 3(a). Since the goal is to demonstrate self-powered operation (i.e., at 0 V bias), the measured dark current and photocurrent at 0 V were 1.02 pA and 4×10^{-10} A, respectively. The low dark current is attributed to the high

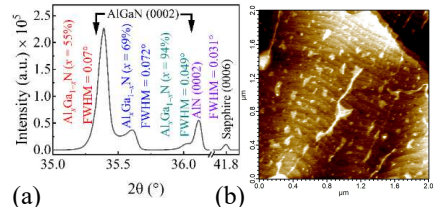


Fig. 2. Displays (a) the HRXRD peaks of the AlGa_N/AlN/Sapphire-based MSM photodetector sample. (b) the AFM of the AlGa_N photoactive epilayer, revealing a root mean square surface roughness of 620 pm over an area of 2 μ m \times 2 μ m.

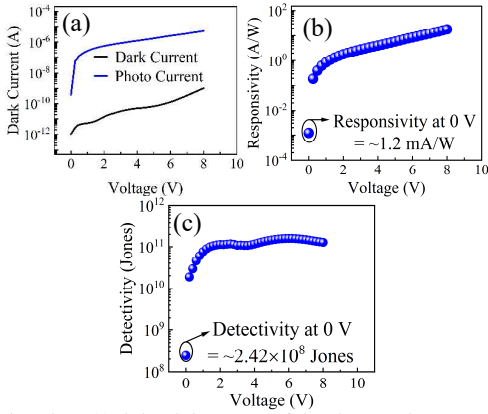


Fig. 3 shows (a). dark and photocurrent of photodetector. The measured dark current is suppressed to 1.02pA, indicating high crystalline quality, while the photocurrent reaches 4×10^{-10} A at 0V, demonstrating a high photo-to-dark current ratio of $>10^2$. (b) responsivity (c) detectivity of PD with varying bias. Our device shows the responsivity of 1.2 mA/W at self-biased mode. Also, it displays high detectivity of 2.42×10^8 Jones at 0 V signifying a lower noise level in the fabricated device at 0V.

crystalline quality of the epilayer, with a screw TDD on the order of $\sim 10^8 \text{ cm}^{-2}$, which minimizes charge carrier trapping and consequently enhances the photocurrent at zero bias. This results in a high sensitivity (photo-to-dark current ratio) of the device, exceeding 10^2 .

The responsivity (R), and detectivity (D) at 0 V bias were calculated using the following equations [4].

$$R = (I_P - I_D) / [(P/S)A] \quad (1)$$

$$D = R \sqrt{A} / \sqrt{(2q I_D)} \quad (2)$$

Thus, the calculated responsivity at 0 V is 1.2 mA/W, demonstrating the self-powered capability of our device, as displayed in Fig. 3(b). Fig. 3(c) demonstrates the detectivity of the device. The recorded detectivity at 0 V is 2.42×10^8 Jones, indicating a low noise level in the fabricated device under zero-bias condition. These performance metrics reflect the high crystalline quality of the grown epilayer.

We compared the responsivity of our device with previously reported results in the literature (Table I) and found that our device achieves a comparable responsivity of 1.2 mA/W, confirming its effectiveness in self-powered operation mode.

Table I. Responsivity comparison of self-powered SBUV PD

Device	Responsivity (mA/W)	Ref.
Al _{0.55} Ga _{0.45} N/AlN/Sapphire Top epilayer x = 0.55	1.2	This Work
p-AlGaIn/n-GaN	22.5	5
GaN/AlGaIn	5	6
AlGaIn Nanorod	3	7
ZnO/Ga ₂ O ₃	9.7	8

IV. CONCLUSIONS

In this article, we have demonstrated the growth of a high-quality AlGaIn thin film for self-powered SBUV photodetector applications. The low screw threading dislocation density (TDD) and dark current (1.02 pA) confirm

the superior crystalline quality of the AlGaIn film. The device exhibits a sensitivity greater than 10^2 , a responsivity of 1.2 mA/W, and a detectivity of 2.42×10^8 Jones at 0 V bias. Therefore, the combination of low dark current, high sensitivity, excellent responsivity, and strong detection capability at zero bias makes AlGaIn a highly promising candidate for self-powered SB UV detection applications.

Further we aim to utilize machine learning (ML) techniques to extract key performance metrics (such as responsivity, external quantum efficiency, UV-to-visible rejection ratio, and detectivity) to validate existing models, particularly those based on gradient-boosted decision trees (e.g., XG Boost, and light gradient-boosting machine). We plan to vary parameters including the input power, Al composition in the AlGaIn active layer, the dimensions of the IDT (i.e., length, width, and spacing), active layer thickness, and buffer layer thickness to train the model and accurately predict the performance metrics. The models effectively learn the nonlinear relationships between device parameters and performance and are expected to accurately replicate experimental results and reveal key sensitivities. We will apply ML-based models to our experimental data and evaluate their performance using error metrics such as rms error and mean absolute error. The low values of these error metrics of the most suitable model should lead to a strong agreement between the model predictions and the experimental data, thereby validating the model. This makes them a valuable tool for optimizing and meaningfully predicting the behaviour of MSM photodetectors.

ACKNOWLEDGMENT

The authors acknowledge Central Instrument Facility of Indian Institute of Technology Jammu, Indian Institute of Technology Bombay Nanofabrication Facility, and Indian Institute of Technology Bombay (under INUP-i2i program, sponsored by MeitY, Government of India) for providing essential fabrication and characterization facilities.

REFERENCES

- [1] X. Liu and S. Zhou, "Progress on photovoltaic AlGaIn photodiodes for solar-blind ultraviolet photodetection," *Chinese Optics Letters*, vol. 20, no. 11, p. 112501, 2022, doi: 10.3788/col202220.112501.
- [2] L. Su, W. Yang, J. Cai, H. Chen, and X. Fang, "Self-Powered Ultraviolet Photodetectors Driven by Built-In Electric Field," *Small*, vol. 13, no. 45, Dec. 2017, doi: 10.1002/sml.201701687.
- [3] A. Yoshikawa, S. Ushida, M. Iwaya, T. Takeuchi, S. Kamiyama, and I. Akasaki, "Influence of trap level on an Al_{0.6}Ga_{0.4}N/Al_{0.5}Ga_{0.5}N metal-semiconductor-metal uv photodetector," *Jpn J Appl Phys*, vol. 58, no. SC, 2019, doi: 10.7567/1347-4065/ab09dc.
- [4] B. Choubey and K. Ghosh, "Ultralow Dark Current and High Speed GaN-Based Visible Blind UV Photodetector," *IEEE Sens J*, 2025, doi: 10.1109/JSEN.2025.3562887.
- [5] Y. Luo *et al.*, "Demonstration of Photoelectrochemical-Type Photodetectors Using Seawater as Electrolyte for Portable and Wireless Optical Communication," *Adv Opt Mater*, vol. 10, no. 10, May 2022, doi: 10.1002/adom.202102839.
- [6] J. Wang *et al.*, "Polarization assisted self-powered GaN-based UV photodetector with high responsivity," *Photonics Res*, vol. 9, no. 5, p. 734, May 2021, doi: 10.1364/prj.418813.
- [7] D. Wang *et al.*, "Pt/AlGaIn Nanoarchitecture: Toward High Responsivity, Self-Powered Ultraviolet-Sensitive Photodetection," *Nano Lett*, vol. 21, no. 1, pp. 120–129, Jan. 2021, doi: 10.1021/acs.nanolett.0c03357.
- [8] B. Zhao *et al.*, "An Ultrahigh Responsivity (9.7 mA W⁻¹) Self-Powered Solar-Blind Photodetector Based on Individual ZnO-Ga₂O₃ Heterostructures," *Adv Funct Mater*, vol. 27, no. 17, May 2017, doi: 10.1002/adfm.201700264.

Design of Polarization Maintaining Fiber Based on Polyethylene Terephthalat Polymer for Sensing Application

Lynda Cherbi

Laboratory of instrumentation (LINS)
Faculty of Electrical Engineering
University of Sciences and Technology
Houari Boumediene (USTHB)
Algiers, Algeria
molvsrs24@gmail.com

Meriem Benlacheb

Laboratory of instrumentation (LINS)
Faculty of Electrical Engineering
University of Sciences and Technology
Houari Boumediene (USTHB)
Algiers, Algeria
mbenlacheheb@usthb.com

Abstract— This study investigates a highly birefringent polymer photonic crystal fiber (PCF) designed for polarization-maintaining applications. The PCF features a triangular arrangement of circular air holes embedded in Polyethylene Terephthalate (PET), with a defected core structure to enhance birefringence. The fiber's optical properties are analyzed using a full-vector finite element method (FEM), incorporating a perfectly matched layer (PML) as the boundary condition. After optimization, the design achieves a notably high birefringence of 4.94×10^{-2} at a wavelength of 1550 nm. Additionally, it demonstrates a low confinement loss of approximately 10^{-7} dB/km and a negative chromatic dispersion of -448 ps/(nm·km) along the y-polarization. Owing to its excellent polarization-maintaining characteristics, the proposed PCF design shows strong potential for optical sensor applications and could also benefit dispersion-compensating devices in high bit-rate transmission networks.

Keywords: Polarization Maintaining Fiber (PMF), Photonic Crystal Fiber (PCF), Polyethylene Terephthalate (PET), sensing applications.

I. INTRODUCTION

The evolution of optical fibers from telecommunications to sensing applications has been pivotal, particularly with the emergence of photonic crystal fibers (PCFs). These fibers boast high birefringence and low confinement loss, making them ideal for chemical and biological sensing. Their inherent polarization maintaining (PM) properties enable precise control over light polarization, enhancing sensitivity and selectivity in detection. Polymer fibers, in particular, offer advantages over silica fibers due to their flexibility and biocompatibility, allowing for easier fabrication and interaction with biological samples [1]. In this study, a high birefringent PM-PCF based on PET polymer with low confinement loss is modeled for sensing purpose. The high birefringence of the proposed fiber enhances its sensitivity, while the polymer material ensures biocompatibility, rendering it suitable for sensing applications.

II. DESIGN AND SIMULATION RESULTS

The core region of optical fibers plays a significant role in birefringence. To achieve high birefringence, we have undertaken the modeling of a microstructured fiber by modifying the core region as shown in Figure 1. The initial PM-PCF design consist of hexagonal circular air holes of refractive index $n_{air}=1$ assembled with silica with a

refractive index of nsilica = 1.45, as depicted in Figure 1a. The light is guided by total internal reflection mechanism into a silica core. Additionally, three small circular air holes are added vertically on the left and right sides along the x-axis of the core area to introduce asymmetry into the structure, impacting the propagation mode. This results in a faster variation along the x-axis, amplifying the difference between the effective refractive indices of the two orthogonal polarization modes, which gives rise to birefringence. Subsequently, for optimization purposes, we replace the three holes with an ellipse on each side, as illustrated in figure 1b.

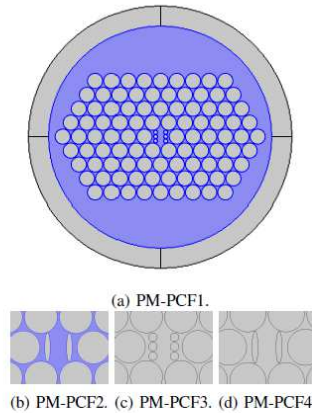


Fig. 1: A cross-section of the different proposed PM-PCFs surrounded by PML as boundary condition with (a) PM-PCF1 circular air holes area and Silica background; (b) PM-PCF2 elliptical air holes area and Silica background; (c) PM-PCF3 circular air holes area and PET background; (d) PM-PCF4 elliptical air holes area and PET background.

Replacing the traditional silica core in optical fibers with polymers, specifically polyethylene terephthalate (PET), introduces several competitive advantages compared to conventional silica fibers. We have utilized PET instead of silica in PM-PCF3 and PM-PCF4, as depicted in Figure 1c and Figure 1d, to enhance biocompatibility and reduce costs. The proposed photonic crystal fibers (PCFs) exhibit specific geometrical parameters crucial for their optical functionality. In the cladding region, air holes are characterized by a diameter (d_1) of $1.5\mu\text{m}$, arranged with a pitch of $1.6\mu\text{m}$ between adjacent holes. In the core region of PM-PCF1 and PM-PCF3, six small circles are organized with a diameter (d_2) of $0.4\mu\text{m}$. To gain a better

understanding of the performance characteristics of our proposed design, we performed FEM simulations. These simulations were specifically aimed at analyzing the modal profiles and modal effective indices of the two orthogonal polarization modes. Initially, we calculated the modal indices of the four designed PM-PCFs over a spectral range extending from 1000 nm to 1700 nm.

According to the simulations, the PET core with elliptical air holes exhibits superior confinement of the fundamental electric field for both x- and y-polarized modes, as depicted in Figure 2.



Fig. 2: Electric field distribution of x- and y -polarized modes of the proposed PET fibers.

Along the x-axis, the spacing (dx) between these circles measures $1.33\mu\text{m}$, while along the y-axis, the spacing (dy) is $0.25\mu\text{m}$. To increase the birefringence of the proposed fibers, we substitute the three holes in PM-PCF1 with ellipses on each side within PMF-PCF2 and PM-PCF4, as depicted in Figure 1b and Figure 1d. The major axis (A_x) of the elliptical air hole is fixed at $1\mu\text{m}$, while the semi-minor axis (A_y) is given by $A_x/2.3$.

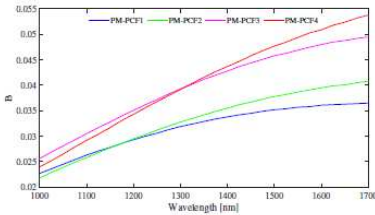


Fig. 3: Modal birefringence variation of the different proposed PM-PCFs as a function of wavelength.

The wavelength dependent modal birefringence of the different PM-PCF structures is presented in Figure3, demonstrating a visible increase with wavelength. This elevated birefringence is attributed to the asymmetry in the core area, which amplifies the difference between the effective refractive indices of the two polarization modes, consequently leading to an increase in modal birefringence. From the Figure 3, it is evident that the elliptical holes result in a higher degree of birefringence compared to the circular holes. In addition, birefringence is also impacted by the background material, and we can observe that PET yields higher birefringence than silica. Specifically, a high birefringence value of 4.94×10^{-2} is observed at 1550nm, while the highest value recorded is 5.38×10^{-2} at 1700nm in PM-PCF4.

Reducing confinement loss in photonic crystal fibers is crucial for improving their performance in various applications, which is why the number of rings has been carefully chosen to minimize it. The confinement losses of the proposed PM-PCFs for both x- and y-polarized modes

are displayed in Figure 4 and 5, respectively. From the plot, we note that the confinement loss for the PM-PCF4 remains at the order of 10^{-7}dB/Km across the entire studied wavelength range. However, beyond 1550nm, an increase in confinement loss is observed in the first three structures.

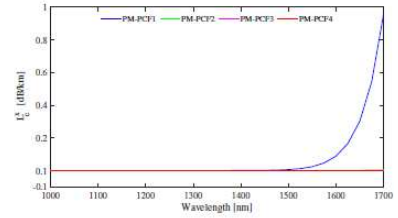


Fig. 4: Confinement loss of the proposed PM-PCFs for the x-polarized mode as a function of wavelength

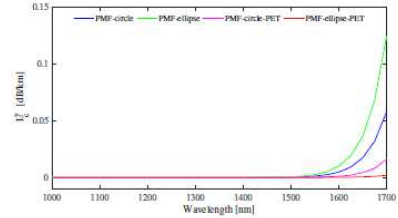


Fig. 5 : Confinement loss of the proposed PM-PCFs for the y-polarized mode as a function of wavelength.

TABLE I: Comparison of Characteristics of Optimized Fibers with those of Previous Works at 1550nm.

Ref	Birefringence, B	Confinement loss, L_c (dB/km)
Ref [2]	3.71×10^{-2}	10^{-7}
Ref [3]	4.51×10^{-2}	10^{-7}
Our work	4.94×10^{-2}	10^{-7}

III. CONCLUSION

A triangular high-birefringence Polyethylene Terephthalate (PET) photonic crystal fiber (PCF) for sensing applications is presented. The various characteristics of the proposed fiber are thoroughly investigated using FEM simulations. The results indicate that the design exhibits a high birefringence of 4.94×10^{-2} , a negative chromatic dispersion of $-448\text{ ps}/(\text{nm.km})$ for y-polarization, and a short beat length of $31\mu\text{m}$ at a wavelength of $1.55\mu\text{m}$. Furthermore, the fiber demonstrates a low confinement loss of 10^{-7} dB/km . Overall, the proposed PM-PCF design based on PET shows promising characteristics, making it a suitable candidate for optical fiber sensor applications

REFERENCES

- [1] Kuncov'a, Gabriela, Fiber Optic Sensors in Chemical and Biological Applications, MDPI-Multidisciplinary Digital Publishing Institute, 2022.
- [2] Halder, A., Slope matched highly birefringent hybrid dispersion compensating fiber over telecommunication bands with low confinement loss, Journal of Optics 49(2), 187–195 2020.
- [3] Alishacelestin, X., Raja, A. S., Muthu, K. E., and Selvendran, S., A novel ultra-high bire-fringent photonic crystal fiber for nonlinear applications, Brazilian Journal of Physics, 1–13 2021.

Numerical models for the analysis of thermal phenomena in nitride edge-emitting lasers and their one-dimensional arrays

Dominika Dąbrowka
Institute of Physics
Lodz University of Technology
Lodz, Poland
dominika.dabrowka@dokt.p.lodz.pl

Robert P. Sarzala
Institute of Physics
Lodz University of Technology
Lodz, Poland
robert.sarzala@p.lodz.pl

Abstract—We present commonly used numerical models for the thermal analysis of edge-emitting semiconductor lasers and their one-dimensional arrays. The modeling approaches are examined in terms of the simplifications they employ, and their results are compared. As a case study, we investigate a nitride-based, green-emitting edge-emitting laser and a one-dimensional array composed of such devices. Our findings demonstrate that well-designed simplified simulations can yield not only qualitatively but also quantitatively accurate results, thus providing a viable alternative to computationally intensive full 3D thermal simulations.

Keywords—nitride edge-emitting lasers, thermal analysis, computer simulations, numerical models

I. INTRODUCTION

Semiconductor lasers are extensively used in modern technologies, with wide-ranging applications in consumer electronics, industry, telecommunications, and medicine. The accurate design of these devices requires a comprehensive understanding of the underlying physical phenomena. However, experimental investigations are often associated with high costs, long development times, and various technological constraints. As a result, numerical simulations have become an indispensable tool for researchers engaged in the design and optimization of such devices.

Since temperature has a direct impact on the performance, lifetime, and stability of semiconductor lasers, thermal analysis is a critical aspect, especially for high-power devices [1–3] and those based on gallium nitride (GaN). Due to the structural complexity of these devices, analytical approaches are generally inadequate [4], and more accurate predictions require numerical modeling. Various types of models are used depending on the level of detail, including thermal models with either localized or distributed heat sources [1,2], electro-thermal models [3], and, in the most advanced cases, opto-electro-thermal models [3]. These models may be self-consistent, accounting for both the temperature dependence of material properties and the coupling between electrical and

thermal effects. In addition, the dimensionality of the model, which can range from one-dimensional (1D) [4,11] to full three-dimensional (3D) simulations [1–3], significantly affects the trade-off between computational cost and accuracy.

In this study, three modeling approaches are compared: a two-dimensional purely thermal model (2D Ts), a two-dimensional electro-thermal model (2D TE), and a three-dimensional electro-thermal model (3D TE). All models incorporate temperature-dependent material parameters. In addition, a hybrid model (3D Tr) is proposed, in which the heat source distribution within the 3D geometry is derived from the results of the 2D TE model. This approach is motivated by the specific geometric characteristics of the simulated structures.

The results demonstrate that the hybrid approach offers accuracy comparable to that of the full 3D model while substantially reducing computational cost. The 2D models provide reliable qualitative insights, and their quantitative accuracy can be enhanced through the use of appropriate correction factors. Due to their computational efficiency and speed, such simplified models are commonly employed in practice. The comparative analysis was performed using a GaN-based green edge-emitting laser (see Fig. 1) and a one-dimensional array consisting of ten such devices.

II. NUMERICAL MODEL

The simulations were performed using proprietary software developed by the Photonics Group at the Institute of Physics, Lodz University of Technology. This tool enables the modeling of semiconductor lasers and their arrays. Thermal calculations were based on the finite element method (FEM) applied to the steady-state heat conduction equation. A constant temperature of 300 K was assumed at the bottom surface of the heat sink, while adiabatic boundary conditions were imposed on all other surfaces. Electrical calculations were carried out by solving Laplace's equation coupled with the diode equation in a self-consistent manner. Detailed descriptions of the numerical models and material parameters are provided in references [5] and [6].

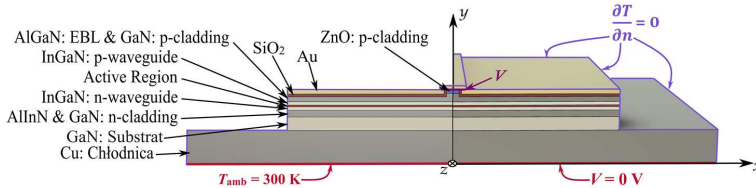


Fig. 1. Schematic of the nitride edge-emitting laser structure designed for green light emission at a wavelength of 540 nm [5]. The laser structure is based on a GaN substrate and incorporates n-type cladding layers composed of $\text{Al}_{0.35}\text{In}_{0.17}\text{N}$ and GaN, along with an n-type waveguide layer made of $\text{In}_{0.06}\text{Ga}_{0.92}\text{N}$. The active region consists of three $\text{In}_{0.29}\text{Ga}_{0.71}\text{N}$ quantum wells separated by GaN barriers. Above the active region, a p- $\text{Al}_{0.2}\text{Ga}_{0.8}\text{N}$ electron blocking layer is followed by a p-type waveguide ($\text{In}_{0.06}\text{Ga}_{0.92}\text{N}$) and a p-type cladding layer composed of p-GaN and ZnO. The top electrical contact is made of gold and is electrically insulated from the structure by a SiO_2 layer. A more detailed description of the device structure is provided in [6].

III. RESULTS

Due to the geometry and boundary conditions of edge-emitting lasers, current and heat transport can be effectively analyzed using two-dimensional models. Self-consistent two-dimensional electro-thermal (2D TE) simulations for a single emitter, assuming a total heat dissipation of 1 W, resulted in a temperature rise of 37.9 K and required 11.5 minutes of computation time. A simplified two-dimensional purely thermal model (2D Ts), employing a concentrated heat source located in the active region, made the simulation 18 times faster but predicted a maximum temperature that was 16% higher.

Since real semiconductor lasers are inherently three-dimensional, 3D modeling provides a more accurate representation of heat dissipation within the structure, albeit at a significantly higher computational cost. The 3D electro-thermal (3D TE) simulations took approximately seven times longer than their 2D counterparts. The maximum temperature rise predicted by the 3D TE model was 9% lower, although the overall temperature distribution remained nearly unchanged. A simplified 3D thermal model (3D Ts), with heat sources confined to the active region, reduced the computation time by a factor of three but produced a 17% higher maximum temperature, while preserving the shape of the temperature distribution.

The discrepancies between the 2D and 3D models arise primarily from the inability of 2D models to account for heat spreading in the vertical (z) direction, which plays a critical role in thermal dissipation through the substrate, heatsink, and metal contacts. As a result, 2D models tend to overestimate the temperature rise compared to full 3D simulations.

To achieve a balance between accuracy and computational efficiency, a hybrid 3D Tr model was proposed, in which the spatial heat source distribution is imported from the 2D TE simulation. This approach reduced the computation time by a factor of 2.5 compared to the full 3D TE model, while preserving nearly identical temperature distributions, with a maximum deviation of less than 0.5%. Temperature distributions in the active region obtained from all considered models are presented in Fig. 2.

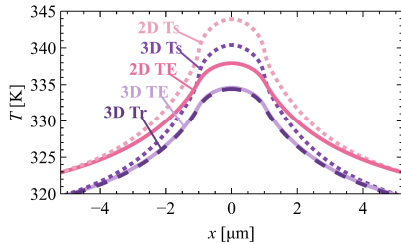


Fig. 2. Temperature distributions in the active region of a single emitter under 1 W of heat dissipation, as computed using various numerical models.

The comparison was further extended to a one-dimensional array consisting of ten edge-emitting nitride lasers. In this case, 3D models also resulted in significantly longer computation times—up to 18 times higher—while predicting average temperatures approximately 33% lower than those obtained from the 2D models. Simplified Ts models further overestimated peak temperatures, by 8% in the 2D case and 10% in the 3D case, relative to their respective TE counterparts. The hybrid 3D Tr model also demonstrated excellent agreement in the array simulations, with temperature

deviations not exceeding 1% in any emitter. Temperature distributions in the active region obtained from all considered models are presented in Fig. 3.

All evaluated models exhibited very similar temperature differences between emitters (11–12 K), indicating that simplified models can be effectively employed for optimization tasks, such as designing arrays with uniform temperature profiles. This allows for a significant reduction in computation time while preserving qualitative accuracy.

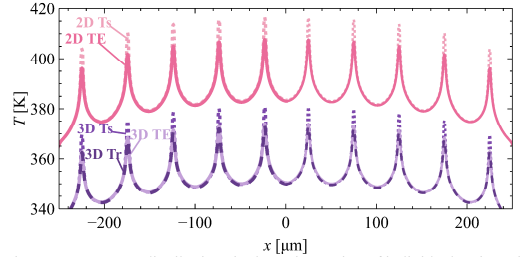


Fig. 3. Temperature distributions in the active region of individual emitters in the 10-element array, calculated for 1 W of dissipated heat per emitter, obtained using the analyzed computational models.

IV. CONCLUSIONS

This work presents a comparison of two-dimensional and three-dimensional thermal and electro-thermal numerical models used for the thermal analysis of nitride-based edge-emitting lasers and their one-dimensional arrays. The results demonstrate that 2D models can significantly reduce computation time, by up to a factor of 18 for arrays, while providing qualitatively accurate results. The average temperature overestimation compared to full 3D models is approximately 9% for a single emitter and 33% for arrays. However, the relative temperature distribution between emitters remains consistent across all models. A hybrid approach combining 2D and 3D simulations was also proposed, in which heat source distributions obtained from a 2D electro-thermal model are used in 3D thermal calculations. This method reduced computation time by a factor of 2 to 2.5 while maintaining high quantitative accuracy, with temperature deviations not exceeding 1%.

ACKNOWLEDGMENT

This research was funded in part by National Science Centre, Poland: 2024/53/N/ST7/02024.

REFERENCES

- [1] D.H. Wu, C.E. Zah and X. Liu, "Three-dimensional thermal model of high-power semiconductor lasers", *Applied Optics*, vol. 58, pp. 3892-3901, 2019.
- [2] A. Bärwolff, R. Puchert, P. Enders, U. Menzel and D. Ackermann, "Analysis of thermal behaviour of high power semiconductor laser arrays by means of the finite element method (FEM)", *Journal of Thermal Analysis* vol. 45, pp. 417-436, 1995.
- [3] M. Hao, X. Liu, L. Tan and H. Zhu, "Thermal analysis of high power laser diodes by electro-thermal indirect coupling finite-element method", 10th International Conference on Reliability, Maintainability and Safety, Guangzhou, China, pp. 93-97, 2014.
- [4] G. Chen and C.L. Tien, "Facet heating of quantum well lasers. *J. Appl. Phys.*, vol. 74, pp. 2167-2174, 1993.
- [5] M. Kuc, L. Piskorski, M. Dems, M. Wasiak, A.K. Sokół, R.P. Sarzała and T. Czyszanowski, "Numerical Investigation of the Impact of ITO, AlInN, Plasmonic GaN and Top Gold Metalization on Semipolar Green EELs", *Materials*, vol. 13, no. 6, 1444, 2020.
- [6] R.P. Sarzała, D. Dąbrowka and M. Dems, "Thermal Optimization of Edge-Emitting Lasers Arrays", *Materials*, vol. 18, no. 1, 107, 2025.

Light Interference Fringe Detection with DBSCAN for Integrated Mirrors

Vahram Voskerchyan¹, N.X. Xu Bonnie¹, Lantian Chang¹ and Sonia Garcia-Blanco¹

¹ University of Twente

v.voskerchyan@utwente.nl

Abstract -

This paper presents a method for detecting light interference fringes and designing integrated optical mirrors using DBSCAN clustering. Conventional edge detection methods struggle with gradual intensity changes in fringe patterns, but DBSCAN effectively identifies peaks while filtering noise. The detected fringe profiles are processed and input into FDTD simulations to analyze the interaction with an aluminum mirror. The results show 78% upward transmission efficiency and a clear far-field distribution. This approach improves mirror design for applications in communication systems and photonic circuits.

1 Introduction

Integrated optical mirrors provide significant advantages in applications requiring broadband coupling and beam manipulation, such as communication systems, sensing, and signal processing. Unlike grating couplers, which are limited to narrow wavelength ranges, these mirrors offer the flexibility to work across a wide range of wavelengths [1]. Additionally, they can function as antennas, enabling precise beam steering for tasks like free-space optical communication, LiDAR, and on-chip beam routing. To further enhance performance, we developed a tool that calculates optimal mirror geometries based on light interference patterns, ensuring maximum coupling efficiency. This approach tailors the mirror's design to the specific wavelength range and system geometry, improving overall device performance [2].

2 Fringe Detection

Detecting light interference patterns, such as fringe interference, is challenging for conventional methods due to gradual intensity variations. Techniques like Canny Edge detection, designed for sharp transitions, fail to capture the smooth changes in these patterns, leading to poor results. However, by designing optical devices that follow the fringe pattern geometry from the start, more precise beam shaping and light control can be achieved, enhancing optical system performance.

Detecting peaks in intensity profiles is further complicated by overlapping constructive interference peaks, especially in noisy environments. Standard peak detection methods often struggle here. Clustering peaks using

Grayscale profile with detected edges (Canny edge)

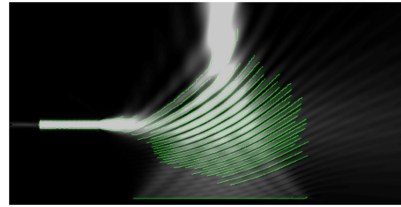


Figure 1. Canny edge detection from the profile.

DBSCAN (Density-Based Spatial Clustering of Applications with Noise) improves accuracy by grouping closely packed peaks while ignoring noise and outliers.

The fringe pattern shown in figure [2] results from the interference between a mode launched from the integrated photonic waveguide and a Gaussian beam, the wavelength of the sources $1 \mu\text{m}$. The Gaussian beam's polarization at 90° interacts with the Transverse Magnetic (TM) mode, generating constructive and destructive interference and leading to the observed fringe pattern.

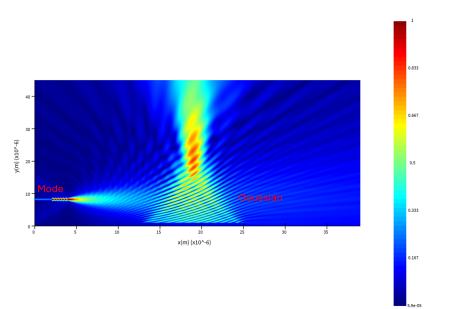


Figure 2. Fringe pattern highlighting the interference between the sources.

DBSCAN (Density-Based Spatial Clustering of Applications with Noise) is a clustering algorithm that groups closely packed data points while identifying and exclud-

ing outliers. The fig. [3] shows the clustered fringes, highlighting the detected regions corresponding to the interference pattern. These clusters were identified using DBSCAN, which effectively isolates the peaks while filtering out noise [3].

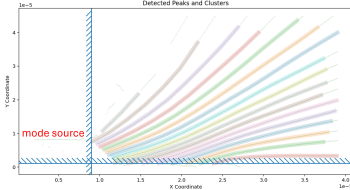


Figure 3. Detected clusters with DBSCAN.

3 Simulation Result

Now that the clusters have been identified, a specific fringe of interest can be selected and passed to a simulation tool such as FDTD for further analysis. The image below shows the selected fringe after extraction. A polynomial extrapolation has been applied to smooth the fringe profile, ensuring a more continuous and physically realistic input for simulation. The fringe profile is made of Aliminium for reflectivity.

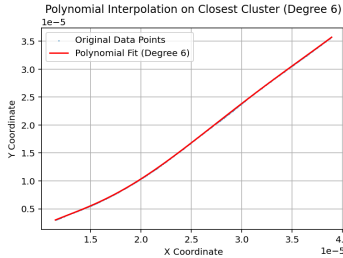


Figure 4. Fringe of interested with polynomial fit.

The image [5] below shows the electric field (E-field) profile resulting from a mode source interacting with an aluminum mirror. The mode propagates upward, heating the mirror surface upon impact. The upward transmission through the mirror structure is calculated to be approximately 78%, indicating high upward directionality.

The far-field profile of the simulated fringe is shown in figure [6], illustrating the angular distribution of the transmitted optical field.

4 Conclusion

This work presented a robust method for detecting and processing optical interference fringes using peak detec-

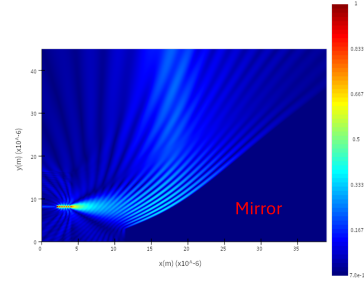


Figure 5. E-field profile with the fringe as a mirror.

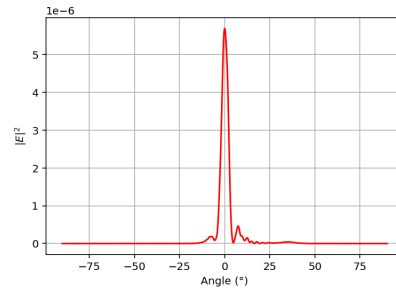


Figure 6. Farfield profile of selected fringe.

tion and DBSCAN clustering. The extracted fringe profiles were smoothed with polynomial extrapolation and used as input for FDTD simulations. A TM mode interacting with an aluminum mirror yielded 78% upward transmission with a well-defined far-field distribution. Current efforts are focused on optimizing the far-field response and fabricating the designed mirror structures using a Nano-scribe system, enabling precise realization of complex geometries informed by the simulated fringe data.

References

- [1] Kong, Y., *3D printed on-chip parabolic mirror for chip-to-fiber and chip-to-chip coupling*, 2022.
- [2] S. Yu, L. Ranno, Q. Du, S. Serna, et. al. "Free-Form Micro-Optics Enabling Ultra-Broadband Low-Loss Off-Chip Coupling," *Research Article*, www.lpr-journal.org
- [3] M. Ester, H.-P. Kriegel, J. Sander, and X. Xu, "A Density-Based Algorithm for Discovering Clusters in Large Spatial Databases with Noise," *Institute for Computer Science, University of Munich*

Legume: A guided-mode expansion method for photonic crystal slabs for inverse design and light-matter interaction

Simone Zanotti*

Physics Department “A. Volta”

University of Pavia

27100 Pavia, Italy

simone.zanotti01@universitadipavia.it

Momchil Minkov

Flexcompute

Watertown, 02472 MA, USA

momchilmm@gmail.com

Davide Nigro

Physics Department “A. Volta”

University of Pavia

27100 Pavia, Italy

davide.nigro@unipv.it

Dario Gerace

Physics Department “A. Volta”

University of Pavia

27100 Pavia, Italy

dario.gerace@unipv.it

Shanhui Fan

Ginzton Lab and Department of

Electrical Engineering

Stanford University

Stanford, 94305, CA, USA

shanhui@stanford.edu

Lucio Andreani

Physics Department “A. Volta”

University of Pavia

27100 Pavia, Italy

lucio.andreani@unipv.it

Abstract— We present a guided-mode expansion (GME) approach – and the corresponding free software named **Legume** – that allows calculating photonic mode dispersion and losses in dielectric photonic crystal slabs, and can be employed for inverse design. We give examples related to (a) symmetry properties and the issue of polarization mixing in coupling to far-field radiation; (b) the occurrence of bound states in the continuum (BICs), with very high Q-factors that are accurately calculated by the method; (c) the description of active two-dimensional layers with an excitonic resonance, allowing to describe the regime of strong coupling leading to photonic crystal polaritons.

Keywords—photonic crystal slabs, guided-mode expansion, exciton-polaritons, inverse design

I. INTRODUCTION

Photonic crystal (PhC) slabs, or patterned multilayer waveguides, are known to support truly guided modes with no losses, as well as quasi-guided modes that lie in the continuum of far-field radiation. In this contribution, we present a guided-mode expansion (GME) approach – and the corresponding free software named **legume** – that allows calculating a number of features of PhC slabs: (a) symmetry properties and the issue of polarization mixing in coupling to far-field radiation; (b) the occurrence of bound states in a continuum (BICs), which have infinite Q-factor and give rise to topological singularities of the far-field polarization; (c) the description of active two-dimensional layers through a suitably formulated light-matter coupling Hamiltonian, allowing to describe the regime of strong coupling leading to photonic crystal polaritons. Comparison with rigorous coupled-wave analysis (RCWA) is also addressed.

II. METHOD AND RESULTS

The method relies on expanding the magnetic field on the basis of guided modes of an effective homogeneous waveguide with an average dielectric constant in each layer, and diagonalizing the resulting eigenvalue problem. The losses of quasi-guided modes are calculated by photonic perturbation theory and are usually very accurate. The **legume** implementation of GME has a backend to the Autograd automatic differentiation library, thereby allowing efficient multiparameter optimization (e.g., complex PhC cavities) and inverse design [1].

In Fig. 1(a,b) we give an example of photonic mode dispersion and Q-factors for a PhC slab structure that displays several BICs. The quality factors are in very good agreement with the results of RCWA calculations. It should be noticed that the GME method is most accurate when radiative losses are small, i.e., in the high-Q limit.

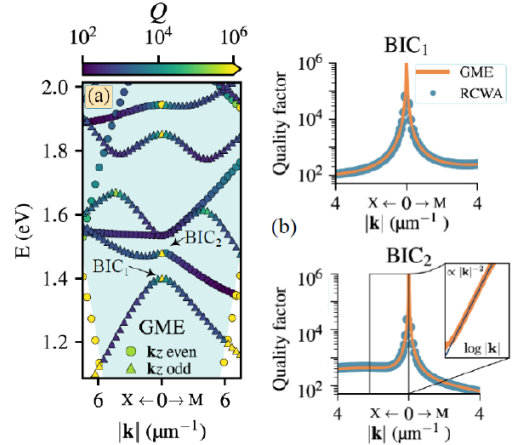


Fig. 1 (a) Dispersion and losses of photonic modes, (b) Q-factor in the proximity of the two BICs indicated in (a), calculated by GME and by RCWA. The PhC slab consists of a square lattice of period $a = 400$ nm, hole radius $r = 100$ nm, etched in a suspended slab of thickness $d = 80$ nm with refractive index $n = 3.45$.

Exciton-polaritons are calculated by a quantum-mechanical theory, in which the interaction between excitons and photons is treated by diagonalizing a Hopfield-like Hamiltonian in second quantization [2-4]. An example of photonic versus polaritonic dispersion is shown in Fig. 2(a,b). Light-matter interaction leads to anticrossing close to resonance and to hybrid excitations in the strong coupling regime, which inherit the properties of the excitons and photons. In particular, polariton BICs with ultralow radiative losses and with specific topological properties can be described.

*Currently at Nanyang Technological University, Singapore.

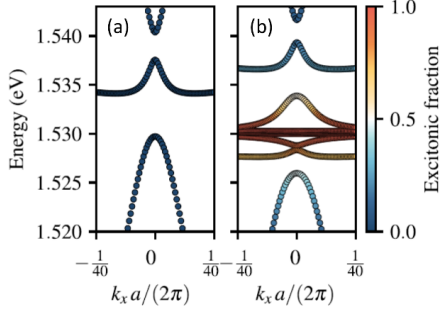


Fig. 2 (a) Dispersion and losses of photonic modes, (b) Q-factor in the proximity of the two BICs indicated in (a), calculated by GME and by RCWA. The PhC slab consists of a square lattice of period $a = 400$ nm, hole radius $r = 100$ nm, etched in a suspended slab of thickness $d = 80$ nm with refractive index $n = 3.45$.

Thus, the GME method in the `legume` implementation can be exploited for direct and inverse design of advanced nanophotonic structures. The code is freely available on github [6]. Notable features of the last release are the implementation of symmetry with respect to vertical mirror plane, thereby allowing to separate the photonic bands according the polarization, and the explicit inclusion of radiation-matter interaction beyond perturbation theory, leading to photonic crystal polaritons.

- [1] M. Minkov, I.A.D. Williamson, L.C. Andreani, D. Gerace, B. Lou, A.Y. Song, T.W. Hughes, S. Fan, "Inverse Design of Photonic Crystals through Automatic Differentiation", *ACS Photonics* 7, 1729-1741 (2020).
- [2] J.J. Hopfield, "Theory of the contribution of excitons to the complex dielectric constant of crystals", *Phys. Rev.* 112, 1555-1567 (1958).
- [3] D. Gerace and L.C. Andreani, "Quantum theory of exciton-photon coupling in photonic crystal slabs with embedded quantum wells", *Phys. Rev. B* 75, 235325 (2007).
- [4] S. Zanotti, H.S. Nguyen, M. Minkov, L.C. Andreani, D. Gerace, "Theory of photonic crystal polaritons in periodically patterned multilayer waveguides", *Phys. Rev. B* 106, 115424 (2022).
- [5] S. Zanotti, M. Minkov, D. Nigro, D. Gerace, S. Fan, L.C. Andreani, "Legume: A free implementation of the guided-mode expansion method for photonic crystal slabs", *Computer Physics Communications* 304, 109286 (2024).
- [6] <https://github.com/fancompute/legume>

Inaccuracy Amplified: Compressed Sensing Under Experimental Misalignment

Başak Ersöz
Politecnico di Torino
Torino, Italy
basak.ersozyildirim@polito.it

Maurizio Dabbicco
Università di Bari Aldo Moro
Bari, Italy
maurizio.dabbicco@uniba.it

Priyanka Chaudhary
Università di Bari Aldo Moro
Bari, Italy
priyanka.chaudhary@uniba.it

Lorenzo Columbo
Politecnico di Torino
Torino, Italy
lorenzo.columbo@polito.it

Paolo Bardella
Politecnico di Torino
Torino, Italy
paolo.bardella@polito.it

Massimo Brambilla
Politecnico di Bari
Bari, Italy
massimo.brambilla@poliba.it

Abstract—Compressed sensing (CS) with single-pixel detectors and optical phased arrays (OPAs) allows efficient image reconstruction by exploiting structured speckle patterns. This study investigates how spatial misalignments affect reconstruction fidelity. We numerically simulate the alignment errors of different magnitude and evaluate the reconstructed image using both the structural similarity index (SSIM) and the peak signal-to-noise ratio (PSNR). These findings highlight the sensitivity of compressed sensing to spatial misalignments, emphasizing the need for precise control in experimental setups to ensure reliable image reconstruction.

Index Terms—Compressed sensing, single pixel, speckle illumination, Structural Similarity Index, Peak Signal to Noise Ratio, reconstruction errors

I. INTRODUCTION

CS with single-pixel detectors represents an efficient solution for the acquisition of a target image. In contrast to faster but more technologically complex solutions where the target image is captured with a single acquisition, e.g. using matrix sensors, or slower but simpler approaches such as raster scanning where the target is acquired one pixel at the time, in CS the target is highlighted by a sequence of deterministic, uncorrelated speckle patterns, and the resulting signal is collected by a single-pixel detector (Fig. 1(a)). Assuming that K total speckle patterns are used, we can introduce the $N^2 \times K$ matrix $I = [I_1, I_2, \dots, I_K]$, with I_k column vector containing the $N \times N$ samples of the k -th illumination pattern, rearranged in lexicographic order; in a similar way we can introduce the column vector A with A_k values returned by the sensors for the k -th acquisition. The reconstructed image \hat{T} can be obtained as $\hat{T} = I^+ A$, with I^+ Moore-Penrose generalized inversion of I [1]. With respect to acquisitions based on raster scanning, CS is generally much faster, since the number of acquisitions K required to reconstruct the fundamental features of the target is smaller than N^2 . In this scenario, it is obvious that a key ingredient is the reproducibility of the patterns that must be measured accurately before the target is processed and must be reproduced with high precision, since errors in the patterns would result in values of A_k not consistent with I_k , introducing degradation in the reconstructed image [1]. A typical device used for the generation of the speckle patterns

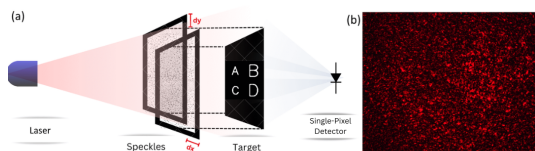


Fig. 1. (a) Conceptual illustration of the imaging process. (b) Example of speckle pattern on glass plate, acquired by a Thorlabs DCC1645C CMOS camera with resolution of 1280×1024 pixels and $3.6 \mu\text{m} \times 3.6 \mu\text{m}$ pixel size.

is the OPA, which can be controlled not only to create a focused beam (e.g., for raster scanning), but also, applying proper control signals, to generate pseudo-random patterns, whose characteristic size depends mainly on the number of branches. The reproducibility of the generated pattern can be affected by the temperature and mechanical displacements of the experimental setup, but is generally very good [2]. An additional solution is represented by a nanocomposite combining electro-spun nanofiber tissue and UV curable resin on a glass plate (Fig. 1(b)), with a total area much larger than the target image. In this way, it is possible to generate the various uncorrelated patterns simply by translating the plate in the x - and y - directions, using different uncorrelated areas. In this scenario, a critical aspect is the proper alignment of the plate in the expected position [1], [3]. In this study, we investigate how spatial misalignment of speckle patterns affects the quality of the reconstruction. Specifically, we simulate the illumination of the target employing speckle patterns that are intentionally shifted with a defined boundary region. This shifting emulates various angular perspectives or aperture displacements that occur during the illumination process, thereby effectively modifying the set of light paths that contribute to each measurement [4]. By modifying the maximum alignment error, we analyze the impact of these inaccuracies on the quality of the reconstructed images using quantitative metrics such as SSIM and PSNR [5].

II. METHODS AND RESULTS

To numerically investigate the effects of misalignments, we consider as a target the boolean 128×128 or original

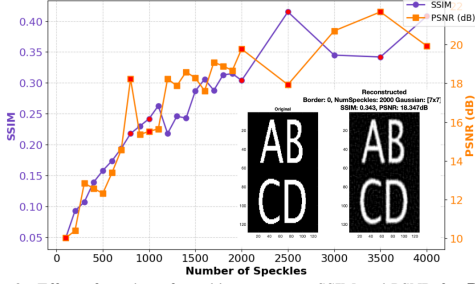


Fig. 2. Effect of number of speckle patterns on SSIM and PSNR for $R = 0$ (perfect alignment). Inset: target image (left) and reconstructed result (right) with 2000 patterns (SSIM = 0.343, PSNR = 18.3 dB).

image shown in the left inset of Fig. 2. In MATLAB, we generate realistic speckle patterns, as matrices of uniformly distributed values in the $(0,1)$ interval. A 2D Gaussian blur with a standard deviation equal to 2 pixels is introduced to mimic the characteristic patterns found on the glass plate. In order to simulate the misalignment, when we calculate the numerical product between speckle patterns and target image, we introduce a shift dx and dy in the correct pattern, as shown in Fig. 1. The values of these two quantities, expressed in pixels, are different for each pattern and are extracted randomly from the range $[-R, R]$ following a uniform distribution. When $R = 0$, we revert to the ideal case of perfect alignment: in this ideal condition, we evaluate the quality of the reconstructed image vs. the number of speckle patterns used. The results are shown in Fig. 2, where both SSIM and PSNR increase with the number of speckles, especially in the range of 100 to 2500. Higher speckle counts improve reconstruction quality, leveling off at approximately 2000 speckles. The inset of Fig. 2 shows a representative reconstruction result of the original target using CS: while the reconstructed image exhibits some blurring effect, it fully captures the main features of the target.

To isolate the impact of spatial misalignment, we fixed the number of speckles to 2000 and varied R . As illustrated in Fig. 3, an increase in R results in a clear degradation in image reconstruction quality, as reflected in both SSIM and PSNR. The SSIM and PSNR decrease from 0.317 and 19.2 dB at $R = 0$ to 0.014 and 4.4 dB at $R = 6$, respectively, indicating a significant loss of structural similarity. Depending on the target application, it is possible to identify a quality threshold, e.g. SSIM=0.1, that specifies which is the maximum allowed alignment error.

Finally, it is interesting to observe that, when $R > 0$, the quality of the reconstructed image is not a monothonic function of the number of patterns used: Fig. 4 shows that when more than 500-1000 misaligned speckle patterns are used, then SSIM significantly decreases. In these situations, in fact, the large number of not perfectly aligned patterns increases the reconstruction noise and leads to quality degradation.

III. CONCLUSION

We have shown through numerical calculations that spatial misalignment can significantly amplify inaccuracies in CS. As

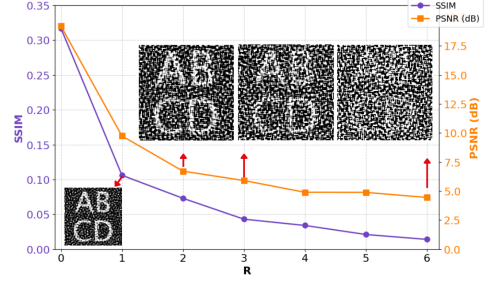


Fig. 3. Effect of misalignment R on the quality of the reconstructed image with 2000 speckle patterns.

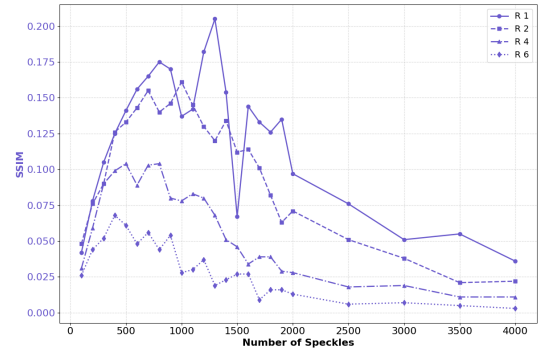


Fig. 4. Comparison of SSIM values versus the number of speckles for different $R = 1, 2, 4$, and 6 .

the alignment error increases, speckle shifts cause significant structural decorrelation, harming reconstruction fidelity.

ACKNOWLEDGMENT

This study was carried out within the *Mid Infrared laBel free Interferometric detectorLess Imaging photonic circuitS - MIRABILIS* project (CUPM. D53D23002780006) – funded by European Union – Next Generation EU within the PRIN 2022 program (D.D. 104 - 02/02/2022 Ministero dell'Università e della Ricerca). This manuscript reflects only the authors' views and opinions and the Ministry cannot be considered responsible for them.

REFERENCES

- [1] T. Fukui *et al.*, "Single-Pixel Imaging Using Multimode Fiber and Silicon Photonic Phased Array," *J. Lightwave Technol.* doi: 10.1109/JLT.2020.3008968 (2021).
- [2] M. Dabbicco *et al.*, "Mid Infrared Label Free Interferometric Detectorless Imaging Photonic Circuit," 2024 IEEE 14th International Conference Nanomaterials: Applications & Properties (NAP) 2024, doi: 10.1109/NAP62956.2024.10739687.
- [3] S. Guerber *et al.*, "Development, calibration and characterization of silicon photonics based optical phased arrays," in [Smart Photonic and Optoelectronic Integrated Circuits XXIII], 11690, 1169006, SPIE (2021), doi: 10.1117/12.2582679.
- [4] M. Dabbicco *et al.*, "Towards a label free coherent detectorless imaging module in photonic integrated circuits," SPIE 13006, Biomedical Spectroscopy, Microscopy, and Imaging III, 130060R (2024), doi: 10.1117/12.3029530.
- [5] T. Ye *et al.*, "Joint supervised and unsupervised deep learning method for single-pixel imaging", *Optics & Laser Technology*, 109278, ISSN 0030-3992, 162 (2023), doi: 10.1016/j.optlastec.2023.109278.

Modeling Gaussian Beam Propagation in Micro-Droplets with Ray Optics

Rouven H. Klenk¹, Simon Abdani¹, Wolfgang Vogel¹, Manfred Berroth¹, Michael Heymann², and Georg Rademacher¹

¹Institute of Electrical and Optical Communications, ²Institute of Biomaterials and Biomolecular Systems

University of Stuttgart

Stuttgart, Germany

rouven.klenk@int.uni-stuttgart.de

Abstract—Grating couplers serve as efficient fiber-chip interfaces. They can also be used to interface optical signals with analytes in optofluidic systems. This study investigates the intensity of a Gaussian beam, emitted from a grating coupler, when interfaced with a droplet. The results can be used to optimize the geometrical setup to maximize the interaction of the optical signal with the analyte. The presented approach can be used as a tool to simplify numerical implementations of droplets in optical simulations.

Keywords—*photonics, optofluidics, droplets, ray optics*

I. OPTOFLUIDIC DROPLET ASSAYS

Droplet sorters are valuable components of optofluidic assemblies in bio-medical research and biological testing. In such systems, analytes are encapsulated in droplets, guided through microfluidic channels. Previously, fiber-based droplet sorters have been demonstrated, where, i.e. fluorescent analytes are stimulated by light emitted from the tip of an optical fiber [1]. To integrate such optofluidic systems, soft lithography using polydimethylsiloxan (PDMS) is employed. To further enhance the integration density of the optical setup, photonic integrated circuits (PICs) can be combined with PDMS-based microfluidic systems. In this work, a photonic-integrated setup is analyzed, where light for excitation and detection is guided to the microfluidic channel via grating couplers, directed to the passing droplets. Grating couplers use diffraction to vertically couple light in and out of a PIC. To optimize the Bragg grating of the coupler, the optical fiber field is often approximated by a Gaussian beam. Although the diffraction grating limits the bandwidth, proposed solutions mitigate this [2], and the concern primarily applies to multi-color assays. The analysis of particles [3] and fluids [4] has already been demonstrated, with a microfluidic channel above the grating coupler. To ensure complete excitation of the analyte within the droplet, the incoming field must be optimized to illuminate the entire droplet volume uniformly. Therefore, the field inside the droplet has to be modeled. Numerically simulating the grating coupler and droplet within a common finite element framework is resource-intensive due to their size mismatch. Droplets typically range from 50 μm to 100 μm in diameter, while grating couplers have much smaller footprints, around (15 μm)². Simulating the curvature of a droplet with sufficient resolution for visible wavelengths requires significant computational resources.

In this work, a Gaussian beam is imaged inside the droplet to describe the field within the droplet. Maximizing the intensity or 3-dB distribution coefficient results in an optimal mode field diameter (MFD) and distance for which the grating coupler can be optimized numerically.

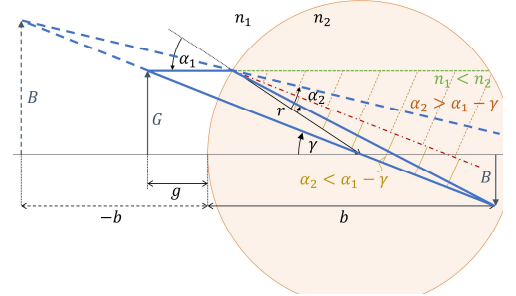


Fig. 1. Ray optics projecting object G with a distance g to the droplet surface resulting in image B with a distance b . Depicted are the ray through the middle of the droplet, and the refracted parallel ray, dependent on the object and the refractive indices.

II. GAUSS IMAGE THROUGH DROPLET SURFACE

A droplet is modeled as a perfectly round sphere with refractive index n_2 , and radius r as shown in Fig. 1. The surrounding area has a refractive index of n_1 . An object with a height G is in front of the droplet with a distance g . To construct the image with the height B , two rays are needed. First, the chief ray, which has an angle of incidence of 0° , passes through the middle of the droplet, due to the perfect spherical shape. Secondly, we consider the ray parallel to the optical axis. Here, the angle of incidence is α_1 . Following Snell's law

$$n_1 \sin(\alpha_1) = n_2 \sin(\alpha_2), \quad (1)$$

the transmitted focal ray is refracted and enters the droplet with an angle α_2 . The crossing point of these two rays is the image of the point of origin. Repeating this imaging process with every point of the object along G results in the image B . In order to have a high confinement inside the droplet, we assume $n_1 < n_2$ [5]. That limits our imaging to two cases, in which the rays could intersect. One, where the image is inside or behind the droplet

$$\alpha_2 < \alpha_1 - \gamma, \quad (2)$$

and the other with the image in front of the droplet,

$$\alpha_2 > \alpha_1 - \gamma. \quad (3)$$

In case of $\alpha_2 = \alpha_1 - \gamma$, chief ray and focal ray do not intersect, the red dashed-dotted line in Fig. 1.

Given the size ratios considered in this study, the small-angle approximation commonly used in the literature is not applied [6]. As illustrated in Fig. 2, the Gaussian beam within the droplet is a projection of the beam that enters it. Analog to the imaging above, the projected object G corresponds to the waist w_0 of the Gaussian beam and the image B to the waist

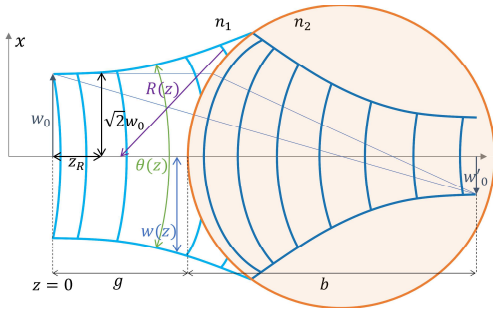


Fig. 2. A gaussian beam originating in $z = 0$ with a waist w_0 and its droplet image originating in $z = g + b$ with an image waist of w'_0 . Additionally, the metrics of a Gaussian beam are sketched in the first beam.

w'_0 of the resulting beam inside the droplet. Together with refractive index n_1 and wavelength λ , the waist defines the Gaussian beam

$$E(x, z) = E_0 \frac{w_0}{w(z)} e^{-\left(\frac{x}{w(z)}\right)^2} e^{-i(n_1 k_0 z - \theta(z) + \frac{n_1 k_0 x^2}{2R(z)})}, \quad (4)$$

where $w(z)$ is the radius at which the field amplitudes decrease to $1/e$ of their axial values at the plane z along the beam. Perpendicular to the beam is the x -axis. The Gouy phase $\theta(z)$ and the radius of curvature $R(z)$ of the beam's wavefront at position z , together with the wave number k_0 , determine the phase of a Gaussian beam. All functions are dependent on the Rayleigh length

$$z_R = \frac{\pi n_1 w_0^2}{\lambda} \quad (5)$$

where the area of the cross section is doubled. The field inside is then dependent on w'_0 and n_2 , with the origin at $z = g + b$.

$$E(x, z) \rightarrow E'(x, z - g - b); r > \sqrt{x^2 + (z - g - b)^2} \quad (6)$$

The amplitude at the origin

$$E'_0 = E_0 \frac{n_1}{n_2} \sqrt{\frac{1 + \left(\frac{b}{z_R}\right)^2}{1 + \left(\frac{g}{z_R}\right)^2}} \quad (7)$$

is normalized to keep the intensity constant at perpendicular entrance into the droplet, i.e. $E(0, g) = E'(0, -b)$. Reflections at the surface are negligible for typical values of $n_1 = 1.29$ and $n_2 = 1.54$ [5].

III. INTENSITY INSIDE MICRO-DROPLETS

Analyzing droplets optically involves exciting the analyte inside. Hence, the intensity of the excitation light within the droplet

$$I = \frac{\sum |E'|^2 n_2 e^{-\alpha_{\text{abs}} r}}{\pi r^2}, \quad r > \sqrt{x^2 + (z - g - b)^2} \quad (8)$$

is a crucial parameter. Included here is the absorption α_{abs} and the refractive index n_2 . In Fig. 3 a) the normalized intensity inside a droplet is calculated over the MFD and the distance g to the droplet surface. The MFD is here the projected object and is double the size of the waist w'_0 . The considered droplet has a radius $r = 25 \mu\text{m}$, the refractive indices are set as stated before, and the excitation wavelength is $\lambda = 488 \text{ nm}$. For a worst-case setting, the absorption is set

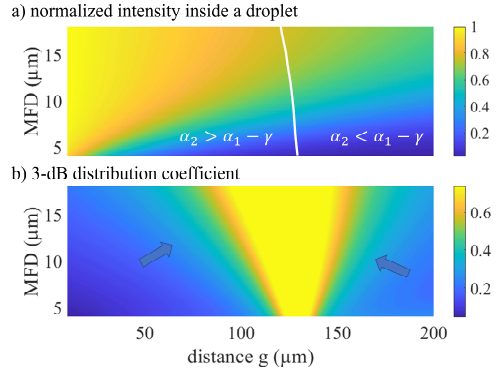


Fig. 3. a) Normalized intensity inside a droplet with $r = 25 \mu\text{m}$, $n_1 = 1.29$, and $n_2 = 1.54$, and b) the 3-dB distribution coefficient.

to the value of PDMS, $\alpha_{\text{abs}} = 20 \text{ cm}^{-1}$ [7]. Depending on the analyte inside the droplet, not only a high intensity, but the intensity distribution within the volume is important. Otherwise, some regions of the droplet may not be excited at all. As a figure of merit, the 3-dB distribution coefficient is defined. For a 2-dimensional case, it is the area inside the droplet where the intensity is greater than 50% of the maximum intensity inside, divided by the total droplet area. The results for varying MFD and distance g are plotted in Fig. 3 b). The measures show different trends. Small distances and large MFDs achieve a high intensity. Meanwhile, the 3-dB distribution coefficient tends towards an optimal configuration, where the distance is between $100 \mu\text{m}$ and $150 \mu\text{m}$. At the same time, the MFD should be as large as possible. The highest 3-dB distribution coefficients are observed along the line defined by $\alpha_2 = \alpha_1 - \gamma$. In theory, the chief and focal rays would intersect at infinity, indicating that ray optics is approaching its limits in this scenario. As a result, interpretations near this region should be approached with caution. Due to the simplifications involved in modeling the Gaussian beam alongside ray optics, the proposed method is intended primarily to identify general trends for optimization. Nonetheless, this model offers a practical and resource-efficient tool for rapid evaluation and optimization tasks.

REFERENCES

- [1] R. H. Cole, N. de Lange, Z. J. Gartner, and A. R. Abate, 'Compact and modular multicolour fluorescence detector for droplet microfluidics', *Lab Chip*, vol. 15, no. 13, Art. no. 13, 2015, doi: 10.1039/C5LC00333D.
- [2] R. H. Klenk *et al.*, 'Integrated dispersive structures for bandwidth-enhancement of silicon grating couplers', *Opt Quant Electron*, vol. 52, no. 2, Art. no. 2, Feb. 2020, doi: 10.1007/s11082-020-2194-0.
- [3] S. Kerman *et al.*, 'Integrated Nanophotonic Excitation and Detection of Fluorescent Microparticles', *ACS Photonics*, vol. 4, no. 8, Art. no. 8, Aug. 2017, doi: 10.1021/acsphotonics.7b00171.
- [4] R. H. Klenk *et al.*, 'Grating Couplers for Chip-Integrated Optofluidic Fluorescence Quantification', in *2021 Kleinheubach Conference*, Miltenberg, Germany: IEEE, Sep. 2021, pp. 1–3. doi: 10.23919/IEEECONF54431.2021.9598417.
- [5] S. K. Y. Tang *et al.*, 'A multi-color fast-switching microfluidic droplet dye laser', *Lab Chip*, vol. 9, no. 19, Art. no. 19, 2009, doi: 10.1039/b914066b.
- [6] E. Hecht, *Optics*, 5 edition. Global edition. Boston: Pearson Education, Inc. 2017.
- [7] S. Alfihed, M. H. Bergen, J. F. Holzman, and I. G. Foulds, 'A detailed investigation on the terahertz absorption characteristics of polydimethylsiloxane (PDMS)', *Polymer*, vol. 153, pp. 325–330, Sep. 2018, doi: 10.1016/j.polymer.2018.08.025.

Signatures of non-classical light emission from semiconductor lasers

Daniele Nello

*Department of Electronics and Telecommunications
Politechnic of Turin
Turin, Italy
daniele.nello@polito.it*

Lorenzo Luigi Columbo

*Department of Electronics and Telecommunications
Politechnic of Turin
Turin, Italy
lorenzo.columbo@polito.it*

Index Terms—quantum optics, semiconductor lasers, and photonics

I. INTRODUCTION

Nowadays, single-photon sources can be generated experimentally through a wide variety of platforms [1]. Semiconductor quantum dots [2] have demonstrated impressive performance in terms of photon purity and indistinguishability, particularly in Hong-Ou-Mandel experiments. Another widely used method involves nonlinear crystals, which can generate entangled photon pairs via nonlinear processes such as spontaneous parametric down-conversion (SPDC) or spontaneous four-wave mixing (SFWM). These are heralded single-photon sources, rather than deterministic ones, yet they remain essential tools in quantum optics [3]. Moreover, among the most commonly used single photon sources, there are NV centres in diamonds [4]. These single-photon sources emit quantum states of light, i.e., those that have no classical counterpart.

In the realm of semiconductor lasers, the seminal work of Yamamoto et al. [5] demonstrated the possibility of reducing the noise of light emission in a quantum well laser below the classical shot noise limit, also known as the standard quantum limit, a clear signature of the quantum nature of the emitted light [6], [7]. This was achieved by minimising noise in the input stream of pumped electrons through the use of high-impedance suppression, resulting in a more regular, so-called “quiet” electron pumping. Recent experimental studies have shown that this effect can also be realised in quantum dot lasers and appears to be more robust in the presence of optical feedback [8], [9].

These developments hold promise for applications in quantum communication, such as continuous-variable quantum key distribution (CV-QKD), by leveraging the mature fabrication capabilities of the semiconductor industry—thus enhancing the commercial feasibility of these platforms [10].

In this work, we will introduce a theoretical framework to study the dynamics of semiconductor lasers based on stochastic rate equations, along with an efficient numerical approach for their simulation. In particular, we will focus on the role of pumping noise in shaping the relative intensity noise (RIN) spectrum, and we will examine the conditions under which this spectrum can be suppressed below the standard quantum limit.

II. SEMICLASSICAL RATE EQUATIONS

The behaviour of semiconductor lasers can be described using a set of coupled stochastic differential equations (SDEs) for the dynamical variables $\vec{X}(t)$ -namely, the carrier densities and the single mode of the electromagnetic field [7]. These equations take the general form:

$$\frac{d\vec{X}}{dt} = \vec{a}(\vec{X}) + \vec{F}(\vec{X}), \quad (1)$$

where $\vec{a}(\vec{X})$ represents the deterministic drift term and $\vec{F}(\vec{X})$ denotes the noise vector.

In the case of quantum dot lasers, we employ a three-level carrier model, following the approach in [11]. The dynamical material variables include the carrier densities in the wetting layer (resonant level), as well as the excited and ground states of the quantum dots, respectively, denoted as (N_{RS}, N_{ES}, N_{GS}) . Photon emission is assumed to occur exclusively from the ground state.

The correlation matrix associated with the noise vector is ultimately derived from the application of the fluctuation-dissipation theorem at the microscopic level, where the laser dynamics are governed by quantum Langevin equations [12].

Within the finite-dimensional dynamical models considered, it is possible to obtain an exact solution of the linearized system for small-signal analysis. This allows for an analytical expression of the relative intensity noise (RIN) spectrum, defined as

$$\text{RIN} = \frac{\delta S_{II}}{I^2}, \quad (2)$$

where

$$\delta S_{II} = |\delta I(\omega)|^2 \quad (3)$$

is given in terms of the Fourier transform $\delta I(\omega)$ of the intensity fluctuations around the stationary solution I .

However, our main interest lies in the output RIN [7], which accounts for the partition noise introduced by the cavity mirrors. This additional noise must be considered to accurately describe the Poissonian photon statistics and thus properly define the standard quantum limit (SQL). The fluctuation of the output power, incorporating the correlated noise term F_0 , is given by

$$\delta P = (\eta_0 h\nu) \delta I + F_0, \quad (4)$$

where η_0 is the output coupling efficiency and ν is the laser frequency.

III. NUMERICAL SIMULATION TECHNIQUES

We have developed and implemented an algorithm to simulate the laser dynamics by numerically integrating the system of stochastic differential equations (Eq. 1). The method is an extension of the classical second-order Runge-Kutta algorithm [13], adapted to rigorously account for noise correlations.

The algorithm takes as input the drift vector $\vec{a}(\vec{X})$ and the correlation matrix $\mathbf{C}(\vec{X})$, where each element is given by $\mathbf{C}_{ij} = \langle F_i F_j \rangle$. The square root of this matrix, $\mathbf{B}(\vec{X})$, is computed at each time step to construct the noise term and multiplied by the vector of random variables $\Delta\vec{W}_k$. Once the

Algorithm 1 Stochastic Runge-Kutta 2nd Order (SRK2)

```

1: procedure SRK2( $\vec{X}_0, \vec{a}, C, T, \Delta t$ )
2:    $n_{\text{steps}} \leftarrow \text{int}(T/\Delta t)$ 
3:    $\vec{X} \leftarrow \vec{X}_0$ 
4:   for  $k = 0$  to  $n_{\text{steps}} - 1$  do
5:      $\Delta\vec{W}_k \leftarrow \text{vec}(\mathcal{N}(0, \sqrt{\Delta t}), \text{dim} = n_W)$ 
6:      $\mathbf{B}(\vec{X}_k) \leftarrow \text{sqrtn}(C(\vec{X}_k))$ 
7:      $\vec{K}_1 \leftarrow \vec{a}(\vec{X}_k)\Delta t + \mathbf{B}(\vec{X}_k) \cdot \Delta\vec{W}_k$ 
8:      $\mathbf{B}(\vec{X}_k + \vec{K}_1) \leftarrow \text{sqrtn}(C(\vec{X}_k + \vec{K}_1))$ 
9:      $\vec{K}_2 \leftarrow \vec{a}(\vec{X}_k + \vec{K}_1)\Delta t + \mathbf{B}(\vec{X}_k + \vec{K}_1) \cdot \Delta\vec{W}_k$ 
10:     $\vec{X}_{k+1} \leftarrow \vec{X}_k + \frac{1}{2}(\vec{K}_1 + \vec{K}_2)$ 
11:  end for
12:  return  $\vec{X} = (\vec{X}_0, \dots, \vec{X}_{n_{\text{steps}}})$ 
13: end procedure
```

stationary state is identified from the rate equations, we verify that it corresponds to a stable fixed point of the dynamics. Post-processing of the resulting trajectories is then used to compute the RIN spectrum, according to Eq. (3).

IV. RESULTS

We analyse both theoretically and numerically the effect of pumping noise on output power fluctuations, considering quantum dot lasers with quantum well lasers. To identify the standard quantum limit (SQL), we assume that the variance of the output power is proportional to its mean value, corresponding to Poissonian statistics. This sets the RIN level at high frequency where shot noise dominates [7] at $\frac{h\nu}{P_{st}}$, where P_{st} is the stationary output power.

In Fig. 1a, we show that for the quantum well laser, the RIN spectrum drops below the SQL in the low-frequency region due to quiet pumping, in agreement with the literature [7]. A similar result for the quantum dot laser is shown in Fig. 1b. Also in this case, our results qualitatively match the recent experimental evidence reported in [8], [9]. In both cases, the high frequency region of the spectrum aligns with the SQL level after the peak associated with relaxation oscillations, while the low frequency region reveals a noise reduction of up to 5–6 dB/Hz.

V. CONCLUSION AND OUTLOOK

In this work, we have theoretically shown that a regular input stream of electrons (quiet pumping regime) can lead to a reduction in relative intensity noise in the low-frequency region, falling below the shot noise level—i.e., below the

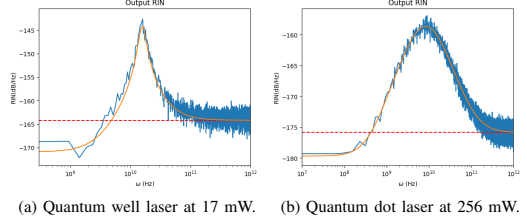


Fig. 1. RIN spectra in the quiet pumping regime using parameters respectively from [7] and [11].

classical detection limit, both in quantum dot and quantum well lasers.

While the RIN spectrum offers a signature of non-classical light emission, a more definitive indicator for the emission of quantum states of light is the second-order correlation function at zero delay. Future work will aim to study the effect of optical feedback on sub-shot noise emission and possibly assess directly the sub-Poissonian statistics of the detected photons through numerical simulations.

REFERENCES

- [1] B. Lounis and M. Orrit, "Single-photon sources" Rep. Prog. Phys. 68 1129 - 2005; doi:10.1088/0034-4885/68/5/R04
- [2] Y. Arakawa, M. J. Holmes, "Progress in quantum-dot single photon sources for quantum information technologies: A broad spectrum overview", Appl. Phys. Rev. - 1 June 2020; 7 (2): 021309; <https://doi.org/10.1063/5.0010193>.
- [3] D. C. Burnham and D. L. Weinberg "Observation of Simultaneity in Parametric Production of Optical Photon Pairs", Phys. Rev. Lett. 25, 84- 13 July, 1970; <https://doi.org/10.1103/PhysRevLett.25.84>.
- [4] I. Aharonovich et al. "Diamond-based single-photon emitters" Rep. Prog. Phys. 74 076501 - 2011; doi:10.1088/0034-4885/74/7/076501
- [5] S. Machida and Y. Yamamoto, "Observation of amplitude squeezing in a constant-current-driven semiconductor laser", Phys. Rev. Lett. 58, 1000 - 9 March, 1987; <https://doi.org/10.1103/PhysRevLett.58.1000>
- [6] M. Fox ; "Quantum Optics: An Introduction (Oxford Master Series in Physics)", Oxford University Press -2006; ISBN: 978-0198566731
- [7] L. A. Coldren, S. W. Corzine, M. L. Mašanović, "Diode Lasers and Photonic Integrated Circuits", Wiley - 2012; ISBN: 9780470484128
- [8] S. Ding, S. Zhao, H. Huang, F. Grillot, "Observation of amplitude squeezing in a constant-current-driven distributed feedback quantum dot laser with optical feedback" APL Quantum - 1 June 2024; 1 (2): 026104; <https://doi.org/10.1063/5.0191416>
- [9] S. Zhao, et. al.; "Broadband amplitude squeezing at room temperature in electrically driven quantum dot lasers" Phys. Rev. Research 6, L032021 - 26 July, 2024; <https://doi.org/10.1103/PhysRevResearch.6.L032021>
- [10] N. J. Cerf, M. Lévy, and G. Van Assche "Quantum distribution of Gaussian keys using squeezed states" Phys. Rev. A 63, 052311 - Published 18 April 2001; doi: <https://doi.org/10.1103/PhysRevA.63.052311>
- [11] J. Duan, X. G. Wang, Y. G. Zhou, C. Wang and F. Grillot, "Carrier-Noise-Enhanced Relative Intensity Noise of Quantum Dot Lasers," in IEEE Journal of Quantum Electronics, vol. 54, no. 6, pp. 1-7 - Dec. 2018; doi: 10.1109/JQE.2018.2880452
- [12] W. Chow, S. Koch, M. Sargent III "Semiconductor-Laser Physics", Springer-21 October 1997; ISBN: 978-3540576143
- [13] R. Honeycutt "Stochastic Runge-Kutta algorithms. I. White noise", Phys. Rev. A 45, 600 - 1 January, 1992; doi: <https://doi.org/10.1103/PhysRevA.45.600>

Coherent and incoherent phenomena in anisotropic periodic gratings

Kamil Postava, Tibor Fordos, Tomáš Kohut, and Lukáš Halagačka
Faculty of Materials Science and Technology and Nanotechnology Center CEET
VSB - Technical University of Ostrava
 Ostrava - Poruba, Czech Republic
 email: kamil.postava@vsb.cz

Abstract—This paper deals with modeling of incoherent and partially coherent effects in structures with lateral periodicity based on scattering matrix formalism. The recurrent formulas are applied in matrix form to describe structures consisting of general anisotropic materials. Incoherent wave summation is presented in the form of infinite geometric series and generalized Mueller matrix calculus describing complete polarimetric response including depolarization phenomena. This method can be combined with any of the existing coherent methods of modeling periodic structures and it offers significantly faster computational performance than partially coherent/incoherent methods based on averaging. The general approach is demonstrated on phenomena emerging from the complex interaction between diffraction grating and thick substrate and the models are compared with experimental spectroscopic data.

Index Terms—periodic structure, incoherent summation, Rigorous Coupled Wave Analysis, Mueller matrix.

I. INTRODUCTION

Majority of widely applied rigorous methods for precise modeling of electromagnetic fields in periodic structures, like Rigorous Coupled-Wave Analysis (RCWA) [1], Finite-Difference Time-Domain method (FDTD) [2], Finite Element Method (FEM) [3], Plane-Wave Admittance Method (PWAM) [4] are based only on illumination by coherent light. In such coherent models interference phenomena occur for arbitrary long optical path difference. This approach is sufficient for many applications, but is not enough in specific areas, as the presence of incoherent or partially coherent light can suppress or attenuate interference oscillations and drastically change the properties of investigated systems.

In spectroscopic or ellipsometric experimental measurements and many cases of practical interest, the incoherency can have multiple origins: the presence of thick transparent substrate, as the thickness of substrate usually exceeds the coherence length of the light source; by inhomogeneity in the thickness of the measured sample over the beam spot; span of incident angles; or the finite spectral bandwidth of the monochromator.

In this paper, we introduce a new method based on Mueller matrix formalism for modeling of incoherent effects in systems containing periodic structures consisting of materials with arbitrary anisotropy. The proposed method combines the scattering matrix (S-matrix) approach, as a way of describing the optical response of a coherent system, with a Partial Wave Summation

Method [5], [7] and Mueller matrix formalism widely used in optical community [6]. As our approach is a matrix method based on Mueller matrix formalism, also depolarization of light by the structure is described and no statistical averaging is needed, which increases the numerical efficiency of the algorithm especially for complex structures. The method also enable deeper understanding and physical insight of a complex wave propagation in periodic systems.

II. MATRIX DESCRIPTION OF POLARIZED LIGHT

Coherent propagation can be effectively described using the 2×2 amplitude-based Jones polarization matrix \mathbf{R} , which consists of the amplitude reflection coefficients r_{ss} , r_{sp} , r_{ps} , and r_{pp} . The lower indexes correspond to incident and reflected polarizations. To describe incoherent effects properly and to avoid spurious interferences, intensity based statistical quantities like Mueller matrices, instead of amplitudes need to be summed. The 4×4 intensity-based Mueller matrices describing the interaction with the sample can be obtained from the amplitude based Jones matrices by the following transformations $\mathcal{R} = \mathbf{A}(\mathbf{R} \otimes \mathbf{R}^*)\mathbf{A}^{-1}$, where \otimes denotes the Kronecker product and \mathbf{A} is a linear transformation matrix [5].

The presence of the grating periodicity Λ introduces diffraction behavior. The effective propagation constant of the n -th mode in one-dimensional case takes the form:

$$N_{y,n} = N_{y,0} + n \frac{\lambda}{\Lambda}, \quad (1)$$

where $N_{y,0}$ describes incident wave, λ denotes the light wavelength.

III. INCOHERENT PARTIAL WAVE SUMMATION

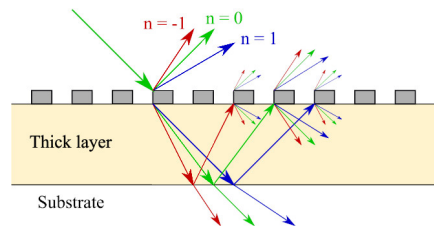


Fig. 1. Partial wave summation in system with lateral periodicity

The incident light upon hitting the first interface is partially reflected and partially transmitted, as seen in Fig. 1. The transmitted waves then propagate through the thick layer, where they can be absorbed, but the phase information is lost. At the second interface the waves are again partially reflected and transmitted. This interaction can be described in the form of matrix sum and leads to a convergent infinite series with finite sum known as Airy summation. This approach leads to partial summation formulas for reflection and transmission Mueller matrices of a thick layer [5], [7]:

$$\mathcal{T} = \mathcal{T}^{(1)} \mathcal{P} (\mathcal{I} - \tilde{\mathcal{R}}^{(0)} \tilde{\mathcal{P}} \mathcal{R}^{(1)} \mathcal{P})^{-1} \mathcal{T}^{(0)}, \quad (2)$$

$$\mathcal{R} = \mathcal{R}^{(0)} + \tilde{\mathcal{T}}^{(0)} \tilde{\mathcal{P}} \mathcal{R}^{(1)} \mathcal{P} (\mathcal{I} - \tilde{\mathcal{R}}^{(0)} \tilde{\mathcal{P}} \mathcal{R}^{(1)} \mathcal{P})^{-1} \mathcal{T}^{(0)} \quad (3)$$

where \mathcal{I} is the identity matrix and \mathcal{P} is the propagation matrix.

Such a simple procedure can be generalized for layers with lateral periodicity and the size of matrices increases significantly according to $([4(2N+1)]^2 \times [4(2N+1)]^2)$ and, the interactions between various diffraction orders need to be accounted properly (for implementation details see Supplement of Ref. [7]).

For partial coherent case, the interference effects are suppressed partially and the Mueller matrix is expressed in the form

$$\mathcal{T} = \mathcal{T}^{(12)} \mathcal{P} (\mathcal{E} - \mathcal{Q})^{-1} \left\{ [\mathcal{E} - \gamma(\tau) (\mathbf{E} \otimes \mathbf{Q}^*)]^{-1} + [\mathcal{E} - \gamma(\tau) (\mathbf{Q} \otimes \mathbf{E})]^{-1} - \mathcal{E} \right\} \mathcal{T}^{(01)}, \quad (4)$$

where $\mathcal{Q} = \tilde{\mathcal{R}}^{(10)} \tilde{\mathcal{P}} \mathcal{R}^{(12)} \mathcal{P}$, $\mathbf{Q} = \tilde{\mathbf{R}}^{(10)} \tilde{\mathbf{P}} \mathbf{R}^{(12)} \mathbf{P}$ and \mathcal{E} is the 4×4 identity matrix and \mathbf{E} is the 2×2 identity matrix. Here $\gamma(\tau)$ is the degree of mutual coherence for quasimonochromatic light of Lorentz spectral shape. Note that for $\gamma = 0$ and $\gamma = 1$ the formula (4) is reduced to (2) and to coherent case $\mathbf{T} = \mathbf{T}^{(12)} \mathbf{P} (\mathbf{E} - \mathbf{Q})^{-1} \mathbf{T}^{(01)}$, respectively. Reflection matrix \mathcal{R} can be obtained in similar form.

IV. GENERALIZATION TO SYSTEMS WITH LATERAL PERIODICITY

To verify applicability of our approach to structures of practical interest, the models were compared with experimental measurements on flexible diffractive components. The sample consisted of a 530 nm thick lamellar grating with the period of 1350 nm printed in a 80 μm thick polymer substrate. The *s*- and *p*- reflectance and transmittance of the zero and first diffraction orders were measured in wavelength range from 350 to 1700 nm on the Cary 7000 Spectrophotometer with Universal Measurement Accessory.

The data shows interesting effect of increased reflection with two peaks around 1250 and 1500 nm originating from the interaction of grating with the substrate, that can not be explained by models with infinite substrate.

ACKNOWLEDGMENT

The authors acknowledge the partial support of the following projects: Czech Science Foundation 25-15775S; project

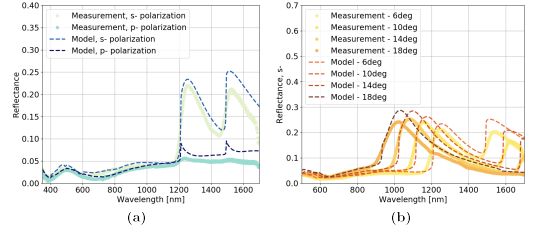


Fig. 2. Comparison of measured and modelled data. a) *s*- and *p*-specular reflectance for the incidence angle $\varphi = 6^\circ$. b) *s*- reflectance for different incidence angles.

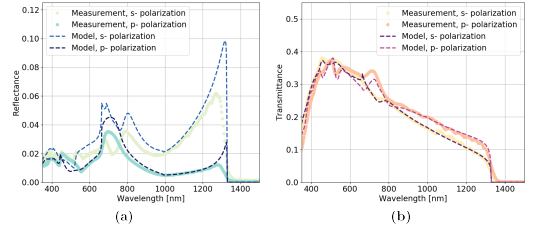


Fig. 3. Comparison of measured and modelled data. a) *s*- and *p*-reflectance of first-order diffracted wave for normal incidence. b) *s*- and *p*-transmittance of first-order diffracted wave.

No. CZ.02.01.01/00/22 008/0004631- “Materials and Technologies for Sustainable Development” and CZ.02.01.01/00/23 021/0008592 “Advanced materials for energetics and environmental technologies”, funded by the European Union and the state budget of the Czech Republic within the framework of the Jan Amos Komenský Operational Program; project REFRESH – Research Excellence For Region Sustainability and High-tech Industries project number CZ.10.03.01/00/22 003/0000048 via the Operational Programme Just Transition; Student Grant System SP2025/090.

REFERENCES

- [1] M. Neviere and E. Popov, *Light Propagation in Periodic Media: Differential Theory and Design*, Marcel Dekker, 2003.
- [2] A. Taflov and S. C. Hagness, *Computational Electrodynamics: The Finite-Difference Time-Domain Method*, Artech House, 2010.
- [3] G. Deméšy, F. Zolla, A. Nicolet, et al., “The finite element method as applied to the diffraction by an anisotropic grating,” *Opt. Express* 15(26), 18089–18102 (2007).
- [4] M. Dems, R. Kotynski, and K. Panajotov, “Planewave admittance method — a novel approach for determining the electromagnetic modes in photonic structures,” *Opt. Express* 13(9), 3196–3207 (2005).
- [5] K. Postava, T. Yamaguchi, and R. Kantor, “Matrix description of coherent and incoherent light reflection and transmission by anisotropic multilayer structures,” *Appl. Opt.* 41(13), 2521–2531 (2002).
- [6] K. Hingerl and R. Ossikovski, “General approach for modeling partial coherence in spectroscopic Mueller matrix polarimetry,” *Opt. Lett.* 41(2), 219–222 (2016).
- [7] K. Postava, P. Ciompa, T. Kohut, M. Drong, R. Ješko, H. Jaffres, T. Fordos, L. Kotačka, H.-J. Drouhin, “Incoherent phenomena in anisotropic periodic structures: from modeling to experimental demonstration,” *Opt. Express* 32(16) 27822 (2024).

Sooner and Better, Perfection in Compromise and Getting it Right First Time : Some Hopes and Realities of Simulation in Industry

D. Childs
Huawei R&D UK Ltd.
Ipswich, IP5 3RE, UK
david.childs@huawei.com

Abstract—We discuss some of the considerations for industrial R&D. From simulation through fabrication to test, we need to make approximations and deal with limitations and reality differing from what is in our model. We shall touch on what makes for a good R&D flow to get it right

Keywords—industry, simulation, photonic components

I. INTRODUCTION

The history of manufacturing has developed from artisan hand crafted products through division of labour and automation and final, with semiconductors at least, to massively parallel manufacturing at wafer scale. In some aspects though, simulation and manufacture of optoelectronic devices still uses a group of veteran artisans, with decades of experience, hand crafting devices with intuition and focused simulation along with tweaking and adjustment of processes. It has long been stated that grand unification in photonics (as can be achieved with the silicon electronics industry) is challenging since electrons are grey, whereas photons are diverse in; colour, phase and polarisation, and the range of materials to make them equally so. Approaches to automate the design process are greatly aided by Moore's law watching/driving computing power which underpins the ability to perform detailed self-consistent simulation that was previously unimaginable. Machine learning and AI optimisation and automation techniques have recently gained popularity, especially in certain areas such as multi-parameter optimisation and simulation code generation. The simulation is, at best, as good as the information fed in to the model.

II. SIMULATION IS ALL WE NEED

The basic requirement for modelling is the ability to build an analogy of the device to explore a single parameter. This may even be qualitative in nature, if it is to be augmented with a manufacturing DoE. The location of any 'cliff edge' (sharp drop in performance as a design parameter is changed) and the width or area of an optimum can be established. Moving on from this, we can go all the way to building a self-consistent model that can allow the devices to be completely optimised. In this case, if we truly believe the model, we do not even need to consider a DoE or a process run but we can just compare the optimum against product specification. In principle, this can eliminate months of R&D fabrication and test and allow the customer to make an informed decision to move directly to new product introduction (NPI).

Many software companies are building ever more complex models where almost all conceivable physics can be turned on, and examples are given where results in papers are dutifully recreated. To modify these examples as a starting point for device simulation appears to be sensible but there is some

caution needed - deviating from these examples may result in unexpected results because the fitting includes entire material libraries stretching back decades and often many more parameters then there are degrees of freedom in the data. In practice, we tend to over-write built in database parameters based on local knowledge using historic device results. We do not even need agree word-wide on these parameters. An example is something that should be pretty simple to understand and agree on e.g. bandgap. A machine grows the semiconductor using flow rates to generate a calibration sample that is measured using photoluminescence. This then dictates adjustments to that layer when it is used in a full QW stack (based on read-across from previous device performance) and we can finally measure spontaneous emission (SE) or gain on those devices over some current range. Knowing the absolute bandgap is not important. On the other hand, a simulation tool often takes atomic compositions and calculates bandgaps. Many additional parameters are used for carrier recombination, leakage, spectral shifts, broadening, etc. contribute to generating SE and gain spectra over some carrier densities. Knowing the absolute bandgap is again not important in itself.

Even in modern times with the exponential growth in computing resource, a fully self-consistent model in terms of carrier dynamics, optical field and temperature, with sufficient 3D resolution is computationally expensive. Nonetheless, a standard desktop machine can handle a large amount of the required simulation for everyday needs. One interesting aspect of modern design is the proliferation of Python based libraries for simulation and machine learning, often in open source format, courtesy of countless thousands of PhD students and academic groups. This lowers the barrier to entry for many companies, and new students. For inverse design approaches, large numbers of designs need to be ran to build the training set and so full simulation is no longer practical. In this case we prefer to use some rapid or home-made compact model that is built for speedy generation of the large numbers of training sets. These models have as little physics as needed to do the job and should compromise everything for speed. The machine learns from these to magically give us our target design.

III. DON'T MODEL IT, MAKE IT

Companies and institutes that possess fabrication facilities have an engineering driven approach at their disposal. This constitutes a more iterative approach, based on repeated cycles of manufacturing. Pushing back against extensive or prolonged simulation is the ability to use a short cycle time to rapidly fabricate devices and test them to truly believe the real performance. In this approach, the combination of the fabrication and the design are intertwined to give the results on the devices that can actually be made, rather than those that

are idealised. The materials, misalignments, shape loss through lithography, etch, deposition, regrowth etc must be considered in the final product anyway.

With all these varied tools at our disposal, and many forms of compromise to take, we can discuss what approach can be taken to develop world class devices as fast as possible.

IV. WE DON'T TEST WHAT WE DESIGNED, BUT WHAT WE MADE

To understand how the device works and verify any simulation output or customer specification is 'merely' a case of testing it. Can we take some equipment in the lab, poke and prod at the chip itself to get all the answers? For example an absorption modulator chip requires a carrier with rf strip-line and termination to make a more complex system so we are not just testing the chip any more. In the case of high-speed components, the test equipment has not quite caught up with the component capability, delivering and collecting high-fidelity 200GHz electrical or optical signals that are calibrated right to the chip is a challenging task. The drivers that we build in products are integrated with the components to work together and deliver system performance. As a result, what we measure at component level in the lab differs from what we build and test at the module level on the production line. System problems are passed back down the line to align with component test data and then on to simulation data to inform design changes.

It may appear that joining the simulation and the real world is 'simply' a case of fitting. This artform takes real or artificial intelligence to adjust hundreds of simulation parameters to agree with the measured data and inform adjustments to hundreds of process parameters. However, different groups in the business use different parameters for materials. E.g. growers often define materials by their strain and SE peak (but in a defined calibration composite structure), since the measurement tools are X-Ray and PL mapper. Simulation often uses just material composition (x,y) since bandgap and strain are then calculated. Simulation is often based on carrier density, whilst experimental data is driven by current. Whilst converting between the two is supposed-

simple, the reality is that multiple data are needed e.g. light-current and relative intensity noise (RIN) spectra are both needed in order to have sufficient degrees of freedom. In addition the device that is actually fabricated can differ significantly from the one in the model. Perfect shaped structures with abrupt interfaces are often modelled but non-uniform shapes with contamination, dopant migration, material alloying, unwanted charge are realised. Structural investigation (SEM, TEM, SIMS) is used to understand the differences, along with specific opto-electrical test structures tailored to de-embedding parameters.

V. MATCHING SIMULATION TO TEST IS NOT THE END

Journals are willing to accept world beating results on their merit alone, but customers are not. There is now a question of reliability. Many devices across many wafers are over-driven to see how they die. The failure modes are investigated at great length and related back to process or design. Once understood we can drive activation energies and acceleration parameters, to derive the failure in time rate and device lifetime for normal operation. If there are any problems relating to design, for instance; the operating current density, junction temperature or strain then a re-design is required. If we have been so bold as to employ new materials, then we may find that further growth studies are needed and we begin the entire R&D cycle again.

Assuming that all is well, we have made a device that meets all the product specifications, exceeds the yield cost model and is beating any competing technology offered by competitors. The company makes money, technology moves forward re-invests in R&D, we keep our jobs. However we are given the enviable task of improving the device again by doubling the speed, power, efficiency or suchlike, and so the cycle continues.

ACKNOWLEDGMENT

We would like to acknowledge the Design Team and other colleagues from IRC who contributed to the work.

Strong light-matter coupling in nanostructures and quantum neural networks

Michał Matuszewski
Institute of Physics
Polish Academy of Sciences
Warsaw, Poland
mmatu@ifpan.edu.pl

Amir Rahmani
Institute of Physics
Polish Academy of Sciences
Warsaw, Poland
rahmani@ifpan.edu.pl

Dogyun Ko
Institute of Physics
Polish Academy of Sciences
Warsaw, Poland
kodo@ifpan.edu.pl

Andrzej Opala
Faculty of Physics
University of Warsaw
Warsaw, Poland
aopala@fuw.edu.pl

Maciej Dems
Institute of Physics
Łódź University of Technology
Łódź, Poland
maciej.dems@p.lodz.pl

Description of many-body light-matter interactions in the regime of strong-light matter coupling is usually presented within the framework of the seminal work of Hopfield, where the concept of polariton was introduced [1]. However, this description has several drawbacks that limit its applicability. The picture of several well-defined modes of light and matter modes interacting with each other is correct as long as the shapes of eigenmodes are not substantially modified by the interaction. Plane-wave description of polariton modes is far from reality in confined systems, while dissipative effects can lead to substantial corrections. This may lead to incompatibility of theoretical descriptions and physical realizations. To date, there is no systematic way to determine a quantum model in the form of a master equation, for a given physical nanostructure, that would take into account all its physical features.

We present a systematic method for obtaining precise form of quantum master equation from first principles, under the assumption of small size of emitters (such as excitons) compared to the wavelength of light, which are strongly coupled to light in a dielectric structure. The method is based on Bogoliubov transformation [2], [3] in the conservative case and on the concept of third quantization [4] in the dissipative case. The procedure involves finding eigenmodes of Maxwell equations coupled to macroscopic polarization field in the classical limit, which can be performed by any solver of choice. We propose that this method can be used for engineering many-body nonlocal interactions between polariton modes in carefully designed structures. In one example, we design a semiconductor structure characterized by high nonlocality of interactions which leads to substantial quantum correlations between modes of emitted light (see Fig. 1). The polariton non-Hermitian eigenmodes are conveniently obtained using the extended Photonic Lasers Simulation Kit (PLaSK), which allows to treat the light-matter coupling in the strong coupling regime.

We demonstrate how the strong interactions resulting from

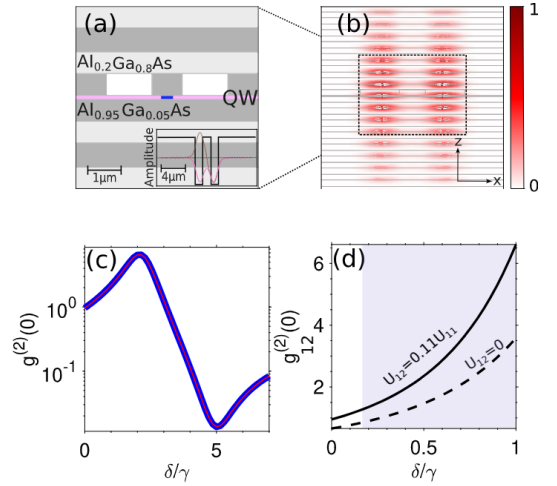


Fig. 1. (a) An example of an engineered semiconductor structure hosting exciton-polariton modes with nonlocal interactions. (b) Electric field intensity in the symmetric eigenmode. (c) second-order correlation function of emitted light in function of detuning. (d) cross-correlation showing enhancement of cross-mode correlations due to nonlocal interactions.

exciton and photon confinement in polaritonic nanostructures can be used to realize a photonic quantum neural network. The concept relies on the idea of quantum reservoir computing [5], which is a special type of recurrent quantum neural network where recurrent node connections do not have to be tuned in the training phase. The training consists of modifications of the output layer connections, which has several important computational advantages. We show how polariton networks can be used in this configuration to realize tasks on quantum inputs, such as quantum feature detection, quantum tomography, and quantum state generation.

REFERENCES

- [1] J. J. Hopfield., "Theory of the Contribution of Excitons to the Complex Dielectric Constant of Crystals," *Phys. Rev.*, vol. 112, pp. 1555–1567 1958.
- [2] N. N. Bogoljubov, "On a new method in the theory of superconductivity," *Il Nuovo Cimento*, vol. 7, pp. 794–805, 1958
- [3] J. G. Valatin, "Comments on the theory of superconductivity," *Il Nuovo Cimento*, vol. 7, pp. 843–857, 1958.
- [4] T. Prosen and T. H. Seligman, "Quantization over boson operator spaces," *J. Phys. A*, vol. 43, 392004 (8pp), 2010.
- [5] S. Ghosh, A. Opala, M. Matuszewski, T. Paterek, T.C.H. Liew, "Quantum reservoir processing," *npj Quantum Information*, vol. 5, 35, 2019.

Dielectric Dipole Nanoantenna Design for highly Directional Emission from SiV Color Centers

1st Mohammed Ashahar Ahamad
Department of Physics
Aligarh Muslim University
 Aligarh, UP 202002, India
 ashaharamu2020@gmail.com

2nd Faraz Ahmed Inam
Department of Physics
Aligarh Muslim University
 Aligarh, UP 202002, India
 faraz.inam@gmail.com

Abstract—We present a novel nanoantenna design investigated using COMSOL Multiphysics, featuring a nanodiamond silicon-vacancy (SiV) center embedded within a polyvinyl alcohol (PVA) layer sandwiched between titanium dioxide (TiO₂) cylinders. Simulation results reveal a 32-fold enhancement in emission at the 738 nm zero-phonon line (ZPL), along with approximately 70 percent collection efficiency in the upward direction, demonstrating strong potential for integrated photonic applications.

Index Terms—Mie resonances, single photon, decay rate.

I. INTRODUCTION

In this era of emerging quantum optical technology, there is a high demand for bright, deterministic, room-temperature single-photon sources with near-unity quantum efficiency (QE) and a collection efficiency (CE) of ≥ 67 percent [1], [2]. Traditional platforms such as photonic cavities, plasmonic nano resonators, and hyperbolic metamaterials suffer intrinsic plasmonic losses that degrade both QE and CE [3], [4]. Here, we propose an all-dielectric Mie-resonant dipole nanoantenna to boost spontaneous emission from a nanodiamond based SiV center at 738 nm ZPL [5]. Our geometry comprises two TiO₂ cylinders coupled with a PVA layer that houses the dipole emitter. The wavelength scale cylinder acts as mie resonator, after interacting with dipole radiation, supports multipolar Mie resonance modes like electric and magnetic dipole mode (ED and MD) and quadrupolar mode (EQ and MQ) respectively [6]. These resonances reshape the local density of optical states (LDOS), directly governing the dipole's spontaneous decay rate [7], [8]. Formally, the LDOS at frequency ω and position \mathbf{r} is given by

$$\rho(\omega, \mathbf{r}) = \sum_{\mathbf{k}, \sigma} |\hat{\mathbf{d}} \cdot \mathbf{E}_{\mathbf{k}, \sigma}(\mathbf{r})|^2 \delta(\omega - \omega_{\mathbf{k}, \sigma}). \quad (1)$$

Here, $\hat{\mathbf{d}}$ is the unit vector specifying the direction of the transition dipole moment, \mathbf{E} is the total electric field at the emitter, comprising its direct emission plus the fields scattered and reflected by the surrounding structure [7]. Here, we investigate how electromagnetic Mie-scattering modes of a TiO₂ coupled-dipolar antenna enhances the decay rates and the directionality of radiation from the SiV single color center embedded within the structure.

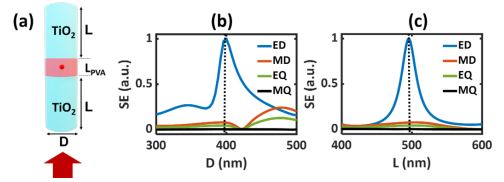


Fig. 1. (a) The schematic of TiO₂ coupled dipole nanoantenna. (b) and (c) The Scattering efficiency (SE) as a function of the diameter (D) and length (L) of the TiO₂ cylinder with maximum SE at D : 400 nm and L : 496 nm respectively.

II. MATERIALS AND METHODS

Simulations were performed using COMSOL RF module with a perfectly matched layer (PML) / scattering boundary (SBC) condition applied on the calculation domain with minimum and maximum mesh sizes of 1 nm and $\frac{\lambda}{2}$, respectively. The optical constants of TiO₂ were taken from [10]. The permittivity of PVA is taken from [11] and the diamond from [12].

A. Scattering efficiency calculation

SE was calculated semi-analytically by integrating electric fields inside the cylinders using custom code that is already programmed inside COMSOL.

B. Relative decay rate calculation

The SiV center was modeled as a point dipole. Relative decay rate was computed as $\Gamma_{rel} = \gamma/\gamma_0 = P/P_0$ [11], where P is the power emitted by point dipole when embedded in nanoantenna and P_0 is the power due to the emission of point dipole in the vacuum.

III. RESULTS AND DISCUSSION

Using the COMSOL RF module, we designed an all-dielectric TiO₂ nanoantenna ($D = 400$ nm, $L = 496$ nm; Fig. 1). The 2D electric field profile shows a strong field confinement at the PVA center under plane wave excitation (Fig. 2(a)). PVA layer's spectral response shows a strong electric-dipole (ED) resonance at 738 nm (Fig. 2(b)), coinciding with the SiV emission—so it acts as a resonant cavity. At the cavity center,

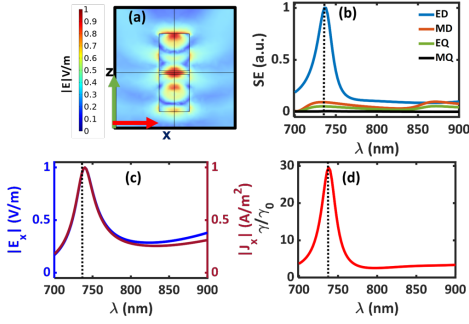


Fig. 2. (a) 2D electric field profile under plane wave excitation in the x - z plane, showing maximum field confinement near the PVA center. (b) PVA layer's spectral response exhibiting a strong electric dipole (ED) resonance at 738 nm. (c) E_x and J_x spectra at the center of the PVA cavity resonant at λ : 738 nm. (d) Relative decay rate spectrum of the SiV center within the PVA cavity.

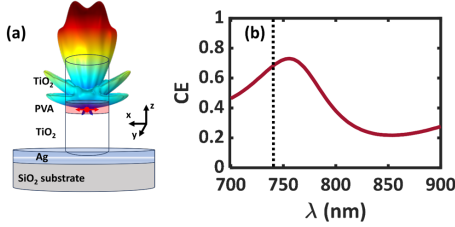


Fig. 3. (a) represents the schematic of the Dipolar antenna with silver reflector and directional 3D far field radiation profile. (b) The CE spectrum of the SiV center dipole radiation directed upward.

both E_x and J_x peak at 738 nm (Fig. 2(c)), boosting the LDOS and increasing the emitter's decay rate by 32 times (Fig. 2(d)). We further investigate the effect of two coupled TiO_2 cylindrical antennas on the radiation pattern of an embedded color center. A nearby dipole emitter placed at the cavity center excites multipolar Mie moments in the antennas, which emit into the far field and interfere with the emitter's radiation. When the electric and magnetic dipole contributions (ED and MD) are balanced, the structure achieves highly directional vertical emission, as shown in Fig. 3(a). For SiV emission, a collection efficiency of approximately 70 percent is achieved in the vertical direction (Fig. 3(b)).

IV. CONCLUSION AND FUTURE WORK

In this work, we explored how multipolar Mie scattering moments influence the local density of states (LDOS), thereby controlling both the decay rate and far-field radiation pattern of a dipole emitter embedded in a nanoantenna. The observed enhancement in emission rate and directionality of single photons positions our design as a promising platform for advancing quantum photonics research in the near future.

V. ACKNOWLEDGEMENTS

We acknowledge the UGC MHRD, INDIA, for SRF.

REFERENCES

- [1] M. Varnava, D. E. Browne, and T. Rudolph, "How Good Must Single Photon Sources and Detectors Be? format?; for Efficient Linear Optical Quantum Computation?," *Phys Rev Lett*, vol. 100, no. 6, p. 060502, 2008.
- [2] I. Aharonovich, D. Englund, and M. Toth, "Solid-state single-photon emitters," *Nat Photonics*, vol. 10, no. 10, pp. 631–641, 2016.
- [3] S. V. Boriskina et al., "Losses in plasmonics: from mitigating energy dissipation to embracing loss-enabled functionalities," *Adv Opt Photonics*, vol. 9, no. 4, pp. 775–827, 2017.
- [4] A. Kala, F. A. Inam, S. Bieh, P. Vaity, and V. G. Achanta, "Hyperbolic metamaterial with quantum dots for enhanced emission and collection efficiencies," *Adv Opt Mater*, vol. 8, no. 15, p. 2000368, 2020.
- [5] I. Aharonovich, S. Castellitto, D. A. Simpson, C.-H. Su, A. D. Green-tree, and S. Praver, "Diamond-based single-photon emitters," *Reports on progress in Physics*, vol. 74, no. 7, p. 076501, 2011.
- [6] R. Alae, C. Rockstuhl, and I. Fernandez-Corbaton, "An electromagnetic multipole expansion beyond the long-wavelength approximation," *Opt Commun*, vol. 407, pp. 17–21, 2018.
- [7] F. A. Inam et al., "Modification of spontaneous emission from nanodiamond colour centres on a structured surface," *New J Phys*, vol. 13, no. 7, p. 073012, 2011.
- [8] M. A. Ahamad and F. Ahmed Inam, "Electromagnetic scattering controlled all-dielectric cavity-antenna for bright, directional, and purely radiative single-photon emission," *J Appl Phys*, vol. 136, no. 8, p. 083104, Aug. 2024, doi: 10.1063/5.0216819.
- [9] F. Inam, T. Gaebel, C. Bradac, L. Stewart, M. Withford, J. Dawes, J. Rabeau, and M. Steel, "Modification of spontaneous emission from nanodiamond colour centres on a structured surface," *New J. Phys.* 13, 073012 (2011).
- [10] J. R. DeVore, "Refractive Indices of Rutile and Sphalerite," *J. Opt. Soc. Am.*, vol. 41, no. 6, pp. 416–419, Jan. 1951, doi: 10.1364/JOSA.41.000416.
- [11] M. J. Schnepf et al., "Nanorattles with tailored electric field enhancement," *Nanoscale*, vol. 9, no. 27, pp. 9376–9385, 2017.
- [12] H. R. Phillip and E. A. Taft, "Kramers-Kronig analysis of reflectance data for diamond," *Physical Review*, vol. 136, no. 5A, p. A1445, 1964.
- [13] Y. Xu, J. S. Vučković, R. K. Lee, O. J. Painter, A. Scherer, and A. Yariv, "Finite-difference time-domain calculation of spontaneous emission lifetime in a microcavity," *Journal of the optical society of America B*, vol. 16, no. 3, pp. 465–474, 1999.

Dependence of optical modes in hyperbolic metamaterials on surrounding medium

Olga A. Kochanowska

Faculty of Physics

University of Warsaw

Warsaw, Poland

olga.kochanowska@fuw.edu.pl

Tomasz J. Antosiewicz

Faculty of Physics

University of Warsaw

Warsaw, Poland

tomasz.antosiewicz@fuw.edu.pl

Abstract—The optical response of an hyperbolic nanostructures is governed by the interplay of two resonances: an electric dipole (ED) and a magnetic dipole coupled with an electric quadrupole (MD-EQ). Their spectral positions and amplitudes are influenced by the medium surrounding the nanoresonator. Here, I present a derivation of resonance conditions dependent on dielectric permittivity of external medium for ED and MD-EQ modes in a quasistatic hyperbolic nanosphere (HNS).

Index Terms—Hyperbolic metamaterials, optical sensors, refractometric sensitivity, resonance conditions

I. INTRODUCTION

Hyperbolic metamaterials (HMMs) significantly broaden the scope of material engineering, opening up new possibilities for controlling the propagation of light [1]. Their unusual optical properties stem from a specific type of anisotropy – in the permittivity tensor of uniaxial HMMs two diagonal elements are of opposite sign to the other one. This anisotropy results in a hyperbolic dispersion relation, which in turn is responsible for the negative refraction of light [2]. HMMs have also been implemented in super-resolution imaging [3], enhanced spontaneous emission [4], or optical biosensors [5].

Arranging subwavelength elements of metal and dielectric materials in artificial HMMs combines the properties of both constituent materials within a single structure. HMMs support both electric and magnetic resonances, resulting in a rich modal optical response. Here, I consider a hyperbolic nanosphere (HNS) made of an Ag:SiO₂ multilayer (see Fig. 1a). In my calculations the dielectric permittivity of silver is described by the Drude model ($\epsilon_m = \epsilon_\infty - \omega_p^2/(\omega^2 + i\gamma\omega)$), with $\epsilon_\infty = 3.37$, $\omega_p = 9.83$ eV, $\gamma = 0.23$ eV and the dielectric is non-dispersive ($\epsilon_d = 2.25$) (see Fig. 1b for the components of the effective medium permittivity tensor). Its extinction spectrum is defined by a strongly scattering electric dipole (ED) resonance and an absorptive magnetic dipole (MD) coupled with an electric quadrupole (EQ) mode (see Fig. 1c–e).

The excitation conditions of these resonances are influenced by numerous factors, such as the size, shape, and fill factor of the metal [6]. Both electric and magnetic resonances in HMMs are affected also by the external medium with its dielectric permittivity ϵ_s . In general, relating the inherent properties

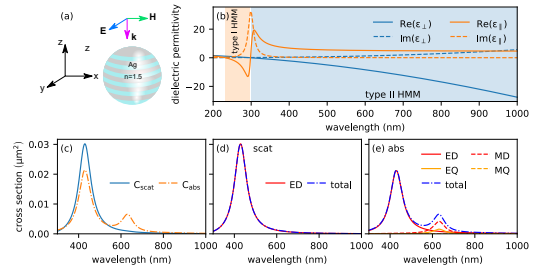


Fig. 1. (a) Hyperbolic nanosphere. (b) Dispersion relation graph of an effective medium Ag:SiO₂ multilayer (with metal fill factor $f_{fm} = 0.5$). (c) Scattering and absorption cross sections of an Ag:SiO₂ nanosphere with 40 nm radius. (d) Scattering and (e) absorption multipole decomposition.

of the nanoparticle and the permittivity of the surrounding medium in a simple resonance condition would be beneficial for a better understanding of excited resonances and the engineering of optical materials.

Caldwell et al. [7] directly tied the resonance energy to the material and geometry of hyperbolic nanocones. They derived resonance condition based on the quantization rule of the geometrical aspect ratio in disk-like particles. Additionally, the resonance condition derived in [8] states that the MD resonance occurs in HMMs when $\epsilon_\perp = -1.65\epsilon_\parallel$. Here, ϵ_\perp (ϵ_\parallel) is the effective dielectric permittivity in the direction perpendicular (parallel) to the anisotropy axis. However, both resonance conditions are limited by (i) the subwavelength size of the resonators and (ii) the omission of the effect of the surrounding external medium. Although the plasmonic ED resonance is determined by the Fröhlich condition, $\epsilon_m = -2\epsilon_s$, an analogous resonance condition for MD has been lacking.

II. RESULTS AND DISCUSSION

In our work we have derived resonance conditions dependent on the dielectric permittivity of the surrounding medium for a quasistatic hyperbolic nanosphere (HNS). We applied the Null-Field Method algorithm [9] in the quasistatic approximation ($x \equiv kr \ll 1$, where r is the sphere's radius and k is the wavenumber in the external medium). By expanding the internal fields into plane waves and solving

the boundary problem, we calculated the transition matrix (T-matrix) of a quasistatic HNS. The T-matrix explicitly describes the multipolar optical response of a single scatterer. Therefore, by expanding the T-matrix components corresponding to the relevant multipoles into a Taylor series, we obtained the T-matrix in simple polynomial form for the ED [10]:

$$T^{ED} = -\frac{2}{3}ix^3 \frac{\epsilon_{\perp} - \epsilon_s}{\epsilon_{\perp} + 2\epsilon_s} \quad (1)$$

and the MD-EQ mode (for simplicity called MD):

$$T^{MD} = ix^5 \frac{\epsilon_s^{3/2} (6\epsilon_s^2 - 4\epsilon_{\perp}\epsilon_{\parallel} - \epsilon_s(\epsilon_{\perp} + \epsilon_{\parallel}))}{90(\epsilon_{\perp} + \epsilon_{\parallel} + 3\epsilon_s)} \quad (2)$$

In case of the ED, the result is consistent with Mie scattering theory and leads to the Fröhlich condition for plasmonic resonances:

$$\epsilon_{\perp} = -2\epsilon_s \quad (3)$$

The ED is a purely plasmonic resonance that is not coupled to any other mode. Contrarily, the MD resonance only occurs in a HMM when coupled to the EQ. Thus, an EQ must be accounted for in the T-matrix calculations. From the pole of the denominator in (2), we derived a material-dependent resonance condition for the MD:

$$\epsilon_{\perp} = -\epsilon_{\parallel} - 3\epsilon_s \quad (4)$$

The above condition explicitly links the dielectric permittivity of a HNS at resonance with the permittivity of the surrounding medium. Moreover, it is satisfied only by a HMM, in which ϵ_{\perp} and ϵ_{\parallel} have opposite signs. However, we did not assume any particular type of anisotropic dispersion in the T-matrix calculations. Therefore, (3) and (4) are applicable to both type I and type II hyperbolic dispersion.

We then verify the accuracy of conditions (3) and (4) by comparing their predictions with full T-matrix calculations for an Ag:SiO₂ hyperbolic nanosphere (see Fig. 1a) with an increasing radius from 5 to 50 nm in 5 nm increments. Numerical simulations were performed using an open-access software called SMUTHI [11]. The nanosphere is surrounded by a medium with dielectric permittivity ϵ_s increasing from 1 to 2.25 (see Fig. 2). The resonant wavelengths of the ED in a quasistatic HNS (5 nm in radius) are in good agreement with the quasistatic predictions from (3). Contrary to the ED, the spectral positions of the MD resonance predicted by (4) follow simulations' results for a 15 nm nanosphere. The discrepancy between the resonance predictions and the full T-matrix calculations stems from the neglect of losses in the derived resonance conditions. Equations (3) and (4) only account for the real part of permittivity. The MD is a predominantly absorptive resonance; therefore, neglecting the material losses causes the predicted resonance wavelength to redshift. Naturally, since the resonance conditions were derived under the quasistatic approximation, the calculated resonance positions of both the ED and the MD further deviate from the quasistatic predictions as the particle radius increases. Overall, however, the simulation results are in good agreement with the resonance predictions for a quasistatic HNS.

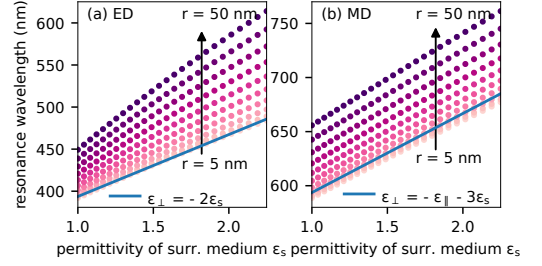


Fig. 2. (a) ED and (b) MD resonance wavelengths vs. permittivity of surrounding medium for hyperbolic nanospheres with radius ranging from 5 nm to 50 nm every 5 nm. Comparison of full T-matrix calculations (circles) with quasistatic predictions (lines).

III. CONCLUSION

In conclusion, the optical response of hyperbolic nanoparticles is determined by ED and MD-EQ resonances. The excitation conditions of these modes are related to the permittivity of the surrounding medium, as we demonstrated in our derived resonance conditions. The predictions of these resonance conditions are in good agreement with the simulation results for a quasistatic HNS.

REFERENCES

- [1] Nicolò Maccaferri et al., *Hyperbolic meta-antennas enable full control of scattering and absorption of light*, Nano Lett. **19** (2019), no. 3, 1851–1859
- [2] Alexander Poddubny, Ivan Iorsh, Pavel Belov and Yuri Kivshar, *Hyperbolic metamaterials*, Nature Photonics **7** (2013), 958–967
- [3] Zhaowei Liu, Hyesog Lee, Yi Xiong, Cheng Sun and Xiang Zhang, *Far-field optical hyperlens magnifying sub-diffraction-limited objects*, Science **315** (2007) no. 5819, 1686–1686.
- [4] C. L. Cortes, W. Newman, S. Molesky and Z. Jacob, *Quantum nanophotonics using hyperbolic metamaterials*, J. Optics **14** (2012), 063001
- [5] Ying Chen et al., *Hyperbolic-metamaterial-based optical fiber SPR sensor enhanced by a smart hydrogel for perspiration pH measurements*, Nano Letters **25** (2025), no. 1, 129–137
- [6] Sema Ebrahimi, Alina Muravitskaya, Ali M. Adawi, Anne-Laure Baudrion, Pierre-Michel Adam, and Jean-Sebastien G. Bouillard *Magnetic mode coupling in hyperbolic bowtie meta-antennas*, The Journal of Physical Chemistry Letters **14** (2023), no. 35, 7824–7832
- [7] Joshua D. Caldwell et al., *Sub-diffractive volume-confined polaritons in the natural hyperbolic material hexagonal boron nitride*, Nat. Commun. **5** (2014), 5221.
- [8] Krzysztof M. Czajkowski, Maria Bancerek, Alexander Korneluk, Dominika Świtlik and Tomasz J. Antosiewicz, *Polarization-dependent mode coupling in hyperbolic nanospheres*, Nanophotonics, **10** (2021), no. 10, 2737–2751.
- [9] Adrian Doicu, Thomas Wriedt and Yuri A. Eremin, *Light scattering by systems of particles*, Springer (2006)
- [10] Olga A. Kochanowska and Tomasz J. Antosiewicz, *Dependence of the magnetic dipole resonance of hyperbolic nanospheres on the external medium*, Optics Letters **50** (2025), 1293–1296
- [11] Amos Egel, Krzysztof M. Czajkowski, Dominik Theobald, Konstantin Ladutenko, Alexey S. Kuznetsov and Lorenzo Pattelli, *SMUTHI: A python package for the simulation of light scattering by multiple particles near or between planar interfaces*, Journal of Quantitative Spectroscopy and Radiative Transfer **273** (2021), 107846.

Theoretical investigation of optical polarisation in alloy disordered (Al,Ga)N quantum well systems

Robert Finn*, Michael O'Donovan[†], Thomas Koprucki[‡] and Stefan Schulz*,[‡]

*Tyndall National Institute, University College Cork, Cork, T12 R5CP, Ireland

[†]Weierstrass Institute (WIAS), Mohrenstr. 39, 10117 Berlin, Germany

[‡]School of Physics, University College Cork, Cork, T12 YN60, Ireland

Email: robert.finn@tyndall.ie

Abstract—Aluminium Gallium Nitride ((Al,Ga)N) is an ideal material for light emitting devices in the UV spectral range. However, these devices still suffer from low external quantum efficiencies, particularly in the deep-UV range. A contributor to the low external quantum efficiency is low light extraction efficiency (LEE), which is tightly linked to the valence band structure of (Al,Ga)N quantum wells. Theoretical studies that account for alloy disorder-induced valence band mixing effects in these structures are sparse. Here, we utilise an atomistic multi-band tight-binding model to gain insight into the degree of optical polarisation in (Al,Ga)N quantum well systems. Special attention is paid to the impact of Al content, well width and carrier density in the wells.

Index Terms—UV-C emitters, alloy disorder, light polarization, Urbach tail energies

I. INTRODUCTION

Thanks to their large direct band gap, Aluminium Gallium Nitride ((Al,Ga)N) alloys have attracted significant attention for UV light-emitting applications [1]. A region of particular interest is the UV-C wavelengths window (< 280 nm), which can be used for applications such as water purification, sterilization, etc. [1]. However, (Al,Ga)N-based light emitting diodes (LEDs) suffer from low quantum efficiencies at wavelengths in the UV-C range, stemming in part from a low light extraction efficiency (LEE) [1]. The overall low LEE is related to differences in the valence band structure of AlN and GaN and how the band character changes with Al content in (Al,Ga)N heterostructures such as quantum wells (QWs). Here, the crystal field splitting energy, Δ_{cf} , plays an important role. For GaN, Δ_{cf} is positive ($\approx +30$ meV), while in AlN Δ_{cf} is negative (≈ -200 meV) [2]. As a result, the valence band edge (VBE) of GaN has Γ_9 symmetry, which is made up of p_x, p_y like orbitals, whereas the VBE in AlN is of Γ_7 symmetry, composed of mainly p_z like orbitals. The symmetry of the highest valence states for GaN and AlN gives rise to the emission of transverse electric (TE) and transverse magnetic (TM) polarized photons, respectively [3]. Given that standard LEDs are surface emitting devices, TM polarised light leads to a very low LEE.

This work received funding from the Leibniz Competition 2022 (UVSimTec, K415/2021), the Sustainable Energy Authority of Ireland and Taighde Éireann – Research Ireland (17/CDA/4789, 12/RC/2276 P2 and 21/FFP-A/9014), and the Leibniz competition 2020 (NUMSEMIC, J89/2019).

The relative emission of TM and TE polarized light can be described by the degree of optical polarisation (DOP), which depends on the orbital character of the valence states contributing to the light emission process. In addition to heterostructure confinement, strain and polarisation fields, alloy disorder also leads to valence band mixing effects, which impact the DOP and thus the LEE. The latter aspect is largely unexplored, as it requires 3D simulations in the framework of a multi-band electronic structure theory. Here, we study the DOP of (Al,Ga)N-based QW systems on the basis of an atomistic tight-binding model (TB). Special attention is paid to (i) the well width, (ii) Al content, and (iii) carrier density in the wells. Our calculations show that in terms of the DOP, in particular for high Al systems, wider wells can offer potential benefits to improve the LEE of such (Al,Ga)N light emitters.

II. THEORETICAL FRAMEWORK

To account for the impact of alloy disorder on the electronic and optical properties of (Al,Ga)N QWs, we employ the atomistic multi-band TB model introduced in Ref. [4]. The model is also coupled with a self-consistent Schrödinger-Poisson solver to account for carrier density dependent screening of internal polarisation fields. To cover TE and TM polarized light emitters, two QW systems have been targeted, namely $\text{Al}_{0.48}\text{Ga}_{0.52}\text{N}/\text{Al}_{0.63}\text{Ga}_{0.37}\text{N}$ for TE and $\text{Al}_{0.75}\text{Ga}_{0.25}\text{N}/\text{Al}_{0.9}\text{Ga}_{0.1}\text{N}$ wells for TM polarized light. The studies are carried out for different well widths and carrier densities. To gain insight into the impact of alloy disorder on the electronic structure, Urbach tail energies have been calculated [5], [6]. In terms of the DOP, we study the orbital character of the valence states [5].

III. RESULTS

As the barrier has a higher AlN composition than the well, the emission characteristics of the QW will depend on how the hole states interact with the barrier material. As such, Fig. 1 shows the average probability of the hole charge density, $|\psi_h^{\text{AVG}}|^2$, confined inside the $\text{Al}_{0.75}\text{Ga}_{0.25}\text{N}$ QW as a function of energy and carrier density for a 1.3 nm wide well. The colour bar gives the orbital character of the different states. Here, blue indicate predominately p_z orbital character or TM polarization while yellow indicates predominately $p_x + p_y$ orbital character or TE polarization.

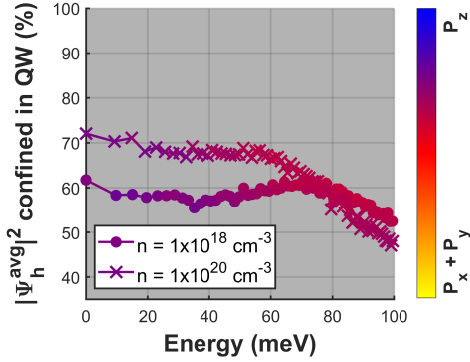


Fig. 1. Average probability of hole charge density, $|\Psi_h^{\text{avg}}|^2$, confined inside a 1.3 nm $\text{Al}_{0.75}\text{Ga}_{0.25}\text{N}$ quantum well as a function of energy. The data are averaged over 150 configurations. The average state energy is plotted with respect to the average ground state energy and for the carrier densities of $n = 1 \times 10^{18} \text{ cm}^{-3}$ (circles) and $n = 1 \times 10^{20} \text{ cm}^{-3}$ (crosses), respectively. The colour coding gives the averaged orbital contribution of each energy level (blue: p_z ; yellow: $p_x + p_y$). Figure adapted from Ref. [5].

Figure 2 shows the data for a 3.3 nm wide well. These figures reveal that for the narrow well width of 1.3 nm, a width often used in deep UV (Al,Ga)N light emitters, the wave functions leak significantly into the barrier material. While this feature may be attractive for carrier transport between wells in multi QW systems, it may also lead to increased non-radiative recombination due to defects in the barrier material. With increasing carrier density, wave functions are more strongly bound in the QW. We attribute this effect to a screening of the built-in polarisation fields.

Increasing the well width has two benefits, it increases carrier confinement in the well and depending on the carrier density the orbital character tends towards p_x and p_y like states. However, with increasing carrier density more p_z like states become available. This observation also correlates with Urbach tail energies, which provide an indication for carrier localisation in the system. For the narrow QW, the Urbach tail energy affected very little by changes in the carrier density. In contrast, for wider wells the Urbach tail energy decreases with increasing carrier densities. This indicates that carrier localisation effects are strongly affected by the screening of the built-in field and as such so is the orbital character of the valence states. Thus, our calculations highlight an interplay of carrier density and well width on the electronic and ultimately optical properties of deep UV light emitters. Therefore, to improve TE polarised emissions and DOP in deep UV light emitters, wider QWs at lower carrier densities may be beneficial. The resulting increase in LEE would need to be balanced with other device characteristics such as radiative recombination rate which can decrease for wider wells.

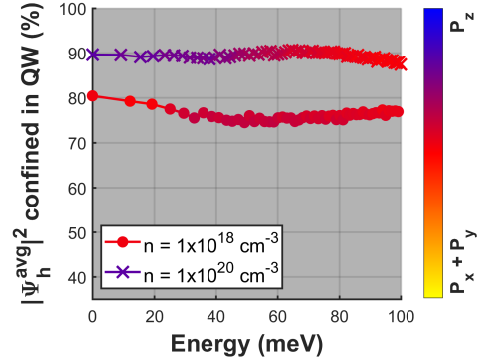


Fig. 2. Average probability of hole charge density, $|\Psi_h^{\text{avg}}|^2$, confined inside a 3.3 nm $\text{Al}_{0.75}\text{Ga}_{0.25}\text{N}$ quantum well as a function of energy. The data are averaged over 150 configurations. The average state energy is plotted with respect to the average ground state energy and for the carrier densities of $n = 1 \times 10^{18} \text{ cm}^{-3}$ (circles) and $n = 1 \times 10^{20} \text{ cm}^{-3}$ (crosses), respectively. The colour coding gives the averaged orbital contribution of each energy level (blue: p_z ; yellow: $p_x + p_y$). Figure adapted from Ref. [5].

IV. CONCLUSION

In this work, we investigated the electronic and optical properties of (Al,Ga)N-based QWs by means of an atomistic TB model. When coupled with self-consistent calculations, the impact of carrier density, well width and Al content on Urbach tail energies and the light polarisation characteristics of deep UV light emitters was studied. In terms of the degree of optical polarisation, our calculations indicate that wider wells at lower carrier densities can be beneficial for enhancing the light extraction efficiency of deep UV light emitters.

REFERENCES

- [1] H. Amano, R. Collazo, C. De Santi, S. Einfeldt, M. Funato, J. Glaab, S. Hagedorn, A. Hirano, H. Hirayama, R. Ishii, Y. Kashima, Y. Kawakami, R. Kirste, M. Kneissl, R. Martin, F. Mehnke, M. Meneghini, A. Ougazaden, P. J. Parbrook, S. Rajan, P. Reddy, F. Römer, J. Ruschel, B. Sarkar, F. Scholz, L. J. Schowalter, P. Shields, Z. Sitar, L. Sulmoni, T. Wang, T. Wernicke, M. Weyers, B. Witzigmann, Y.-R. Wu, T. Wunderer, and Y. Zhang. The 2020 UV emitter roadmap. *J. Phys. D: Appl. Phys.*, 53:503001, 2020.
- [2] P. Rinke, M. Winkelkemper, A. Qteish, D. Bimberg, J. Neugebauer, and M. Scheffler. Consistent set of band parameters for the group-III nitrides AlN, GaN, and InN. *Phys. Rev. B*, 77:075202, 2008.
- [3] M. Guttman, F. Mehnke, B. Belde, F. Wolf, C. Reich, L. Sulmoni, T. Wernicke, and M. Kneissl. Optical light polarization and light extraction efficiency of AlGaIn-based LEDs emitting between 264 and 220 nm. *Japanese Journal of Applied Physics*, 58(SC):SCCB20, 2019.
- [4] R. Finn and S. Schulz. Impact of random alloy fluctuations on the electronic and optical properties of (Al,Ga)N quantum wells: Insights from tight-binding calculations. *J. Chem. Phys.*, 157:244705, 2022.
- [5] R. Finn, M. O'Donovan, T. Koprucki, and S. Schulz. Theoretical study of the impact of carrier density screening on Urbach tail energies and optical polarization in (Al,Ga)N quantum well systems. *arXiv:2501.16808*, 2025.
- [6] J. M. McMahon, D. S. P. Tanner, E. Kioupakis, and S. Schulz. Atomistic analysis of radiative recombination rate, Stokes shift, and density of states in *c*-plane InGaIn/GaN quantum wells. *Appl. Phys. Lett.*, 116:181104, 2020.

Numerical and experimental investigation of erbium (III) ion doped fluoride glass fiber laser operation at threshold

Slawomir Sujecki
Faculty of Electronics
Military University of Technology
Warsaw, Poland
slawomir.sujecki@wat.edu.pl

Lukasz Sojka
Faculty of Informatics and
Communication Technology
Wroclaw University of Science and
Technology Wroclaw, Poland
lukasz.sojka@pwr.edu.pl

Lukasz Pajewski
Faculty of Informatics and
Communication Technology
Wroclaw University of Science and
Technology Wroclaw, Poland
lukasz.pajewski@pwr.edu.pl

Samir Lamrini
LIMA Photonics GmbH
Goettingen., Germany
S.Lamrini@lima-photonics.de

Mark Farries
Faculty of Engineering
Nottingham University
Nottingham, UK
mark.farries@nottingham.ac.uk

Angela Seddon
Faculty of Engineering
Nottingham University
Nottingham, UK
angela.seddon@nottingham.ac.uk

David Furniss
Faculty of Engineering
Nottingham University
Nottingham, UK
david.furniss@nottingham.ac.uk

Emma Barney
Faculty of Engineering
Nottingham University
Nottingham, UK
emma.barney@nottingham.ac.uk

Sendy Phang
Faculty of Engineering
Nottingham University
Nottingham, UK
sendy.phang@nottingham.ac.uk

Abstract—Lanthanide ion doped, fiber lasers are characterized by high brightness, circular beam shape, tuning ability and short pulse generation. In this contribution, we study experimentally and numerically near threshold operation of a erbium (III) ion doped fluoride glass fiber laser which operates near 2800 nm. The results obtained are useful for engineers developing novel fiber lasers, as the results help in detecting the onset of stimulated emission.

Keywords—Fiber lasers, time domain analysis, laser threshold

I. INTRODUCTION

The erbium (III) ion doped, fluoride glass, fiber laser is an important milestone in the development of fiber lasers operating in the mid-infrared wavelength region. It is, at the moment, still the only fiber laser capable of delivering near 3000 nm a nanosecond pulse with peak power exceeding 10 kW and M^2 near 1 [1]. Further, this laser can be conveniently pumped using a 980 nm laser diode with a double-clad, fiber, cross-sectional arrangement and it reaches output powers exceeding 10 W near 3000 nm [2].

Currently, the main effort in the development of mid-infrared fiber lasers is focused on reaching wavelengths exceeding 4000 nm [3,4]. An important element of this effort is the correct identification of lasing, coming from a newly developed, laser setup. An erroneous identification of lasing may result in a misdirection of the fiber development effort, which can be very costly.

In this paper, we focus on the study of the temporal behavior of output light coming from an erbium (III) ion doped fluoride glass fiber laser. We focus exclusively on the output wavelengths near 2800 nm. In our study, we combine both experimental methods and numerical modelling.

II. EXPERIMENTAL SETUP AND NUMERICAL MODEL

The experimental setup is presented in Fig.1. The pump light emitted by a 980 nm laser diode is focused on the coupling facet of the erbium (III) ion doped fluoride glass fiber. It propagates through the fiber and is reflected of the air / glass interface at the other end of the cavity. The 2800 nm light is collected from the fiber end opposite to the launch end and delivered to the detector, and oscilloscope to record the temporal traces of the laser output. The pumping laser diode is modulated directly from a current drive.



Fig. 1. Experimental setup of an erbium (III) ion doped fluoride glass fiber laser.

The one dimensional time domain, numerical model used in this study relies on the finite difference method to convert a set of partial differential equations, that govern the photon distribution within the laser cavity, to a set of ordinary differential equations. These latter equations are then solved, together with rate equations describing the level populations, in MATLAB programming environment [5]. The simulation parameters have been taken from [6]. The numerical calculations have been performed on a standard PC with 13th Gen Intel(R) Core(TM) i5-1335U 1.30 GHz processor using Windows operating project.

III. RESULTS

The length of the fiber used in the laser cavity assembled according to Fig.1 was 0.7 meters. The laser cavity was terminated by the cleaved ends of the fiber where a reflectivity

of 4 % is assumed. The fiber was double-clad. The core diameter was 15 μm , the inner-cladding double D diameter was 240/260 μm , while the doped core erbium III ion concentration was 70000 ppm. The pump laser diode operated at 980 nm and was coupled into a 100 mm pigtail, undoped fluoride fiber. We assumed that the pump power coupled to the erbium (III) ion doped fiber, had losses attributed only to the 4 % Fresnel reflection at the air-glass interface of the fiber end. The pump laser diode was modulated with a near square wave waveform having the repetition frequency of 10 Hz. The pulse rise and fall time was approximately 1 μs , while the pulse ramp time was: $T_{\text{on}} = 50$ ms followed by 50 ms of off time (Fig.2).

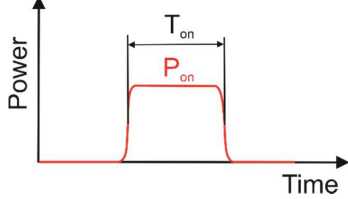


Fig. 2. Laser pump diode pulse shape.

Fig. 3 shows the measured dependence of the fiber laser output power on time, at selected values of the pump power P_{on} (Fig.2). Below threshold (black trace in Fig.3), the output waveforms differ qualitatively from those collected above threshold (blue and green color in Fig.3). Above threshold at the pulse leading edge, the pulse was preceded by a significant overshoot of the output power [7]. On the trailing edge a noticeably slower decay below threshold was observed. This is because below threshold the light decay time is equal approximately to the upper lasing level life time while above threshold it is in principle determined by the lasing cavity photon lifetime, though for a specific experimental setup (cf. Fig.1) it is limited by the pump pulse switch-off time. It is noted that there is a non-zero output power intensity recorded before the pumping pulse arrival, which is due to thermal radiation background incident upon the detector. This background light was extracted from experimental results during the postprocessing of measured results.

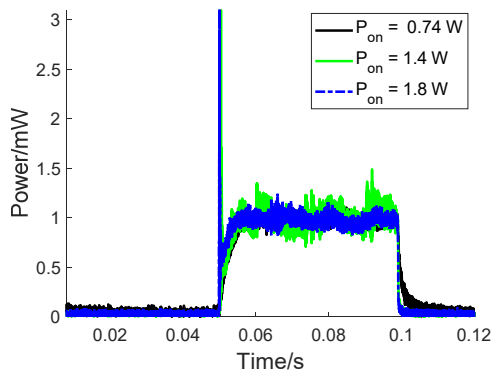


Fig. 3. Measured output pulse shapes at selected values of the pump power.

Fig. 4 shows the numerically calculated dependence of the fiber laser output power on time at selected values of the pump

power. Similarly to the experimental results, the numerical results have been rescaled to one for the ramp (P_{on} in Fig.2) so that the attention can be focused on the shape of each waveform. It is interesting to note that the model reproduces the waveforms with a distinct leading peak which is observed above threshold. Concerning the trailing edge, similarly to experimental results a distinctly longer light decay is observed below threshold. Further, there are oscillations observed experimentally that are not reproduced by the model. This discrepancy can be attributed to wavelength hopping, as observed in [7]. Also, the numerically calculated waveform at 0.74 W pump power has a significantly larger delay than the one observed experimentally. This requires further investigation.

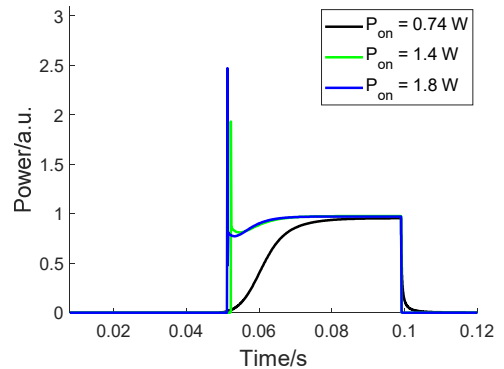


Fig. 4. Numerically calculated output pulse shapes at selected values of the pump power compared with an experimentally obtained pulse shape.

ACKNOWLEDGMENT

The authors from Military University of Technology and Wrocław University of Science and Technology acknowledge support from statutory activity.

REFERENCES

- [1] L. Sójka, L. Pajewski, S. Lamrini, M. Farries, T. M. Benson, A. B. Seddon, S. Sujecki, "High peak power Q-switched Er: ZBLAN fiber laser," *Journal of Lightwave Technology*, vol. 39, pp. 6572-6578, October 2021.
- [2] V. Fortin, M. Bernier, S. T. Bah, R. Vallée, "30 W fluoride glass all-fiber laser at 2.94 μm ," *Optics Letters*, vol. 40, pp. 2882-2885, June 2015.
- [3] J.J. Nunes, L. Sójka, R.W. Crane, D. Furniss, Z.Q. Tang, D. Mabwa, B. Xiao, T.M. Benson, M. Farries, N. Kalfagiannis, E. Barney, S. Phang, A.B. Seddon, S. Sujecki, "Room temperature mid-infrared fiber lasing beyond 5 μm in chalcogenide glass small-core step index fiber," *Optics Letters*, vol. 46, pp. 3504-3507, July 2021.
- [4] V. Koltashev, B.I. Denker, B.I. Galagan, G.E. Snopatin, M.V. Sukhanov, S. E. Sverchkov, A.P. Velmuzhov, V.G. Plotnichenko, S. Sujecki, "150 mW Tb³⁺ doped chalcogenide glass fiber laser emitting at $\lambda > 5 \mu\text{m}$," *Optics and Technology*, vol. 161, pp. 109233, June 2023.
- [5] S. Sujecki, "Numerical analysis of Q-switched erbium ion doped fluoride glass fiber laser operation including spontaneous emission," *MDPI Applied Sciences*, vol. 8, pp. 803, May 2018.
- [6] J. Li, S. D. Jackson, "Numerical Modeling and Optimization of Diode Pumped Heavily-Erbium-Doped Fluoride Fiber Lasers," *IEEE Journal of Quantum Electronics*, vol. 48, pp. 454-464, April 2012.
- [7] M. Gorjan, M. Marinček, M. Copic, "Spectral dynamics of pulsed diode-pumped erbium-doped fluoride fiber lasers," *Journal of the Optical Society of America B*, vol. 27, pp. 2784-2793, December 2010.

Simulating a High Extinction Ratio Interferometric Electroabsorption-Modulated Laser Transmitter

R. Spalding¹, D. Moodie¹, R. Cronin¹, N. Hattasan¹, J. Griffiths¹, and D. Childs¹

¹Huawei IRC, Ipswich, United Kingdom, richard.spalding@huawei.com

Abstract—We present the design and simulation of a high-speed laser integrated transmitter, capable of high extinction ratios whilst maintaining good optical modulation amplitude, even at short modulator lengths. The key to this device's performance is the configuration of its components, wherein two electroabsorption modulators - modulated with data and data-bar - are combined with a multi-mode interferometer.

Index Terms—InP, electroabsorption modulator, externally modulated laser, interferometric, extinction ratio

I. INTRODUCTION

Optical transceivers are key components in telecoms and datacoms applications, and demand from technologies, such as AI, high-performance computing (HPC) and next generation mobile networks, apply pressure to improve data speeds. Electroabsorption modulated lasers (EMLs), comprising monolithically integrated distributed feedback lasers (DFBs) and electroabsorption modulators (EAMs) fabricated on InP, are widely used in these applications as they offer a highly compact and energy efficient means to modulate optical signals at very high speeds [1], [2]. Future EML developments to try and operate at even higher bit rates and baud rates face a challenge in that this may push EAM designs to shorter lengths to reduce capacitance at the cost of the extinction ratio (ER). An interferometric version of the EML has been proposed [3] and demonstrated to reduce EML power consumption, potentially allowing higher speed modulation [4]. This initial demonstration had an asymmetric Mach-Zehnder (MZ) interferometer comprising an EAM in the arm that had most light directed along it and a DC phase shifter on the other arm so that destructive interference could enhance the extinction afforded by the EAM. In this work, we simulate an interferometric EML (i-EML) with two potential improvements. Firstly, the interferometer utilises light from both ends of the DFB laser to reduce the number of multimode interference couplers (MMIs) needed [5]. Secondly - as in [3] - we consider a design with EAMs in both arms of the interferometer that are driven in antiphase with one another to minimise the destructive interference in the on-state, thereby improving the output ER and optical modulation amplitude (OMA).

II. DESIGN AND THEORY

A schematic of the i-EML layout is illustrated in Fig. 1. The key components of the i-EML are: a DFB with a quarter wavelength phase shift - designed for high single-mode yield,

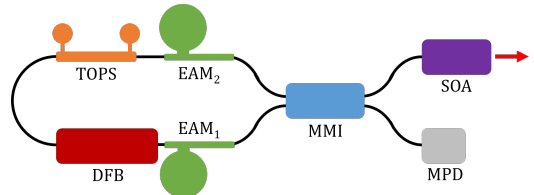


Fig. 1: Schematic layout of the i-EML. Optical output of the device is indicated by red arrow.

giving equal output powers at each end – two EAMs, a thermo-optic phase shifter (TOPS), a 2x2 MMI, a monitor photodiode (MPD), and a semiconductor optical amplifier (SOA). Both EAMs are identical, with a voltage dependent transmission and phase; in the simulations, we utilise a lookup table based on experimentally measured optical loss versus bias voltage data from a previously fabricated and tested EAM, taken at low optical power to minimise thermal effects. Similarly, a lookup table for measured chirp versus bias voltage is used to calculate the phase shifts accompanying the intensity modulation. The transmissions through the two EAMs is controlled by their respective DC bias voltages, V_{DC1} and V_{DC2} , and a common peak-to-peak modulating voltage, V_{pp} . The light that passes through the TOPS acquires an additional phase shift, ϕ_{TOPS} , which can be adjusted by varying the voltage over the TOPS. The power entering the SOA, P , can be calculated according to

$$P = P_0 \left\{ (1-k)T_1 + kT_2 + 2\sqrt{k(1-k)T_1T_2} \cos(\phi_1 - \phi_2 - \phi_{TOPS}) \right\}, \quad (1)$$

where P_0 is the power leaving each end of the DFB, k is the MMI split ratio, T_1 and T_2 are the voltage dependent transmissions of each EAM, and ϕ_1 and ϕ_2 are the voltage dependent phase shifts of each EAM.

The key principal in enhancing the ER with this device is to create destructive interference in the off-state by tuning ϕ_{TOPS} ; this effect can be further enhanced by modulating one EAM with the data-bar of the other – this affords us the desired destructive interference in the off-state whilst minimising it in the on-state. The phase shifts accompanying the intensity modulation in each EAM can also help by simultaneously

minimising and maximising the destructive interference in the on- and off-state.

III. RESULTS

An analytical model is developed in Python to map and explore key figures of merit (FOMs), namely ER, OMA, and optical crossing percentage (CP), which can be calculated efficiently by sweeping multiple parameters in a nested loop; insights from this exploratory phase help us to understand the behaviour of the i-EML and devise methods to optimise its performance. The key parameters we explore in this work are V_{DC1} , ϕ_{TOPS} , and k , and EAM length, L , with $P_0=10\text{mW}$, $V_{pp}=1\text{V}$, and $V_{DC2} = V_{DC1}$. The ER, OMA, and CP are calculated as functions of V_{DC1} and ϕ_{TOPS} using Eq. 1; these FOMs - with combinations of fixed k and L - are overlaid in Fig. 2. Notably, Fig. 2 shows that only a small value of k is

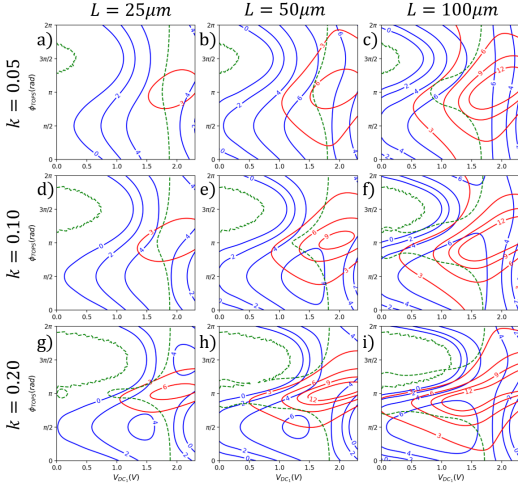


Fig. 2: Contour plots of ER (dB) (red, solid) and OMA (dBm) (blue, solid) as functions of V_{DC1} and ϕ_{TOPS} for $k=0.05$, $k=0.10$ and $k=0.20$ (rows top to bottom respectively) and $L=25\mu\text{m}$, $L=50\mu\text{m}$ and $L=100\mu\text{m}$ (columns left to right respectively). The CP=50% contour is indicated by the green dashed lines.

required to create a strong enough interference to achieve high ER, e.g. with $L=50\mu\text{m}$, one can access $\text{ER}>6\text{dB}$, $\text{ER}>9\text{dB}$ and $\text{ER}>12\text{dB}$ with $k=0.05$, $k=0.10$ and $k=0.20$ respectively (ignoring CP). However, as k is increased, regions of high ER, high OMA and CP \sim 50% begin to separate.

To more clearly understand how ER and OMA behave as we vary k and L , we benchmark the performance of the i-EML against an EML – comprising a single EAM and identical DFB, and equivalent to the i-EML with $k=0$ – in Fig. 3. At each value of k , the value of V_{DC1} and ϕ_{TOPS} are selected such that ER is maximised whilst CP = $50 \pm 1\%$. Fig. 3 shows that the optimal value of k to maximise ER is lower for longer EAM lengths; in shorter EAMs, the off-state power is higher relative to the on-state power, so a larger intensity of light

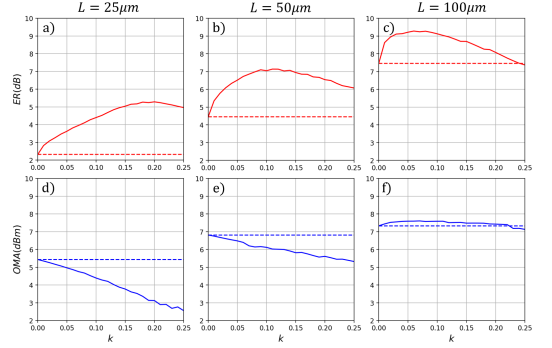


Fig. 3: ER (red, solid) and OMA (blue, solid) of the i-EML with optimised setup conditions (V_{DC1} and ϕ_{TOPS}) as a function of k , with $L=25\mu\text{m}$ (a, d), $L=50\mu\text{m}$ (b, e), and $L=100\mu\text{m}$ (c, f). These results are benchmarked against the ER (red, dashed) and OMA (blue, dashed) of conventional EMLs with the same EAM length and DFB design, equivalent to the i-EML with $k=0$.

from the second EAM is required to create the destructive interference. In addition, the ER enhancement of the i-EML compared to the conventional EML becomes more pronounced at shorter EAM lengths – albeit at the cost of OMA – an important result as we consider shorter EAMs for ultrafast modulation speeds. These calculated OMA values are before the SOA, which in practice would boost the output OMA.

IV. CONCLUSION

We have presented a theoretical overview of a novel transmitter design, wherein high ER and good OMA can be simultaneously achieved with an interferometric configuration of two EAMs driven in antiphase of one another. This approach predicts improved performance for EAM lengths that are shorter than typically used, which could enable higher-speed operation thanks to their reduced capacitance. These results suggest that a highly asymmetric MMI design is an attractive solution to achieve such high performance, whilst maintaining good eye quality. We hope that further exploration of devices like these will pave the way towards ever-higher transmitter speeds.

REFERENCES

- [1] A. Uchiyama et al., “Demonstration of 155-Gbaud PAM4 and PAM6 Using a Narrow High-Mesa Electro-Absorption Modulator Integrated Laser for 400 Gb/s Per Lane Transmission,” *J. Lightwave Technol.* 43, 1868-1873 (2025)
- [2] X. Chen et al., “540Gbps IMDD Transmission over 30km SMF using 110GHz Bandwidth InP EML,” *Proc. OFC, Th4B.2*, 2025.
- [3] I. Kang, “Phase-shift-keying and on-off-keying with improved performances using electroabsorption modulators with interferometric effects,” *Optics Express*, Vol. 15, No. 4, pp. 1467-1473, 2007.
- [4] Y. Ueda et al., “Low Driving Voltage Operation of MZI-Type EA Modulator Integrated With DFB Laser Using Optical Absorption and Interferometric Extinction,” in *IEEE Journal of Selected Topics in Quantum Electronics*, vol. 21, no. 6, pp. 195-200, Nov.-Dec. 2015.
- [5] D. Moodie, “Interferometric enhancement of an electroabsorptive modulated laser,” *EUROPEAN PATENT EP3903146B1*, Application date 2019-04-30.

Development of 2D carrier transport model for random dopant effect and exciton coupling model

Min-Hsuan Chang
Graduate Institute of Photonics and
Optoelectronics
National Taiwan University
Taipei, Taiwan
min1262070252@gmail.com

Li-An Huang
Graduate Institute of Photonics and
Optoelectronics
National Taiwan University
Taipei, Taiwan
andy900105@gmail.com

Yuh-Renn Wu
Graduate Institute of Photonics and
Optoelectronics
National Taiwan University
Taipei, Taiwan
yrwu@ntu.edu.tw

Abstract—A novel 2D simulation solver for doped OLEDs, incorporating a random doping model, overcomes 1D constraints. Validated experimentally, it shows low doping creates current-limiting traps (via deeper guest levels) rather than altering mobility. The model pinpoints EML/ETL recombination and identifies host triplet-triplet annihilation and guest hole-polaron quenching as key losses at high currents, offering routes for OLED optimization.

Keywords—OLED, 2D random dopant model, Carrier Transport, Exciton Diffusion, Efficiency Optimization

I. INTRODUCTION

Organic optoelectronic materials are foundational to modern display, lighting, and communication technologies. However, a persistent challenge limiting their emission efficiency is exciton spin statistics. In conventional closed-shell materials, electrical excitation predominantly generates non-emissive triplet excitons (75%) over emissive singlet excitons (25%), as only the latter undergo spin-allowed radiative decay [1]. While thermally activated delayed fluorescence (TADF) and phosphorescent materials offer pathways to harness triplet excitons, they often contend with issues like long exciton lifetimes, significant efficiency roll-off, and complex fabrication [1, 2].

An innovative approach involves open-shell radical materials, which feature doublet ground and excited states. This configuration permits rapid, spin-allowed radiative decay via $D_1 \rightarrow D_0$ transitions [2]. Crucially, recent advancements have demonstrated that in well-designed host-guest systems, triplet excitons generated in the host can be efficiently converted to doublet excitons in the radical emitter through a process known as triplet-to-doublet energy transfer [3-7]. This mechanism effectively bypasses the spin blockade.

The process itself can involve distinct energy transfer pathways: Förster resonance energy transfer (FRET), typically mediating $S_1 \rightarrow D_1$ transitions and dependent on spectral overlap and dipole-dipole coupling, and Dexter energy transfer, facilitating $T_1 \rightarrow D_1$ transitions through direct orbital overlap and energy level alignment [3, 4]. Since the $D_1 \rightarrow D_0$ decay in doublet excitons is spin-allowed, the circumvents the need for intersystem crossing (ISC) or reverse ISC (RISC). Combined with the nanosecond-scale lifetimes of radical excitons, this leads to significantly faster emission kinetics than traditional TADF materials [5, 6, 8], making the luminescence mechanism highly attractive for applications demanding rapid responses, such as optical communication [4, 7].

Detailed kinetic modeling of these exciton transitions is essential to fully understand and optimize the efficiency of

these systems and elucidate the dominant pathways and rate-limiting steps. This study will present a comprehensive model to simulate these dynamic processes.

II. METHODOLOGY

A: Carrier transport:

Our laboratory developed a finite element method to solve the 2D Poisson and drift-diffusion equations at steady state, a widely used approach for modeling the electrical characteristics of organic light-emitting diodes (OLEDs). In this study, we combine the Poisson-drift-diffusion equations with a Gaussian density of states (DOS) model and Poole-Frenkel field-dependent mobility to simulate carrier transport in OLED host-guest systems, incorporating the effects of random doping. To address the influences of doping effect, a 2D random doping model is used [9]. In this approach, the doping region is divided into small grid units to represent the positions of molecules. The Gaussian weighting method is used to determine it dopant concentration.

A: Exciton diffusion and energy transfer model for singlets, triplets, and doublets:

When electrons and holes recombine, they form excitons, which can then diffuse and decay within the material. In this study, the emission mainly relies on the conversion of triplets to doublets, with triplet excitons making up 75% of exciton generation. The exciton dynamics are modeled by the following diffusion equation:

$$\frac{dS}{dt} = D^S \nabla^2 S - (k_r^S + k_{nr}^S + k_e^S n + k_h^S p + k_{ISC} + k_{FRET})S - k_{RISC}T + \alpha G_S \quad (1)$$

$$\frac{dT}{dt} = D^T \nabla^2 T - (k_r^T + k_{nr}^T + k_e^T n + k_h^T p + k_{RISC} + k_{DET})T - k_{TT}T^2 + k_{ISC}S + \beta G_T \quad (2)$$

$$\begin{aligned} \frac{dD}{dt} = D^D \nabla^2 D - (k_r^D + k_{nr}^D + k_e^D n + k_h^D p)D - k_{DD}D^2 \\ + k_{FRET}S + k_{DET}T \\ + (1 - \alpha - \beta) G_D \end{aligned} \quad (3)$$

Here, S, T and D represents singlet, triplet and doublet exciton density, D is the exciton diffusion coefficient, and γ is the exciton annihilation coefficient. α and β are the generation fraction coefficients of excitons. The term G corresponds to the initial distribution of exciton density. Additionally, n and p refer to the densities of electron and hole carriers, respectively.

III. RESULT AND DISSUSSION

To validate the accuracy of the proposed model, OLED devices, as well as electron-only (EOD) and hole-only (HOD) devices with a 3% doping concentration, were fabricated by

Prof. Cho. The devices utilized CzDBA as the host material and TPA-PyBTM³ as the guest material. The experimental results demonstrate that at low doping concentrations, the guest molecules introduce trap states that hinder carrier transport, reducing current density. This observation is consistent with the simulated result presented in Fig. 1(a–c). The decrease in current density is primarily attributed to the formation of deeper energy states by the guest material rather than a direct change in charge carrier mobility.

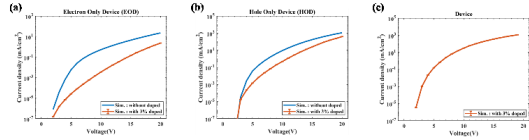


Fig. 1. (a), (b), and (c) are EOD, HOD and OLED, respectively, along with the J-V curves for different cases with 3% dopant concentration.

Figures. 2(a) and 2(b), show that the current density decreases as the doping concentration increases from 0% to 3%. In contrast, when the doping concentration exceeds 3%, the current density begins to increase. This trend can be attributed to the energy gap between the LUMO or HOMO levels of the host and guest materials, which affects carrier injection and transport efficiency.

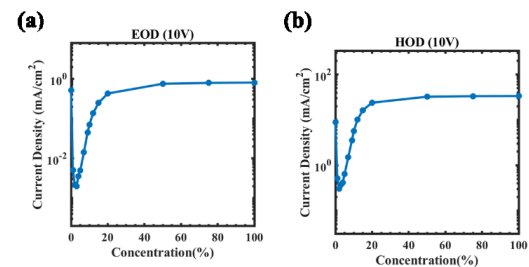


Fig. 2. (a-d) The current density under voltages of 5V and 10V for electron-only and hole-only devices.

Owing to the low dopant concentrations, the guest material becomes isolated. As a result, carriers passing through these localized guest states are more likely to become trapped. This behavior is clearly illustrated in Fig. 3(b) and 3(c), where clusters of high carrier density indicate the presence of trap sites. Such trapping impacts the charge balance and recombination efficiency within the device.

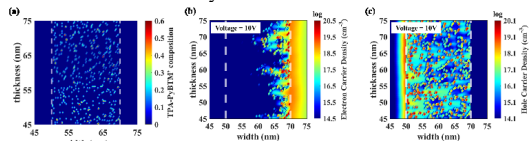


Fig. 3. (a) The composition of the EML with random doping. (b) and (c) are electron and hole carrier density distribution at 10 V.

Fig. 4(a) and (b) illustrate the two-dimensional distribution of the radiative recombination region under different applied voltages, providing an initial indication of exciton generation locations. As the voltage increases from 5 V to 10 V, a clear trend is observed: the recombination region becomes more concentrated and is primarily located at the interface between the emission layer (EML) and the electron transport layer (ETL).

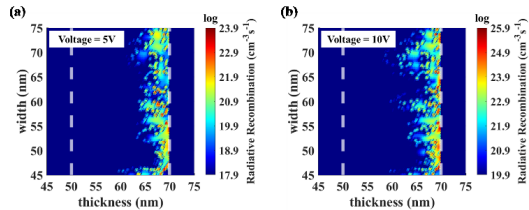


Fig. 4. (a) and (b) are radiative recombination at 5.0 V and 10.0 V, respectively.

To gain deeper insight into the spatial dynamics of exciton behavior under high-bias conditions, the exciton concentration and various loss processes were mapped at 10 V, as shown in Fig. 5, which further highlights the diffusion of excitons from the host to the guest material, where energy transfer plays a crucial role in determining emission efficiency. The loss mechanism in this system is relatively complicated, as it is decided by doublet and triplet exciton carrier quench mechanism. The details will be discussed at this conference presentation.

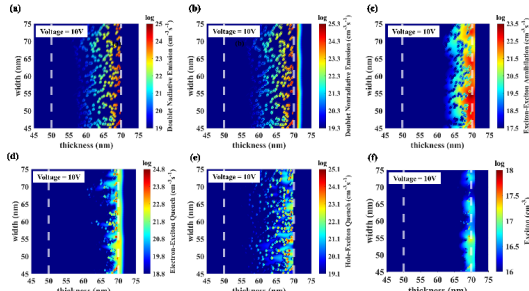


Fig. 5. (a-f) Two-dimensional distributions of exciton density, radiative emission, nonradiative emission, annihilation, electron quenching, and hole quenching at 10.0 V.

REFERENCES

- [1] S. Gao, Z. Cui, and F. Li, "Doublet-emissive materials for organic light-emitting diodes: exciton formation and emission processes," *Chemical Society Reviews*, vol. 52, no. 9, pp. 2875-2885, 2023.
- [2] X. Ai *et al.*, "Efficient radical-based light-emitting diodes with doublet emission," *Nature*, vol. 563, no. 7732, pp. 536-540, 2018.
- [3] J. M. Hudson, T. J. Hele, and E. W. Evans, "Efficient light-emitting diodes from organic radicals with doublet emission," *Journal of Applied Physics*, vol. 129, no. 18, 2021.
- [4] Q. Gu, S. Gorgon, A. S. Romanov, F. Li, R. H. Friend, and E. W. Evans, "Fast transfer of triplet to doublet excitons from organometallic host to organic radical semiconductors," *Advanced Materials*, vol. 36, no. 30, p. 2402790, 2024.
- [5] E. W. Evans *et al.*, "Singlet and triplet to doublet energy transfer: improving organic light-emitting diodes with radicals," *arXiv preprint arXiv:2109.13522*, 2021.
- [6] F. Li *et al.*, "Singlet and triplet to doublet energy transfer: improving organic light-emitting diodes with radicals," *Nature Communications*, vol. 13, no. 1, p. 2744, 2022.
- [7] Q. Gu, S. Gorgon, A. S. Romanov, F. Li, R. H. Friend, and E. W. Evans, "Spin control with triplet and doublet excitons in organic semiconductors," *arXiv preprint arXiv:2312.10595*, 2023.
- [8] A. Abdurahman *et al.*, "Understanding the luminescent nature of organic radicals for efficient doublet emitters and pure-red light-emitting diodes," *Nature materials*, vol. 19, no. 11, pp. 1224-1229, 2020.
- [9] Huang, Jun-Yu, *et al.*, "Revealing the mechanism of carrier transport in host-guest systems of organic materials with a modified Poisson and drift-diffusion solver," *Physical Review Materials* 4.12.125602, 2020.

Machine learning enhanced design optimization and knowledge discovery for multi-junction photonic power converters

Karin Hinzer
SUNLAB
University of Ottawa
Ottawa, Canada
khinzer@uottawa.ca

Robert F. H. Hunter
SUNLAB
University of Ottawa
Ottawa, Canada

Gavin P. Forcade
SUNLAB
University of Ottawa
Ottawa, Canada

Yuri Grinberg
Digital Technologies Research Centre
National Research Council Canada
Ottawa, Canada

D. Paige Wilson
SUNLAB
University of Ottawa
Ottawa, Canada

Meghan N. Beattie
SUNLAB
University of Ottawa
Ottawa, Canada

Christopher E. Valdivia
SUNLAB
University of Ottawa
Ottawa, Canada

Mathieu de Lafontaine
SUNLAB
University of Ottawa
Ottawa, Canada

Louis-Philippe St-Arnaud
SUNLAB
University of Ottawa
Ottawa, Canada

Oliver Höhn
Fraunhofer Institute for Solar Energy
Systems
Freiburg, Germany

David Lackner
Fraunhofer Institute for Solar Energy
Systems
Freiburg, Germany

Carmine Pellegrino
Fraunhofer Institute for Solar Energy
Systems
Freiburg, Germany

Jacob J. Krich
SUNLAB
University of Ottawa
Ottawa, Canada

Alexandre Walker
Quantum and Nanotechnologies
Research Centre
National Research Council Canada
Ottawa, Canada

Henning Helmers
Fraunhofer Institute for Solar Energy
Systems
Freiburg, Germany

Abstract—We compare some classical and machine-learning enhanced design optimization methodologies. We investigate the design of the complex structures of ten-junction InP lattice-matched photonic power converters with $\text{In}_{0.53}\text{Ga}_{0.47}\text{As}$ absorbers optimized for operation at 1550 nm with $53.6\% \pm 1.3\%$ conversion efficiency. We find that the implicit pattern recognition capabilities of dimensionality reduction using principal component analysis accelerates design discovery, optimization, and the understanding of complex optical phenomena in the simulated devices.

Keywords—machine learning, dimensionality reduction, design discovery, optimization acceleration, knowledge discovery, multi-junction photonic power converters

I. INTRODUCTION

Free-space and fiber-based optical links with photonic power converter (PPC) receiver elements offer the potential for fast, flexible, high-fidelity data and power transmission. We target novel high-efficiency ($\geq 50\%$) and high output voltage (≥ 5 V) 10-junction PPCs using InGaAs absorbers lattice-matched to InP for operation in the 1550 nm telecommunications C-band. The design landscape of these devices is high-dimensional and highly correlated. We leverage the pattern recognition capabilities of dimensionality reduction and machine learning algorithms, alongside classical optimization, to efficiently explore the design space of our PPCs. The wider survey that the machine-learning enhanced methods allow empowers a more informed design choice, where growth considerations and other criteria help select from the multiple high-performance designs that may

exist. We calibrate our device model with fabricated devices. We study the role of luminescent coupling in device performance. And, we investigate the potential for our machine learning enhanced methodology to expand the design perspective and supplement understanding of the design space for on-substrate multi-junction PPCs and those employing flat back-reflectors [1-4].

II. RESULTS AND DISCUSSION

We designed and grew lattice matched 1-junction photovoltaic (PV) samples by metalorganic vapor phase epitaxy on p-InP substrates at Fraunhofer ISE. For testing purposes thin absorbers of different thickness were grown and fabricated: 60, 180, and 540 nm. The absorber layer is sandwiched between higher bandgap front surface field (FSF) and back surface field (BSF) layers. We developed an optoelectronic model to simulate the PV devices using a drift-diffusion model in Synopsys Sentaurus TCAD software. Our 1-dimensional model treats the devices as laterally infinite layered structures.

The root-mean-square difference between measured & simulated EQE is within 1%, which supports our method of extracting the extinction coefficient for InGaAs. These 1-junction devices converted 1540 nm laser light with 2.66 W/cm² input power into electrical power at 2%, 5%, and 14% efficiency, for the 60 nm, 180 nm, and 540 nm devices, respectively. Using optimization techniques, we predict a maximum efficiency of 46% for an absorber layer thickness of 4380 nm and input power of 2.56 W/cm². We fabricated 2- & 10-junction devices, which consist of InGaAs cells

connected in series with transparent tunnel diodes. We measured fabricated 10-junction InGaAs photonic power under 1.52 μm laser illumination at room temperature and observed a maximum efficiency of $46.4 \pm 1.6\%$ with an output power density of 16 W/cm^2 , a voltage output at maximum power of 5.01 V, and an open circuit voltage of 5.78 V. We will show fitting results of our model to these multi-junction devices, which include a detailed model of luminescent coupling between subcells & 10-junction optimization results.

We quantify the impact of luminescent coupling on device performance by calculating the coupling between each emission and absorption event using a transfer matrix method. For a test 2-junction structure, up to 85% of the emission events in the InGaAs absorber layers are re-absorbed within the device. This number increases to 96% when a planar back-reflector is included due to improved light management.

To further improve device efficiency using back reflectors, we have developed a computational framework employing Python and standard libraries to explore optoelectronic device design using machine learning. For our analysis, we apply principal component analysis as a dimensionality reduction technique. Dimensionality reduction enhanced optimization uses an optical model based on rigorous coupled wave analysis to produce current-matched subcells. Full efficiencies are determined by coupling to a drift-diffusion solver, with luminescent coupling. Fig. 1 illustrates the principal computational steps.

We find that for on-substrate 10-junction PPC devices, the absorber thicknesses converge to a unique optimum, which varies slightly ($\leq 5\%$) but systematically from Beer-Lambert expectations. For 10-junction devices with a flat Au back-reflector, the design space is richer, with a continuous subspace of similar performance optima with total absorber thicknesses varying by up to 25%. The optimization figure of merit (FOM) is defined as

$$\text{Photocurrent FOM} = \frac{\text{device photocurrent [\#e]}}{\text{incident photons per subcell [\#y]}} \quad (1)$$

The optical generation current in number of electrons is divided by one-tenth of the input power, in number of photons,

as it is shared over the 10 subcells or segments of the device. The maximum value is 1. Optimized results display photocurrent FOM above 0.9925.

ACKNOWLEDGMENT

Funding provided by: Government of Canada's AI for Design National Research Council Collaborative Science, Technology, and Innovation Program under Grant INT-014-1. Government of Canada's National Research Council under Grant HSTN-645. National Sciences and Engineering Research Council of Canada Discovery Research Program under Grant RGPIN-2022-03877. National Sciences and Engineering Research Council of Canada under Grant 497981. The Canadian Foundation for Innovation. The Government of Ontario. The German Federal Ministry of Research, Technology and Space under Grant 01DM21006A. ERC grant PHASE (No. 101125948).

We acknowledge Dr. Daniel Poitras of the National Research Council of Canada for his help in generating the anti-reflection coating designs with simpler underlying epitaxial stacks. We also acknowledge CMC Microsystems for the provision of products and services that facilitated this research, including Synopsys Sentaurus TCAD.

REFERENCES

- [1] R.F.H. Hunter, G.P. Forcade, Y. Grinberg, D.P. Wilson, M.N. Beattie, C.E. Valdivia, M. de Lafontaine, L.P. St-Arnaud, H. Helmers, O. Hohn, D. Lackner, C. Pellegrino, J.J. Krich, A.W. Walker, and K. Hinzer, "Machine learning enhanced design and knowledge discovery for multi-junction photonic power converters", Scientific Reports, under review.
- [2] G. P. Forcade, D. P. Wilson, M. N. Beattie, C. Pellegrino, H. Helmers, R. F. H. Hunter, O. Höhn, D. Lackner, L. P. St-Arnaud, T. N. D. Tibbitts, D. Poitras, C. E. Valdivia, Y. Grinberg, A. W. Walker, J. J. Krich, and K. Hinzer, "Multi-junction laser power converters exceeding 50% efficiency in the short wavelength infrared", Cell Rep. Phys. Sci, 6, 102610 (2025). DOI: [10.1016/j.xcrp.2025.102610](https://doi.org/10.1016/j.xcrp.2025.102610)
- [3] M. M. Wilkins, C. E. Valdivia, A. M. Gabr, D. Masson, S. Fafard, and K. Hinzer, "Luminescent coupling in planar opto-electronic devices", J. Appl. Phys. 118, 143102 (2015). DOI: [10.1063/1.4932660](https://doi.org/10.1063/1.4932660)
- [4] N. Nouri, C. E. Valdivia, M. N. Beattie, J. J. Krich, and K. Hinzer, "Light management in ultra-thin photonic power converters for 1310 nm laser illumination", Optics Express 30 (13) (2022). DOI: [10.1364/OE.459680](https://doi.org/10.1364/OE.459680)

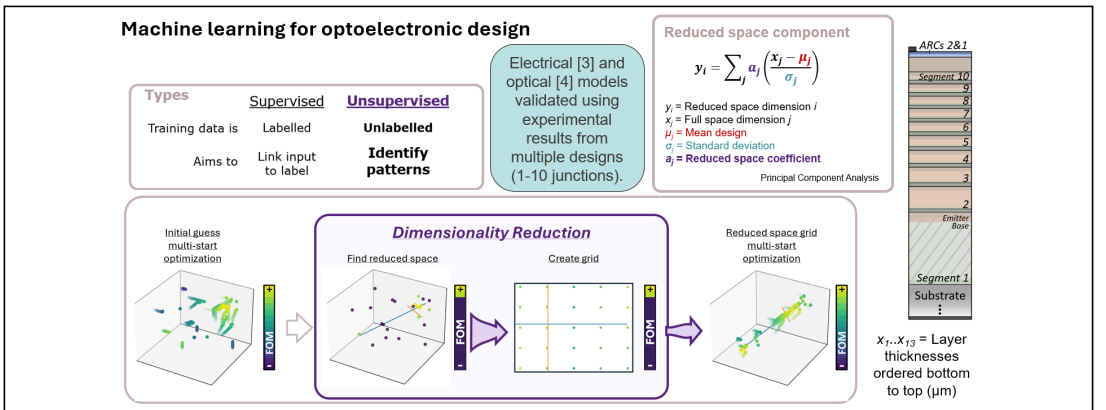


Fig. 1. Top: Results presented are generated using unsupervised machine learning with principal component analysis. Simplified schematic of the modeled on-substrate photonic power converter devices. Bottom: Simplified design flow for the machine learning enhanced design optimization. Step 1; classical multi-start optimization. Step 2; top designs from step 1 according to a chosen figure of merit (FOM) are used to train a dimensionality reduction algorithm and generate a reduced dimension subspace. Step 3; the reduced dimensional subspace is used to generate start points. Step 4; extension of the method, classical multi-start optimization from the step 3 grid points to mitigate information loss during steps 2 and 3.

Degradation Lifetime Modeling for Perovskite Photovoltaic Modules

Matthias Auf der Maur
University of Rome Tor Vergata
Rome, Italy
auf.der.maur@ing.uniroma2.it

Peyman Amiri
University of Rome Tor Vergata
Rome, Italy
peyman.amiri@uniroma2.it

Abstract—We describe a workflow for the lifetime simulation of Perovskite solar modules, that combines modeling of water ingress and of the resulting local effects due to humidity with simulation of the cell stack, possibly including other degradation channels like defect formation, and with a lumped element SPICE model of the solar module. Such a model would allow to predict module performance throughout module lifetime. Here we present in particular an initial implementation of water ingress simulation linked to the lumped element module model.

Index Terms—Photovoltaics, Perovskite, solar module, water ingress, simulation

I. INTRODUCTION

Since their first appearance, metal halide Perovskite based solar cells have by now reached record efficiencies of 26.95% for single junctions and 34.6% for Perovskite/Silicon tandems [1]. One of the main issues impeding large scale deployment and thus still to be resolved is related to long-term stability of Perovskite-based cells. Although progress has been made, device stability and degradation is an active area of research. Presence of moisture is known to be of major importance in Perovskite material degradation [2], [3]. Therefore, proper encapsulation of Perovskite modules is a critical step in slowing down ingress of moisture into the active material. In addition, carrier-injection induced formation of point defects can be an issue in halide Perovskites [4], which could result in reversible or irreversible and possibly mobile ionic defects, inducing additional time-dependent performance variation.

II. PROPOSED SIMULATION MODEL

We propose a composite model linking the following three submodels, illustrated in Fig. 1. The first model describes water ingress into the module, based on Fick's law, driven by the water vapour pressure in the atmosphere surrounding the module [5]. The problem is described by the parabolic partial differential equation

$$\frac{\partial Sp}{\partial t} = \nabla \cdot (D \nabla Sp) \text{ on } \Omega, \quad p = Sp_0 \text{ on } \partial\Omega, \quad (1)$$

where p is the water vapour partial pressure, S is the solubility, D is the diffusivity, and Ω is the simulation domain including the encapsulation. The water concentration is given by $c = Sp$. We assume the module to be encapsulated between two

This work was supported by the Horizon Europe research and innovation programme under grant agreement No 101084422 “SUNREY”.

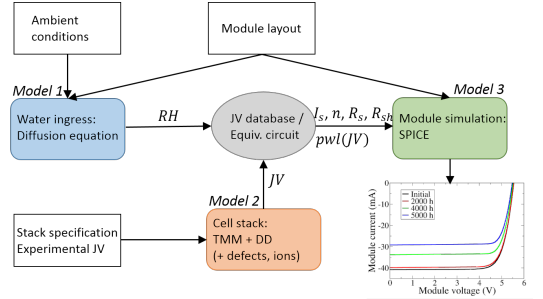


Fig. 1. Simplified scheme of the modeling approach, highlighting the three linked simulation models and their connections.

glass sheets, so that a 2D approximation with lateral ingress is justified.

The second model describes the cell stack, and provides locally the current-voltage characteristic in a 1D approximation. Here, a drift-diffusion model could be used to create a dataset of device characteristics under different operating conditions (degradation state, illumination, defect formation, etc.), in order to form a parameterized dataset for the third model. At this stage, fitting to experimental data on degraded research cells could be useful.

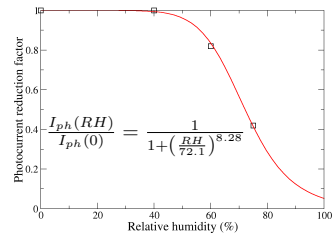


Fig. 2. Reduction factor for short circuit current, fitted to the data (symbols) extracted from [3].

The third model uses an electronic circuit approximation of the module in terms of concentrated elements, using SPICE to solve the circuit model [6]. The 2D module layout is discretized into finite patches, and to each patch an elementary

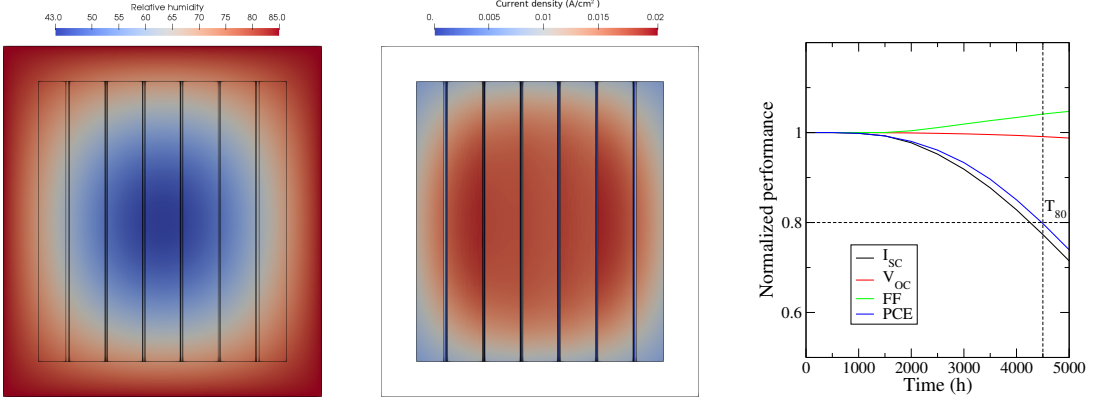


Fig. 3. Relative humidity in the module (left), and local current density across the elementary cells (middle), after 4500 h in 85% humidity and room temperature. On the right the time evolution of the normalized module performance parameters. The fill factor (FF) increases slightly, because the model used here only results in a reduction of the short circuit current, while open circuit voltage (V_{OC}) remains almost unchanged. At $T_{80} \approx 4500$ h, the PCE reaches 80% of its initial value.

cell stack is assigned, while different cells are connected on the top and bottom layers via lumped resistors, obtained from the contact layer sheet resistivities. The elementary cell can be described via its numeric JV characteristic, using a piecewise-linear voltage controlled source (pwl), or via an equivalent circuit. In both cases, the data from the cell stack model can be used to obtain a SPICE model parameterized in terms of relevant quantities such as relative humidity, temperature, light intensity etc. The connecting resistors are obtained from a 2D finite element or finite volume discretization of a steady-state diffusion equation. The implementation allows thus for unstructured discretizations of the module geometry, increasing versatility. All models are implemented in tibercad software [7], while for the SPICE engine we used ngspice [8]

III. PRELIMINARY RESULTS

We have performed a preliminary simulation of a 10.96 cm^2 minimodule with five $4 \times 0.5 \text{ cm}^2$ subcells in series, assuming an additional 5 mm lateral sealing. For the water ingress simulation we used parameters of EVA, i.e. diffusivity $D = 3.43 \times 10^{-11} \text{ m}^2/\text{s}$ and solubility $S = 0.45 \text{ g/m}^3\text{Pa}$ [5]. For sake of simplicity, we did not consider water diffusion in the perovskite itself, leading to an overestimation of the lifetime. Data on reduction of absorption in a Perovskite cell as a function of relative humidity has been taken from [3], and fitted to a humidity-dependent model of the short circuit current density as shown in Fig. 2. A measured JV characteristic of a research cell has been used to fit a one-diode equivalent circuit, that has been used as elementary cell for the SPICE model. For the water ingress simulation, we assumed a boundary condition of 85% relative humidity at 300 K. The water diffusion model has then been solved until 5000 h, and every 500 h the module model has been solved, using the relative humidity in every cell to modify the I_{SC} .

Figure 3 shows the spatial distribution of relative humidity in the module after 4500 h, the resulting vertical current density through the elementary cells, and the time evolution of the module performance. For the used parameters and geometry, a T_{80} of approx. 4500 h is obtained.

The initial implementation presented here will be further extended. In particular, the elementary cell equivalent circuit will be generalized to 2- and 3-diode models, and an alternative definition of the elementary cell patches based on the primal mesh elements will be implemented. Also, the model needs to be tested under realistic conditions.

REFERENCES

- [1] National Renewable Energy Laboratory, “Best research-cell efficiency chart,” <https://www.nrel.gov/pv/cell-efficiency.html>, 2025, accessed: 2025-05-30.
- [2] J. Huang, S. Tan, P. D. Lund, and H. Zhou, “Impact of H_2O on organic-inorganic hybrid perovskite solar cells,” *Energy & Environmental Science*, vol. 10, no. 11, pp. 2284–2311, 2017.
- [3] P. Bhatt, M. Kumar, P. Chandra Kant, M. K. Pandey, and B. Tripathi, “Optoelectronic modelling of perovskite solar cells under humid conditions and their correlation with power losses to quantify material degradation,” *Organic Electronics*, vol. 39, pp. 258–266, 2016.
- [4] F. P. Sabino, G. M. Dalpian, and A. Zunger, “Light-induced frenkel defect pair formation can lead to phase-segregation of otherwise miscible halide perovskite alloys,” *Advanced Energy Materials*, vol. 13, no. 44, p. 2301539, 2023.
- [5] A. Dadaniya and N. V. Datla, “Water diffusion simulation in photovoltaic module based on the characterization of encapsulant material using in-situ gravimetric technique,” *Solar Energy Materials and Solar Cells*, vol. 201, p. 110063, 2019.
- [6] D. Giaffreda, M. Debucquoy, P. Magnone, N. Posthuma, and C. Fiegna, “A distributed electrical model for interdigitated back contact silicon solar cells,” *Energy Procedia*, vol. 55, pp. 71–76, 2014, proceedings of the 4th International Conference on Crystalline Silicon Photovoltaics (SiliconPV 2014).
- [7] OLAB Research Group, “tibercad: Multiscale cad tool for nanoelectronic and optoelectronic devices,” <https://github.com/tiberlab/tibercad>, 2025. [Online]. Available: <https://www.tibercad.org>
- [8] H. Vogt, G. Atkinson, and P. Nenzi, *Ngspice User's Manual*, 2023, version 42. [Online]. Available: <https://ngspice.sourceforge.io/docs/ngspice-42-manual.pdf>

Optimal bandgap of GaInAsN for integration in a space four-junction photovoltaic cell

Antoine Féés

ONERA,

LAAS-CNRS

Université de Toulouse, CNRS,

Toulouse, France

antoine.fees@onera.fr

Julien Mekki

Centre National d'Etudes Spatiales

Toulouse, France

julien.mekki@cnes.fr

Thierry Nuns

ONERA

Toulouse, France

thierry.nuns@onera.fr

Guilhem Almuneau

LAAS-CNRS,

Université de Toulouse, CNRS,

Toulouse, France

guilhem.almuneau@laas.fr

Abstract—We use Poisson-Drift-Diffusion simulations to optimize a dilute nitride subcell architecture for an integration in a monolithic lattice-matched 4-junction multijunction solar cell under 1-sun AM0 spectrum. We explore a way to systematically explore how a variation of the subcell bandgap changes the power conversion efficiency of the whole multijunction cell. We first compare our Poisson-Drift-Diffusion results to approximate analytical solutions. Then, we compute the dilute nitride material bandgap-dependent absorption coefficients used as input values for the device simulation. We finally derive the evolution of the multijunction cell power conversion efficiency with regards to the dilute nitride subcell bandgap.

Index Terms—dilute nitride, photovoltaic, multijunction

I. INTRODUCTION AND OBJECTIVES

GaInAsN alloys are particularly interesting for spatial lattice-matched multi-junction solar cells (MJSCs) [1]. Owing to the alloy nature of this compound, one can select independently the bandgap of $\text{GaIn}_x\text{AsN}_y$, predicted by the band-anticrossing (BAC) framework [2], and its lattice constant, predicted by the ratio x/y . It allows to increase the number of junctions from 3 to 4 (GaInP_2 - GaAs - GaInAsN - Ge) while choosing the added subcell bandgap to perfectly match Shockley-Queisser's efficiency optimum and keeping the structure lattice-matched to GaAs. The ideal bandgap of GaInAsN subcells in a 4-junction architecture next to GaInP_2 , GaAs and Ge has been predicted to be 1eV, reaching $\approx 40\%$ power conversion efficiency (PCE) [3]. However, no four-junction solar cell made from these materials has yet reached the desired efficiency levels, due to low diffusion lengths in the dilute nitride layers. This can be circumvented by using a double-heterostructure solar (sub)cell (DHSC) architecture, but it has proven difficult to predict its optimal design, as it results in a trade-off between photogeneration and field-assisted carrier collection. As a consequence, the multi-junction cell performance and its optimal design are dependent on the dilute nitride material parameters [4], [5]. In a recent paper, we used a Poisson-Drift-Diffusion (PDD) framework on top of Transfer-Matrix-Method optics and BAC theory to compute the 4-junction cell performance under 1-sun AM0.

We showed that the 1eV absorption coefficient of [6] was insufficient to provide the necessary short-circuit-current for MJSC integration ($\approx 18 \text{ mA/cm}^2$) for realistic GaInAsN layer thicknesses and SRH lifetime [5].

In the present paper, we explore how the multi-junction cell performance depends on the bandgap of the GaInAsN layer E_g . We hypothesize that decreasing E_g would alleviate the constraints on the GaInAsN layer thickness needed for equal output short-circuit current. In turn, this could help move the optimal subcell design window towards lower minority carrier lifetimes, which are hopefully experimentally attainable. Calculating how the MJSC PCE evolves thus requires to derive the change in the GaInAsN absorption coefficient and its impact on the device main factors of merit (V_{OC} , J_{sc} , P_{MPP}). As the PDD scheme can prove too computationally expensive to allow a quick exploration of the whole parameter space, we first assess the analytical model of [4]. Indeed, such an analytical model can be extremely useful to provide first estimations before performing PDD simulations or to fit experimental data. At each GaInAsN bandgap, BAC theory provides the input absorption coefficient used by the simulation tool to compute the cell PCE. We use those results to further optimize the MJSC design under the AM0 spectrum.

II. METHODS AND PRELIMINARY RESULTS

The analytical model of [4] gives precious insights on the effect of the field on the photocollection of minority carriers in the i-GaInAsN layer. Using the same parameters for minority carriers and the same absorption coefficient than in our PDD simulation, and integrating the analytically derived QE, we compare our PDD simulations with the model. To do so, we use parametric curves of varying short-circuit currents with varying SRH lifetime, residual doping, and i-layer thickness. For example, we simulated the short-circuit currents of a n-p-p 1eV GaInAsN (with the absorption coefficient from Kurtz et al. [6]) with varying i-layer SRH lifetime, and compared it with the analytical QE integrated between 875 and 1270 nm (figure 1).

Reiterating the same work as in Fig. 1 at various residual dopings shows that, as in Wolf's original article [7], variations in the magnitude of the electric field in the QE model can

The authors thank the Défi-Clé PV-STAR (Région Occitanie) and the Centre National des Etudes Spatiales (CNES) for their financial support.

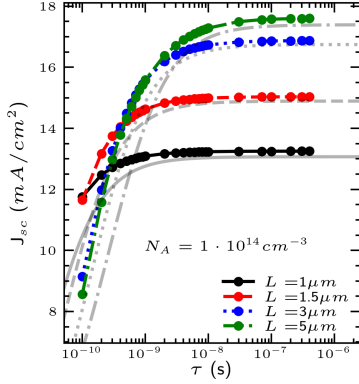


Fig. 1. Comparison of short-circuit currents obtained from PDD simulations for a n-p ($1 \times 10^{14} \text{ cm}^{-3}$)-p subcell (dotted, colored lines) with the short-circuit currents obtained from the analytical quantum efficiency model and a homogeneous electric field of $E = 0.75V/L$ (grey lines).

explain the photocollection gain as the residual doping in the intrinsic layer decreases.

We propose computing the bandgap-dependent absorption coefficient α of near-1 eV GaInAsN from a minimal set of parameters. This method is as follows:

- Compute a realistic bandstructure for the dilute nitride material,
- Calculate the joint density of states (JDOS) between each of the valence subbands and each of the conduction bands,
- Recombine all of the interband contributions to compute the final $\alpha(E)$.

Here, we try to take two different routes, either following a calculation of the fractional Γ character of the BAC model using the approach of Seifkar et al. [8], or directly constructing a Green's function with for a single N level and calculating the absorption coefficient from it, following the approach of Wu et al. [2]. The first step for computing the absorption coefficient is to construct a realistic description of the conduction and valence bands. In Seifkar's model [8], this is done by constructing and diagonalizing a 5-level $\mathbf{k} \cdot \mathbf{p}$ -like hamiltonian, and the topmost valence band is replaced with the Light-Hole (LH) and Heavy-Hole (HH) bands. In Wu's approach [2], the hamiltonian is constructed from a simple 2-level BAC approach and augmented with the LH, HH and Split-Off (SO) valence bands. The JDOS is then computed numerically, either defining a Green's function $G_{kk}(E)$ with broadening $i\Delta_N$ (Wu's approach), or using an expression of the fractional gamma character $f_\Gamma(E)$ (Seifkar's approach). The absorption coefficient is then calculated from the sum of the JDOS of all transitions between valence band i and conduction band j multiplied by their transition strength $a_{i \rightarrow j}$. We compare our predictions with the experimental values taken from the literature for near-1eV GaInAsN. For example, in Fig. 2, the absorption coefficient of n-type GaInAsN from

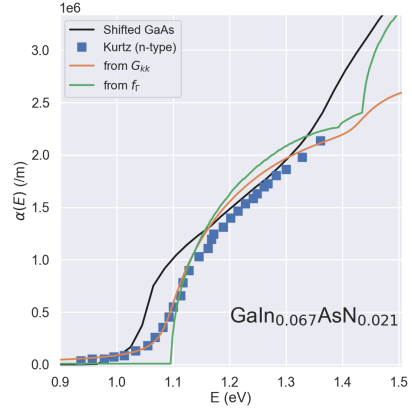


Fig. 2. Comparison of our calculations with experimental n-type 1eV GaInAsN of [6] as well as 0.315 eV red-shifted GaAs absorption coefficient.

Kurtz et al. [6] seem to be well-fitted with a bandgap slightly above 1eV (1.087 eV). Although both methods give similar results, the broadening $i\Delta_N$ in Wu's approach allows to better match near-bandgap absorption smoothness than Seifkar's approach.

Finally, we use all the ingredients of our study together to compute the efficiency maps of GaInP₂ - GaAs - GaInAsN - Ge photovoltaic cells, using the optical absorption coefficients provided by the models. This demonstrates that the absorption coefficient also has an important impact on the optimal design of the multi-junction cell, and that achieving short-circuit currents of up to 18 mA/cm² is difficult. Our preliminary results indicate that the best efficiencies computed so far are approximately 37-40 %, in accordance with [3]. However, for a given cell performance, equivalent or even superior designs can be found by decreasing both the bandgap and the thickness of the GaInAsN layer simultaneously.

REFERENCES

- [1] J. Li et al., "A brief review of high efficiency III-V solar cells for space application," *Frontiers in Physics*, vol. 8, p. 631925, 2021.
- [2] J. Wu, W. Walukiewicz, and E. Haller, "Band structure of highly mismatched semiconductor alloys: Coherent potential approximation," *Physical Review B*, vol. 65, no. 23, p. 233210, 2002.
- [3] S. R. Kurtz, D. Myers, and J. M. Olson, "Projected performance of three- and four-junction devices using GaAs and GaInP," in *Proc. of the 36th IEEE Photovoltaic Specialists Conference*, 1997, pp. 875–878.
- [4] D. Friedman, A. Ptak, S. Kurtz, and J. Geisz, "Analysis of depletion-region collection in GaInAs solar cells," in *Proc. of the 31st IEEE Photovoltaic Specialists Conference*, 2005, pp. 691–694.
- [5] A. F  es et al., "Simulation of a GaInP₂ - GaAs - GaInAsN - Ge Photovoltaic Cell for Space Applications," *IEEE Photonics Journal*, vol. 17, no. 3, pp. 1–11, 2025.
- [6] S. R. Kurtz et al., "InGaAsN solar cells with 1eV bandgap lattice matched to GaAs," *Applied Physics Letters*, vol. 74, no. 5, pp. 729–731, 1999.
- [7] M. Wolf, "Drift fields in photovoltaic solar energy converter cells," *Proceedings of the IEEE*, vol. 51, no. 5, pp. 674–693, 1963.
- [8] M. Seifkar, E. P. O'Reilly, and S. Fahy, "Optical absorption of dilute nitride alloys using self-consistent green's function method," *Nanoscale Research Letters*, vol. 9, pp. 1–11, 2014.

Tight-binding model for mixed perovskites

Alessia Di Vito

Department of Electronic Engineering
University of Rome Tor Vergata
Rome, Italy
alessia.di.vito@uniroma2.it

Anh-Luan Phan

Department of Electronic Engineering
University of Rome Tor Vergata
Rome, Italy
anh.luan.phan@uniroma2.it

Daniele Soccodato

Department of Electronic Engineering
University of Rome Tor Vergata
Rome, Italy
daniele.soccodato@uniroma2.it

Alessandro Pecchia

CNR-ISMN
Monterotondo, Italy
alessandro.pecchia@cnr.it

Matthias Auf der Maur

Department of Electronic Engineering
University of Rome Tor Vergata
Rome, Italy
auf.der.maur@ing.uniroma2.it

Aldo Di Carlo

CNR-ISM
Frascati, Italy
aldo.dicarlo@cnr.it

Abstract—We present a tight-binding description of mixed perovskites showing an application to Sn-Pb mixed systems. We discuss the parameterization procedure and the preliminary results obtained for $\text{MASn}_{0.5}\text{Pb}_{0.5}\text{I}_3$. Our model shows a treatment of the band gap bowing observed for this perovskite alloy when Sn segregation is considered. Note that our method can be easily extended to include the description of all the perovskite crystal phases and more refined strain effects.

Index Terms—tight-binding, perovskites, Sn-Pb mix, segregation

I. INTRODUCTION

Perovskite semiconductors have represented a breakthrough for photovoltaic applications and are gaining increasing attention in the field of optoelectronic devices, due to the combination of suitable and tunable electronic properties with scalable and cost-effective production techniques. While perovskite-based light-emitting diodes, sensors, and detectors are being developed, the optimization of perovskite materials is now crucial to push the efficiency and stability of perovskite solar cells. Multiscale numerical approaches that embed atomic-scale information in device simulations are paramount in this context to design, understand, and predict how the device performance is affected by the microscopic features. In multiscale frameworks, the tight-binding (TB) model has emerged as the best trade-off between computational burden and accuracy. TB is ideal for large systems where *ab-initio* methods become unfeasible, but, as an empirical method, high-quality sets of parameters are vital for the TB model. One typical example is the transferability of parameters sets from pure materials to mixed materials, or alloys.

Here, we propose a TB parameterization procedure to describe mixed perovskites. We show the application to $\text{MASn}_x\text{Pb}_{1-x}\text{I}_3$ for a sp^3 TB implementation based on Jancu scheme [1]. Note, however, that the presented approach is a reduced version of a more complex procedure developed in our group [2], easily extendable to a wide class of semiconductors,

$sp^3d^5s^*$ basis set, or advanced TB schemes such as the one of Tan et al. [3].

II. COMPUTATIONAL APPROACH

The onsite and coupling integrals of the TB Hamiltonian are treated as fitting parameters to reproduce target band structures obtained by density functional theory (DFT) calculations [4] at the PBE0 level of approximation, including spin orbit coupling (SOC). We employ a genetic algorithm for the fitting procedure [2]. In the first step, onsite energies and coupling integrals are optimized to reproduce the DFT band structures of unstrained pure materials. We impose that onsite energies and SOC parameters of I atoms are the same for both MASnI_3 and MAPbI_3 perovskites. The initial guess for the optimization is taken from Boyer-Richard et al. [1]. Then, the band structures of hydrostatically strained samples of pure materials are fitted to determine the TB Harrison scaling parameters. In Fig. 1, we show the results obtained, e.g., for MASnI_3 . Note that an advanced multi-objective optimization, that fits both the band structures and the wavefunctions characters, is possible following the extended version of the procedure [2].

Finally, the band offset between pure materials is derived from DFT analysis following the method of Weston et al. [5]. This involves two bulk calculations, giving the position of the valence band edge with respect to the average electrostatic potential, and a supercell calculation to determine the electrostatic potential alignment between different materials.

III. PRELIMINARY RESULTS AND FUTURE WORK

Using the TB implementation available in TiberCAD [6], we tested our TB parameters simulating uniform and Sn-segregated $\text{MASn}_{0.5}\text{Pb}_{0.5}\text{I}_3$ random alloys, for several supercell size values, where the Sn segregation is obtained following the convention in [7], [8] with only 1% of uniformity. When segregation is included, localization of carriers is expected, as shown in Fig. 2, where the spatial distributions of the electron and hole ground-state wavefunctions are represented along with the band alignment between MASnI_3 and MAPbI_3 .

The authors want to acknowledge the support of EU Project SUNREY under grant agreement number 101084422.

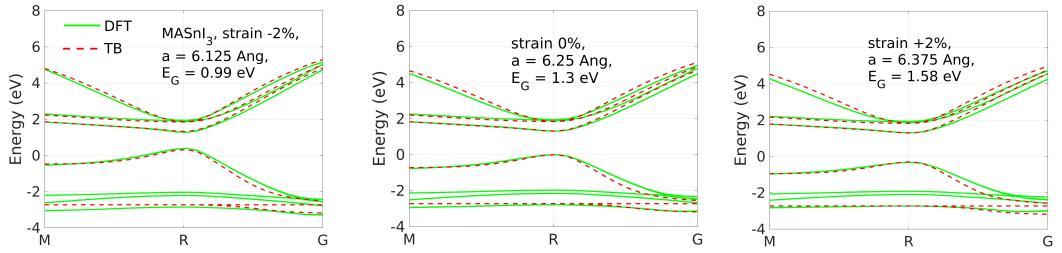


Fig. 1. The band structures of MASnI_3 for different hydrostatic strain values reproduced by our TB parameters (red dashed lines) and by PBE0-DFT (green solid lines).

Moreover, the band gap is expected to decrease due to localized states [7], [8]. This effect is shown in Fig. 3, where we report the value of energy gap (E_G) obtained for all the simulated structures. Of course, the size of the supercell becomes important if segregation is considered, since the non-uniform atomic structures produce more scattered results that need statistical significance, highlighting the importance of models capable of handling large systems.

Even if alloy disorder is considered an important factor that strongly affects the electronic properties of semiconductor alloys, other studies [9], [10] demonstrate that the bowing of E_G in Sn-Pb perovskites can be induced by the interplay between SOC and steric effects. As mentioned before, our model includes SOC, but it does not account for structural relaxation, distortion, or even phase transition that is required to reproduce the behavior in [10]. This point will be the focus of our future work. In fact, our parameterization is now restricted to the pseudo-cubic perovskite, but it can be easily extended to the other perovskite phases using the Tan TB scheme [3] and our general parameterization procedure [2]. Moreover, based on molecular dynamics, or even machine-learned force fields, a treatment of structural relaxation could be added.

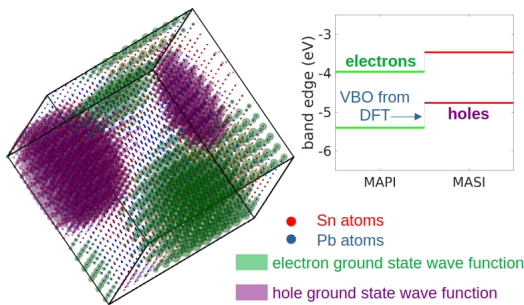


Fig. 2. Spatial distributions of the electron and hole ground-state wavefunctions (isosurfaces containing 50% of the total density are represented) where the presence of Sn segregation is considered. Electrons and holes are localized on Pb and Sn rich regions, respectively, as expected from the band alignment derived by DFT calculations.

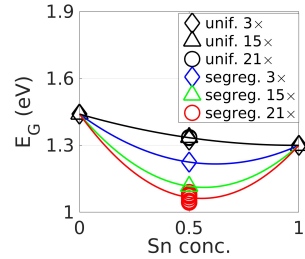


Fig. 3. Trend of E_G as a function of Sn concentration. Several supercell size values are considered for both uniform and segregated structures.

REFERENCES

- [1] Boyer-Richard, S., Katan, C., Traore, B., Scholz, R., Jancu, J. M., and Even, J. (2016). Symmetry-based tight binding modeling of halide perovskite semiconductors. *The Journal of Physical Chemistry Letters*, 7(19), 3833-3840.
- [2] Phan, A. L., Soccolato, D., Pecchia, A., Di Vito, A., and Auf der Maur, M.. An effective and pragmatic parameterization procedure for empirical tight-binding models. Unpublished. The accompanying code implementation is available at https://github.com/tiberlab/ETB_parameterizer.
- [3] Tan, Y., Povolotskiy, M., Kubis, T., Boykin, T. B., and Klimeck, G. (2016). Transferable Tight-binding model for strained group IV and III-V materials and heterostructures. *Physical Review B*, 94(4), 045311.
- [4] Smidstrup, S., Markussen, T., Vancraeyveld, P., Wellendorff, J., Schneider, J., Gunst, T., ... and Stokbro, K. (2019). QuantumATK: an integrated platform of electronic and atomic-scale modelling tools. *Journal of Physics: Condensed Matter*, 32(1), 015901.
- [5] Weston, L., Tailor, H., Krishnaswamy, K., Bjaalie, L., and Van de Walle, C. G. (2018). Accurate and efficient band-offset calculations from density functional theory. *Computational Materials Science*, 151, 174-180.
- [6] TiberCAD multiscale simulator <http://www.tibercad.org/>
- [7] Di Vito, A., Pecchia, A., Di Carlo, A., and Auf der Maur, M. (2020). Simulating random alloy effects in III-nitride light emitting diodes. *Journal of Applied Physics*, 128(4).
- [8] Phan, A. L., Pecchia, A., Di Vito, A., and Auf der Maur, M. (2024). Empirical tight-binding method for large-supercell simulations of disordered semiconductor alloys. *Physica Scripta*, 99(7), 075903.
- [9] Lee, H., Kang, S. B., Lee, S., Zhu, K., and Kim, D. H. (2023). Progress and outlook of Sn-Pb mixed perovskite solar cells. *Nano Convergence*, 10(1), 27.
- [10] Im, J., Stoumpos, C. C., Jin, H., Freeman, A. J., and Kanatzidis, M. G. (2015). Antagonism between spin-orbit coupling and steric effects causes anomalous band gap evolution in the perovskite photovoltaic materials $\text{CH}_3\text{NH}_3\text{Sn}_{1-x}\text{Pb}_x\text{I}_3$. *The Journal of Physical Chemistry Letters*, 6(17), 3503-3509.

Trying to understand semiconductor lasers for 40 years

Hans Wenzel

Ferdinand-Braun-Institut (FBH)

Gustav-Kirchhoff-Straße 4, 12489 Berlin, Germany

ORCID 0000-0003-1726-0223

Abstract—Selected aspects of the mathematical modelling and numerical simulation of semiconductor lasers will be presented.

Index Terms—semiconductor laser, mathematical modeling, numerical simulation

I. INTRODUCTION

The semiconductor laser is a fascinating object for a theoretical physicist. Mathematical modeling of such a device must incorporate several physical disciplines, including the transport of charged carriers and heat, as well as the generation, guidance and propagation of photons. The physics involved extends to both the macroscopic and microscopic levels. Examples include the classical drift-diffusion and wave equations, and the quantum-theoretical based calculation of mobilities and the dielectric susceptibility. Quantum laser theory is required to calculate noise spectra. Another aspect to consider is the range of spatial and temporal scales involved, which vary from nanometers to millimeters and picoseconds to continuous wave. It is nearly impossible to include all disciplines, levels, and scales in a single simulation program. Instead, the entire problem must be broken down into smaller parts. The results can be transferred from one part to another using determined parameters, analytical functions, or look-up tables. Further simplifications are often necessary because numerical implementations must be compatible with the computer resources available when writing the code, such as memory and processing. However, when making such simplifications, it is important to start from first principles and observe basic physical principles.

The three modeling issues I will discuss in my talk are as follows: (i) local charge neutrality; (ii) filamentation; and (iii) orthogonality of cavity modes.

(i) The van Roosbroeck system describes the semi-classical transport of free electrons and holes in a quasi-static electric field using a drift-diffusion approximation [1]. It consists of the Poisson equation for the electric potential and continuity equations for the electron and hole current densities which are driven by the gradients of the quasi-Fermi potentials. The electron and hole densities are related to the electric potential as well as the quasi-Fermi potentials of electrons and holes via so-called state equations [2]. The numerical solution of this highly non-linear system of differential equations is non-trivial [3] and different numerical schemes have been proposed [4]. However, since the Debye length $\lambda_D = \sqrt{\varepsilon_0 \varepsilon_s k_B T / q^2 n}$

is much smaller than the thicknesses of the bulk layers of diode lasers driven above threshold, the solution of the Poisson equation can be avoided by applying the zero-space charge approximation and setting the right-hand side of the Poisson equation to zero [5],

$$n(\xi) - p(\xi) - C = 0 \quad (1)$$

with

$$n = N_c F_{1/2}(\xi) \quad \text{and} \quad p = N_v F_{1/2}\left(\frac{\varphi_F - E_g}{k_B T} - \xi\right) \quad (2)$$

where $F_{1/2}(\cdot)$ is an Fermi integral and $C = N_D^+ - N_A^-$ is the ionized net doping. The solution of the neutrality condition (1) yields the relation between the electron and hole densities n and p , respectively, and the Fermi voltage φ_F which depends on the energy gap E_g , but not on the conduction and valence band edges separately. In my talk I will compare the results of a full numerical solution of the drift-diffusion system and with a solution based on (1) [6].

(ii) For many years, the multi-peaked lateral field profiles of BA lasers have been often interpreted in terms of filamentation. As first demonstrated by Beppalov and Talanov [7], plane waves propagating in a uniform medium with a focusing Kerr nonlinearity spontaneously break up into small filaments. In diode lasers an indirect Kerr-type nonlinearity can be induced by the dependence of the real part of the susceptibility on the carrier density (often described by Henry's α -factor) which in turn depends on the field intensity via the rate of stimulated recombination. There are several reasons why this indirect Kerr-type nonlinearity does not result in the development of filaments. First, the susceptibility in the active region of a laser is complex-valued. In regions with a high intensity the real part of the susceptibility (refractive index) is increased, but the imaginary part (gain) is decreased. This results in both focusing and defocusing phenomena at the same time. Secondly, the medium of an injection laser is always nonuniform because of the formation of a lateral waveguide due to the dependence of the susceptibility on carrier density, local temperature, or on external factors such as etched index-guiding trenches or implanted regions. Third, the excitation of several lateral waveguide modes with different wavelengths leads to mode beating that drives oscillations of the carrier density via the stimulated recombination. Thus, BA lasers exhibit an inherently non-stationary behavior, see Fig. 1. I

will show in my talk that the lateral field profile can be surprisingly well understood as the result of the competition and superposition of stationary lateral waveguide modes [8], [9], [10], [11].

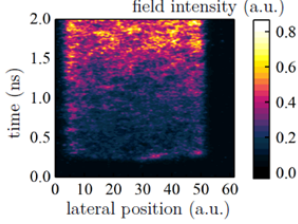


Fig. 1. Near field intensity of a BA laser measured with a streak camera (courtesy of H. Christopher).

(iii) The forward and backward propagating longitudinal modes Φ_m^\pm of a laser cavity fulfill a special orthogonality relationship due to the openness of the cavity and the presence of gain,

$$(\Phi_\mu, \Phi_\nu) := \int_0^L [\Phi_\mu^+ \Phi_\nu^- + \Phi_\mu^- \Phi_\nu^+] dz = 0 \quad \text{for } \mu \neq \nu, \quad (3)$$

which can be also considered as a consequence of time-reversal symmetry. A similar relation holds also for the transverse modes. The relation (3) has two consequences. Firstly, it is evident that the integral does not define a scalar product, as the Φ s are complex-valued. Indeed, it has been demonstrated that $(\Phi_\mu, \Phi_\nu) = 0$ can occur even for $\mu = \nu$ at specific parameter configurations, which is the consequence of a mode degeneracy [12], [13]. The occurrence of such exceptional points is not restricted to lasers but is inherent to non-Hermitian systems [14]. Secondly, the relation (3) results in an enhancement of the intrinsic spectral linewidth compared to the case of power-orthogonal modes. This enhancement is often described in terms of the Petermann factor. In my talk I will demonstrate the occurrence of exceptional points in two-section DFB lasers and I will address the origin of the Petermann factor in the context of calculating the intrinsic spectral linewidth in terms of the cavity mode [15].

ACKNOWLEDGMENT

I'm grateful to H.-J. Wünsche, U. Bandelow, A. Zeghuzi, and M. Radziunas for their contributions to this work.

REFERENCES

- [1] W. Van Roosbroeck, "Theory of the flow of electrons and holes in germanium and other semiconductors," *The Bell System Technical Journal*, vol. 29, no. 4, pp. 560–607, 1950.
- [2] P. Farrell, N. Rotundo, D. H. Doan, M. Kantner, J. Fuhrmann, and T. Koprucki, "Drift-diffusion models," in *Handbook of optoelectronic device modeling and simulation*. CRC Press, 2017, pp. 733–772.
- [3] H. Gajewski, "On the uniqueness of solutions to the drift-diffusion model of semiconductor devices," *Mathematical Models and Methods in Applied Sciences*, vol. 4, no. 01, pp. 121–133, 1994.
- [4] M. Kantner, "Generalized Scharfetter–Gummel schemes for electro-thermal transport in degenerate semiconductors using the Kelvin formula for the Seebeck coefficient," *Journal of Computational Physics*, vol. 402, p. 109091, 2020.
- [5] H.-J. Wünsche and H. Wenzel, "Influence of surface recombination on the rate of electron leakage in ridge-waveguide injection lasers," *physica status solidi (a)*, vol. 111, no. 1, pp. 377–386, 1989.
- [6] A. Boni, H.-J. Wünsche, H. Wenzel, and P. Crump, "Impact of the capture time on the series resistance of quantum-well diode lasers," *Semiconductor Science and Technology*, vol. 35, no. 8, p. 085032, 2020.
- [7] V. Bespalov and V. Talanov, "Filamentary structure of light beams in nonlinear liquids," *JETP Lett*, vol. 3, p. 307, 1966.
- [8] A. Zeghuzi, M. Radziunas, H.-J. Wünsche, J.-P. Koester, H. Wenzel, U. Bandelow, and A. Knigge, "Traveling wave analysis of non-thermal far-field blooming in high-power broad-area lasers," *IEEE Journal of Quantum Electronics*, vol. 55, no. 2, pp. 1–7, 2019.
- [9] A. Zeghuzi, H.-J. Wünsche, H. Wenzel, M. Radziunas, J. Fuhrmann, A. Klehr, U. Bandelow, and A. Knigge, "Time-dependent simulation of thermal lensing in high-power broad-area semiconductor lasers," *IEEE Journal of Selected Topics in Quantum Electronics*, vol. 25, no. 6, pp. 1–10, 2019.
- [10] A. Zeghuzi, *Analysis of spatio-temporal phenomena in high-brightness diode lasers using numerical simulations*. Cuvillier Verlag, 2020, vol. 59.
- [11] J.-P. Koester, A. Putz, H. Wenzel, H.-J. Wünsche, M. Radziunas, H. Stephan, M. Wilkens, A. Zeghuzi, and A. Knigge, "Mode competition in broad-ridge-waveguide lasers," *Semiconductor Science and Technology*, vol. 36, no. 1, p. 015014, 2020.
- [12] H. Wenzel, U. Bandelow, H.-J. Wünsche, and J. Rehberg, "Mechanisms of fast self pulsations in two-section DFB lasers," *IEEE Journal of Quantum Electronics*, vol. 32, no. 1, pp. 69–78, 1996.
- [13] J. Rehberg, J. Rehberg, H.-J. Wünsche, U. Bandelow, and H. Wenzel, "Spectral properties of a system describing fast pulsating DFB lasers," *ZAMM-Journal of Applied Mathematics and Mechanics/Zeitschrift für Angewandte Mathematik und Mechanik*, vol. 77, no. 1, pp. 75–77, 1997.
- [14] J. Kullig, J. Wiersig, and H. Schomerus, "Generalized Petermann factor of non-Hermitian systems at exceptional points," *arXiv preprint arXiv:2506.15807*, 2025.
- [15] H. Wenzel, M. Kantner, M. Radziunas, and U. Bandelow, "Semiconductor laser linewidth theory revisited," *Applied Sciences*, vol. 11, no. 13, p. 6004, 2021.

Density Matrix Simulations of Quantum Cascade Lasers: Optical and Microwave Dynamics

Christian Jirauschek

*TUM School of Computation, Information and Technology
Technical University of Munich (TUM)*

Garching, Germany

jirauschek@tum.de

Abstract—We discuss a self-consistent simulation approach for the dynamic modeling of quantum cascade lasers (QCLs). These feature a quantum-engineered active region, enabling unique functionalities such as frequency comb generation in the mid-infrared and terahertz range. The model combines a density matrix description of the active region with electromagnetic modeling of the microwave and optical propagation in the laser waveguide. Based on simulations of experimental QCL structures, we demonstrate the accuracy and numerical efficiency of the model. Due to its versatility, the approach can be adapted to different waveguide configurations and also to other quantum optoelectronic devices.

Index Terms—Quantum cascade lasers, laser mode locking, microwave photonics

I. INTRODUCTION

Quantum-engineered optoelectronic devices feature a nanostructured active region, offering unprecedented possibilities. The most prominent examples are the quantum dot, interband cascade and quantum cascade laser (QCL). The latter is a unipolar device, utilizing transitions between quantized states in the conduction band of a multi-quantum-well structure. In this way, the lasing wavelength becomes independent of the material band gap and can be custom-tailored over a wide range of the mid-infrared and terahertz region. Furthermore, the quantum active region exhibits unique dynamic gain properties and strong nonlinear effects such as four-wave mixing. These features can be exploited for the realization of compact, electrically pumped short-pulse and frequency comb sources at wavelengths hardly accessible to conventional diode lasers [1], [2]. More specifically, mode-locking techniques are utilized to generate periodic waveforms, including short-pulse trains and optical fields featuring broadband comb-like spectra. These laser sources open up a wide range of applications in fields such as sensing, metrology, imaging and communications. Recently, also more exotic optical waveforms have been realized, such as soliton crystals and other harmonic states featuring multiple optical waveform periods within a single roundtrip [3], [4].

Besides the quantum active region, also the optical waveguide plays an important role for dynamic operation, for example in the context of dispersion compensation [1]. Furthermore, adequately designed waveguides simultaneously act as microwave transmission lines, enabling propagation of microwave modulations in the pump bias along with the

optical waveform. Recent research has started exploiting this design degree of freedom for the implementation of novel functionalities. For active mode-locking where waveform generation is triggered by external bias modulation, the optical and microwave co-propagation increases the modulation efficiency and has for example enabled the realization of quantum walk combs in QCLs, which are especially flat and broadband [5]. On the other hand, in free-running QCLs the optical dynamics leads to a modulation of the current along the waveguide, which has been exploited for photonics-based millimeter wave generation and can perspectiveally also be utilized for the self-stabilization of frequency combs [6], [7].

A targeted development of waveform-generating QCLs requires dynamic simulation models combining accuracy and versatility with numerical efficiency. In this context, semiclassical approaches employing a density matrix model for the quantum active region and a description of the optical waveguide field based on Maxwell's or related equations have proven particularly useful [8]. To incorporate above discussed microwave effects, the waveguide model has recently been adequately extended [9]. In the following, we describe the model and discuss simulation results of an experimental structure for photonics-based millimeter wave generation. Notably, by using a generalized multilevel Hamiltonian rather than the two-level model employed in Maxwell-Bloch equations, the electron dynamics in the active region due to light-matter and potentially also microwave-matter interaction can be self-consistently described.

II. MODEL

Our simulation approach combines a multi-level density matrix model of the quantum active region with optical and microwave propagation equations for the waveguide. The active region is at any spatial grid point modeled by a representative quantum system with the density operator $\hat{\rho}$. The time evolution is governed by a Lindblad-type equation

$$i\hbar\partial_t\hat{\rho} = \left[\hat{H}_0 - \hat{d}E, \hat{\rho}\right] + \hat{D}(\hat{\rho}), \quad (1)$$

with the Hamiltonian \hat{H}_0 , optical dipole operator \hat{d} , and dissipator $\hat{D}(\hat{\rho})$. For numerical efficiency, we introduce the widely used rotating-wave approximation. To this end, we

write the optical field in terms of its forward and backward propagating envelopes $E^\pm(x, t)$ as

$$E = \Re \{ [E^+ \exp(i\beta x) + E^- \exp(-i\beta x)] \exp(-i\omega_c t) \}, \quad (2)$$

with the propagation constant β and center frequency ω_c , and discard the rapidly oscillating terms arising in (1). To further reduce the numerical effort, we assume that the waveguide geometry allows reduction of the model to a single spatial coordinate x along the optical propagation direction [8]. Within this framework, the optical propagation in the waveguide can be modeled by [8]

$$\partial_t E^\pm = \mp v_g \partial_x E^\pm + f^\pm - v_g a E^\pm / 2 - i v_g \beta_2 \partial_t^2 E^\pm / 2, \quad (3)$$

with the power loss coefficient a , group velocity v_g and group velocity dispersion coefficient β_2 . The polarization contribution of the quantum system $f^\pm(x, t)$ is computed from (1). By adding the transmission line equations

$$\begin{aligned} \partial_x u &= -L' \partial_t i - R' i, \\ \partial_x i &= -C' \partial_t u - J w \end{aligned} \quad (4)$$

to the model, microwave propagation along the waveguide can be described in terms of the voltage $u(x, t)$ and current $i(x, t)$. Here, the microwave properties of the waveguide are characterized via the distributed inductance L' , capacitance C' and resistance R' . For realistic simulation results, especially the frequency dependence of R' must be accounted for in the numerical scheme [9]. The current density $J(x, t)$ through the quantum active region of width w is again computed from (1). On the other hand, \hat{H}_0 , \hat{d} and \hat{D} in (1) generally depend on u obtained from (4). A coupled simulation of (1), (3) and (4) provides a closed model for the quantum, optical and microwave dynamics in the device.

III. SIMULATION RESULTS

We apply above simulation approach to an experimental QCL structure for photonics-based millimeter wave generation [6]. The Hamiltonian, optical dipole moments and dissipation rates in (1) are extracted from carrier transport simulations [10]. Furthermore, the optical waveguide parameters are obtained from literature, and the microwave model is taken from [9]. The setup is simulated over 10,000 roundtrips to ensure convergence. The results depend on the exact choice of transmission line parameters, demonstrating the influence of the waveguide microwave characteristics on the overall dynamic QCL operation. In Fig. 1, the simulated instantaneous intensity and bias at the right facet are displayed for an exemplary waveguide, along with the associated power spectral densities. Overall, the results show good agreement with experimental data [6].

In conclusion, the presented simulation approach enables the targeted design of QCL devices for the generation of optical waveforms and microwave fields. Furthermore, since the model employs a multi-level density matrix description of the active region, it is quite versatile and may be adapted to other quantum optoelectronic devices, such as interband cascade and quantum dot lasers.

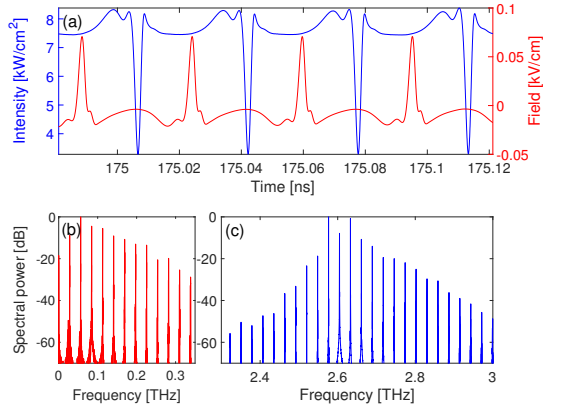


Fig. 1. (a) Outcoupled optical intensity and AC bias field at the right facet. (b) Power spectral density of the microwave signal. (c) Optical power spectrum.

REFERENCES

- [1] J. Faist, G. Villares, G. Scalari, M. Rösch, C. Bonzon, A. Hugi, and M. Beck, "Quantum cascade laser frequency combs," *Nanophotonics*, vol. 5, no. 2, pp. 272–291, 2016.
- [2] E. Riccardi, V. Pistori, S. Kang, L. Seitner, A. De Vetter, C. Jirauschek, J. Mangeney, L. Li, A. G. Davies, E. H. Linfield, A. C. Ferrari, S. S. Dhillon, and M. S. Vitiello, "Short pulse generation from a graphene-coupled passively mode-locked terahertz laser," *Nat. Photonics*, vol. 17, pp. 607–614, 2023.
- [3] N. Opačak, D. Kazakov, L. L. Columbo, M. Beiser, T. P. Letsou, F. Pilat, M. Brambilla, F. Prati, M. Piccardo, F. Capasso *et al.*, "Nozaki–Bekki solitons in semiconductor lasers," *Nature*, vol. 625, no. 7996, pp. 685–690, 2024.
- [4] T. S. Mansuripur, C. Vernet, P. Chevalier, G. Aoust, B. Schwarz, F. Xie, C. Caneau, K. Lascola, C.-e. Zah, D. P. Caffey *et al.*, "Single-mode instability in standing-wave lasers: The quantum cascade laser as a self-pumped parametric oscillator," *Phys. Rev. A*, vol. 94, no. 6, p. 063807, 2016.
- [5] I. Heckelmann, M. Bertrand, A. Dikopoltsev, M. Beck, G. Scalari, and J. Faist, "Quantum walk comb in a fast gain laser," *Science*, vol. 382, no. 6669, pp. 434–438, 2023.
- [6] V. Pistori, H. Nong, P.-B. Vigneron, K. Garrasi, S. Houver, L. Li, A. G. Davies, E. H. Linfield, J. Tignon, J. Mangeney, R. Colombelli, M. S. Vitiello, and S. S. Dhillon, "Millimeter wave photonics with terahertz semiconductor lasers," *Nat. Commun.*, vol. 12, no. 1, p. 1427, 2021.
- [7] H. Li, P. Laffaille, D. Gacemi, M. Apfel, C. Sirtori, J. Leonard, G. Santarelli, M. Rösch, G. Scalari, M. Beck, J. Faist, W. Hänsel, R. Holzwarth, and S. Barbieri, "Dynamics of ultra-broadband terahertz quantum cascade lasers for comb operation," *Opt. Express*, vol. 23, no. 26, pp. 33 270–33 294, 2015.
- [8] C. Jirauschek, M. Riesch, and P. Tzenov, "Optoelectronic device simulations based on macroscopic Maxwell–Bloch equations," *Adv. Theory Simul.*, vol. 2, no. 8, p. 1900018, 2019.
- [9] C. Jirauschek, "Theory of hybrid microwave–photonic quantum devices," *Laser Photonics Rev.*, vol. 17, p. 2300461, 2023.
- [10] C. Jirauschek and P. Tzenov, "Self-consistent simulations of quantum cascade laser structures for frequency comb generation," *Opt. Quant. Electron.*, vol. 49, no. 12, p. 414, 2017.

Computational Techniques for Optimization and Design of InGaAlAs MQW Lasers

D. Paige Wilson
SUNLAB, School of Electrical
Engineering and Computer Sciences
University of Ottawa
Ottawa, Ontario
pwwilson3@uottawa.ca

Bernard Paquette
Canadian Photonics Fabrication
Centre,
National Research Council of Canada
Ottawa, Ontario
bernard.paquette@nrc-cnrc.gc.ca

Muhammad Mohsin
Quantum and Nanotechnologies
Research Centre,
National Research Council of Canada
Ottawa, Ontario
muhammad.mohsin@nrc-cnrc.gc.ca

Mohamed Rahim
Quantum and Nanotechnologies
Research Centre,
National Research Council of Canada
Ottawa, Ontario
mohamed.rahim@nrc-cnrc.gc.ca

Yuri Grinberg
Digital Technologies Research Centre,
National Research Council of Canada
Ottawa, Ontario
yuri.grinberg@nrc-cnrc.gc.ca

Karin Hinzer
SUNLAB, School of Electrical
Engineering and Computer Sciences,
Department of Physics
University of Ottawa
Ottawa, Ontario
khinzer@uottawa.ca

Abstract—Semiconductor lasers present several challenges in terms of both design and understanding. Their numerous epitaxial layers, material properties, and physical structures generate a complex and high-dimensional space of parameters that must be optimized. We develop and demonstrate the use of a computational model capable of exploring this high-dimensional space. We validate this model against experimentally obtained data to ensure high-quality inputs are generated for use in future machine learning analyses.

Keywords—Fabry-Perot, buried heterostructure, multi-quantum well, machine learning, model validation

I. INTRODUCTION

Semiconductor lasers have become ubiquitous in today's technological and scientific industries. Diode lasers are key components in telecommunication, power-beaming, and sensors [1], [2], [3]. The wide-range of applications creates a high number of possible designs to select from, presenting a challenge for laser designers who must not only select the appropriate design parameters for the application but must then optimize the design to maximise the relevant performance metrics.

Techniques for optimization of various types of lasers have included genetic algorithms, binary search, simulated annealing, and Bayesian methods [4], [5], [6]. These techniques are useful for finding optimal conditions for device design or best fits in large parameter spaces. While these methods are valuable for model validation and extracting physical parameters they may not be the most efficient choice for developing novel designs or providing a physical understanding of device performance (i.e. "knowledge discovery"). Other methods employing machine learning (ML) techniques, such as neural networks [7], have been suggested. In particular, dimensionality reduction methods such as principal component analysis (PCA) [8], [9], can significantly reduce the complexity and computational cost of laser design studies by reducing the dimensionality of the problem and offering interpretability.

Nonetheless, in order to facilitate the use of ML techniques, it is important to ensure that training data is based on a validated device model in order to produce physically meaningful results. Therefore, optimization techniques to fit data to experiment still play an important role. We present a

model of a Fabry-Perot (FP) buried heterostructure (BH) laser that is calibrated to experimental results. The model will be used as a foundation for future ML applications.

II. METHODS

A. Experimental

We perform measurements of LIVs, spectrum, and net optical gain on FP-BH lasers. The devices are grown on InP substrates. The active region consists of four multi-quantum well layers composed of compressively strained InGaAlAs. The lasers have cavity lengths of 2 mm.

The lasers are mounted on a temperature-controlled stage and the net optical gain is measured at temperatures of 20 °C, 35 °C, and 50 °C. The gain is measured just below the threshold current (I_{th}) of the laser at 17 mA, 22 mA, and 29 mA for each respective temperature. These measured curves are shown in Fig. 1. The method follows that of Ref. [10].

B. Modelling and Numerical Optimization

We combine commercially available laser simulation packages with Python tools to simulate and study the BH lasers. The measurements described in Section II.A are used to validate the model. The commercially available software packages are Photon Design's Harold and PICWave. In Harold we generate the material gain (G_{mat}) of the BH laser modeled as a 1-dimensional epitaxial stack. This is followed

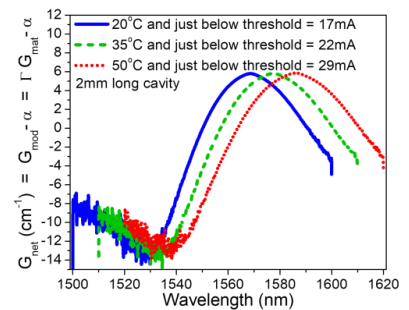


Fig. 1. Experimental G_{net} curves for an FP-BH laser with four quantum well layers. Measurements are performed on a temperature controlled stage at 20 °C, 35 °C, and 50 °C. Measurements are performed just below the I_{th} of the laser.

by simulations in PICWave which returns the modal gain (G_{mod}), confinement factor (Γ), modal loss (α) and calculates the LIV curve. The net gain and LIV curves are extracted and compared with the experimental data.

These two standalone software packages are tied together to provide uninterrupted flow of the simulations using Python, facilitating data extraction in order to fit the data and validate the model.

We select five material properties as fitting parameters: the scattering loss of the laser cavity, the electron and hole net recombination lifetimes, the intraband lifetime, and the bandgap narrowing factor in the QW regions. A differential evolution algorithm [11] is used to narrow down the initial parameter space. The best solution is further refined using a Nelder-Mead algorithm. The residual is the root sum of squares of I_{th} and the differential efficiency (η_d).

III. RESULTS AND DISCUSSION

We report the final values of the fitting parameters for the scattering loss of the laser cavity, the electron and hole net recombination lifetimes, the intraband lifetime, and the QW bandgap narrowing factor as 8.6 cm^{-1} , $9.4\text{e-}12 \text{ s}$, $4.1\text{e-}13 \text{ s}$, $7.9\text{e-}14 \text{ s}$, and $-1.3\text{e-}9$ respectively. The results of this best fit to the 2 mm cavity BH laser with four quantum well layers operating at 20°C are shown in Figure 2. The fitting was performed against the root sum of squares of the η_d and I_{th} . Experimentally we observe an I_{th} of 16.852 mA and a η_d of 0.116 W/A under continuous wave operation. The optimizer returns a result of 16.859 mA and 0.115 W/A for these parameters respectively. We note that there is good agreement between the experimentally extracted cavity mode loss 14.03 cm^{-1} and the mode loss generated by the simulations 15.02 cm^{-1} . The net gain also shows good agreement between

experiment and simulation with respect to the gain peak. This gives further weight to our model validity since neither the modal loss nor the gain were considered in the residual calculations but were instead extracted as a result of the fitted simulations. Further agreement between the modal loss and the gain could be obtained by defining a figure of merit that includes these elements.

The validated material parameters provide confidence in the simulation outcomes of these FP-BH lasers and will be used as a foundation for future machine learning techniques in combination with the process flow we have detailed here.

IV. CONCLUSIONS

We present a validated model of an FP-BH laser grown on InP substrates with four InGaAlAs quantum well layers. The simulation process flow combines multiple software packages (Photon Design's Harold and PICWave) as well as in-house techniques implemented through Python to extract simulation results and parameters to accurately fit the experimental data. A differential evolution algorithm is used to assess five different material parameters. The solution is refined with a Nelder-Mead algorithm. We achieve a robust fit to the data, ensuring high quality inputs are available for further study using machine learning analyses.

ACKNOWLEDGMENT

The author's acknowledge funding support from the National Research Council Canada's AI for Design (AI4D) Challenge Program.

REFERENCES

- [1] R. J. K. Obhi, S. W. Schaefer, C. E. Valdivia, J. R. Liu, Z. G. Lu, P. J. Poole, and K. Hinzer, "Indium arsenide single quantum dash morphology and composition for wavelength tuning in quantum dash lasers," *Appl. Phys. Lett.*, vol. 122, p. 051104, 2023.
- [2] F. Kehl, D. Bischof, M. Michler, M. Keka, and R. Stanley, "Design of a label-free, distributed bragg grating resonator based dielectric waveguide biosensor," *Photonics*, vol. 2, pp. 124–138, 2015.
- [3] M. N. Beattie, H. Helmers, G. P. Forcad, C. E. Valdivia, O. Höhn, and K. Hinzer, "InP- and GaAs-Based Photonic Power Converters Under O-Band Laser Illumination: Performance Analysis and Comparison," *IEEE J. Photovolt.*, vol. 13, pp. 113–121, 2023.
- [4] T. G. Folland, and S. Chakraborty, "Dual-frequency defect-mode lasing in aperiodic distributed feedback cavities," *IEEE Photonics Technology Letters*, vol. 28, pp. 1617–1620, 2016.
- [5] A. Bismuto, R. Terazzi, B. Hinkov, M. Beck, and J. Faist, "Fully automatized quantum cascade laser design by genetic optimization," *Appl. Phys. Lett.*, vol. 101, p. 021103, 2012.
- [6] M. Franckić, and J. Faist, "Bayesian Optimization of Terahertz Quantum Cascade Lasers," *Phys. Rev. Appl.*, vol. 13, p. 034025, 2020.
- [7] A. C. Hernandez, and C. F. Gmachl, "Application of Machine Learning to Quantum Cascade Laser Design," [2023 57th Annual Conference on Information Sciences and Systems (CISS), pp. 1–6, 2023].
- [8] S. Ayesha, M. K. Hanif, and R. Talib, "Overview and comparative study of dimensionality reduction techniques for high dimensional data," *Information Fusion*, vol. 59, pp. 44–58, 2020.
- [9] I. T. Jolliffe, and J. Cadima, "Principal component analysis: A review and recent developments," *Philosophical Transactions of the Royal Society A: Mathematical, Physical and Engineering Sciences*, vol. 374, p. 20150202, 2016.
- [10] G. E. Shtengel, R. F. Kazarinov, G. L. Belenky, M. S. Hybertsen, and D. A. Ackerman, "Advances in measurements of physical parameters of semiconductor lasers," *Int. J. High Speed Electron. Syst.*, vol. 9, pp. 901–940, 1998.
- [11] R. Storn and K. Price, "Differential evolution – A simple and efficient heuristic for global optimization over continuous spaces," *J. Global Optim.*, vol. 11, pp. 341–359, 1997.

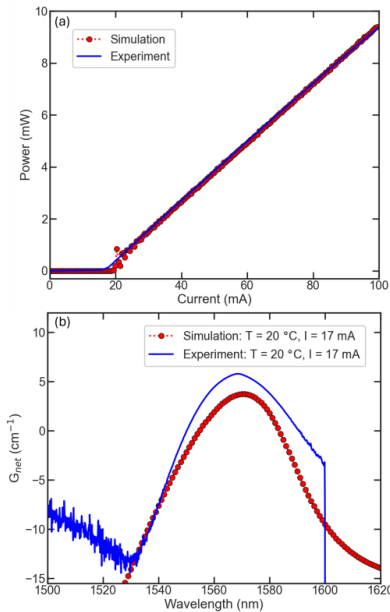


Fig. 2. The (a) simulated and experimental LIV and (b) G_{net} for a 2 mm cavity FP-BH laser. Both experimental gain measurements and simulated results were performed with a substrate temperature of 20°C and a drive current of 17 mA.

Asymmetric Electron-Hole Model for Gain-Switched InAs/InP Quantum Dot Laser

Nuran Dogru*
Electrical&Electronics Engineering
Gaziantep University
Gaziantep, Türkiye
dogru@gantep.edu.tr

Isa Akkaya
Electrical&Electronics Engineering
Gaziantep University
Gaziantep, Türkiye
isaakkaya@gantep.edu.tr

Abstract— The electron-hole model of InAs/InP quantum dot laser under gain-switching condition is investigated. The results show that the threshold current of the excited state decreases while that of ground state increases slightly for electron-hole model. Therefore, the current range where gain-switched pulses are generated increases. However, it has been observed that since the pulses generated from the exciton and electron-hole models are not narrow, an optical pulse needs to be applied to the excited state to obtain short pulses from both models.

Keywords—gain-switching, quantum-dot laser, short pulses, exciton model, electron-hole model

I. INTRODUCTION

Optical data communication, ultrafast spectroscopy, metrology and medical biotechnology etc. are fields that require short pulses with high frequency and peak power [1]. Due to the extraordinary properties such as low threshold current, chirp-free behavior, and temperature insensitivity of quantum dot lasers, they are preferred sources for these fields over quantum well lasers. Therefore, many studies have been conducted in this field using quantum dot (Q-Dot) lasers [2–3]. The symmetric exciton model and the asymmetric electron-hole model are two models used to theoretically investigate the nonlinear dynamics of quantum dot lasers. Although the excitonic model explains some characteristics of Q-Dot laser such as modulation and noise characteristics, the electron-hole model successfully describes the Light-Current characteristics [4], the temperature dependence of photoluminescence [5–6], and the phase and gain dynamics of the Q-Dot laser. To our knowledge, no work has been done to generate short pulses from Q-Dot lasers using the electron-hole model. Therefore, here we numerically studied the gain-switched characteristics of the InAs/InP Q-Dot laser using the electron-hole model. Since 1.55 μm laser emission is a significant demand in applications such as biomedical technology and optical communication, an InAs-InP(113)B Q-Dot laser, in which the InAs Q-Dot laser is grown on an InP substrate, is the most suitable choice with its emission wavelength [7].

II. NUMERICAL MODEL

The numerical model used here is based on reference [2]. The carriers and photons rate equations in the ground state (Grs) and excited state (Exs) of the Q-Dot laser are used as the basis of the direct relaxation model. The Runge-Kutta method was used to resolve the rate equations of single-mode laser. This method is a numerical integration technique frequently used in solving differential equations. Q-Dot size fluctuations, line broadening and temperature effect were neglected in our analysis. Moreover, it was assumed that carriers are injected directly into the wetting layer (Wly) from the contact points. The laser rate equations include densities of electrons and

holes for the Wly, Grs, Exs and the photon densities for Grs and Exs (i.e output is two state lasing). It was also assumed that the energy level spacing between the ground state and the excited state in the valence band is 0.5 times that in the conduction band since the holes have a much heavier effective mass than electrons [8]. Since the holes effective mass is a much heavier than electrons, the electron energy spacing in all InAs/InP Q-Dots is two times larger than that of the holes.

III. RESULTS AND DISCUSSION

In our simulation, the values of laser parameters were taken from [2]. The gain compression factor was included and it was taken as $1 \times 10^{-16} \text{ cm}^{-3}$. To obtain the short pulses in the simulation, the AC current given below was applied.

$$I(t) = I_f 2 (|\cos(2\pi f t)| - \cos(2\pi f t))$$

Where I_f is the peak value of the current and f indicates the frequency. The frequency range in which gain-switching pulses were generated was obtained between 350 MHz–1 GHz for electron-hole model and 400 MHz–1 GHz for exciton model. 1 GHz was chosen as operating frequency.

The Light-Current characteristics of symmetric exciton model and asymmetric electron-hole model are given Fig. 1 and 2 and the corresponding threshold currents for Grs, Exs and total (Grs+ Exs) are summarized in Table 1.

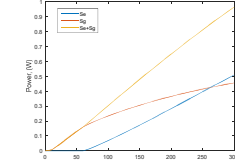


Fig. 1. Light-Current characteristic for exciton model.

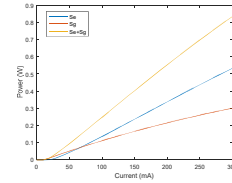


Fig. 2. Light-Current characteristic for electron-hole model.

As seen in the figures, for the electron-hole model threshold current of Exs decreases while the threshold current of Grs is approximately the same. In the electron-hole model, since electron energy spacing larger than the hole energy spacing, a smaller electron escape rate occurs compared to the hole escape rate. Therefore, for the electron-hole model, the threshold current of Exs decreases while the threshold current of Grs increases. Although similar behavior was observed in InAs/GaAs Q-Dot lasers, as the current increases,

the power of Exs increases, while the power of the Grs decreases and eventually decreases to zero, making the laser a single state lasing [4]. However, in the exciton model of the InAs/GaAs Q-Dot lasers Grs saturated with the increasing current.

Table I. Threshold currents of Grs and Exs

	Gr _s , mA	Ex _s , mA	Total (Gr _s +Ex _s), mA
Exciton model	8	61	8
Electron-hole model	10	20	10

Fig.3 and Fig. 4 show output pulses of Grs and Exs for both models. As seen in the figures peak power of Exs increases whereas the peak power of Grs decreases for the electron-hole model due to low threshold current of Exs. The pulse width of the output pulses (Gr_s+Ex_s) are obtained 265 ps and 256 ps for the exciton and electron-hole model, respectively. These results showed that the pulses generated from both models are not narrow. To obtain shorter pulses, we need to apply optical pulses to Exs as seen in Figure 5. A Gaussian peak pulse of 20 mW and I_f of 60 mA give a pulse width of 47 ps and peak power of about 1 W.

Our results also show that the Exs threshold current decreases with fast electron escape time from Grs to Exs and slow capture time from Wly to Exs , while the Grs threshold current slightly change as seen in Fig. 6. However, slow electron escape time and fast capture time the Exs threshold current increases whereas the Grs threshold current remains approximately the same (see Fig. 7). These results confirm the results of the exciton model in [2]. However, in InAs/GaAs lasers it was observed that, the Exs threshold current first decreases with decreasing electron escape time from Grs to Exs and then it becomes constant, while the Grs threshold current first remains constant and then Grs lasing stop [4].

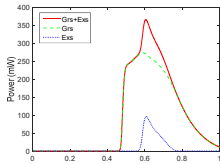


Fig. 3. Output power for exciton model for an I_f current of 100 mA.

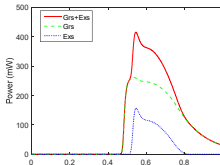


Fig. 4. Output power for electron-hole model for an I_f current of 100 mA.

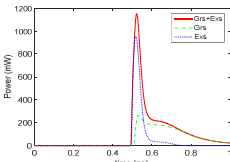


Fig. 5. Output power for electron-hole model for an I_f current of 60 mA and Gaussian peak pulse of 20 mW.

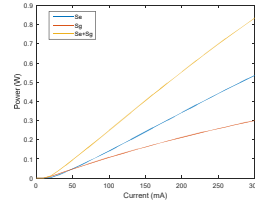


Fig. 6. Light-Current characteristic for fast electron escape time.

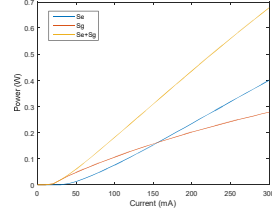


Fig. 7. Light-Current characteristic for slow electron escape time.

In summary, for the electron-hole model, as the current increases, the threshold current of Exs decreases and its power increases, but the threshold current of Grs increases slightly and its power decreases. Moreover, the fast electron escape time from Grs to Exs causes the threshold current of Exs to decrease. Our results also showed that optical pulses should be applied to Exs as in the exciton model to produce shorter pulses for the electron-hole model.

REFERENCES

- [1] K. Akahane, A. Matsumoto, T. Umezawa, and N. Yamamoto, "High-frequency short-pulse generation with a highly stacked InAs quantum dot mode-locked laser diode," *Japanese Journal of Applied Physics*, vol. 60, no. SB, p. SBBH02, Jan. 2021, doi: 10.35848/1347-4065/abd2a1.
- [2] N. Dogru, E. Cengiz, and H. S. Duranoglu Tunc, "Relative Intensity Noise of Gain-Switched Dual-State Lasing for an Insein(113)B Quantum Dot Laser," *Nanomaterials*, vol. 15, no. 7, p. 511, Mar. 2025, doi: 10.3390/nano15070511.
- [3] M. Nady Abdul Aleem, K. F. A. Hussein, and A.-E.-H. A.-E.-A. Ammar, "Semiconductor quantum dot lasers as pulse sources for high bit rate data transmission," *Progress In Electromagnetics Research M*, vol. 28, pp. 185–199, 2013, doi: 10.2528/pierm12112505.
- [4] E. A. Viktorov, P. Mandel, Y. Tanguy, J. Houlihan, and G. Huyet, "Electron-hole asymmetry and two-state lasing in quantum dot lasers," *Applied Physics Letters*, vol. 87, no. 5, Jul. 2005, doi: 10.1063/1.1995947.
- [5] P. Dawson, O. Rubel, S. D. Baranovskii, K. Pierz, P. Thomas, and E. O. Göbel, "Temperature-dependent optical properties of InAs/GaAs quantum dots: Independent carrier versus exciton relaxation," *Physical Review B*, vol. 72, no. 23, Dec. 2005, doi: 10.1103/physrevb.72.235301.
- [6] P. Moreno, M. Rossetti, B. Deveaud-Plédran, and A. Fiore, "Modeling of gain and phase dynamics in quantum dot amplifiers," *Optical and Quantum Electronics*, vol. 40, no. 2–4, pp. 217–226, Mar. 2008, doi: 10.1007/s11082-008-9219-4.
- [7] S. C. Heck *et al.*, "Experimental and Theoretical Study of InAs/InGaAsP/InP Quantum Dash Lasers," *IEEE Journal of Quantum Electronics*, vol. 45, no. 12, pp. 1508–1516, Dec. 2009, doi: 10.1109/jqe.2009.2020814.
- [8] G. Ming *et al.* "Electronic structure of self-assembled InAs/InP quantum dots: A Comparison with self-assembled InAs/GaAs quantum dots," arXiv:0708.3469. [Online]. Available: <https://arxiv.org/abs/0708.3469>.

Intermediate Value Wavefront Matching Method for InP Waveguide Design

Alexander Schindler
Fraunhofer Heinrich Hertz Institute
Technical University Berlin
Berlin, Germany
alexander.schindler@hhi-
extern.fraunhofer.de

Patrick Runge
Fraunhofer Heinrich Hertz Institute
Berlin, Germany
https://orcid.org/0000-0001-7158-6385

Martin Schell
Fraunhofer Heinrich Hertz Institute
Technical University Berlin
Berlin, Germany
martin.schell@hhi.fraunhofer.de

Abstract—An adapted wavefront matching (WFM) method for the optimization of high-index contrast waveguides is presented. Amending the WFM method by introducing intermediate refractive index values enables the method to be used for the design of waveguide structures in indium phosphide. As an example, the design of a TE₀ to TE₁ mode converter is presented.

Keywords—Wavefront Matching Method, Inverse Design, Beam Propagation Method, Indium Phosphide, Mode converter

I. INTRODUCTION

In the design of optical waveguide structures, optimization techniques offer significant benefits. Especially inverse design techniques are gaining popularity. These techniques fundamentally involve defining an input and a desired output field and transforming an initial structure to effectively convert the input field into the output field. The wavefront matching (WFM) method, as presented in [1], is a beam propagation method (BPM)-based inverse design approach originally suited for low index contrast platforms, such as silica. Table I summarizes the WFM methods applied to different material platforms. In [2], the full vector BPM-based WFM method was introduced. However, on high index contrast platforms, this approach becomes ineffective. To address this, a finite element method (FEM)-based WFM method was developed for silicon [3, 4], but its high computation time restricts its use to small-scale structures. Applying both methods to the indium phosphide (InP) platform is problematic due to its large-scale structures and high index contrast, leading to inefficiencies: the FEM-based WFM incurs high computation times, while the BPM-based method becomes ineffective. Although in [6] the BPM-based WFM method incorporating the effective index method has been successfully applied to the InP platform, this is not a general approach due to its limited accuracy [5, 6].

TABLE I. LIST OF PUBLISHED WFM METHODS

Reference	Material system	Index Contrast	Simulation Method
[1]	Silica	0.01	2D BPM
[2]	Si + SiNx	1.4	3D FV-BPM
[3]	Si	2.0	3D FEM
[4]	Si	2.0	3D FEM + stabilization
[5]	Si	0.4 – 2.0	Scalar-/FV-BPM
[6]	InP	2.2	2D BPM + Effective Index
This work	InP	2.2	3D BPM + intermediate values

To address this gap and generally enable the WFM method for the InP platform, we present an adapted WFM method based on the full vector finite difference BPM.

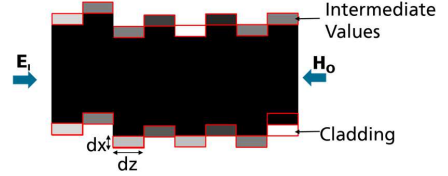


Fig. 1 IWFM method. Only red-boxed pixels are allowed to change.

II. THE INTERMEDIATE VALUE WFM METHOD

The originally proposed WFM method is based on the beam propagation method [1, 2]. An input field E_i is launched and propagated through an initial structure. At the end position the desired output Field H_o is launched and is propagated backward through the structure (Fig. 1). The simulation domain is discretized into an optimization grid with pixel size $dx \times dz$. To enhance the coupling factor

$$\eta = |\iint (E_i \times H_o) \cdot \hat{z} dx dy|^2$$

of input and output field, for each pixel at the border of the structure,

$$D = \text{Im}\{E_i \times H_o\} \cdot \hat{z}$$

is computed. Based on the sign of D , a pixel will be changed. For $D < 0$, the pixel changes from n_{wg} (waveguide material) to n_{clad} (cladding material) and for $D > 0$ from n_{clad} to n_{wg} . For low index contrast platforms, this method generates an optimized waveguide shape. However, for high index contrast platforms, this optimization progress is limited as shown in [4]. To overcome this issue, we propose an intermediate value wavefront matching (IWFM) method that allows the refractive index of a border pixel to change by a factor of

$$\Delta n = \frac{n_{wg} - n_{clad}}{m}, m \geq 1.$$

For $m = 1$, we have the standard WFM method. For $m \geq 2$ the method generates an intermediate structure with a lower refractive index contrast between waveguide and cladding. When $D < 0$, the refractive index n_b of a border pixel is

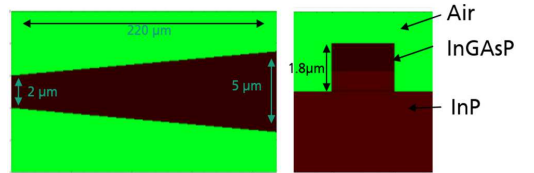


Fig. 2 Initial structure and material stack for the design to the TE₀ to TE₁ mode converter

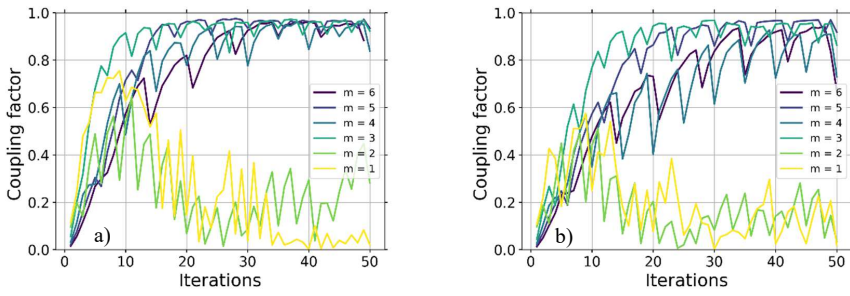


Fig. 3 Coupling factor for different settings of m and a) $dz = 1 \mu\text{m}$ and b) $dz = 0.5 \mu\text{m}$

reduced by Δn and for $D > 0$, it increases by Δn , with the restriction that $n_{clad} \leq n_b \leq n_{wg}$. Furthermore, only one layer of pixels with intermediate values is permitted between pixels with n_{wg} and n_{clad} (Fig. 1). After $M \geq m$ iterations (cycle length), the intermediate refractive indices are converted back to the original materials. This is followed by a linearization step. For this step, the structure is divided in sections of length L_{Lin} (linearization length), where, the border of the structure is linearized. This process removes small ripples, enhancing the accuracy of the BPM simulation, and facilitating the subsequent fabrication of the optimized waveguide structure. Thanks to its efficiency, the BPM-based method can simultaneously optimize multiple wavelengths or polarizations.

III. EXAMPLE DESIGN

As in [3, 4], the capabilities of the IWFM method are demonstrated by designing a TE_0 to TE_1 mode converter. Fig. 2 illustrates the $220 \mu\text{m}$ long tapered initial structure with $1.8 \mu\text{m}$ deep etched rib waveguide structure based on an InP platform. Optimization is performed for the wavelengths 1.55 , 1.61 and $1.6 \mu\text{m}$, with a linearization length of $2 \mu\text{m}$. The pixel size ($dx \times dz$) of the optimization grid is $0.05 \mu\text{m} \times 1.0 \mu\text{m}$ or $0.05 \mu\text{m} \times 0.5 \mu\text{m}$. For the intermediate values the cycle length is set to $M = m + 1$. Fig. 3 presents a study of the number of intermediate values used in the IWFM method for the design of the TE_0 to TE_1 mode converter. For both pixel sizes, the classical WFM method with $m = 1$ fails to converge to a solution. For $m \geq 3$, the IWFM method converges to a viable solution, with the setting $m = 5$ delivering the highest field conversion. The conversion factors for $dz = 1 \mu\text{m}$ are generally higher as for $dz = 0.5 \mu\text{m}$, due to less scattering. The dips in the curves are due to the refractive index conversion and linearization step, altering the computed structure and typically worsen field conversion. Given that the IWFM method is based on the approximate BPM, the result for $m = 5$, $dz = 1 \mu\text{m}$ is verified through a finite

difference time domain (FDTD) simulation. For the wavelength of $1.55 \mu\text{m}$ the FDTD coupling efficiency for the TE_0 to TE_1 mode coupler is -0.29 dB , being in excellent agreement with the -0.30 dB of the IWFM method after 50 iterations. Fig. 4 shows the intensity distribution of the designed converter waveguide. The 50 iterations for generating the optimized result for $m = 5$, $dz = 1$ took approximately 2 hours on a 64-core simulation server, whereas the validation via the FDTD method took about 10 hours. The example shows, that introducing intermediate values with $m > 2$ generally enhances the performance of the optimization, making the IWFM method superior to the standard WFM method. However, determining the optimal settings for m , M , and dz requires conducting a series of optimizations.

IV. CONCLUSION

We have presented the IWFM method, an enhanced WFM method, by allowing the use of intermediate values for the refractive index during optimization. This adaptation enables the WFM method to be effectively employed in the design of high index contrast InP waveguide structures. A robust FDTD simulation confirmed the efficiency of the results produced by this adapted WFM method.

REFERENCES

- [1] T. Hashimoto, T. Saida, I. Ogawa, M. Kohtoku, T. Shibata, and H. Takahashi, "Optical circuit design based on a wavefront-matching method," *OPTICS LETTERS* / Vol. 30, No. 19 / October 1, 2005
- [2] S. Makino, T. Fujisawa and K. Saitoh, "Wavefront Matching Method Based on Full-Vector Finite-Element Beam Propagation Method for Polarization Control Devices," in *Journal of Lightwave Technology*, vol. 35, no. 14, pp. 2840-2845, 15 July 15, 2017, doi: 10.1109/JLT.2017.270048
- [3] Y. Sawada, T. Sato, T. Fujisawa and K. Saitoh, "Development of the Wavefront Matching Method Based on the 3-D Finite-Element Method and Its Application to Si-wire Mode Converters," in *Journal of Lightwave Technology*, vol. 36, no. 17, pp. 3652-3659, 1 Sept. 1, 2018, doi: 10.1109/JLT.2018.2843383
- [4] Y. Sawada, T. Fujisawa, T. Sato and K. Saitoh, "A Novel Algorithm of Wavefront-Matching Method for Stable and Efficient Design of Si Waveguides," in *IEEE Photonics Technology Letters*, vol. 34, no. 7, pp. 359-362, 1 April 1, 2022, doi: 10.1109/LPT.2022.3159830.
- [5] Y. Sawada, T. Fujisawa, T. Sato and K. Saitoh, "Comparison of Scalar and Vector WFM Method Through the Design of High- Δ Waveguide Lenses," in *IEEE Photonics Technology Letters*, vol. 34, no. 10, pp. 533-536, 15 May 15, 2022, doi: 10.1109/LPT.2022.3170940.
- [6] Takeshi Fujisawa, Tsutomu Kitoh, Kei Watanabe, Kenya Suzuki, Masaki Kotoku, and Hiroshi Takahashi, "Wide-bandwidth, low-waveguide-width-sensitivity InP-based multimode interference coupler designed by wavefront matching method," *IEICE Electronics Express*, Vol. 8, No. 24, 2100–2105, November, 2011

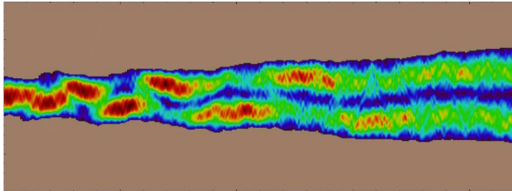



Fig. 4 Intensity distribution for the optimized converter structure with the setting $m = 5$, $dz = 1 \mu\text{m}$

Exciton Dynamics and Charge Carrier Transport in SiGeSn based MQW devices

1st Alan Abdi 

Chair for Communication Technology
TU Dortmund University
Dortmund, Germany
alan.abdi@tu-dortmund.de

2nd Tim Alexewicz

Chair for Communication Technology
TU Dortmund University
Dortmund, Germany
tim.alexewicz@tu-dortmund.de

3rd Dirk Schulz 

Chair for Communication Technology
TU Dortmund University
Dortmund, Germany
dirk2.schulz@tu-dortmund.de

Abstract—SiGeSn alloys have emerged as a versatile material system for integrated photonics, combining tunable bandgap engineering with strong light-matter interaction across the near- to mid-infrared spectrum. In this work, we investigate the dynamics of excitons and charge carriers in SiGeSn quantum-confined heterostructures using a tight-binding framework. The coupled equations of motion for electrons, holes, and excitons are solved in Liouville superoperator form, enabling a modular incorporation of optical excitation, relaxation, and boundary conditions via a density-matrix approach. The interplay between electronic and optical responses is explicitly modeled, with a coherent light-field source term driving the system out of equilibrium, including polarization dynamics and absorption. Our method has been applied to study non-equilibrium exciton dynamics in SiGeSn nanostructures and complements recent experimental work on MQW devices by reproducing key trends in the device performance, thereby offering a predictive and scalable framework for the design of integrated mid-infrared photonic components.

Index Terms—SiGeSn heterostructures, exciton dynamics, tight-binding, density matrix, Liouville superoperator, photonics

I. INTRODUCTION

Experimental studies have demonstrated improved LED performance in SiGeSn-based MQW structures compared to homojunction devices, due to enhanced electron confinement and efficient light emission, key for electrically pumped GeSn lasers [1]. In this work, we explore the potential of SiGeSn heterostructures for light-emitting applications. To this end, we develop a tight-binding-based simulation framework that captures both the electronic and optical properties of the structures, explicitly including Coulomb interactions between charge carriers. While similar modeling approaches have been applied, for instance to describe higher-harmonic generation in CdSe semiconductors [2], excitonic effects are often neglected in those studies.

We adopt a two-band, spin-less Hubbard formalism and employ localized Wannier functions. Phenomenological scattering, dephasing, and relaxation terms and the Coulomb interaction between excitons are taken into account. To solve the transient dynamics, we employ the master equation in Lindblad form. The observables studied include the electron

and hole populations, the current, the absorption, and the exciton dynamics.

II. CONCEPT

The dynamics of the coupled electron-hole-photon system are governed by the following tight-binding Hamiltonian

$$\hat{H} = \hat{H}_0 + \hat{H}_{em} + \hat{H}_C, \quad (1)$$

where each term represents a significant physical contribution:

- \hat{H}_0 : The free tight-binding Hamiltonian, describing the kinetic energy and on-site potentials of electrons and holes.
- \hat{H}_{em} : The light-matter interaction in dipole approximation, coupling the electronic system to an external optical field.
- \hat{H}_C : The Coulomb interaction between electrons and holes.

The Heisenberg equation of motion for any operator \hat{O} (e.g., excitonic \hat{Y}_{ij} , electron \hat{C}_{ij} , or hole \hat{D}_{ij} operators) yields:

$$i\hbar \frac{d}{dt} \hat{O} = [\hat{O}, \hat{H}] = [\hat{O}, \hat{H}_0] + [\hat{O}, \hat{H}_{em}] + [\hat{O}, \hat{H}_C]. \quad (2)$$

By systematically evaluating these commutators as in [3], we derive a set of coupled nonlinear equations for the electronic and excitonic variables. To numerically solve this system, we use the master equation in Lindblad form

$$\frac{d}{dt} \vec{\Psi} = \mathcal{L} \vec{\Psi} + \vec{F}[\vec{\Psi}], \quad (3)$$

with \mathcal{L} being the Liouville superoperator, containing the linear dynamics (coherent evolution, dissipation, and absorption) and $\vec{F}[\vec{\Psi}]$ capturing the nonlinear many-body effects, such as Coulomb renormalization and optical driving terms. The state vector $\vec{\Psi}$ contains the site-resolved coefficients of the tight-binding basis.

III. NUMERICAL EVALUATION

We first analyze a single quantum well (SQW) cell consisting of a GeSn well embedded in SiGeSn barriers, where the well width is varied to assess its influence on the optical properties. In a next step, several such cells are periodically arranged to form a multi-quantum well (MQW) structure,

This work was supported by the Deutsche Forschungsgemeinschaft DFG under Grant SCHU 1016/8-3.

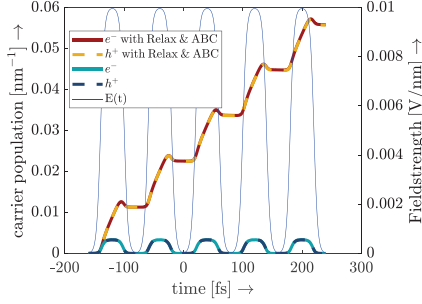


Fig. 1: Carrier excitation under a periodic modulated field. Relaxation and absorbing boundaries enable smooth carrier buildup and suppress reflections.

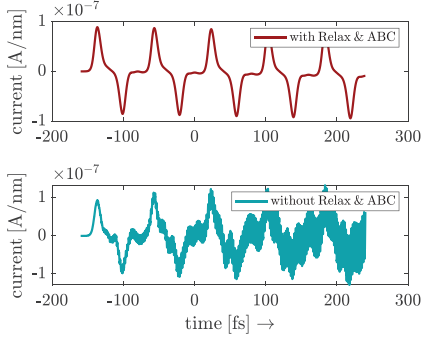


Fig. 2: Time evolution of the current density. The top panel demonstrates the effect of including relaxation and ABC, leading to a cleaner current flow.

allowing us to study the influence of inter-well coupling within the tight-binding framework. The first two Figs. 1 and 2 highlight the electronic structure and carrier dynamics by showing the charge carrier densities and the resulting current flow through the structure. In this context, we demonstrate the influence of relaxation terms and the use of an absorbing boundary condition (ABC) similar to [2] at the edges of the simulation domain, both of which significantly affect the system's behavior and the steady-state transport characteristics.

In contrast, Figs. 3 and 4 focus on the optical response of the system after excitation with an oscillating gaussian pulse by comparing the absorption spectra with and without Coulomb interaction. Additionally, a SQW is compared with a corresponding MQW structure composed of 5 cells to assess how quantum confinement and layer repetition influence absorption strength and spectral features.

IV. DISCUSSION AND CONCLUSION

We have developed a tight-binding-based simulation framework to study the electronic and optical properties of SiGeSn quantum well heterostructures, explicitly including Coulomb

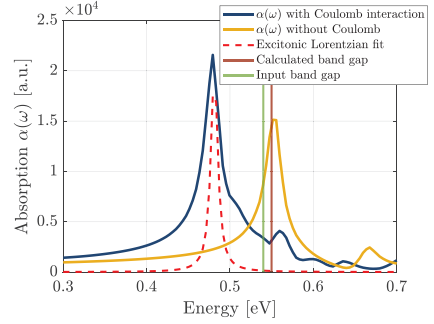


Fig. 3: Absorption spectra $\alpha(\omega)$ with (blue) and without (orange) Coulomb interaction, showing a redshift due to excitonic effects. The Lorentzian fit (red dashed) serves as a reference for both spectra. The red and green lines indicate the simulated and input band gaps, respectively.

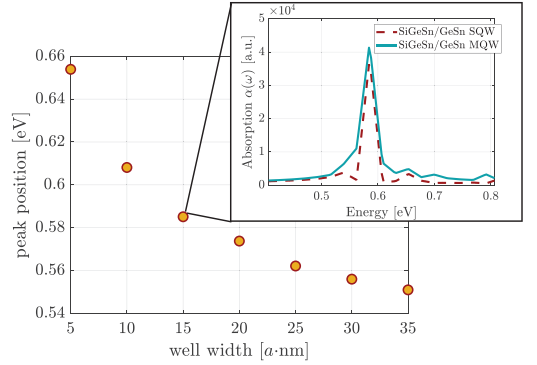


Fig. 4: Simulated absorption peak positions for varying well widths in SiGeSn/GeSn heterostructures. As the well width increases, the peak position approaches the bulk band-gap. The inset compares the normalized absorption spectrum of a single quantum well (SQW) and a multiple quantum well (MQW, 5 cells) structure at a well width of 15 nm, illustrating enhanced absorption in the MQW case.

interaction and external fields. The model complements experimental studies by providing detailed insight into carrier dynamics and absorption processes across different well widths. Simulations reveal how relaxation and boundary effects influence carrier transport, while the optical response highlights excitonic shifts and enhanced absorption in MQW structures. These results establish a basis for the predictive design of efficient mid-infrared emitters using group-IV heterostructures.

REFERENCES

- [1] Stange, D. et al. *Short-wave infrared LEDs from GeSn/SiGeSn multiple quantum wells*, Optica 4, 185-188 (2017).
- [2] Peschel, U., Thümmel, M., Lettau, T., Gräfe, S. and Busch, K. *Two-particle tight-binding description of higher-harmonic generation in semiconductor nanostructures*, Phys. Rev. B **106**, 24 (2022).
- [3] Hahn, W. and Stahl, A. *Self-Consistent Field Theory Applied to the Semiconductor Band Edge*, phys. stat. sol. **124**, **167**, 167-179 (1984).

Ultrafast grating-based spin VCSELs

1st Oliver Jan Hejtman

Faculty of Materials Science and Technology
VSB-Technical University of Ostrava
Ostrava-Poruba, Czech Republic
oliver.jan.hejtman@vsb.cz

2nd Tibor Fördös

Faculty of Materials Science and Technology
VSB-Technical University of Ostrava
Ostrava-Poruba, Czech Republic
tibor.fordos@vsb.cz

3rd Maciej Dems

Institute of Physics
Lodz University of Technology
Łódź, Poland
maciej.dems@p.lodz.pl

Abstract—Conventional VCSELs are bandwidth-limited to 30–50 GHz due to carrier dynamics in intensity modulation. Polarization modulation (PM) via birefringence-induced mode splitting enables much higher frequencies, offering a path toward ultrafast optical interconnects. We employ Plane-Wave Admittance Method (PWAM) to design monolithic surface gratings that engineer high phase anisotropy (γ_p) while minimizing loss anisotropy (γ_a). By optimizing grating period, fill factor, depth, and cap layer thickness, we achieve >280 GHz frequency splitting with low dichroism and practical photon lifetimes. Our results present a compact, integrable solution for birefringence control in spin-VCSELs, paving the way for efficient PM-based data transmission.

Index Terms—spin-VCSEL, grating, anisotropy, Polarization Modulation

I. INTRODUCTION

Vertical-Cavity Surface-Emitting Lasers (VCSELs) are compact, energy-efficient light sources used in optical interconnects, 3D sensing, and photonic integration. While conventional VCSELs rely on intensity modulation (IM), their bandwidth is fundamentally limited to 30–50 GHz by carrier dynamics and photon lifetime [1].

Polarization modulation (PM) via birefringence-induced splitting in spin-VCSELs offers a high-speed alternative. Here, oscillations between orthogonal polarizations are governed by the birefringence-induced frequency splitting $\delta\nu = \gamma_p/\pi$, with values exceeding 200 GHz demonstrated in GaAs-based devices [2], [3]. Key to effective PM is combining large birefringence (high γ_p) with low dichroism (low γ_a), ensuring stable, ultrafast polarization switching.

Early methods to enhance birefringence used strain engineering, mechanical stress, or thermal tuning, but suffered from complexity, hysteresis, or device degradation. Integrated surface gratings emerged as a compact alternative, allowing engineered birefringence with reduced fabrication overhead [3], [4]. However, previous designs often introduced excess loss anisotropy, reducing photon lifetime τ and damping polarization oscillations.

Our work builds on these efforts by optimizing grating geometry and cap layer thickness to achieve over 280 GHz

frequency splitting with near-zero γ_a and practical τ , enabling efficient PM beyond the limits of IM.

II. GRATING DESIGN FOR HIGH LIFETIMES

VCSELs lack inherent polarization preference due to their symmetric cavity and polarization-independent Bragg mirrors. Although weak polarization selection can arise from crystal alignment, the two orthogonal modes remain nearly degenerate, making polarization switching likely under small perturbations.

To suppress this instability, we introduce anisotropy via a monolithic GaAs surface grating [5], integrated into a VCSEL emitting at $\lambda = 980$ nm. The grating, infinite along the y -axis, is defined by pitch L , fill factor f , and lamella thickness d_{grat} . It breaks in-plane symmetry, splitting resonance conditions for TE and TM modes ($\lambda_x \neq \lambda_y$), as discussed in the following Section.

Grating performance depends strongly on L , which governs three regimes: diffraction, high reflectivity, and effective permittivity (Fig. 1). Scaling L shifts these regions spectrally, enabling design around the VCSEL emission. Fig. 1a–1c show reflectivity evolution with $L = 0.28, 0.56$, and $0.84 \mu\text{m}$ (scaling by factors of 1–3). We select $L = 0.84 \mu\text{m}$ to center the emission in the high-reflectivity regime, which also aligns with typical lithography limits.

The fill factor f is then optimized at this fixed L . In this case, $f = 0.6$ yields high reflectivity $\geq 70\%$ for both polarizations across a broad thickness range. This ensures similar photon lifetimes and reduced polarization-dependent loss. Modal properties found using the Fourier modal method [6] are examined.

III. GRATING DESIGN FOR ULTRAFAST MODULATION

To enable polarization switching, a large frequency separation between TE and TM modes—termed phase anisotropy γ_p —is essential. It is defined as:

$$\gamma_p \approx \pi c \left| \frac{1}{\Re(\lambda_{\text{TE}})} - \frac{1}{\Re(\lambda_{\text{TM}})} \right| \quad (1)$$

yielding the oscillation frequency $\delta\nu = \gamma_p/\pi$. Conversely, loss anisotropy γ_a arises from differences in modal losses:

$$\gamma_a = \frac{|\Im(\omega_{\text{TE}}) - \Im(\omega_{\text{TM}})|}{2} \quad (2)$$

This work was supported in part by project No. CZ.02.01.01/00/22_008/0004631- "Materials and Technologies for Sustainable Development", Ministry of Education, Youth and Sports of the Czech Republic under SP2025/090, GACR under 25-15775S and REFRESH under CZ.10.03.01/00/22_003/0000048.

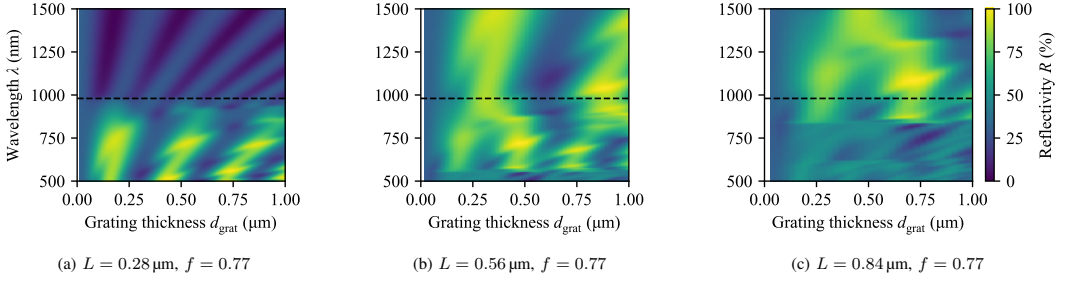


Fig. 1: Calculated TE reflectivity on GaAs grating. The band edge shifts as period increases from $L = 0.28 \mu\text{m}$ to $0.56 \mu\text{m}$ and $0.84 \mu\text{m}$, scaling by factors of 2 and 3, respectively. This vertical shift of boundaries is independent of f and is identical for TM polarization.

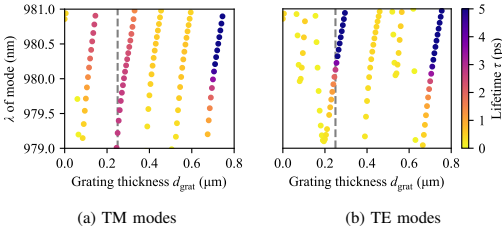


Fig. 2: Resonant wavelengths with photon lifetimes for TE and TM modes of a VCSEL with $d_{\text{cap}} = 100 \text{ nm}$, $L = 0.84 \mu\text{m}$, and $f = 0.4$. The gray dashed line highlights $d_{\text{grat}} = 0.25 \mu\text{m}$.

γ_a is undesired — it causes the polarization to stabilise at the mode (symmetry) with the higher lifetime, thus removing the polarization oscillation behaviour. Moreover, loss anisotropy reduces $\delta\nu$ via $\delta\nu = (\gamma_p - \alpha\gamma_a)/\pi$, where α is line-width enhancement factor, so it must be minimized.

We scanned grating thicknesses from $0 - 1 \mu\text{m}$, optimizing γ_p and γ_a by calculating them from the complex frequencies of the found modes. A first optimal point was found at $d_{\text{grat}} = 0.58 \mu\text{m}$ with $\gamma_p = 159 \text{ GHz}$ and acceptable photon lifetimes. A second viable solution at $d_{\text{grat}} = 0.30 \mu\text{m}$ showed lower lifetimes but significantly reduced γ_a .

To enhance birefringence, the number of top DBR pairs was reduced from 15 to 10, increasing γ_p to 594 GHz but also γ_a to 32.5 ns^{-1} . To mitigate this, we modified the cap layer thickness d_{cap} and re-optimized the grating to $d_{\text{grat}} = 0.23 \mu\text{m}$. This shifted the modal spectrum while enabling lower losses at $d_{\text{cap}} = 105 \text{ nm}$, reaching $\gamma_p = 711 \text{ GHz}$ and $\gamma_a = 8.7 \text{ ns}^{-1}$. However, the photon lifetimes dropped below 1 ps .

To recover τ_{ph} , we refined the fill factor to $f = 0.4$, improving both τ_{TM} and τ_{TE} to $\approx 2.7 \text{ ps}$ while maintaining high γ_p . A final d_{cap} adjustment to 100 nm yielded matched lifetimes and minimized dichroism to $\gamma_a = 0.01 \text{ ns}^{-1}$ at $\gamma_p = 889 \text{ GHz}$, resulting in a splitting of 283 GHz .

IV. CONCLUSION

We have simulated VCSELs with surface gratings using the Fourier modal method, addressing the need for compact devices with fabrication-ready birefringence control for ultra-fast polarization dynamics [4]. Our results show that tailoring grating parameters enables high phase anisotropy γ_p while minimizing loss anisotropy γ_a —a key challenge in birefringent VCSELs—without compromising photon lifetime τ . The grating period L is tuned to align the reflectivity peak with the emission wavelength, the fill factor f ensures $>85\%$ reflectivity for both TE and TM modes, and d_{grat} is optimized for birefringence. Loss balancing is achieved by adjusting the cap layer thickness d_{cap} . This method also offers a path to compensate for interface anisotropy in realistic devices.

REFERENCES

- [1] N. Ledentsov, M. Agustin, V. Shchukin, J.-R. Kropp, N. Ledentsov, L. Chorchos, J. Turkiewicz, Z. Khan, C.-L. Cheng, J.-W. Shi, and N. Cherkashin, “Quantum dot 850 nm vcsels with extreme high temperature stability operating at bit rates up to 25 Gbit/s at 150°C ,” *Solid-State Electronics*, vol. 155, 03 2019.
- [2] M. Lindemann, G. Xu, T. Pusch, R. Michalzik, M. Hofmann, I. Žutić, and N. Gerhardt, “Ultrafast spin-lasers,” *Nature*, vol. 568, pp. 1–4, 04 2019.
- [3] T. Pusch, P. Debernardi, M. Lindemann, F. Erb, N. Gerhardt, M. Hofmann, and R. Michalzik, “Vertical-cavity surface-emitting laser with integrated surface grating for high birefringence splitting,” *Electronics Letters*, vol. 55, 09 2019.
- [4] M. Lindemann, N. Jung, N. Manrique-Nieto, T. Pusch, R. Michalzik, N. Gerhardt, and M. Hofmann, “Polarization dynamics in spin-vcsels with integrated surface grating for high birefringence splitting,” *Electronics Letters*, vol. 59, 07 2023.
- [5] M. Gębski, M. Dems, A. Szerling, M. Motyka, L. Marona, R. Kruska, D. Urbańczyk, M. Walczakowski, N. Pałka, A. Wójcik-Jedlińska, Q. J. Wang, D. H. Zhang, M. Bugajski, M. Wasiak, and T. Czystanowski, “Monolithic high-index contrast grating: A material independent high-reflectance VCSEL mirror,” *Opt. Express*, vol. 23, no. 9, p. 11674, 2015.
- [6] M. Dems, “Modelling of high-contrast grating mirrors. The impact of imperfections on their performance in VCSELs,” *Opto-Electronics Rev.*, vol. 19, no. 3, pp. 340–345, 2011.

Controlling Spontaneous Emission in SiC Pillar Metasurface with Color Centers

1st Mohammed Ashahar Ahamad
Department of Physics
Aligarh Muslim University
Aligarh, UP 202002, India
 ashaharamu2020@gmail.com

2nd Faraz Ahmed Inam
Department of Physics
Aligarh Muslim University
Aligarh, UP 202002, India
 faraz.inam@gmail.com

Abstract—Using COMSOL RF Module, we fabricate a periodic Silicon carbide (SiC) pillar lattice embedded with Silicon vacancy (SiV) centers emitting at 862 nm. Engineered pillar geometry and spacing induce coherent Mie resonances, enhancing the local optical density of states. We achieve over fifteen-fold increase in SiV spontaneous decay rate via resonant field confinement and inter-pillar coupling, demonstrating a route to boost solid-state quantum emitter performance.

Index Terms—Mie resonances, single photon, decay rate.

I. INTRODUCTION

Metasurfaces are ultrathin nanostructures engineered to manipulate electromagnetic waves via resonant interactions with electric and magnetic fields [1], [2]. Silicon carbide (SiC) has gained attention in metasurface design due to its robust optical properties and ability to host color centers such as silicon vacancies (SiV), which act as stable single-photon sources at 862 nm [3]. In this work, we fabricate a periodic array of SiC nanopillars, each embedded with a SiV center. These wavelength-scale pillars act as Mie resonators, where dipole emission excites multipolar charges and current distributions that support Mie resonances [4]. The interference of these multipolar modes enhances the local optical density of states (LDOS), enabling control over spontaneous emission [5]. We further analyze how the geometry and environment influence scattering efficiency through individual multipole contributions, providing insights into emitter–metasurface coupling mechanisms [6]. The total scattering efficiency (SE) of different multipoles is expressed as [4]. In a periodic SiC–pillar array, inter-pillar coupling of Mie resonances boosts the overall scattering efficiency [7]. The coherent superposition of these multipolar modes increases the local density of optical states (LDOS), directly governing the dipole’s spontaneous decay rate [8]. Formally, the LDOS at frequency ω and position \mathbf{r} is given by

$$\rho(\omega, \mathbf{r}) = \sum_{\mathbf{k}, \sigma} |\hat{\mathbf{d}} \cdot \mathbf{E}_{\mathbf{k}, \sigma}(\mathbf{r})|^2 \delta(\omega - \omega_{\mathbf{k}, \sigma}). \quad (1)$$

Here, $\hat{\mathbf{d}}$ is the unit vector specifying the direction of the transition dipole moment, \mathbf{E} is the total electric field at the emitter, comprising its direct emission plus the fields scattered and reflected by the surrounding periodic pillar [9]. Thus, by tailoring Mie-scattering modes with periodicity, one can

precisely tune the local field at the source and, hence, the emitter’s decay dynamics.

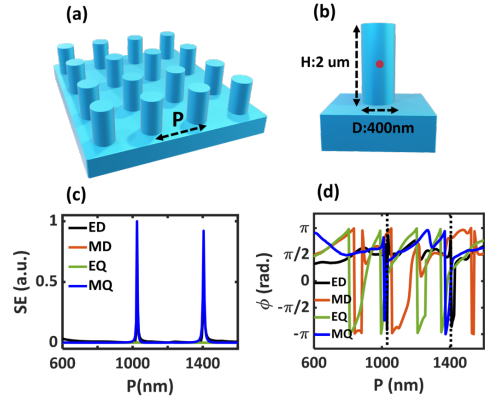


Fig. 1. (a) and (b) are schematics of SiC pillar lattice and unit cell embedded with dipole emitter, respectively. (c) and (d) Mie resonance response and corresponding phases as a function of the periodicity of the Pillar, respectively.

II. MATERIALS AND METHODS

Simulations were performed using COMSOL RF module with periodic boundary and scattering boundary condition applied on the domain of unit cell to generate a periodic array of pillars, with mesh sizes between 1 nm and $\lambda/7$. SiC optical constants were taken from Singh et al. [10].

A. Scattering efficiency calculation

SE was calculated semi-analytically by integrating electric fields inside the nanopillars using custom code that is already programmed by us inside COMSOL.

B. Relative decay rate calculation

The SiV center was modeled as a point dipole. Relative decay rate was computed as $\Gamma_{rel} = \gamma/\gamma_{\infty} = P/P_{\infty}$ [11], where P is the power emitted by point dipole when embedded in SiC pillars lattice and P_{∞} is the power due to the emission of point dipole in the bulk SiC.

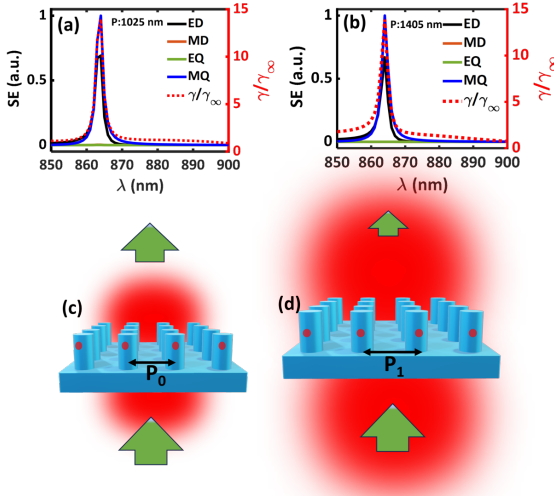


Fig. 2. (a) and (b) The spectral response of Mie-scattering moments together SiV relative decay rate in the SiC pillar lattice as a function of wavelength for P_1 resonant values respectively under point dipole excitation. (c) and (d) The schematic representation of tuning the SiV emission with the lattice periodicity, P_0 (off-resonant) and P_1 (resonant) respectively.

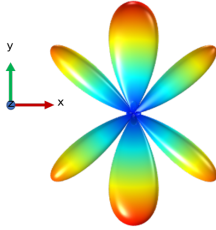


Fig. 3. represents the 2D far-field emission spectra confined in the x-y plane only.

III. RESULTS AND DISCUSSION

We have computationally optimized the meta-surface using a commercial Comsol Multiphysics RF module to achieve the optimum dimension of the pillar lattice shown in schematic Fig. 1. (a) and (b). The optimization of the meta-surface is done using a plane wave having excitation wavelength λ_{exc} : 862 nm moving in $\pm z$ direction with electric field aligned in the $+x$ direction. Finally by fixing the optimized values of the pillars, the periodicity (pillars to pillars distance), P of the metasurface is optimized from $P:600$ nm to $P:1600$ nm shown in Fig. 1 (c). The maximum value in SE is observed for electric dipole (ED) and magnetic quadrupole (MQ) at periodicity of $P:1025$ nm and $P:1405$ nm respectively, with ED and MQ being in phase at this resonant periodicity P_1 Fig. 1 (d). Finally, we obtained SE and relative decay rate as a function of the wavelength for the resonant Periodicity P_1 over

the spectral ranges from 850 nm to 900 nm shown in Fig. 2 (a) and (b). It is observed that both the ED and MQ are well resonant around the 862 nm wavelength. Thus, their coherent superposition results in increasing the total electric field E at the source position and hence the local density of optical states (LDOS) (refers to Eq 1). This led to an enhancement of almost 15 times in the relative decay rate of the color center embedded in the SiC pillars. Further, we get a less bright SiV emission when interaction among Pillars being out of phase that is at P_0 and a very bright emission at P_1 when interaction being in phase shown in Fig. 2 (c) and (d) respectively.

IV. CONCLUSION AND FUTURE WORK

By tuning the metasurface periodicity, we selectively excite the electric dipole and magnetic quadrupole Mie resonances, which modulate the LDOS and enhance the emitter's decay rate by 15-fold, promising for quantum technological applications. However, the far-field emission remains largely non-directional (Fig. 3), indicating that control over the relative phases of these Mie modes is required to achieve directional emission.

V. ACKNOWLEDGEMENTS

We acknowledge the UGC MHRD, INDIA, for SRF.

REFERENCES

- [1] Stanislav B. Glybovski, Sergei A. Tretyakov, Pavel A. Belov, Yuri S. Kivshar, Constantin R. Simovski, Metasurfaces: From microwaves to visible, Physics Reports, Volume 634, 2016, Pages 1-72, ISSN 0370-1573, <https://doi.org/10.1016/j.physrep.2016.04.004>.
- [2] J. Wang, "Metasurfaces enabling structured light manipulation: advances and perspectives [Invited]," Chin. Opt. Lett. 16, 050006- (2018).
- [3] Castelletto, Stefania, and Alberto Boretti. "Silicon carbide color centers for quantum applications." Journal of Physics: Photonics 2.2 (2020): 022001.
- [4] R. Alaei, C. Rockstuhl, and I. Fernandez-Corbaton, "An electromagnetic multipole expansion beyond the long-wavelength approximation," Opt. Commun. 407, 17-21 (2018).
- [5] Ahamad, Mohammed Ashahar, et al. "Silicon carbide pillar lattice for controlling the spontaneous emission of embedded color centers." Journal of Lightwave Technology 42.2 (2023): 689-695.
- [6] H. K. Shamkhi, K. V. Baryshnikova, A. Sayanskiy, P. Kapitanova, P. D. Terekhov, P. Belov, A. Karabchevsky, A. B. Evlyukhin, Y. Kivshar, and A. S. Shalin, "Transverse scattering and generalized kerker effects in all-dielectric mie- resonant metaoptics," Phys. Rev. Lett. 122, 193905 (2019).
- [7] Bezares, Francisco J., et al. "Mie resonance-enhanced light absorption in periodic silicon nanopillar arrays." Optics Express 21.23 (2013): 27587-27601.
- [8] F. Inam, T. Gaebel, C. Bradac, L. Stewart, M. Withford, J. Dawes, J. Rabeau, and M. Steel, "Modification of spontaneous emission from nanodiamond colour centres on a structured surface," New J. Phys. 13, 073012 (2011).
- [9] Ahamad, Mohammed Ashahar, and Faraz Ahmed Inam. "Electromagnetic scattering controlled all-dielectric cavity-antenna for bright, directional, and purely radiative single-photon emission." Journal of Applied Physics 136.8 (2024).
- [10] S. Singh, J. Potopowicz, L. Van Uiter, and S. Wemple, "Nonlinear optical properties of hexagonal silicon carbide," Appl. Phys. Lett. 19, 53-56 (1971).
- [11] Y. Xu, J. S. Vuckovic, R. K. Lee, O. J. Painter, A. Scherer, and A. Yariv, "Finite-difference time-domain calculation of spontaneous emission lifetime in a microcavity," J. Opt. Soc. Am. B 16, 465 (1999).

Renormalization Theory and Monte Carlo Simulation of HgCdTe Single Carrier Avalanche Process

Runzhang Xie

State Key Laboratory of Infrared Physics
Shanghai Institute of Technical Physics, Chinese Academy of Sciences
Shanghai, China
xierunzhang@mail.sitp.ac.cn

Abstract—This paper presents a theoretical and computational framework that employs two methodologies to model the single-carrier avalanche process in HgCdTe: renormalization theory for microscopic mechanisms and Monte Carlo simulations for device-level behavior. This integrated approach overcomes the limitations of traditional deterministic models that cannot capturing the stochastic and non-local nature of impact ionization. Our results demonstrate the strong dependence of avalanche efficiency on electron incidence angles, providing valuable insights for device optimization. This work offers a robust methodology for designing next-generation infrared detectors with enhanced performance.

Keywords—HgCdTe, Single Carrier Avalanche Process, Renormalization Theory, Monte Carlo Simulation, Infrared Detectors

I. INTRODUCTION

Infrared detectors are foundational components in a vast range of scientific and technological applications, from remote sensing to critical military surveillance[1] and non-invasive medical imaging[2]. The ultimate performance of these devices, particularly in conditions of low-photon flux, is fundamentally constrained by their signal-to-noise ratio. To circumvent this limitation and achieve high sensitivity, avalanche photodiodes (APDs) have emerged as a critical technology[3]. By leveraging the intrinsic carrier multiplication process, APDs can amplify the signal significantly while maintaining low excess noise and preserving the detector's intrinsic temporal resolution.

The accurate and predictive modeling of the avalanche process is thus paramount for understanding and optimizing the performance of next-generation infrared detectors. Traditional modeling approaches, such as deterministic rate equations or simplified empirical fits based on local field assumptions (e.g., the Schockley's lucky-drift model)[4] fall short. They are fundamentally unable to capture the rich and intricate physics of impact ionization, which is inherently a stochastic, non-local, and rare-event phenomenon. These models neglect crucial details such as the carrier history-dependent effects and the statistical fluctuations that are dominant at the microscopic level, rendering them inadequate for precise device design and performance prediction. Consequently, a more rigorous theoretical and computational framework is required to achieve a comprehensive and predictive understanding of these complex dynamics.

Among the various semiconductor materials employed in infrared detection, mercury cadmium telluride (HgCdTe) is a

preeminent choice. [5] A key feature of HgCdTe is its ability to support near-ideal single-carrier avalanche behavior, a property that is highly effective at minimizing excess noise and making it a leading candidate for APDs with superior gain-bandwidth products. However, modeling the single-carrier avalanche process in HgCdTe remains a formidable challenge.[6] The complexity arises from both the intricate nature of the impact ionization dynamics and the multiscale character of carrier transport, which spans from the quantum-mechanical interactions at the atomic level to macroscopic device-scale behavior.

To address these fundamental modeling challenges, this paper presents two methodologies: renormalization theory for microscopic mechanisms and high-performance Monte Carlo simulations for device-level behavior. The renormalization approach provides a systematic way to coarse-grain the microscopic dynamics, revealing the universal scaling laws and collective phenomena that govern the avalanche process. Separately, the Monte Carlo method is employed as a powerful tool to accurately capture the full stochasticity and microscopic details of carrier transport and impact ionization events. Each method offers a robust solution for its respective domain, together providing a comprehensive understanding of the complex dynamics of the HgCdTe single-carrier avalanche process, and establishing a solid methodology for the design and optimization of advanced infrared detectors.

II. RENORMALIZATION THEORY OF SCATTERING IN SINGLE CARRIER AVALANCHE

The concept of renormalization, originally proposed by Kenneth G. Wilson in the context of critical phenomena and the Ising model, has since found widespread application in diverse fields such as quantum field theory and condensed matter physics.[7]

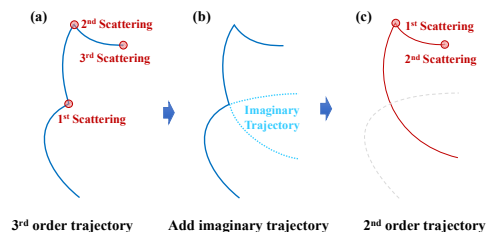


Fig. 1. Renormalization theory applied in electronic trajectory analysis

The core principle of renormalization theory lies in a scale-transformation approach, where a complex problem is

transformed into a new, equivalent problem that exhibits a recursive relationship with the original one. In the single-carrier avalanche process, electrons undergo a series of diverse scattering events. These scattering events significantly alter the electron's energy and momentum, making the overall avalanche process highly sensitive to these interactions. By initiating our analysis from a prior impact ionization event, we can assign an ordered index to each subsequent scattering process. This index serves not only as a unique identifier for each impact but also captures the inherent historical dependence of the process, as the N^{th} impact presupposes the occurrence of the preceding $N-1$ events. This scattering sequence is defined to terminate upon the next impact ionization event. A sequence containing Q scattering events is therefore denoted as a Q^{th} -order scattering sequence.

Upon analyzing these collision processes, we observe that the collection of all Q^{th} -order scattering sequences forms a set, denoted as $\{S_Q\}$. Under a first-order approximation, this set can be mapped subjectively to the set $\{S_{Q-1}\}$ via a specific operation[8]. By iteratively applying this recursive operation, a hierarchical, tree-like relationship can be established among all sets $\{S_Q\}$ of varying orders. This enables a renormalization group analysis on a scale defined by the order of the operation. Ultimately, this renormalization process provides a powerful means to systematically correct and refine the most critical microscopic scattering mechanisms that govern the electron avalanche process.

III. MONTE CARLO SIMULATION OF HgCdTe SINGLE CARRIER AVALANCHE PROCESS

Based on the idea of renormalization, our simulation framework is a Monte Carlo scheme designed to accurately model electron transport and avalanche processes in HgCdTe. As depicted in Fig. 2, the simulation follows a detailed, iterative process. It begins by initializing scattering rates, time resolution, and the electron's initial state, including its energy and momentum. Unlike traditional deterministic models, this stochastic approach is particularly well-suited for capturing the random and rare nature of impact ionization events.[9] The core of the scheme involves solving the non-parabolic electron dynamics to accurately describe the electron's motion within the device, providing a more realistic representation of carrier behavior than simplified models.

The simulation progresses by updating the electron's state and calculating the local electric field. The trajectory of each electron is tracked in a step-by-step manner until it either undergoes a scattering event, exits the device, or initiates an impact ionization event. This approach allows us to generate a rich dataset on carrier drift and scattering, providing a robust foundation for a comprehensive device noise analysis.

To understand the fundamental physics of the avalanche process, we investigated the behavior of electrons under different incidence angles: normal, oblique, and shallow. Fig. 2 illustrates the impact of these angles on the energy and number of electrons. From the electron energy distribution, we can see that as the incidence angle changes from normal to oblique to shallow, the phonon scattering of electrons intensifies. This is because electrons entering the active region at a steeper angle have a longer travel path and are more likely to undergo a greater number of phonon scattering events, which in turn reduces their energy and momentum.

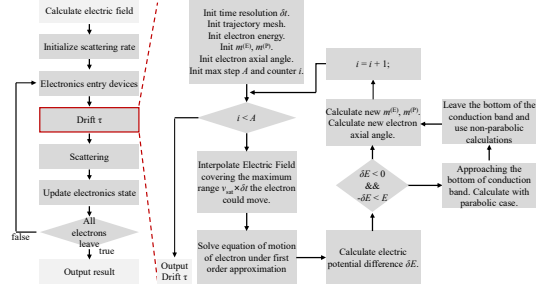


Fig. 2. Monte Carlo simulation program flowchart

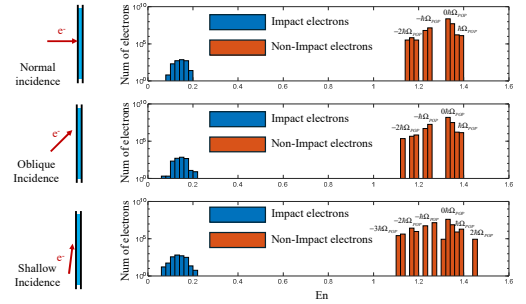


Fig. 3. Energy distribution of electrons incident at different angles

IV. CONCLUSION

In this paper, we successfully implemented a comprehensive framework that employs renormalization theory and Monte Carlo simulations to model the single-carrier avalanche process. Our approach provides a powerful tool for understanding this complex phenomenon by bridging the gap between microscopic physics and macroscopic device behavior.

REFERENCES

- [1] C. Park, J. Kim, and J. W. Hahn, "Integrated Infrared Signature Management with Multispectral Selective Absorber via Single-Port Grating Resonance," *Advanced Optical Materials*, vol. 9, no. 13, p. 2002225, 2021.
- [2] M. Moreno-Moreno, J. Fierrez, and J. Ortega-Garcia, "Biometrics beyond the Visible Spectrum: Imaging Technologies and Applications," in *Biometric ID Management and Multimodal Communication*, J. Fierrez, J. Ortega-Garcia, A. Esposito, A. Drygajlo, and M. Faundez-Zanuy, Eds., Berlin, Heidelberg: Springer, 2009, pp. 154–161.
- [3] J. Miao and C. Wang, "Avalanche photodetectors based on two-dimensional layered materials," *Nano Res.*, vol. 14, no. 6, pp. 1878–1888, 2021.
- [4] W. Shockley, "Problems related top-n junctions in silicon," *Czech J Phys*, vol. 11, no. 2, pp. 81–121, 1961.
- [5] M. A. Kinch, J. D. Beck, C.-F. Wan, F. Ma, and J. Campbell, "HgCdTe electron avalanche photodiodes," *J. Electron. Mater.*, vol. 33, no. 6, pp. 630–639, 2004.
- [6] P. Martyniuk *et al.*, "Infrared avalanche photodiodes from bulk to 2D materials," *Light Sci Appl*, vol. 12, no. 1, Art. no. 1, 2023.
- [7] K. G. Wilson, "The renormalization group and critical phenomena," *Rev. Mod. Phys.*, vol. 55, no. 3, pp. 583–600, 1983.
- [8] R. Xie *et al.*, "Spatial description theory of narrow-band single-carrier avalanche photodetectors," *Optics Express*, vol. 29, no. 11, pp. 16432–16446, 2021.
- [9] R. Xie *et al.*, "Role of neutral impurities and non-parabolic dispersive electrons in HgCdTe avalanche photodiodes," *Opt. Lett.*, vol. 50, no. 8, p. 2723, 2025.

Numerical Analysis of Different Impact Ionization Models in Single-Photon Avalanche Diodes

Li-An, Huang
Graduate Institute of Photonics and
Optoelectronics
National Taiwan University
Taipei, Taiwan

Jau Yang Wu
College of Industry-Academia
Innovation
National Taiwan University of Science
and Technology
Taipei, Taiwan

Yuh-Renn Wu*
Graduate Institute of Photonics and
Optoelectronics
National Taiwan University
Taipei, Taiwan
yrwu@ntu.edu.tw

Abstract—Two impact ionization models are examined within our custom TCAD framework to analyze the intensity and spatial distribution of impact ionization in the SPAD under different bias voltages and compare the breakdown voltage to the experimental results. The goal is to reduce the noise levels and improve the efficiency for quantum key distribution applications.

Keywords—TCAD, Impact Ionization, SPAD

I. INTRODUCTION

The Single-Photon Avalanche Diode (SPAD) is widely used in Quantum Key Distribution (QKD) and various other low-light applications such as Light Detection and Ranging (LIDAR). SPADs are capable of detecting single photons with extremely high sensitivity and precise timing resolution, making them essential in applications that require high-speed and low-noise photon detection. Its operation relies on the creation of a strong electric field to accelerate a photo-generated electron-hole pair. One of the most common methods is creating a pn junction, then applying high reverse bias to create a depletion region. As this carrier pair gains energy, it undergoes collisions with the crystal lattice, generating additional pairs through a process known as impact ionization multiplication, leading to an avalanche effect.

In this research, we first used our own TCAD software, 2D-DDCC, to replicate the results of the device in [1] (Schematic structure 2, S2) as shown in Fig.1 (a) and the doping concentration shown in Fig. 1(b). The 2D FEM based Poisson and drift-diffusion equation solver with cylindrical coordinates are used in the simulation. The generation term in the equation of continuity is used to treat the impact ionization. Two models, the Chynoweth model [2] and the Okuto-Crowell model [3], were applied to simulate the electric characteristics of SPAD to determine the avalanche breakdown voltage. By tuning the doping profile, we were able to modify the impact ionization distribution and even restrict the impact ionization process in the specific region to avoid the current flow through defect-prone areas such as the Si/SiO₂ interface.

A higher excess bias results in a stronger electric field, thereby increasing the trigger probability of the SPAD. Also, the shorter buildup time for avalanche reduces the time jitter [4]. Therefore, the applied voltage is usually set as high as the dark count rate allows. However, numerical simulation beyond the breakdown voltage fails due to unstable positive loop gain, which makes it hard to get convergence.

TABLE I DOPING CONCENTRATION OF EACH REGION

P++	N++	HVPW	HVNW	NBL	P-sub
1×10^{20}	1×10^{20}	2.8×10^{16}	1×10^{16}	9×10^{16}	5.8×10^{15}

Unit: 1/cm³

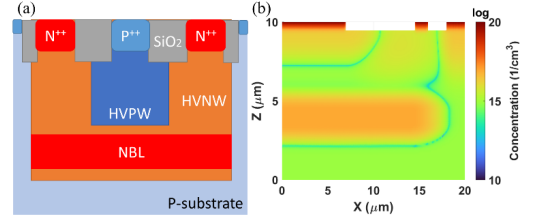


Fig 1 (a) Cross-sectional structure of the simulated device. (b) Doping concentration profile used in the simulation. Owing to structural symmetry, only one half of the device is considered in the simulation domain.

II. METHODOLOGY

Accurately modeling impact ionization is crucial for simulating the avalanche process, as even small variations in n th generation rate can substantially influence the simulation outcomes. We choose parameters of the Chynoweth model in [5] and the Okuto-Crowell model in [6]. The generation rate of impact ionization is calculated by the equations (1) and (2):

$$G_n = \alpha_n \times \frac{|J_n|}{e} \quad (1)$$

$$G_p = \alpha_p \times \frac{|J_p|}{e} \quad (2)$$

G_n and G_p represent the impact ionization generation rate for electron and hole, respectively, with unit cm⁻³. α_n, α_p are the impact coefficients for electrons and holes. J_n and J_p are the current densities for carriers, and e is the elementary charge. The Chynoweth model is shown in the equation below:

$$\alpha_n(E) = A_n \exp \left(\left| \frac{B_n}{E} \right| C_n \right) \quad (3)$$

$$\alpha_p(E) = A_p \exp \left(\left| \frac{B_p}{E} \right| C_p \right) \quad (4)$$

A_n and A_p are prefactors with the unit of cm⁻¹. B_n and B_p are the critical fields with unit V/cm. C_n and C_p are the tuning factors with no unit. E is the local field. The parameters for the Chynoweth model are shown in Table II

TABLE II CHYNOWETH MODEL PARAMETERS FOR SILICON

	A (1/cm)	B (V/cm)	C
Electron	7.03×10^5	1.231×10^6	1.0
Hole	1.582×10^6	2.036×10^6	1.0

Unlike the Chynoweth formulation, this extended model introduces a field-dependent polynomial prefactor and a

tunable exponential field sensitivity, allowing better agreement with experimental results over a wide range of electric fields. The impact ionization coefficient can be described in equations (5) and (6), and the magnitudes are shown in the Table. III.

$$\alpha_n(E) = A_n \left(\frac{E}{E_0} \right)^{\gamma_n} \exp \left(\left| \frac{B_n}{E} \right|^{\Delta_n} \right) \quad (5)$$

$$\alpha_p(E) = A_p \left(\frac{E}{E_0} \right)^{\gamma_p} \exp \left(\left| \frac{B_p}{E} \right|^{\Delta_p} \right) \quad (6)$$

TABLE III OKUTO-CROWELL MODEL PARAMETERS FOR SILICON

	A (1/cm)	B (V/cm)	γ	Δ
Electron	0.426	4.81×10^5	1.0	2.0
Hole	0.243	6.53×10^5	1.0	2.0

By comparing the two models in Fig 2, it is observed that significant differences arise under low electric field conditions; the Okuto-Crowell model was not activated until the electric field reached 4.2×10^4 V/cm. Even though the magnitude of the coefficients is quite small in the low electric field region, they cause remarkable influences in the calculation.

Considering the alignment between the current and the electric field, E in Eq (3) and (5) is substituted by $\frac{\bar{J}_n \cdot \bar{E}}{|\bar{J}_n|}$ and E in Eq. (4) and (6) is substituted by $E_{eff} = \frac{\bar{J}_p \cdot \bar{E}}{|\bar{J}_p|}$.

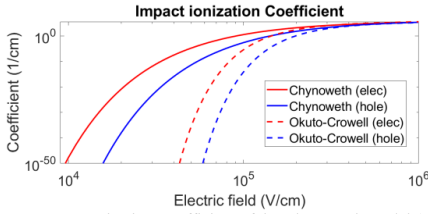


Fig 2 Impact Ionization Coefficient of the Chynoweth model (solid line) and the Okuto-Crowell model (dash line).

III. RESULT AND DISCUSSION

Fig. 8 in Ref. [1] shows that both simulation drain current and measured drain current were breakdown at about the $V_D = -77$ V, which is quite close to our results using the Okuto-Crowell model, and the magnitude of current is better agreement with the measured one than simulation results, so we'll focus on results of Okuto-Crowell model in following discussion. The Chynoweth model has a smaller breakdown voltage around -74V but exhibits a smoother transition in the region before avalanche breakdown.

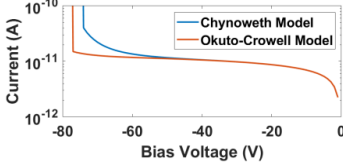


Fig 3 I-V characteristics of the device using two different models.

To investigate the avalanche mechanism in the device, the spatial distribution profiles of impact ionization were analyzed at the breakdown voltage and shown in Fig 4 (a) and 3(b). It's obviously the impact ionization was crowded in lateral and vertical junction between the HVPV and the HVNV. The separation of the distribution into two distinct regions is

presumed to result from the poor alignment of the current and the electric field.

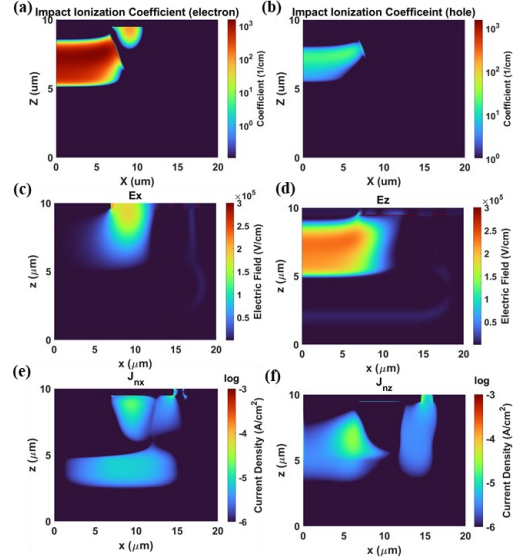


Fig 4 (a) and (b) show the impact ionization coefficient distribution of the Okuto-Crowell model at breakdown voltage ($V = -77V$) generated by electron and by hole, respectively. (c) and (d) show the electric field in the x direction and the z direction in a linear scale. (e) and (f) show the J_{nx} and J_{nz} in log scale, respectively.

IV. CONCLUSION

We successfully reproduced the experimental results by applying the Okuto-Crowell model. The simulated I-V characteristic exhibits a sharp transition at the breakdown voltage, indicating the occurrence of the avalanche effect. To prevent current from flowing into the region near the oxide, the lateral electric field must be suppressed, while a stronger vertical electric field is preferred. Additionally, the location of the impact ionization "hot spot" plays a critical role. Due to the non-uniform current distribution, the generation rate can vary significantly across the junction, even if the impact ionization coefficient remains nearly constant.

REFERENCES

- [1] J.-Y. Wu, P.-K. Lu, and S.-D. Lin, "Two-dimensional photo-mapping on CMOS single-photon avalanche diodes," *Optics Express*, vol. 22, no. 13, 2014, doi: 10.1364/oe.22.016462.
- [2] A. G. Chynoweth, "Ionization Rates for Electrons and Holes in Silicon," *Physical Review*, vol. 109, no. 5, pp. 1537–1540, 1958, doi: 10.1103/PhysRev.109.1537.
- [3] Y. Okuto and C. R. Crowell, "Ionization coefficients in semiconductors: A nonlocalized property," *Physical Review B*, vol. 10, no. 10, pp. 4284–4296, 1974, doi: 10.1103/PhysRevB.10.4284.
- [4] M. A. Itzler et al., "Avalanche buildup and propagation effects on photon-timing jitter in Si-SPAD with non-uniform electric field," presented at the Advanced Photon Counting Techniques III, 2009.
- [5] R. Van Overstraeten and H. De Man, "Measurement of the ionization rates in diffused silicon p-n junctions," *Solid-State Electronics*, vol. 13, no. 5, pp. 583–608, 1970, doi: 10.1016/0038-1101(70)90139-5.
- [6] Y. Okuto and C. R. Crowell, "Threshold energy effect on avalanche breakdown voltage in semiconductor junctions," *Solid-State Electronics*, vol. 18, no. 2, pp. 161–168, 1975, doi: 10.1016/0038-1101(75)90099-4.

Triple-mesa InGaAs/InP SPAD for heterogenous integration with InP waveguides

Davide Orlandelli
Dipartimento di Elettronica,
Informazione e Bioingegneria
Politecnico di Milano
Milano, Italy
*davide.orlandelli@polimi.it

Simona Sorrentino
Dipartimento di Elettronica,
Informazione e Bioingegneria
Politecnico di Milano
Milano, Italy
simona.sorrentino@polimi.it

Lorenzo Finazzi
Dipartimento di Elettronica,
Informazione e Bioingegneria
Politecnico di Milano
Milano, Italy
lorenzo.finazzi@polimi.it

Fabio Telesca
Dipartimento di Elettronica,
Informazione e Bioingegneria
Politecnico di Milano
Milano, Italy
fabio.telesca@polimi.it

Alberto Tosi, *Member, IEEE*
Dipartimento di Elettronica,
Informazione e Bioingegneria
Politecnico di Milano
Milano, Italy
*alberto.tosi@polimi.it

Abstract— We present the design of a novel triple mesa InGaAs/InP SPAD and compare it with a well-developed planar version. The mesa detector is considered as an easier path towards its heterogenous integration with InP waveguides for quantum photonic applications. Electrical and optical parameters of both the mesa and planar SPADs were investigated, at the typical temperature of 225 K for such devices. Despite the different geometries and approaches for electric field control and confinement, similar results can be obtained thanks to proper design and sizing. In particular, high photon detection efficiency (PDE) at 1550 nm wavelength was achieved (30% for the planar, 29% for the mesa), with front-side illumination.

Keywords—InGaAs/InP, single-photon avalanche diode (SPAD), mesa, avalanche photodiode (APD), TCAD simulations, photon detection efficiency, quantum communication, photonic integrated circuit (PIC)

I. INTRODUCTION

Single-photon detectors working in the short-wavelength infrared (SWIR) are a topic of great interest in many applications, such as quantum communications [1] and eye-safe light detection and ranging (LIDAR) [2]. Among SWIR single-photon detectors, InGaAs/InP SPADs are widely employed due to their good performance, low cost and compactness. The most widespread InGaAs/InP SPAD structure is planar, where a double zinc diffusion defines the detector active area. In applications like heterogenous integration with Photonic Integrated Circuits (PICs) the SPAD active area must be defined after the integration due to alignment between waveguide and detector active area. However, the temperature at which the double zinc diffusion is performed can severely damage the bonding of the detector wafer to that of the waveguides. Additionally, the zinc diffusion is not a widespread process and not all the III-V fabs have an established recipe. For these reasons, a new SPAD structure is here presented.

In this paper, we present the design of a novel triple mesa SPAD, which can solve the above-mentioned issues. The key parameters of SPAD detectors were simulated at the typical operating temperature of 225 K, and we provide a direct comparison with planar SPADs.

II. DEVICE STRUCTURE

The planar SPAD architecture is described in detail in [3] and it is shown in Fig. 1(a). The design of the mesa SPAD started from the core of the planar one, since the goal

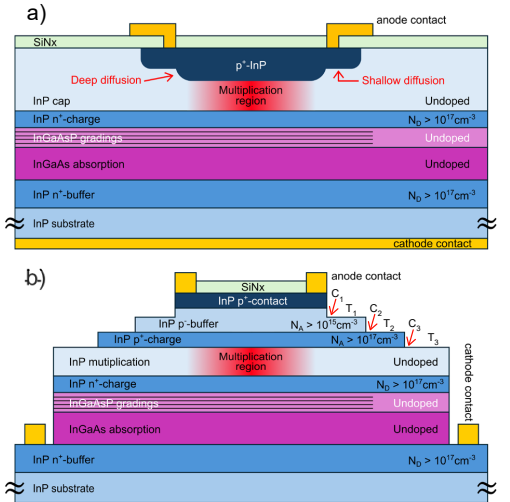


Fig. 1. a) Schematic layer stack of planar InGaAs/InP SPAD, with its typical separate absorption, grading, charge and multiplication (SAGCM) heterostructure. b) Schematic layer stack of mesa InGaAs/InP SPAD: bottom layers are as in the planar one, while additional layers are present in the top region.

was to replicate the state-of-the-art performance of the latter one. Indeed, the two approaches present the same active area size (25 μm diameter) and the same layer stack, up to the InP n^+ -charge, in order to obtain similar photon absorption probability and temporal response. Additionally, the InP multiplication layer of the mesa SPAD was sized to match the multiplication region thickness of the planar SPAD. The fundamental difference between the two structures is how the detector active area is defined. The planar SPAD presents a double zinc diffusion, while the mesa one relies on a series of etching steps. Indeed, the newly added layers (InP p^+ -charge, InP p^+ -buffer and InP p^+ -contact) are all etched, as they show mesa terraces (i.e., the stepped surface regions left after etching, called T_i in Fig. 1). The main cause of failures in the mesa SPAD is related to the critical corners (i.e., the corners at the end of the terraces, called C_i in Fig. 1) where the electric field reaches very large values. The InP p^+ -buffer is thus introduced to place the first critical corner (C_1) in a low electric field region. The mesa etch must be close enough to the InP p^+ -contact to confine the electric field following the latter, but it also needs to be far enough

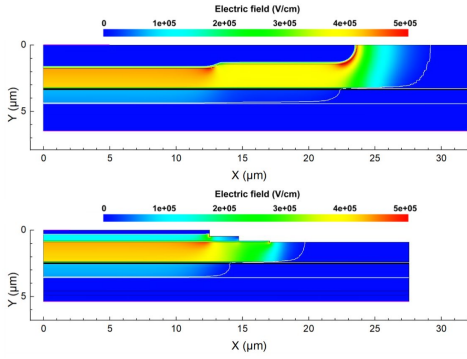


Fig. 2. Electric field distribution at 225 K for planar (top) and mesa (bottom) SPADs, both biased 5 V beyond their breakdown voltages. Thin white line represents depletion region.

from the contact/buffer and the charge/buffer interfaces to avoid premature breakdown. The InP p^+ -charge layer accommodates the electric field difference with the high field InP multiplication layer: it must be thin and highly doped and it contributes to the horizontal electric field confinement, preventing the depletion region from reaching the edges of the device. Finally, the introduction of two additional corners (C_2 and C_3) is beneficial in avoiding failures of the mesa SPAD because the high electric field results to be distributed over more angular points.

The width of the mesa terraces is another critical design parameter, since a proper balance must be found: terraces horizontally confine the electric field, thus they have to be long enough to avoid high electric field peaks at the critical corners. However, they must be limited to achieve better field confinement and to reduce the expected detector noise.

III. SIMULATION RESULTS

Electrical and optical simulations were performed using a technology computer-aided design (TCAD) simulator (Synopsys Sentaurus) to investigate the breakdown voltage, the electric field distribution, the avalanche triggering probability and the absorbed photon density. The simulations were then processed using MATLAB to derive an estimation of the detector PDE. The simulation parameters, such as ionization coefficients and complex refractive indexes, were calculated at 225 K following [4], and employing the datasets there reported.

A. Electrical simulations

Firstly, I-V curves were simulated at 225 K for both structures. The punch-through voltages for the planar and mesa SPADs are 53.7 V and 55 V, while the breakdown voltages are 67.5 V and 73.4 V, respectively. The higher breakdown voltage of the mesa is a consequence of the newly added layers in the detector layer stack. Then, the electric field was simulated with the SPADs biased 5 V beyond their respective breakdown voltages. The results are shown in Fig. 2. The electric field distributions are quite comparable inside the active area of both detectors, but the two confinement approaches define a different profile outside of the central region. The most critical region in the planar SPAD is represented by the edges of the double zinc diffusion, while the highest electric field value in the mesa structure is reached at the critical corners.

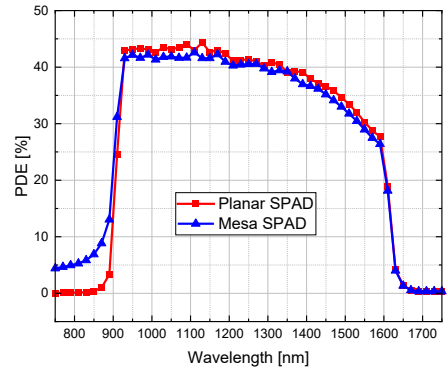


Fig. 3. Simulated PDE at 225 K for planar (red with squares) and mesa (blue with triangles) SPADs, both biased 5 V beyond their breakdown. At 1550 nm (our wavelength of interest) the PDE is 30% and 29% for planar and mesa respectively.

B. Optical simulations

By combining avalanche triggering probability simulations with finite-difference-time-domain (FDTD) optical absorption simulations, we compared the PDE of the two SPADs. Fig. 3 presents the PDE spectrum calculated from 750 nm to 1750 nm illuminating both detectors from the front side with a plane wave. The simulations show a good agreement between PDE values for the planar and for the mesa SPADs. In particular, at 1550 nm, the simulated PDE is 30% for the planar SPAD and 29% for the mesa SPAD.

IV. CONCLUSIONS

We presented a comparison between models of a well-developed planar SPAD and a novel triple-mesa SPAD. The main performance parameters are comparable, opening the possibility of employing mesa SPADs in quantum photonic applications, with the advantage of easier fabrication and integration processes with waveguides.

ACKNOWLEDGMENT

This work was partially supported by European Union's Horizon Europe program under Grant Agreement no. 101135785 (QPIC1550 project). Views and opinions expressed are, however, those of the authors only and do not necessarily reflect those of the European Union or the European Commission. Neither the European Union nor the granting authority can be held responsible for them.

REFERENCES

- [1] N. Gisin e R. Thew, «Quantum communication», *Nature Photon*, vol. 1, fasc. 3, pp. 165–171, mar. 2007, doi: 10.1038/nphoton.2007.22.
- [2] C. Yu, M. Shanguan, H. Xia, J. Zhang, X. Dou, e J.-W. Pan, «Fully integrated free-running InGaAs/InP single-photon detector for accurate lidar applications», *Opt. Express*, OE, vol. 25, fasc. 13, pp. 14611–14620, giu. 2017, doi: 10.1364/OE.25.014611.
- [3] F. Signorelli *et al.*, «Low-Noise InGaAs/InP Single-Photon Avalanche Diodes for Fiber-Based and Free-Space Applications», *IEEE Journal of Selected Topics in Quantum Electronics*, vol. 28, fasc. 2: Optical Detectors, pp. 1–10, mar. 2022, doi: 10.1109/JSTQE.2021.3104962.
- [4] F. Telesca, F. Signorelli, e A. Tosi, «Temperature-dependent photon detection efficiency model for InGaAs/InP SPADs», *Opt. Express*, OE, vol. 30, fasc. 3, pp. 4504–4514, gen. 2022, doi: 10.1364/OE.444536.

Small-signal compact modeling and TCAD validation of ultra-fast lateral Ge-on-Si waveguide photodetectors

Matteo G. C. Alasio*, Giuseppe Divincenzo*, Angelo Mudanò*, Giovanni Ghione*, Marco Vallone*, Michele Goano*[†]

*Department of Electronics and Telecommunications, Politecnico di Torino, Corso Duca degli Abruzzi 24, 10129 Torino, Italy

[†]IEIIT-CNR, Corso Duca degli Abruzzi 24, 10129 Torino, Italy

Email: matteo.alasio@polito.it

Abstract—We present a compact small-signal equivalent circuit for ultra-fast lateral Ge-on-Si waveguide photodetectors, validated against full 3D drift-diffusion TCAD simulations. By evaluating the contributions of intrinsic and parasitic elements, the model enables prediction of device performance and offers direct insight into the RC limitations of the photodetector, useful in circuit level designs.

I. INTRODUCTION

Silicon photonics [1], [2] have become increasingly important in optical interconnects, enabling chip-level integration of optical links. This is particularly useful in datacenters [3], [4] where the high modulation bandwidth is an essential feature. A key advantage is its CMOS compatibility, making it both cost-effective and integrable [5].

Ge-on-Si waveguide photodetectors are used for operation in the typical wavelengths exploited in optical communications, i.e. in the O- and C-band and beyond [6]. Among the explored configurations, the ultra-fast lateral structure studied in this work offers > 200 GHz electro-optic bandwidth, as measured in the literature [7], but at the cost of reduced responsivity.

This device features a Ge absorber between highly doped silicon contacts, resembling a FinFET structure. Figure 1 illustrates the geometry and lists the key parameters. This work extends a known small-signal equivalent model by extracting parameter values from 3D TCAD simulations.

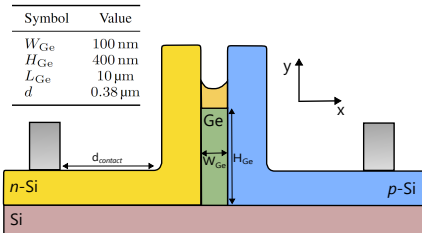


Fig. 1: Cross-section of the lateral Ge-on-Si photodetector. Key device dimensions are reported in the table.

II. METHODOLOGY

Following prior work [8]–[10], drift-diffusion TCAD simulation [11] is used to extract the overall electro-optic frequency response, showing good agreement between measurements and simulations. Here this methodology is used to evaluate the frequency-dependent electrical small-signal admittance. A compact model is developed using the topology in [12], [13], reported in Figure 2.

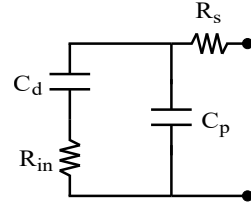


Fig. 2: Small-signal equivalent circuit of the lateral Ge-on-Si photodetector. C_d and R_{in} represent the intrinsic components; R_s and C_p represent the parasitic components.

The impedance in the Laplace domain is:

$$Z(s) = R_s + \frac{1}{sC_p + \frac{1}{R_{in} + \frac{1}{sC_d}}} \quad (1)$$

which expands to:

$$Z(s) = \frac{s^2 R_s R_{in} C_p C_d + s R_s (C_p + C_d) + s R_{in} C_d + 1}{s(s R_{in} C_p C_d + C_p + C_d)} \quad (2)$$

The admittance $Y = A + i\omega C$ is extracted from TCAD, providing a characterization of the device's small-signal behavior for a wide range of frequency, here reported between GHz and tens of THz to facilitate the fitting procedure.

III. RESULTS

Figure 3 shows the admittance comparison between the model and the simulation. Plateaus in the real and imaginary

parts reveal the series resistance and total capacitance respectively. In the imaginary part, at low frequency, the intrinsic junction dominates; at high frequency, parasitic effects prevail.

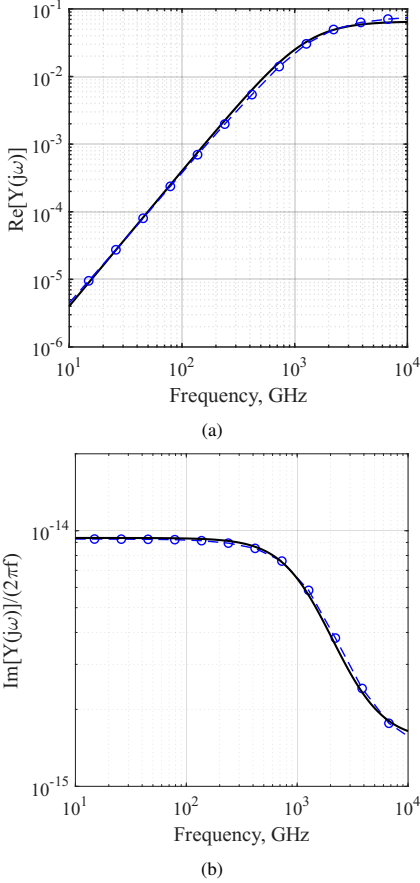


Fig. 3: Admittance from TCAD (dots) and fitted circuit model (line): (a) real part, (b) imaginary part versus frequency.

The fitted circuit values are summarized in Table I.

TABLE I: Fitted circuit parameters at -2 V.

Component	Value
R_s	17.2 m Ω
R_{in}	15.3 Ω
C_p	1.51 fF
C_d	7.86 fF

Displacement current analysis further confirms these results:

- 1) At low frequency, current is localized in the Ge absorber and close to silicon;
- 2) At high frequency, current spreads to parasitic paths.

Figure 4 shows the imaginary part of the displacement current at 1 THz in the cross-section, where the impact of the capacitance can be observed.

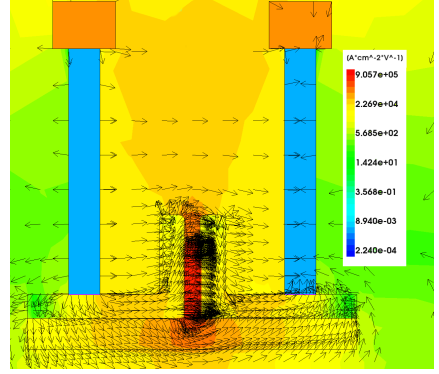


Fig. 4: Displacement current (imaginary part) at 1 THz in the cross-section, showing effects of both intrinsic and parasitic capacitance.

IV. CONCLUSION

A compact equivalent circuit for lateral Ge-on-Si photodetectors was developed and validated with TCAD simulations. The model captures parasitic and intrinsic effects, enabling performance prediction and design integration in high-speed photonic systems.

ACKNOWLEDGMENT

This work was supported in part by the European Union under two initiatives of the Italian National Recovery and Resilience Plan (NRRP) of NextGenerationEU: the partnership on Telecommunications of the Future (PE00000001 – program “RESTART”), and the National Centre for HPC, Big Data and Quantum Computing (CN00000013 – CUP E13C22000990001).

REFERENCES

- [1] J. Michel, J. Liu, L. C. Kimmerling, *Nature Photon.* **4**, 527 (2010).
- [2] J. Liu, S. Cristoloveanu, J. Wan, *Phys. Status Solidi A* **218**, 2000751 (2021).
- [3] Y. Li, Y. Zhang, L. Zhang, A. W. Poon, *Photon. Res.* **3**, B10 (2015).
- [4] Z. Zhou, R. Chen, X. Li, T. Li, *Optical Fiber Technology* **44**, 13 (2018).
- [5] S. Shekhar, *et al.*, *Nature Commun.* **15**, 751 (2024).
- [6] D. Steckler, *et al.*, *IEEE Photon. Technol. Lett.* **36**, 775 (2024).
- [7] S. Lischke, *et al.*, *Nature Photon.* **15**, 925 (2021).
- [8] M. G. C. Alasio, *et al.*, *23rd International Conference on Numerical Simulation of Optoelectronic Devices (NUSOD 2023)* (Torino, Italy, 2023), pp. 107–108.
- [9] M. G. C. Alasio, *et al.*, *J. Lightwave Technol.* **42**, 3269 (2024).
- [10] M. G. C. Alasio, *et al.*, *SPIE OPTO. Smart Photonic and Optoelectronic Integrated Circuits 2025* (San Francisco, CA, 2025), vol. 13370, Proceedings of the SPIE, p. 133700L.
- [11] Synopsys, Inc., Mountain View, CA, *Sentaurus Device User Guide. Version W-2024.09-SPI* (2024).
- [12] G. Ghione, *Semiconductor Devices for High-Speed Optoelectronics* (Cambridge University Press, Cambridge, U.K., 2009).
- [13] J.-M. Lee, S.-H. Cho, W.-Y. Choi, *IEEE Photon. Technol. Lett.* **28**, 2435 (2016).

Study of Hexagonal Photo-diode for Efficient Side-coupling to Silicon Wave-guide

Saurabh Sant
SemiVi LLC
Zurich, Switzerland.
saurabh.sant@semivi.ch

Abstract—We present the study of a hexagonal photo-diode design for efficient top/side coupling to Silicon waveguide optimized for $1.35\mu\text{m}$ wavelength. We calculate the coupling strength between the waveguide and the photo-diode by using hardware-accelerated finite-difference time-domain (FDTD) simulations. In the study, hexagonal geometry of the photo-diode is compared with the conventional rectangular stripe-based diode. The study shows, that use of hexagonal geometry enables better coupling between the wave-guide and the photo-diode. This is achieved by the activation of the whispering-gallery-like internal reflections happening inside the hexagonal photo-diode.

Index Terms—Silicon photonics, photodiode, hexagonal whispering gallery mode, hardware-accelerated FDTD solver.

I. INTRODUCTION

Recent advancements in AI have brought the necessity of large data-centers to the forefront. High-speed optical data-receivers in these data-centers requires ultra-fast and broadband detection of optical signals. Monolithically integrated photodiodes (PD) are well suited for the receiver applications [1]. Performance and speed of the PDs can be improved by shrinking the structure. Structure shrinkage while still ensuring sufficient coupling strength can be achieved by using plasmonic enhancements [2] or by utilizing a hexagonal geometry which exhibit whispering-gallery modes (WGM). The Template Assisted Selective Epitaxy (TASE) technology [3] enables monolithic integration of III-V materials on a Si platform and allows for side-coupling of Si waveguide with InGaAs PD. In this study, we design a side-coupled waveguide photodetector in hexagonal geometry and compare its strength with that of the conventional rectangular photodetector. For the structure design and simulation, we use the hardware-accelerated FDTD simulator by SemiVi [4].

II. SIMULATION SETUP

A. Photodiode structure

In order to study the effect of hexagonal structure on coupling strength of the photodiode, we performed a comparative study of two photo-diode geometries - traditional rectangular stripe, and hexagonal whispering-gallery-like structure. The two structures are shown in Fig. 1. Note that, the waveguide and the diode are embedded in the cladding oxide as shown in Fig. 1(d). The cladding oxide is hidden in the other figures. The simulation domain is defined by a cubic box of ‘vacuum’ around the structure such that there is padding of $0.32\mu\text{m}$ on all sides of the cuboid.

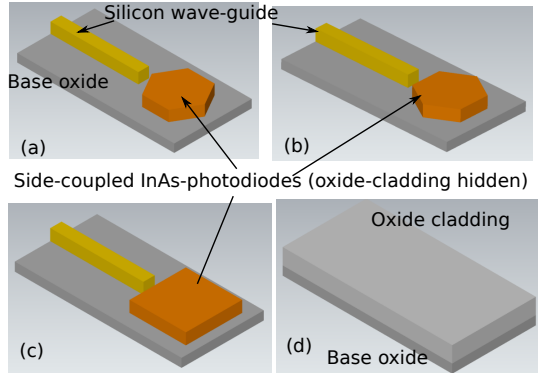


Fig. 1. Hexagonal $\text{In}_{0.53}\text{GaAs}$ photo-diode at the end of Si waveguide, with two configurations (a) and (b). (c) rectangular photo-diode coupled to the waveguide at the end. (d) Waveguide embedded in oxide cladding.

The waveguide cross-section is optimized for compactness and mode-confinement. The optimized waveguide cross-section of $260\text{nm} \times 260\text{nm}$ is used for this study. This waveguide has a TM mode with the refractive index of 2.37. The mode confinement is shown in Fig. 2(b). Length of the waveguide is $2.15\mu\text{m}$. Hexagonal $\text{In}_{0.53}\text{GaAs}$ photo-diode structure has a side-length of $0.65\mu\text{m}$, which is set such that the diode can exhibit a whispering-gallery-like mode at the refractive index of 2.44. Modes of the hexagonal structure are shown in Fig. 2(d) and (e). The rectangular structure has a side-length of $1.3\mu\text{m}$. In all the structures, the waveguide and the photo-diode are separated by a 200nm oxide layer. Cubic grid-spacing of 20nm is used along x,y,z axes in all the FDTD simulations.

B. Light source and boundary conditions

Coupling strength of waveguide and photo-diode structures is probed by exciting the waveguide by a uniform plane-wave source at 200nm away from the end. The source of intensity 1000W and wavelength of $1.35\mu\text{m}$, was placed in the plane perpendicular to the waveguide and was confined to the cross-section of the waveguide.

Convolutional perfectly matched layer (CPML) boundary conditions (BCs) were active at all the boundaries of the

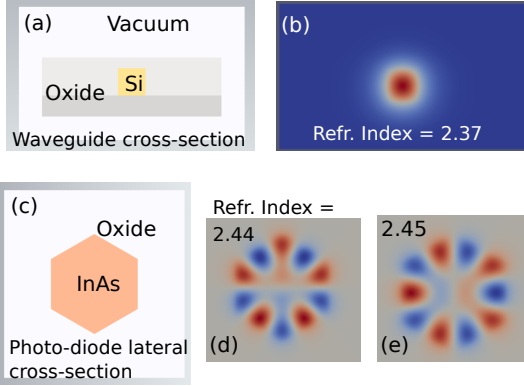


Fig. 2. (a) Cross-section of the waveguide and (b) Modal field in it. (c) Lateral cross-section of the hexagonal InGaAs disc. (d) and (e) Whispering gallery modes supported by it.

simulation domain. The CPML BCs were active on the last ten boundary layers. All the boundary layers were located in the ‘vacuum’ padding.

The above structures and mesh are created by the Python interface of the ‘Structure Generator and Mesher’ by SemiVi. It is simulated using the hardware-accelerated FDTD simulator by SemiVi [4]. Nvidia GPU ‘GTX3090’ is used for FDTD simulations.

III. RESULTS AND DISCUSSION

FDTD simulations were performed for 200 fsec (8994 time-steps). At time of 190 fsec, spatial intensity is calculated in the photo-diode. In a photo-diode, electron-hole generation is proportional to the light intensity at that location. Current generated by the photo-diode is proportional to the integrated spatial intensity. Integration of the intensity is performed and presented in Table I. The table shows that, integrated intensity in the photo-diode region of the side-coupled and top-coupled hexagonal structures is higher than that in the traditional rectangular structures. This confirms, that hexagonal whispering-gallery-like structure provides better coupling to the waveguide. It is likely to provide better sensitivity.

Fig. 3 shows absolute spatial distribution of electric field averaged over the last 20 fsec in the horizontal cut-plane in the three designs. The figure shows that the field develops a peculiar pattern in the hexagonal structures similar to the WGMs. The hexagon in Fig. 3(a) exhibits superposition of WGM with the waveguide, whereas that in Fig. 3(b) primarily shows the WGM. In contrast, rectangular PD in Fig. 3(c) does not exhibit these modes and shows lower coupling with the waveguide.

IV. CONCLUSIONS

We studied the effect of hexagonal whispering-gallery-like photodiode structure on the coupling strength between Silicon wave-guide and $\text{In}_{0.53}\text{GaAs}$ photodiode. Geometry of the

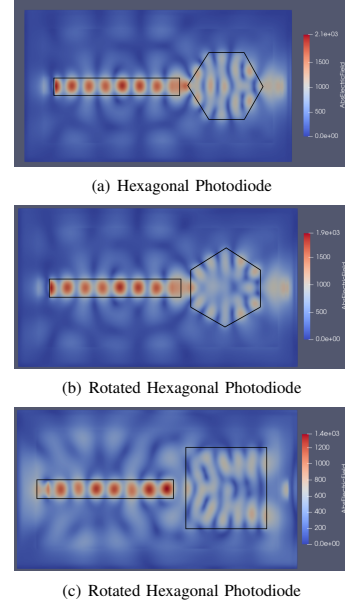


Fig. 3. Spatial distribution of abs. electric field in the horizontal cross-section at the middle of the waveguide height (i.e. 130nm above the base-oxide). The figures show that, in the hexagonal structures, whispering-gallery mode is indeed actuated by the waveguide.

TABLE I
INTEGRATED ELECTRIC FIELD AND INTENSITY VALUES. INTEGRATION IS PERFORMED IN THE PHOTODIODE REGION

Structure	Integrated abs. field $\text{V/m} \cdot \mu\text{m}^3$	Integrated intensity $\text{W/m}^2 \cdot \mu\text{m}^3$
WGM diode type-I	245.5	413.18
WGM diode type-II	221.77	378.87
Rect. diode	167.49	206.99

waveguide and the hexagonal photodiode are designed such that the hexagonal structure exhibits whispering-gallery mode close to the refractive index of the waveguide. The system is simulated by using the FDTD solver by SemiVi and the coupling strength between the waveguide and the photodiode. Simulations confirm that hexagonal structures increase the waveguide-photodiode coupling, compared to the traditional rectangular structure. This is due to the whispering-gallery modes of the photodiode.

REFERENCES

- [1] P. Wen Eli al, “Waveguide coupled III-V photodiodes monolithically integrated on Si,” *Nature Communications* 13, 909, 2022.
- [2] J. Gosciniaik and M. Rasras, “High-bandwidth and high-responsivity waveguide-integrated plasmonic germanium photodetector,” *J. Opt. Soc. Am. B* 36, 2481, 2019.
- [3] H. Schmid et al “Template-assisted selective epitaxy of III-V nanoscale devices for co-planar heterogeneous integration with Si,” *Applied Physics Letters* 106(23), 233101, 2015.
- [4] FDTD Solver User Guide, SemiVi LLC, Switzerland, 2025.

Numerical study of spatio-temporal dynamics in all semiconductor PCSELs

Lilli Kuen*, Eduard Kuhn*, Hans Wenzel†, Paul Crump†, and Mindaugas Radziunas*

*Weierstrass Institute (WIAS), Mohrenstrasse 39, 10117 Berlin, Germany. Email: lillifriederike.kuen@wias-berlin.de

†Ferdinand-Braun-Institut (FBH), Gustav-Kirchhoff-Str. 4, 12489 Berlin, Germany.

Abstract—We present a numerical study of all semiconductor photonic crystal surface-emitting lasers with two types of photonic crystals. We utilize time-domain simulations that are performed using the three-dimensional coupled-wave theory. Our evaluation includes examining carrier density, output power, optical spectra, near- and far-field.

Photonic crystal (PC) surface-emitting lasers (SELs), see Fig. 1(a), are devices engineered to achieve single-mode operation and a narrow far-field emission pattern by utilizing a photonic crystal structure [1]. Typically, these lasers explore a two-dimensional (2D) PC layer with a -periodic air voids in both lateral directions (x and y), where the lattice constant a defines the edge length of the square unit cell of the PC. The best to date high-power PCSELs [2] rely on the PCs defined by a pair of elliptic features located along the diagonal of the unit cell. It is expected that such devices should enable continuous wave operation in a single-mode [3]. In this work, we present the design of an *all-semiconductor*

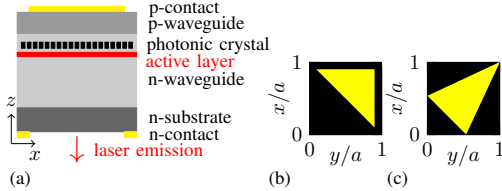


Fig. 1. Cross-section of a PCSEL based on [8] (a), rectangular isosceles triangle (RIT) feature (b), and stretched isosceles triangle (SIT) feature (c).

PCSEL featuring a PC layer composed of isosceles triangular InGaP features embedded within a GaAs matrix, see Figs. 1(b) and 1(c). Through dynamic simulations, we demonstrate that a proper choice of triangles, following the proposal of [4], can enable stable single-mode lasing in PCSELs with emission areas exceeding several mm^2 [5].

We use the three-dimensional coupled-wave theory [6], [7] to simulate the dynamical behavior of PCSELs within the in-domain plain $Q_L = [0, L] \times [0, L]$. The complex field \mathbf{E} consists of four components, the slowly varying complex field amplitudes propagating in $\pm x$ - and $\pm y$ -directions, stated as $\mathbf{E} = [E_x^+, E_x^-, E_y^+, E_y^-]^T$, respectively. According to [5], [7],

This work was performed in the frame of the German Leibniz Association funded project “PCSELence” (K487/2022).

the field equations are given as a system of four linear PDEs with according boundary conditions

$$\frac{1}{v_{gr}} \partial_t \mathbf{E}(x, y, z) = [\mathbf{D} + i(\mathbf{C} - \Delta\beta(N))] \mathbf{E} + \mathbf{F}_{sp}, \quad (1)$$

$$E_x^+(0, y, t) = E_x^-(L, y, t) = E_y^+(x, 0, t) = E_y^-(x, L, t) = 0,$$

$$\mathbf{D} = \begin{pmatrix} \sigma \partial_x & 0 \\ 0 & \sigma \partial_y \end{pmatrix}, \quad \sigma = \begin{pmatrix} -1 & 0 \\ 0 & 1 \end{pmatrix}.$$

Here, v_{gr} and \mathbf{F}_{sp} are the group velocity and the spontaneous emission [8]. \mathbf{C} is the complex $[4 \times 4]$ field coupling matrix [6], [7], depending on the design of the PC and the vertical structure of the PCSEL. The spatially-distributed relative propagation factor $\Delta\beta$ [5], [8] is given by

$$\Delta\beta(N) = k_0 \Delta n(N) + \frac{i}{2} [g(N) - \alpha - \mathcal{D}] \quad (2)$$

with the central wave vector $k_0 = 2\pi/\lambda_0$, central wavelength $\lambda_0 = an_{\text{eff}}$, and the effective refractive index n_{eff} . $\Delta n(N)$ denotes the refractive index change, $g(N)$ the carrier-dependent logarithmic gain, α the total field loss, and \mathcal{D} is a linear operator modeling the Lorentzian-shaped gain dispersion. This model does not account for dependencies on temperature. Finally, the carrier density $N(x, y, t)$ in the active region is described by the diffusive carrier rate equation [7],

$$\begin{aligned} \partial_t N &= \nabla_{\perp} \cdot (D_N \nabla_{\perp}) N + \frac{j}{ed} - R_{sp}(N) - R_{st}(N, \mathbf{E}), \\ R_{sp} &= \frac{N}{\tau_N} + BN^2 + CN^3, R_{st} \propto \Re[\mathbf{E}^* \cdot (g(N) - \mathcal{D}) \mathbf{E}], \end{aligned} \quad (3)$$

with $\nabla_{\perp} = [\partial_x, \partial_y]^T$, carrier diffusion D_N , injected current distribution $j(x, y)$, the elementary charge e , thickness of the active zone d , spontaneous emission R_{sp} and stimulated emission R_{st} . To perform time-dependent simulations, (1) and (3) are discretized using finite differences. For more details, see [5], [9].

In our simulations, we use a PCSEL with vertical structure and parameters from [5], [8], a sketch is given in Fig. 1(a). The PCSEL is of size $L = 2.4 \text{ mm}$ with a circular contact with diameter $D = 1.6 \text{ mm}$. We explore the following features of the PC: a rectangular isosceles triangle (RIT), as shown in Fig. 1(b) and considered in [8] and [6], and a stretched isosceles triangle (SIT), as shown in Fig. 1(c) and first introduced in [4]. During time integration, we use discretization steps $h = 9.6 \mu\text{m}$ in space and $\Delta t = h/v_{gr} \approx 0.12 \text{ ps}$ in time.

The carrier density and the output power of the time-dependent simulations are shown for both PCSELs in Fig. 2.

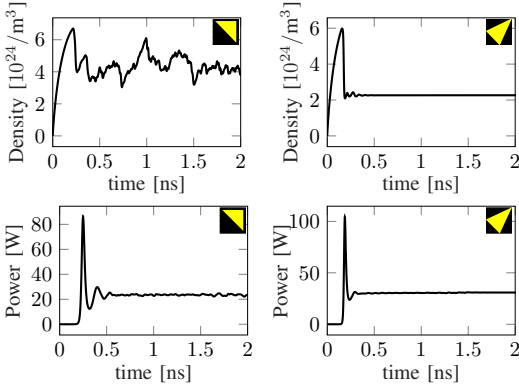


Fig. 2. Carrier density and optical output power for the RIT-PCSEL on the left and the SIT-PCSEL on the right side. The oscillation is part of the switching-on behavior of the laser; after about 1.5 ns, the stabilization of the transients is reached. Top-right corner insets represent the corresponding PC features.

In the case of RIT, see the left part of Fig. 2, the carrier density shows never-vanishing fluctuations, determined by the interaction of multiple modes. In comparison, for the SIT in the right part of Fig. 2, the carrier density and the output power reached by a single fundamental mode converge to a steady state in approximately 1.5 ns. The optical spectra and far-field for both structures are presented in Fig. 3. For the RIT-PC-based PCSEL case, the far-field shows several side lobes in addition to the main peak in the center, while the far-field of the SIT-PCSEL consists of a single spot in the center. This is also visible in the optical spectra. In the case of the RIT-PCSEL, the shift is $\Delta\lambda \approx 1.5$ nm, and a peak broadened by multiple contributing modes can be observed. This aligns with the multimodal behavior already described for the carrier density. For the SIT-PCSEL, one main peak exists, slightly above $\Delta\lambda = 0$. The time-averaged near-field distributions for both PCSELs are depicted in Fig. 4. The RIT-PCSEL shows the emission pattern corresponding to the contact shape, exhibiting multiple small-scale intensity fluctuations. In contrast, the SIT-PCSEL shows a much smoother profile with decreasing intensity to the sides. The degradation from a perfectly circular beam profile is the result of a phase mismatch between counterpropagating fundamental mode components.

In conclusion, we have performed time-domain simulations using a 3D-TW model for all semiconductor PCSELs featuring two types of PC. We demonstrated the difference in the time-dependent behavior of both structures. It was shown that the choice of PC features has a crucial impact on the type of operation. Our preliminary simulations show that employing SIT-type PC features can facilitate single-mode lasing in PCSELs with contact areas extending to 10 mm² and beyond.

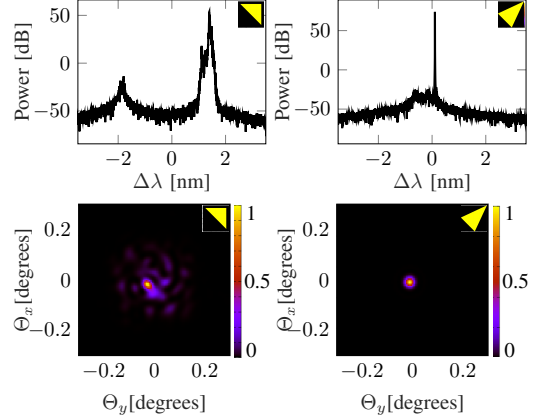


Fig. 3. Optical spectra and far-field on the top side of the PCSEL for the RIT-PCSEL on the left and the SIT-PCSEL on the right side.

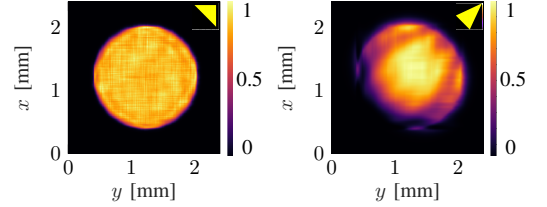


Fig. 4. Time-averaged near-field on the bottom side of the PCSEL for a RIT-PCSEL on the left and a SIT-PCSEL on the right side.

REFERENCES

- [1] S. Noda, K. Kitamura, T. Okino et al., "Photonic-crystal surface-emitting lasers: Review and introduction of modulated-photonic crystals," *IEEE J. Sel. Top. Quantum Electron.* **23**, 4900107, 2017.
- [2] M. Yoshida, S. Katsuno, T. Inoue et al., "High-brightness scalable continuous-wave single-mode photonic-crystal laser," *Nature* **618**, 727, 2023.
- [3] T. Inoue, M. Yoshida, J. Gelletta et al., "General recipe to realize photonic-crystal surface-emitting lasers with 100-W-to-1-kW single-mode operation," *Nat. Commun.* **13**, 3262, 2022.
- [4] B. King, H. Wenzel, E. Kuhn et al., "Design of very-large area photonic crystal surface emitting lasers with an all-semiconductor photonic crystal," *Opt. Express* **32**, 44945, 2024.
- [5] M. Radziunas, H. Wenzel, B. King et al., "Dynamical simulations of single-mode lasing in large-area all-semiconductor PCSELs," *Opt. Lett.* **50**, 1953, 2025.
- [6] Y. Liang, C. Peng, K. Sakai et al., "Three-dimensional coupled-wave analysis for square-lattice photonic crystal surface emitting lasers with transverse-electric polarization: finite-size effects," *Opt. Express* **20**, 15945, 2012.
- [7] T. Inoue, R. Morita, M. Yoshida et al., "Comprehensive analysis of photonic-crystal surface-emitting lasers via time-dependent three-dimensional coupled-wave theory," *Phys. Rev. B* **99**, 035308, 2019.
- [8] H. Wenzel, E. Kuhn, B. King et al., "Theory of the linewidth-power product of photonic-crystal surface-emitting lasers," *IEEE J. Quantum Electron.* **61**, 2400114, 2025.
- [9] M. Radziunas, E. Kuhn, and H. Wenzel, "Solving a spectral problem for large-area photonic crystal surface-emitting lasers," *Math. Model. Anal.* **29**, 575, 2024.

Simulation and Design of InGaAlAs O Band PCSELS

K. Boylan ⁽¹⁾, D. Moodie ⁽¹⁾, R. Spalding ⁽¹⁾, S. Rihani ⁽¹⁾, N. Hattasan ⁽¹⁾, M. Silva ⁽¹⁾, D. Childs ⁽¹⁾, G. Berry ⁽¹⁾, Jixiaochen⁽¹⁾, B. Lang ⁽²⁾, P. Sewell ⁽²⁾, A. Vukovic ⁽²⁾

⁽¹⁾ Huawei IRC, B83 Adastral Park, Martlesham Heath, Ipswich, IP5 3RE, UK samir.rihani@huawei.com

⁽²⁾ School of Electrical and Electronic Engineering, University of Nottingham, Nottingham, NG7 2RD, UK

Abstract We present a high power, high efficiency, single mode InGaAlAs PCSEL, designed using 3D coupled wave theory approach. An output power of more than 400mW with a wall plug efficiency of 15% at 25 °C was measured.

Introduction

Photonic Crystal Surface Emitting Lasers (PCSELS) are emerging as a promising and disruptive new technology, attracting significant attention due to their potential applications in laser processing, free space optical communication (FSO), structured light, and light detection and ranging (LIDAR). There is also potential for the PCSEL to displace incumbent laser technologies such as distributed feedback lasers (DFBs) and vertical cavity surface emitting lasers (VCSELS) in communications applications.

In this work, we report on the simulation and design of an InGaAlAs PCSEL at 1.3 μ m. Our study aims to simulate and design a high efficiency, single mode Indium Phosphide based PCSEL to improve on those recently reported at 1.3 μ m and at 1.55 μ m [1-5]. Our results suggest that, as with previously reported PCSELS, the devices presented here offer distinct advantages over incumbent technologies. PCSELS are scalable in power and area while maintaining single transverse mode emission, low beam divergence and have a symmetric near field and far-field, which improves coupling efficiency. Furthermore, the use of an InGaAlAs active region results in improvements to over temperature and dynamic performance, due to a higher conduction band offset and higher differential gain than InGaAsP.

This paper discusses the design of the PCSEL including the photonic crystal (PC) design based on Coupled Wave Theory (CWT).

Simulation and Design

CWT is a very fast - 0.1s, successful semi-analytic model for simulating PCSELS. Detail of the theory is presented in [3]. Light generated in the active is evanescently coupled into the Photonic Crystal (PC). Standing waves are formed through diffraction in the PC: 180° direct and 90° indirect coupling at the symmetric Γ point. Coupling of the 4 Bloch waves within the PC occurs, leading to vertical emission. The four-wave coupling at the Γ point is described by a set of matrices, determined by the Fourier component of the

PC, the 1D slab vertical mode and the Green's slab function within a 3D framework of CWT. The eigenvalue equation is solved and the solutions are the radiation constants and resonant frequencies of the 4 waves in either the infinite or finite domain, identifying the highest Q (lowest modal threshold gain) mode. Consequently, PCSELS can exhibit single mode, high brightness and low beam divergence lasing with output powers that can scale with area.

The PC pattern used is based on a double

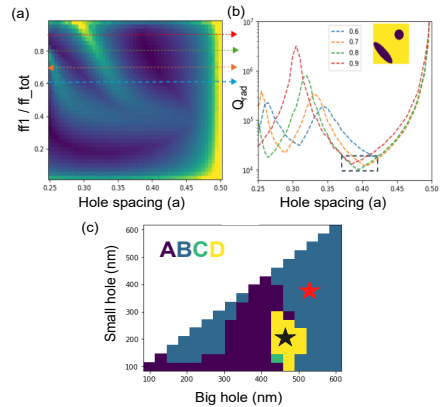


Fig. 1: Simulations: (a) Contour plot: Q_{rad} (color) as a function of FF ratio and hole-spacing (units = lattice constant a), (b) slice through contour plot4 the inset shows a PC design (c) 2D plot – dominant lasing mode for given hole depths in DL design.

lattice (DL) with elliptical and circular holes. CWT is used in the simulation and design of the device: key parameters are spacer layer thickness, fill factor (FF), lattice design, PCSEL area, hole spacing usually quoted relative to the unit cell width a , ellipticity, hole depth and the position of the back reflector. The coupling strength between the active and the PC is strongly influenced by the high refractive index of the PC and the InP spacer layer which constitutes the gap between the PC and active.

Figure 1(a) the design has a FF = 17% and a

spacer thickness = 205nm, shows a simulated contour plot of FF ratio (FF-ellipse/FF-DL) and hole spacing in the DL design. A slice through the contour plot in (b) shows when the ellipse is greater than the circle (FF ratio > 0.5) the lowest Q_{rad} values occur for hole spacing of 0.4constant). Figure 1(c) shows a contour plot of dominant lasing mode for an Ellipse-Circle PC design (mode A=purple, B=blue, C=yellow, D=green), with respect to the small and big hole depths. For high lasing output power and low threshold gain, the small hole depth must exceed 350nm (red star) to avoid lasing across the bandgap to a degenerate mode (black star). The red star in the plot indicates the optimal region where lasing occurs on the B mode ensuring high efficiency, and high SMSR. This sensitivity to the hole depth is pertinent to the DL design and the impact of the position of the reflector that the PC-modes are affected by. The choice of InGaAlAs based active material is driven by its superior properties, including higher conduction band offset and high differential gain, leading to an improvement in over temperature performance and higher intrinsic bandwidth [6].

Measurements

A PCSEL with a circular 330 μm diameter P-side contact window and a 500 μm PC was tested at 25°C. Figure 2 (a) shows no significant roll-over up to 2.5A at voltage < 1.2V. Measured maximum power = 413mW, slope efficiency (SE) = 0.22W/A, and PCE = 15%. Figure 2(b) shows pulsed LI results at 25°C with a pulse width of 3 μs and 4% duty cycle, achieving greater than 1W. The measurements in figure 3 show the lasing spectrum and band-edge modes at 25°C with an SMSR >50dB at 1.2A.

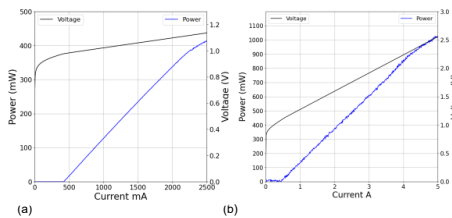


Fig. 2: (a) CW LIV at 25°C. Power at 2.5A is 413mW at $V < 1.2\text{V}$, (b) Pulsed LIV at 25°C. Power > 1W at 5A.

Conclusions

We have presented the first InGaAlAs-based PCSELS operating at 1.3 μm , demonstrating promising performance. We have demonstrated the use of CWT in simulating and finding the optimum designs based on trade-offs between key

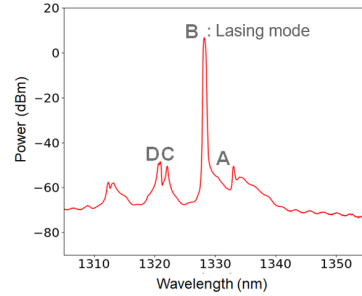


Fig. 3: CW Spectra at 25°C.

parameters.

Acknowledgements

We would like to acknowledge other colleagues from IRC who contributed to the work.

References

- [1] Yuhki Itoh, Takeshi Aoki, Kosuke Fujii, Hiroyuki Yoshinaga, Naoki Fujiwara, Makoto Ogasawara, Yusuke Sawada, Rei Tanaka, Kenichi Machinaga, Hideki Yagi, Masaki Yanagisawa, Masahiro Yoshida, Takuya Inoue, Menaka De Zoysa, Kenji Ishizaki, and Susumu Noda, "Power Scalability of 1.55- μm -Wavelength InP-Based Double-Lattice Photonic-Crystal Surface-Emitting Lasers With Stable Continuous-Wave Single-Mode Lasing", IEEE JSTQE, Vol. 31, No. 2, MARCH/APRIL 2025, DOI: <https://doi.org/10.1109/JSTQE.2024.3454202>
- [2] Yuhki Itoh, Takeshi Aoki, Kosuke Fujii, Hiroyuki Yoshinaga, Naoki Fujiwara, Kenshi Takada, Makoto Ogasawara, Yusuke Sawada, Hideki Yagi, Masaki Yanagisawa, Masahiro Yoshida, Takuya Inoue, Menaka De Zoysa, Kenji Ishizaki, and Susumu Noda, "High-power and high-efficiency operation of 1.3 μm -wavelength InP-based photonic-crystal surface-emitting lasers with metal reflector", Opt. Express 32, 12520-12527, (2024), DOI: <https://doi.org/10.1364/OE.521109>
- [3] Susumu Noda, Takuya Inoue, Masahiro Yoshida, John Gellata, Menaka De Zoysa, and Kenji Ishizaki, "High-power and high-beam-quality photonic-crystal surface-emitting lasers: a tutorial", Advances in Optics and Photonics, Vol. 15, No. 4, December 2023. /, DOI: <https://doi.org/10.1364/AOP.502863>
- [4] Yuhki Itoh, Naoya Kono, Daisuke Inoue, Naoki Fujiwara, Makoto Ogasawara, Kosuke Fujii, Hiroyuki Yoshinaga, Hideki Yagi, Masaki Yanagisawa, Masahiro Yoshida, Takuya Inoue, Menaka De Zoysa, Kenji Ishizaki, and Susumu Noda, "High-power CW oscillation of 1.3- μm wavelength InP-based photonic-crystal surface-emitting lasers," Opt. Express 30, 29539-29545, (2022), DOI: <https://doi.org/10.1364/OE.461048>
- [5] Inoue, T., Yoshida, M., Gellata, J. *et al.* General recipe to realize photonic-crystal surface-emitting lasers with 100-W-to-1-kW single-mode operation. *Nat Commun* 13, 3262, (2022), DOI: <https://doi.org/10.1038/s41467-022-30910-7>
- [6] T. Ishikawa, T. Hashiguchi, T. Uchida, T. Fujii, T. Yamamoto, H. Shoji, M. Kobayashi, "Evaluation of differential gain of 1.3 μm AlGaInAs/InP strained MQW lasers," Conference Proceedings. 1998 International Conference on Indium Phosphide and Related Materials (Cat. No.98CH36129), Tsukuba, Japan, 1998, pp. 729-732, doi: <https://doi.org/10.1109/ICIPRM.1998.712746>

Simulation of Finite-Size Photonic Crystal Surface Emitting Lasers with Efficient Eigenmode Solver

Yuan-Chun Han

Institute of Electronics

National Yang Ming Chiao Tung University

Hsinchu City 30010, Taiwan

ychan.stanley.ee12@nycu.edu.tw

Gray Lin

Institute of Electronics

National Yang Ming Chiao Tung University

Hsinchu City 30010, Taiwan

graylin@nycu.edu.tw

Abstract—We present an efficient eigenmode solver to simulate finite-size photonic-crystal (PC) surface-emitting lasers. Instead of calculating the full eigenspectra, a number of modes with lowest modal losses are extracted from the Krylov-Schur method and refined further using the shifted inverse power method. The device characteristics are then calculated and analyzed in terms of cavity size and PC fill factor.

Index Terms—Photonic Crystals, Surface-Emitting Lasers, Coupled Wave Theory, Krylov-Schur Method, Shifted Inverse Power Method

I. INTRODUCTION

The potential of photonic-crystal (PC) surface-emitting lasers (SELs) has been demonstrated by their high output power and narrow beam divergence. These properties make them suitable for applications in free-space optical communication, light detection and ranging [1]. However, continuing progress toward optimization is not an easy task. To avoid aimless test, simulation should be submitted as an exploratory tool at an early stage.

Due to limitations in computational resources, three-dimensional (3D) coupled wave theory (CWT) is introduced to model PCSEL devices [2]. In simulating infinite PC cavity, solving the basic eigenmodes is trivial, while in finite-size cavity with large area or large grid number, solving a huge number of eigenmodes is time-consuming. Therefore, it is formidable to investigate the dependence of parameters in addition to cavity size on device behaviors.

This paper presents an efficient eigenmode solver for finite-size PCSEL devices in the 3D-CWT formulation. The hybrid iterative approach combines the shift-and-invert Krylov-Schur method (KSM) [3] and the shifted inverse power method (SIPM), which enables identification of the lowest-loss modes for iterative refinement in an efficient and accurate manner. This is important for the subsequent analysis of surface emission characteristics.

II. SIMULATION DETAILS

A. Device Structure

Fig. 1 shows the schematic of PCSEL device in the 940 nm wavelength range. The air-pillar PC structure is incorporated

by deeply etching the topmost layers and no epitaxial regrowth is required [4]. In this simulation, square-lattice photonic crystals patterned in the shape of a right-isosceles triangle (RIT) are assumed. Moreover, the 400-nm thin-cladding layer is completely etched to maximize the diffraction coupling.

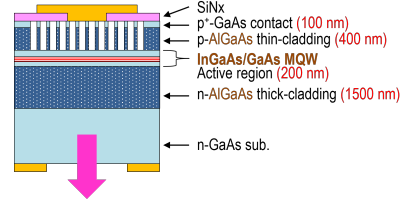


Fig. 1: Air-pillar PCSEL device under simulation

B. Coupled-Wave Model

In 3D-CWT model, the field profile in the z direction is decoupled from the in-plane profile and solved by the transfer matrix method. Four basic waves of R_x , S_x , R_y , and S_y represent the field amplitudes in the $+x$, $-x$, $+y$, and $-y$ directions, respectively. The coupled wave equations formulated in matrix form are given as,

$$\left(\delta + i\frac{\alpha}{2}\right) \begin{pmatrix} R_x \\ S_x \\ R_y \\ S_y \end{pmatrix} = C \begin{pmatrix} R_x \\ S_x \\ R_y \\ S_y \end{pmatrix} + i \begin{pmatrix} \partial R_x / \partial x \\ -\partial S_x / \partial x \\ \partial R_y / \partial y \\ -\partial S_y / \partial y \end{pmatrix} \quad (1)$$

where C is the coupling matrix as derived in [3], δ is the normalized frequency detuning and α is the modal power losses, including surface radiation loss (α_{rad}) and edge loss (α_{edge}). The above threshold slope efficiency (S.E.) can be estimated according to the formula,

$$S.E. \approx \frac{1.24}{\lambda_0} \frac{(1/2)\alpha_{rad}}{\alpha_{rad} + \alpha_{edge} + \alpha_{int}} \left(\frac{W}{A}\right) \quad (2)$$

where λ_0 is lasing wavelength in μm and α_{int} is internal power loss of 5 cm^{-1} [4]. The factor $1/2$ assumes that only downward emissions contribute to the optical output.

C. Numerical Methods

To simulate PCSEL in a finite-size area, the laser cavity is discretized into $N \times N$ mesh grids where appropriate boundary conditions are imposed [2]. The 3D-CWT matrix in Eqn. 1 is then transformed into the eigenvalue problem of a large sparse matrix ($4N^2 \times 4N^2$). Our proposed approach for the large eigenproblem is to apply the KSM in combination with the SIPM. The KSM requires a reduced time frame to obtain, for example, $N/2$, N or $2N$ approximate eigenvalues with lowest modal losses. Afterward, the SIPM is iterated to refine the accurate and precise eigenmodes.

III. RESULTS AND DISCUSSIONS

A. Simulation Time

The simulation time of three eigenmode solvers was compared: Schur decomposition, KSM, and KSM+SIPM. As shown in Fig. 2, Schur decomposition is the most time consuming, while KSM follows closely behind. In contrast, KSM+SIPM solver requires less than half the time of the former approach. However, KSM+SIPM solver is subject to variation in simulation times, depending on how many approximated eigenvalues are selected for iterative refinement. Considering a laser cavity of $400 \times 400 \mu\text{m}^2$ discretized to mesh grids of 51×51 ($N = 51$, $\Delta x = \Delta y \approx 7.84 \mu\text{m}$), the simulation time using KSM+SIPM is reduced to one-seventh of that using Schur or KSM.

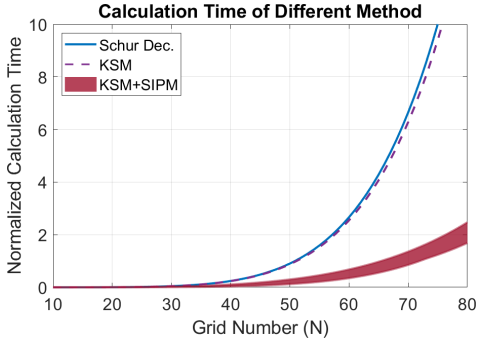


Fig. 2: The normalized simulation time of eigenmode solvers.

B. Cavity Design and FF Dependence

To demonstrate the powerful eigenmode solver, various emission characteristics of modal frequency, modal loss, slope efficiency, and loss discrimination are calculated and analyzed in terms of cavity size and fill factor (FF) as shown in Fig. 3.

In Fig. 3a, higher slope efficiency is observed in cavity sizes between $200 \mu\text{m}$ and $400 \mu\text{m}$, with FF ranging from 18 % to 30 %. Focusing on the region of interest in Fig. 3c, total modal losses are not the lowest, but acceptable for high-power applications. Notably, a change or switch in frequency detuning can be observed in Fig. 3b. In fact, we have observed this modal frequency switch between modes A and B at

$FF \approx 25\%$ in the analysis of infinite-cavity RIT-PCSELS [4]. It is interesting that in a finite-size cavity, the modal frequency switches at lower FF and increases with cavity size, as shown in Fig. 3c. Besides, the mode switching indicates that there is change in total losses, i.e. loss discrimination is minimized, which results in multi-mode emissions. Therefore, the loss discrimination minimum, corresponding to the dark line in Fig. 3d, should be excluded in the design of single-mode emissions.

In summary, there are two windows for fabrication design,

- 1) $FF = 18 - 20\%$ with cavity size $280 - 320 \mu\text{m}$
- 2) $FF = 25 - 30\%$ with cavity size $200 - 250 \mu\text{m}$

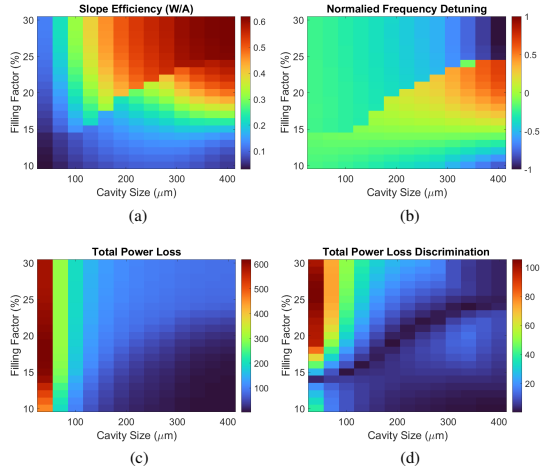


Fig. 3: The (a) slope efficiency, (b) normalized frequency detuning, (c) modal power loss, and (d) loss discrimination of the threshold mode in the RIT-PCSEL

IV. CONCLUSIONS

An efficient eigenmode solver for simulating finite-size PCSELS has been demonstrated. The dependence of the investigated parameters on the output characteristics can therefore be analyzed comprehensively. It is advantageous to speed up the optimum design for epitaxial structure, PC pattern and fill factor, or other fabrication conditions.

REFERENCES

- [1] R. Morita et al., "High-Speed High-Power Free-Space Optical Communication via Directly Modulated Watt-Class Photonic-Crystal Surface-Emitting Lasers," *Optica*, vol. 11, pp. 971-979, 2024.
- [2] Y. Liang, C. Peng, K. Sakai, S. Iwahashi, and S. Noda, "Three-Dimensional Coupled-Wave Analysis for Square-Lattice Photonic Crystal Surface Emitting Lasers with Transverse-Electric Polarization: Finite-Size Effects," *Opt. Express*, vol. 20, pp. 15945-15961, 2012.
- [3] T. M. Huang, W. J. Chang, Y. L. Huang, W. W. Lin, W. C. Wang, and W. C. Wang, "Preconditioning bandgap eigenvalue problems in three-dimensional photonic crystals simulations," *J. Comput. Phys.*, vol. 229, pp. 8684-8703, 2010.
- [4] Z.-X. Yang, C.-Y. Kuo, and G. Lin, "Simulation of photonic-crystal surface-emitting lasers with air-hole and air-pillar structures," *Photonics*, vol. 8, p. 189, 2021.

Experimental and theoretical study of frequency combs in hybrid lasers with a narrow-band mirror.

S. Cucco¹, A. Memon², C. Rimoldi³, M. Novarese², L. L. Columbo¹, K. J. Boller², and M. Gioannini¹

1. Department of Electronic and Telecommunication, Politecnico di Torino, Torino, Italia.

2. Department of Science and Technology, University of Twente, Enschede, Netherlands.

3. Istituto Nazionale di Ottica (CNR-INO), Firenze, Italia

stefania.cucco@polito.it marco.novarese@polito.it

Abstract— We present experimental and theoretical evidence of a self-pulsing regime in III-V/SiN hybrid integrated lasers featuring a frequency-selective mirror. While such a regime has been previously theoretically predicted in microcavity laser, as in the case of Fano laser, our research demonstrates its occurrence in a simpler and more accessible silicon photonics platform. Our findings demonstrate that these lasers can generate narrow free spectral range (FSR) frequency combs, with FSR of just a few gigahertz and smaller than the cavity FSR. The experimental observations are also supported by a theoretical model.

Keywords— Silicon photonics, hybrid integrated laser, multimode dynamics, optical frequency combs, self-pulsing regime.

I. INTRODUCTION

The recent focus on optical frequency combs (OFCs) is motivated by the many applications they find in various photonic systems. Here we investigate generation of OFC in semiconductor lasers integrated in silicon photonic (SiPh) platform. Indeed recent progress in the field of optical communication has driven the development of hybrid and heterogeneous integration of laser sources in this platform. This facilitates the development of low-cost, CMOS-compatible devices suitable for scalable deployment. Specifically, on-chip OFCs realised with SiPh integration, a development that represents significant progress towards scalable and fully integrated photonic circuits.

In this contribution, both experimental and theoretical investigations are presented about the generation of OFCs in a hybrid integrated tunable laser. We investigate the relation between the onset of OFC generation and the intensity modulation (IM) response of the laser, measured for various injection currents and lasing frequencies before the comb formation. The device is simulated using a model based on time-delayed algebraic equations [1]. We previously theoretically predicted that OFCs can emerge when the laser emission frequency is asymmetrically detuned from the reflectivity peak of the purely passive mirror, under a simple DC bias applied to the gain sections and without the need of a saturable absorber [2]. This process is known as self-pulsing and it has also been theoretically predicted in Fano lasers [3]. Principles in [3] and [2] are very similar, but they have never been experimentally proved. While the realization of the Fano laser based on photonic crystals proposed in [3] is quite

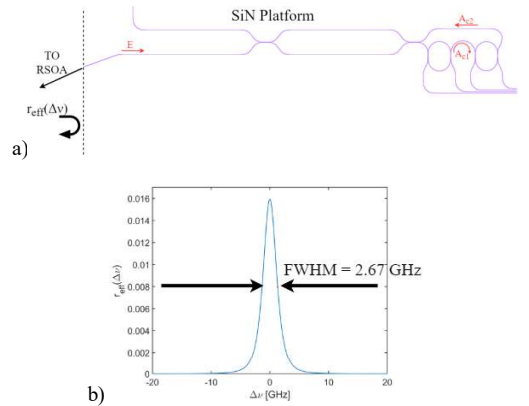


Fig. 1. (a) Schematic of the right mirror of the III-V/SiN hybrid laser. The laser cavity is composed by a MQW reflective SOA (RSOA) and closed on the right by the SiPh passive mirror here displayed. (b) Reflection coefficient of the passive mirror with FWHM of 2.7 GHz.

complicated, we rely here on a simpler and more accessible hybrid laser in silicon photonics. (see Fig.1 (a)). The experimental and numerical IM responses in CW conditions are analyzed to investigate the role of relaxation oscillations (RO) just before self-pulsing occurs. The comb regime observed in simulations is in good agreement with experiments.

II. RESULTS.

The device under test is a hybrid tunable laser, illustrated in Fig. 1 (a), integrating an active MQW HR/AR reflective semiconductor optical amplifier (RSOA) and a passive silicon nitride photonic integrated circuit (PIC) that functions as the front narrow band passive mirror. The PIC is fabricated using TriPleX technology with low-loss Si₃N₄/SiO₂ waveguides [4]. Lasing frequency detuning from the mirror reflection peak, defined as $\Delta\nu = \nu_s - \nu_0$, is controlled via current injection into an integrated phase control shifter (PS). The mirror incorporates two coupled microring resonators which, generate a narrow band reflection via Vernier effect (full width at half-

maximum (FWHM) ~ 2.67 GHz, as shown the Fig. 1 (b)). By studying the numerical IM response in the CW regime for increasing frequency detuning and fixed bias current at 195 mA, we are able to identify the frequency of RO. We compare this with the experimental measurements, as shown in Fig. 2. We observe that the RO peak is at a frequency of 3.3 GHz and this peak becomes less damped as the detuning increases. Subsequently, increasing the current and detuning leads to the comb regime shown in Fig. 3. In Fig. 3 (a), we compare the numerical and experimental optical spectrum, showing an FSR of the comb lines equal to 3.4 GHz, while in Fig. 3 (b) we compare the numerical radio frequency spectrum with the experimental measurements.

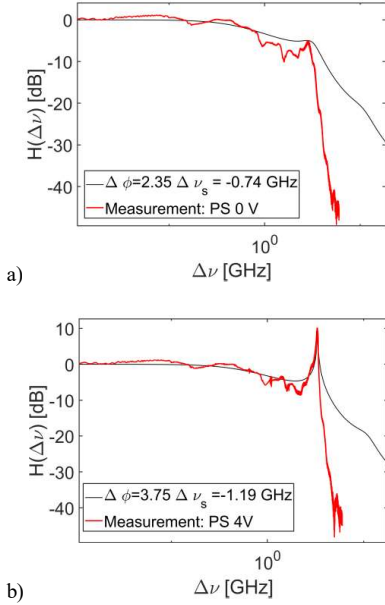


Fig. 2. Simulated (black) and experimental (red) intensity-modulation response (IM) at a current of 195 mA, when the laser is in single mode. a) phase control section equal to 0 V corresponding to stable CW single mode emission; b) Phase control section at 4 V close to comb formation. Measurements are limited at about 5 GHz due to the RF modulation bandwidth.

In conclusion we see that the comb is at an FSR comparable with the RO frequency and hence we prove for first time that undamped RO can lead to combs. This is possible only thanks to the very narrow band passive reflector and to the rather high (about 5) α -parameter of the RSOA.

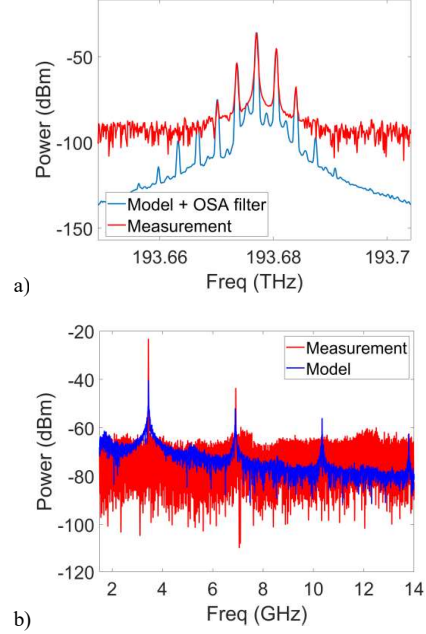


Fig. 3. (a) Experimental (red) and numerical (blue) optical spectrum in OFC regime at a current of 200 mA and detuning -1.60 GHz. (b) Experimental (red) and numerical (blue) data of radio-frequency spectrum for the same current and detuning.

ACKNOWLEDGMENT

This work was partially supported by the European Union under the Italian National Recovery and Resilience Plan (PNRR) of NextGenerationEU, partnership on "Telecommunications of the Future" (PE00000001 –program "RESTART").

REFERENCES

- [1] Rimoldi, C., Columbo, L. L., Bovington, J., Romero García, S., and Gioannini, M., "Damping of relaxation oscillations, photon-photon resonance, and tolerance to external optical feedback of iii-v/sin hybrid lasers with a dispersive narrow band mirror.," *Opt Express* (2022 Mar 28).
- [2] Rimoldi, C., Columbo, L. L., and Gioannini, M., "Optical frequency combs in external cavity sin hybrid lasers," *IEEE Photonics Journal* 16(2), 1–5 (2024).
- [3] Seegert, K., Heuck, M., Yu, Y., & Mørk, J. (2024). Self-pulsing dynamics in microscopic lasers with dispersive mirrors. *Physical Review A*, 109(6).
- [4] Mak, J., et al., "Linewidth narrowing via low-loss dielectric waveguide feedback circuits in hybrid integrated frequency comb lasers," *Opt. Express* 27, 13307–13318 (Apr 2019)

Efficient Photonic Component Analysis via AAA Rational Approximation

Lin Zschiedrich

JCMwave GmbH, Berlin, Germany

<https://orcid.org/0000-0002-1969-0633>

Fridtjof Betz

Zuse Institute Berlin, Germany

<https://orcid.org/0000-0003-2193-7188>

Felix Binkowski

Zuse Institute Berlin, Germany

JCMwave GmbH, Berlin Germany
<https://orcid.org/0000-0002-4728-8887>

Lilli Kuen

Weierstrass Institute Berlin, Germany

<https://orcid.org/0000-0002-3183-4222>

Martin Hammerschmidt

JCMwave GmbH, Berlin, Germany

<https://orcid.org/0000-0003-0291-1599>

Sven Burger

Zuse-Institute, Berlin

JCMwave GmbH, Berlin Germany
<https://orcid.org/0000-0002-3140-5380>

Abstract—We review the application of the AAA algorithm for rational approximation of the optical response function in photonic devices. Originally developed to efficiently interpolate sampled response data, the AAA algorithm also enables the accurate and stable computation of resonances, e.g., quasinormal modes (QNMs), along with their corresponding field distributions. Our approach applies to general nonlinear eigenproblems and can handle branch cuts without introducing spurious or artificial modes. It can further be applied to analyze VCSEL systems and photonic waveguides.

Index Terms—Photonic modes, rational approximation, AAA algorithm, quasinormal modes (QNM), nonlinear eigenvalue problems, resonance analysis, optical response, VCSEL.

I. PROBLEM SETUP

We consider time-harmonic light scattering problems as described by the second-order Maxwell's equation

$$\nabla \times \mu^{-1} \nabla \times \mathbf{E} - \omega^2 \epsilon \mathbf{E} = i\omega \mathbf{J}, \quad (1)$$

where $\mathbf{E}(\mathbf{r}, \omega) \in \mathbb{C}^3$ is the scattered electric field and $\omega \in \mathbb{C}$ is the angular frequency. The source is modeled as an electric current density $\mathbf{J}(\mathbf{r}) \in \mathbb{C}^3$. The material properties are integrated into the model through the permittivity $\epsilon(\mathbf{r}, \omega)$ and permeability $\mu(\mathbf{r}, \omega)$ tensors, and $\mathbf{r} \in \mathbb{R}^3$ is the position. Light scattering problems with an extended illumination such as a plane wave can be transformed in the above form (1). Furthermore, Maxwell's equation (1) is supplemented with a radiation condition, realized by perfectly matched layers (PMLs), and/or periodic boundary conditions which may also depend nonlinearly on ω .

In this work, we review the recently introduced approaches from Refs. [1]–[4] based on the AAA algorithm [5]. To analyze or to optimize the optical system, a measurable quantity of interest $f(\omega)$ (response function) is extracted from the electromagnetic field such as far-field amplitudes, Purcell factors, coupling coefficients, etc. As our framework relies on the meromorphic nature of the response $f(\omega)$, special care is needed for quadratic quantities to circumvent complex conjugation; see [6]. From the perspective of this work, the numerical solver for Maxwell's equation (1) is a complete black box. We want to characterize the system only from

the knowledge of the response function $f(\omega)$ at discrete sampling points (ω_k, f_k) [5]. The efficiency of the algorithm corresponds to the number of required sampling points to reach a desired accuracy.

This is in contrast to a traditional QNM computation [7], [8] with an eigensolver such as Arpack [9]. An algebraic eigensolver relies on the application of the system matrices together with their sparse inversion and needs adaptations to cope with the nonlinearity of the material tensors or the boundary conditions [10]. The advantage of our approach is that the excitation source as well as the relevant quantity of interest are included in the analysis step, so that the framework is considered as *physically driven*. We can prioritize the computed modes by their impact on the quantity of interest and how strongly they are excited by the given source. In this way, an intrinsic mode selectivity allows to easily filter out non-physical modes which may be caused by the truncation of the PML system.

II. AAA RATIONAL APPROXIMATION

The Adaptive Antoulas–Anderson (AAA) algorithm [5] gives an approximation of a scalar-valued function $f(\omega)$ by a rational function $r(\omega)$ in a barycentric representation. A number M of freely selectable sampling points $\omega_k \in Z \subseteq \mathbb{C}$ and corresponding function values $f_k = f(\omega_k)$ are the input for the algorithm. The algorithm greedily adds sampling points $\hat{\omega}_j$ to a subset $\hat{Z} \subset Z$, together with the corresponding function values \hat{f}_j until reaching the demanded accuracy. Then, each iteration within the algorithm leads to a rational approximation $r(z)$ of order $m - 1$,

$$r(\omega) = \frac{n(\omega)}{d(\omega)} = \frac{\sum_{j=1}^m \hat{w}_j \hat{f}_j}{\sum_{j=1}^m \hat{w}_j} \frac{1}{\omega - \hat{\omega}_j}, \quad (2)$$

where the weights \hat{w}_j minimize the error

$$\sum_{\omega_k \in Z \setminus \hat{Z}} |f_k d(\omega_k) - n(\omega_k)|^2. \quad (3)$$

The barycentric representation of the $r(\omega)$ forms the foundation of the AAA algorithm and enables the efficient computation of the rational approximation. It has removable singularities at $\hat{z}_j \in \hat{Z}$ and the limit $\lim_{z \rightarrow \hat{z}_j} r(z) = \hat{f}_j$ exists. Therefore, the approximation $r(z)$ interpolates the function values \hat{f}_j . The zeros of $n(z)$ and $d(z)$ are the zeros and poles of $r(z)$, respectively. They are provided as the eigenvalues of generalized eigenproblems. The residues of the approximative response function $r(\omega)$ are considered as the *modal contributions* of the corresponding poles.

III. APPLICATIONS

Characterization of chiral metasurfaces, sensitivity analysis

In [1], we characterized a chiral metasurface by its modal contributions. As a surplus of the AAA algorithm, the sensitivities on the geometrical parameters can be easily computed just from derivative data of the response function. Furthermore, the AAA algorithm is exploited to directly solve the eigenproblems, i.e., we show how to superimpose the field values at the sampling points to form an approximation of the QNM field, which is scaled according to its excitation by the chosen source.

Finding relevant VCSEL resonance modes

This example is taken from [2], where we applied the Riesz contour integral method [11] to compute the fundamental mode of a vertical-cavity surface-emitting laser (VCSEL). We fare much better with the new AAA based approach. The following table gives the convergence of the fundamental mode eigenvalue with the number of sampling points that were equidistantly chosen within the wavelength interval [986nm, 976nm].

#n	$\Re(\lambda)$ [nm]	$\Im(\lambda)$ [nm]	rel. err
2	9.8107e+02	0.0000e+00	1.48e-03
3	9.7919e+02	2.9976e+00	2.89e-03
5	9.7936e+02	1.5045e+00	1.36e-03
9	9.7965e+02	1.9669e-01	2.46e-05
17	9.7963e+02	2.0128e-01	5.99e-07
33	9.7963e+02	2.0121e-01	2.29e-08
65	9.7963e+02	2.0120e-01	1.29e-08
81	9.7963e+02	2.0122e-01	4.49e-09

TABLE I: Convergence of the fundamental mode eigenvalue with the number of equidistant sampling points on the real axis. Five sampling points are needed to observe convergence. The saturation from 33 sample points onwards is due to the numerical condition of the FEM system.

Dealing with branch cuts

In [3], we applied the AAA algorithm to a periodic scattering problem where the response function exhibits branch cuts due to vanishing diffraction orders. When sampling along the real frequency axis, these branch cuts manifest as clusters of poles, complicating the analysis. This issue can be resolved using a complex coordinate transformation that maps the frequency plane onto a Riemann surface without branch cuts.

This transformation reveals resonance modes that would otherwise be obscured, thereby clarifying the underlying physical mechanisms.

Waveguide analysis

For waveguide problems, the optical response is preferable considered as dependent on the propagation constant k_z . Our framework also applies to that case; see [4]. For many practical applications involving photonic crystal fibers, the fundamental mode is embedded in a cluster of cladding modes which renders eigenvalue computations costly and requires to filter out the relevant mode. Here, our framework allows to choose a source term located in the core region of the fiber which only weakly excites the cladding modes.

ACKNOWLEDGMENT

We thank Jan David Fischbach, Carsten Rockstuhl and A. Femius Koenderink for fruitful collaboration. We acknowledge funding by the German Federal Ministry of Research, Technology and Space (BMFTR, project number 16KIS1821, MultiCoreSPS; BMBF Forschungscampus MODAL, project 05M20ZBM) and by the Deutsche Forschungsgemeinschaft (DFG, German Research Foundation) under Germany's Excellence Strategy - The Berlin Mathematics Research Center MATH+ (EXC-2046/1, project ID: 390685689). The project is funded by the Senate of Berlin, within the Program for the Promotion of Research, Innovation and Technology (ProFIT) co-financed by the European Regional Development Fund (ERDF, application no. 0206824, SQALE).

REFERENCES

- [1] F. Betz, M. Hammerschmidt, L. Zschiedrich, S. Burger, and F. Binkowski, "Efficient Rational Approximation of Optical Response Functions with the AAA Algorithm," *Laser Photonics Rev.*, vol. 18, p. 2400584, 2024.
- [2] L. Kuen, F. Betz, F. Binkowski, P.-I. Schneider, M. Hammerschmidt *et al.*, "Applying a Riesz-projection-based contour integral eigenvalue solver to compute resonance modes of a VCSEL," *Proc. SPIE*, vol. 12575, p. 125750J, 2023.
- [3] F. Betz, F. Binkowski, J. D. Fischbach, N. Feldman, L. Zschiedrich *et al.*, "Uncovering hidden resonances in non-hermitian systems with scattering thresholds," 2025, arXiv:2503.03549.
- [4] F. Binkowski, F. Betz, M. Hammerschmidt, L. Zschiedrich, and S. Burger, "Resonance modes in microstructured photonic waveguides: efficient and accurate computation based on AAA rational approximation," *Nanophotonics*, vol. 14, p. 1665, 2025.
- [5] Y. Nakatsukasa, O. Sète, and L. N. Trefethen, "The AAA algorithm for rational approximation," *SIAM J. Sci. Comput.*, vol. 40, p. A1494, 2018.
- [6] F. Binkowski, F. Betz, R. Colom, M. Hammerschmidt, L. Zschiedrich, and S. Burger, "Quasinormal mode expansion of optical far-field quantities," *Phys. Rev. B*, vol. 102, p. 035432, 2020.
- [7] P. Lalanne, W. Yan, A. Gras, C. Sauvan, J.-P. Hugonin *et al.*, "Quasinormal mode solvers for resonators with dispersive materials," *J. Opt. Soc. Am. A*, vol. 36, p. 686, 2019.
- [8] G. Demésy, A. Nicolet, B. Gralak, C. Geuzaine, C. Campos, and J. E. Roman, "Non-linear eigenvalue problems with GetDP and SLEPc: Eigenmode computations of frequency-dispersive photonic open structures," *Comput. Phys. Commun.*, vol. 257, p. 107509, 2020.
- [9] R. B. Lehoucq, D. C. Sorensen, and C. Yang, *ARPACK Users' Guide*. Society for Industrial and Applied Mathematics, 1998.
- [10] A. Gras, W. Yan, and P. Lalanne, "Quasinormal-mode analysis of grating spectra at fixed incidence angles," *Opt. Lett.*, vol. 44, p. 3494, 2019.
- [11] F. Binkowski, F. Betz, R. Colom, P. Genevet, and S. Burger, "Poles and zeros in non-Hermitian systems: Application to photonics," *Phys. Rev. B*, vol. 109, p. 045414, 2024.

Topological insights into tight-binding descriptions of three-dimensional photonic crystals

Thomas Christensen

Department of Electrical and Photonics Engineering
Technical University of Denmark

Kgs. Lyngby, Denmark

thomas@dtu.dk, <https://orcid.org/0000-0002-9131-2717>

Abstract—Unlike their influential role in solid-state physics, tight-binding models have historically played a relatively modest role in photonic crystal research. This is especially so for three-dimensional photonic crystals, where efforts to apply Wannierization techniques have been hindered by the transverse polarization of light. I will discuss how insights from symmetry analysis and topology inform a new approach.

Index Terms—symmetry, topology, photonic crystals, tight-binding.

I. INTRODUCTION

Despite substantial efforts in method development [1], [2], tight-binding models have not seen wide use in photonic crystals research, except in 1D and 2D settings. This stands in sharp contrast to the popularity of tight-binding models and Wannierization techniques not only in solid-state physics [3], [4] but also for e.g., phononic crystals [5], [6]. Since the majority of archetypal models in topological band theory are underlied by a tight-binding perspective, their absence in 3D photonic crystals has been especially felt in the field of topological photonics.

The failure of tight-binding modeling efforts for 3D photonic crystals is directly tied to the polarization of light. Two facts conspire in this spoiling: (1) solutions to the Maxwell equations must be transverse, i.e., divergence free $\nabla \cdot \mathbf{B} = 0$, and (2) solutions near zero frequency, $\omega \rightarrow 0$, solutions must necessarily be plane-wave-like, since the effective-medium limit is realized exactly at zero frequency. Since the two lowest bands of any 3D photonic crystal necessarily connect to $\omega = 0$ at zero wave-vector $\mathbf{k} = \mathbf{0} \equiv \Gamma$ (Fig. 1a), their polarization state is necessarily ill-defined at this point. This is clear since a transverse plane-wave $\hat{\mathbf{e}}_{\mathbf{k}} e^{i\mathbf{k} \cdot \mathbf{r}}$ must have its polarization vector $\hat{\mathbf{e}}_{\mathbf{k}}$ orthogonal to \mathbf{k} : consequently, if we attempt to determine $\hat{\mathbf{e}}_{\mathbf{k}}$ precisely at Γ , we find that it depends on the \mathbf{k} -space angle with which Γ is approached (Fig. 1b). Effectively, the Bloch state basis exhibits a vortex with an associated non-analytic singularity at $(\mathbf{k} = \mathbf{0}, \omega = 0)$. Since any tight-binding model must be founded in a set of Wannier orbitals—which are nothing but a Fourier transform of the Bloch states—this singularity implies that the Wannier orbitals cannot be localized, spoiling the outlook for effective tight-binding modeling of these bands [1], [7].

T.C. acknowledges the support of a research grant (Project No. 42106) from Villum Fonden.

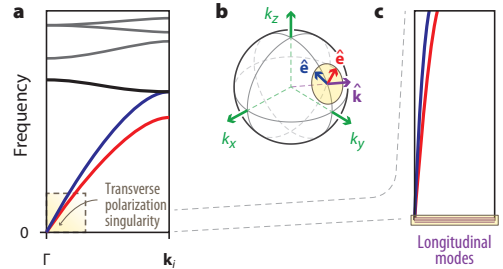


Fig. 1. **Transverse polarization singularity at zero frequency.** **a**, The lowest two bands (red and blue) of a 3D photonic crystal necessarily connect to zero frequency at Γ . **b**, There, they exhibit a polarization singularity because their polarization vectors $\hat{\mathbf{e}}$ must be orthogonal to the direction of the wave-vector \mathbf{k} , whose direction is ill-defined at $\mathbf{k} = \mathbf{0}$. **c**, An infinite set of longitudinal modes exist at zero frequency. By incorporating a subset of them as auxiliary bands, the singularity can be side-stepped because the space spanned by the sum of longitudinal and transverse polarization vectors is independent of the directionality of \mathbf{k} .

II. REGULARIZATION THROUGH AUXILIARY MODES

This singularity also appears in a seemingly unrelated context, namely when attempting to adapt recent symmetry-based frameworks of topological band analysis to 3D photonic crystals [7], where the singularity prevents a regular assignment of band symmetry at zero frequency. In Ref. 7, we recently demonstrated that the problem can be effectively regularized by viewing the situation as the *difference* of two auxiliary problems. The key idea is the incorporation of a set of auxiliary longitudinal modes (Fig. 1c). Such longitudinal modes are unphysical since they are not divergence-free—but are nevertheless valid solutions of the photonic wave equation. However, by incorporating an appropriately chosen longitudinal band alongside the two singular transverse bands, the space spanned by their sum becomes well-defined at $(\mathbf{k} = \mathbf{0}, \omega = 0)$. By solving this regularized problem—a sum of transverse and longitudinal bands, which we call the *apolar* problem—and suitably “subtracting” the added longitudinal bands afterwards, the singularity is overcome, enabling use of symmetry-based topological frameworks. The singularity, in turn, endows photonic crystals with special band symmetry properties that translate to unique band connectivities, different

from those of other quasiparticles [7].

III. SYMMETRY AND PHOTONIC TIGHT-BINDING MODELS

Building on this insight, Morales-Pérez et al. [8] recently proposed a new approach to the photonic tight-binding problem, building a tight-binding model for the set of apolar bands rather than just the transverse bands. With outset in this approach, we have developed a fully general software implementation [9] by interfacing with another set of software packages previously developed for symmetry-based topological analysis [10], [11].

The implementation involves three technical elements:

- (1) Determine the band symmetry content (i.e., irreps at high-symmetry k -points) of the photonic bands of interest.
- (2) Convert this information from reciprocal space to real space, adding longitudinal bands as necessary, to extract a decomposition in so-called band representations. This gives the orbital character (s -like, p -like, etc.) and orbital locations of sites in the associated tight-binding model.
- (3) Determine the possible tight-binding terms compatible with these orbitals.

Point 3 is perhaps the most broadly interesting, owing to the familiarity of manual tight-binding model building in simple contexts. To move from manual to automatic and from simple to general, recall that the Bloch Hamiltonian $h_{\mathbf{k}}$ must be invariant under each symmetry g of the space group G in the sense that $gh_{\mathbf{k}}g^{-1} = h_{g\mathbf{k}}$ for all $g \in G$. For the matrix form of Bloch Hamiltonian, $\mathbf{h}_{\mathbf{k}}$, implicitly formulated relative to an orbital basis, the action of g is represented by a matrix as well. In the language of space group theory, g is represented by $\mathbf{D}_{\mathbf{k}}(g)$: (a Fourier transform of) the space group representation induced by the orbitals of the tight-binding sites (equivalently, it is a band representation). The operator constraints then reduce to simple linear constraints $\mathbf{D}_{\mathbf{k}}(g)\mathbf{h}_{\mathbf{k}}\mathbf{D}_{\mathbf{k}}^\dagger(g) = \mathbf{h}_{\mathbf{k}}$. Aggregated over all $g \in G$ (and solved simultaneously for all \mathbf{k}), these symmetry constraints can be encoded as a homogeneous linear system, whose kernel defines the allowed Hamiltonian terms. By this approach, we obtain a general tool for determining all possible tight-binding terms consistent with a set of orbitals.

Figure 2 illustrates an application of the approach for an inverse opal design in space group 225 ($\text{Fm}\bar{3}\text{m}$). An apolar tight-binding model is built from 3-fold degenerate orbitals with T_2 symmetry (Mulliken notation) placed at the $8c$ Wyckoff positions (i.e., at $\frac{a}{4}(\hat{x} + \hat{y} + \hat{z})$ and $\frac{3a}{4}(\hat{x} + \hat{y} + \hat{z})$ in the cubic unit cell of side length a) and subsequently fitted to the spectrum of the lowest 5 bands, obtained from full-wave calculations in MPB. Excellent agreement between full-wave calculations and tight-binding fit is evident.

IV. OUTLOOK

While our current implementation requires spectral fitting to obtain hopping amplitudes, the conceptual approach involving auxiliary longitudinal modes is general. This suggests that a general application of Wannierization techniques—long assumed unworkable for 3D photonic crystals due to their polarization singularity—might be within reach, provided a

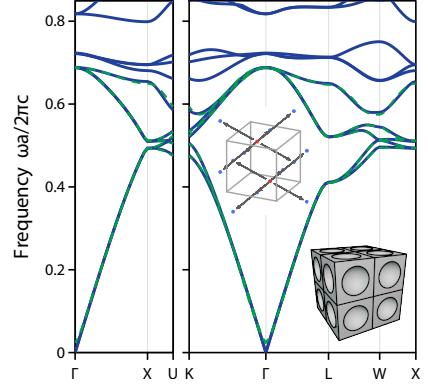


Fig. 2. **Full-wave and tight-binding band structure of inverse opal photonic crystal.** The tight-binding fit (dashed green; full-wave calculations in solid blue) is constructed using 31 hopping terms and restricted to the lowest five transverse bands (including one auxiliary longitudinal band, whose frequencies are imaginary and not shown); the dominant type of hopping term is shown in the central inset. The photonic crystal is a face-centered cubic inverse opal, in a touching void configuration (radius $a/\sqrt{8}$) with permittivity $\varepsilon = 13$; the lower left inset shows a 2×2 tiling of the cubic unit cell (side length a).

suitable scheme for incorporating the auxiliary longitudinal bands can be found.

ACKNOWLEDGMENTS

I thank Antonio Morales-Pérez, Aitzol García-Etxarri, Maia G. Vergniory, and co-authors for the collaboration on Ref. 9.

REFERENCES

- [1] C. Wolff, P. Mack, and K. Busch, “Generation of wannier functions for photonic crystals,” *Phys. Rev. B*, vol. 88, p. 075201, 2013.
- [2] J. Albert, C. Jouanin, D. Cassagne, and D. Monge, *Opt. Quantum Electron.*, vol. 34, p. 251, 2002.
- [3] N. Marzari and D. Vanderbilt, “Maximally localized generalized Wannier functions for composite energy bands,” *Phys. Rev. B*, vol. 56, p. 12847, 1997.
- [4] A. A. Mostofi, J. R. Yates, G. Pizzi, Y.-S. Lee, I. Souza, D. Vanderbilt, and N. Marzari, “An updated version of wannier90: A tool for obtaining maximally-localised Wannier functions,” *Comput. Phys. Commun.*, vol. 185, p. 2309, 2014.
- [5] J. A. López-Toledo, G. Báez, and R. A. Méndez-Sánchez, “Tight-binding model for torsional and compressional waves in high-quality coupled-resonator phononic metamaterials,” *Mech. Adv. Mater. Struct.*, vol. 29, p. 6301, 2021.
- [6] Z.-G. Chen and Y. Wu, “Tunable topological phononic crystals,” *Phys. Rev. Appl.*, vol. 5, p. 054021, 2016.
- [7] T. Christensen, H. C. Po, J. D. Joannopoulos, and M. Soljačić, “Location and topology of the fundamental gap in photonic crystals,” *Phys. Rev. X*, vol. 12, p. 021066, 2022.
- [8] A. Morales-Pérez, C. Devescovi, Y. Hwang, M. García-Díez, B. Bradlyn, J. L. Mañes, M. G. Vergniory, and A. García-Etxarri, “Transversality-enforced tight-binding models for three-dimensional photonic crystals aided by topological quantum chemistry,” *Phys. Rev. B*, vol. 111, p. 235206, 2025.
- [9] A. Morales-Pérez et al., *in preparation*, 2025.
- [10] T. Christensen, “Crystalline.jl and MPBUtils.jl,” Available at <https://github.com/thchr/Crystalline.jl> and <https://github.com/thchr/MPBUtils.jl>.
- [11] A. Ghorashi, S. Vaidya, M. C. Rechtsman, W. A. Benalcazar, M. Soljačić, and T. Christensen, “Prevalence of two-dimensional photonic topology,” *Phys. Rev. Lett.*, vol. 133, p. 056602, 2024.

A New Analytical Model of Gain in Highly-Saturated SOAs

Pascal Morel¹, Bárbara Dumas Feris^{2,1}, Thierry Rampone¹, Jana Ramadan¹, Ammar Sharaiha¹

¹Bretagne INP, ENIB, Lab-STICC, CNRS, UMR 6285, Brest, France

²School of Electrical Engineering, Pontificia Universidad Catolica de Valparaíso (PUCV), Valparaíso, Chile
morel@enib.fr, barbara.dumas@pucv.cl, rampone@enib.fr, ramadan@enib.fr, sharaiha@enib.fr

Abstract—This contribution presents a new analytical model in good agreement with experimental data for gain in highly-saturated SOAs. This model, based on Lambert W function, only needs two parameters and offers fast-computing simulations.

Index Terms—Semiconductor Optical Amplifier, Gain, Lambert W function.

I. INTRODUCTION

Modeling the nonlinear behavior of Semiconductor Optical Amplifier (SOA) behavior is a challenging task [1]. Multisection models have been used to obtain a suitable behavior [2], [3]. Here, we introduce a monosection-analytical model, so we can limit the number of parameters involved. This not only makes our model computing efficient, but also allows to render the SOA-nonlinear-gain behavior over a large range of optical-input-power values. Indeed, understanding nonlinearities permits to better adapt the predistortion strategy in order to enhance the optical transmission performance [4]. The proposed model is validated using the experimental characterization of the SOA from [5] (see Fig. 3.13).

II. MATHEMATICAL MODEL

The saturated gain G of an SOA can be expressed in a general way as a function of the SOA total input power P_{in} , linear gain G_0 , and saturation power P_{sat} as [6]:

$$G = G_0 e^{-(G-1) \frac{P_{in}}{P_{sat}}} \quad (1)$$

One should note the term G in both sides of (1), as in this case the gain is necessarily saturated as the optical-input power is non-zero. A simple way to handle this is to compute the 1st order nesting expression as:

$$G = G_0 e^{-(G_0-1) \frac{P_{in}}{P_{sat}}} \quad (2)$$

Willing to have a better saturation behavior, we can use (1) as a nested relationship of higher orders, setting $G = G(G(\dots(G(G_0))))$. Fig. 1 presents with markers the reference experimental gain as a function of the SOA-optical-input power. The solid line presents the gain using (2), while dashed and dotted lines present the gain using nested relationships of respectively 8th and 9th orders as an example. The following parameters are used for all analytical results: $G_0 = 16.2$ dB and $P_{sat} = 7$ dBm. These parameters were obtained by fixing the analytical small-signal gain G_0 as the experimental one, and optimizing P_{sat} for better reproducing the experimental

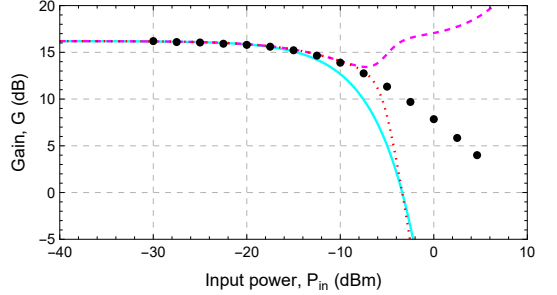


Fig. 1. Gain as a function of the optical-input power. Markers: experimental data. Solid, dashed and dotted lines: analytical gains using respectively 1st, 8th and 9th nesting orders with $G_0 = 16.2$ dB and $P_{sat} = 7$ dBm.

data. At high input powers, working with even nesting orders (8th order in Fig. 1), the obtained gain increases with optical-input power, which is not a physical behavior. Working with higher odd nesting orders permits to better reproduce the experimental data up to a given optical-input power after which the behavior moves away from the reference curve, still not being fully satisfactory.

In order to analytically solve (1), we rework it to obtain the following expression:

$$G \frac{P_{in}}{P_{sat}} e^{G \frac{P_{in}}{P_{sat}}} = G_0 \frac{P_{in}}{P_{sat}} e^{\frac{P_{in}}{P_{sat}}} \quad (3)$$

The formal solution of (3), in which we recognize an expression $xe^x = y$, is $x = W(y)$, where $W(y)$ is the Lambert W function [7], giving finally:

$$G = \left(\frac{P_{in}}{P_{sat}} \right)^{-1} W \left(G_0 \frac{P_{in}}{P_{sat}} e^{\frac{P_{in}}{P_{sat}}} \right) \quad (4)$$

Fig. 2 presents again the previous experimental data that we aim to reproduce. The solid line presents now the use of (4) with the same parameters as before ($G_0 = 16.2$ dB and $P_{sat} = 7$ dBm). We show in dashed and dotted lines the previously obtained gains using nested relationships of respectively 1st and 9th orders. The comparison shows a behavior closer to experimental data and physically realistic for the gain of saturated SOAs in favor of using Lambert W function.

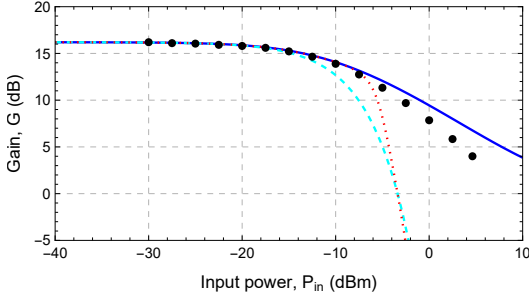


Fig. 2. Gain as a function of the optical-input power. Markers: experimental data. Solid, dashed and dotted lines: analytical gains using respectively Lambert W function, 1st and 9th nesting orders with $G_0 = 16.2$ dB and $P_{sat} = 7$ dBm.

The average distance between analytical and experimental behaviors can be minimized by varying P_{sat} parameter. We show in Fig. 3 the same experimental and analytical behaviors as in Fig. 2 (markers and solid line), to which we add in dotted line the analytical behavior obtained setting $P_{sat} = 4$ dBm.

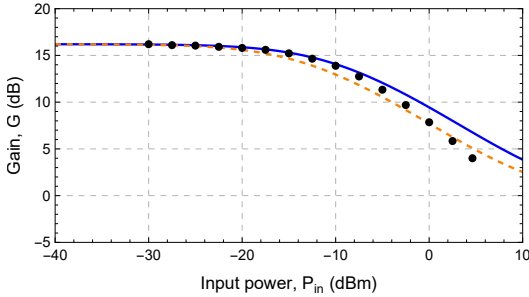


Fig. 3. Gain as a function of the optical-input power. Markers: experimental data. Solid and dashed lines: analytical gains using Lambert W function with $G_0 = 16.2$ dB and respectively $P_{sat} = 7$ dBm and $P_{sat} = 4$ dBm.

We finally show in Fig. 4 the benefit of using our analytical model in term of simulation performance. To do so we use Mathematica, in which we computed as a reference (4) (noted “Lambert W”, called “ProductLog” in Mathematica). We see that using nested relationships (noted respectively as “1st nesting order” and “9th nesting order”) comes with slightly faster performance but with non fully satisfying the physical behavior. Another solution would be to numerically solve (1), searching for a numerical value for G satisfying this relationship. We also show in Fig. 4 that this solution (noted “NSolve” as calling “NSolve” function in Mathematica) is nearly 70 times slower than the analytical one, while having the same behavior as using (4) (not represented in previous figures).

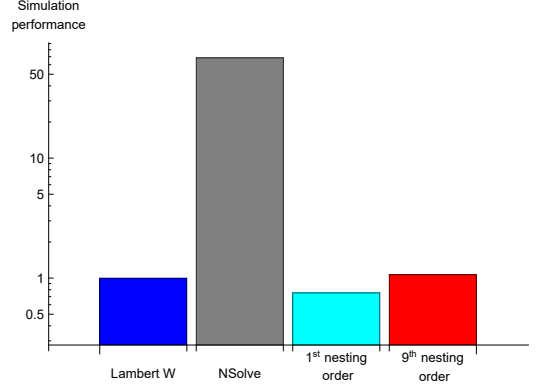


Fig. 4. Relative simulation performance (simulation duration) with reference to using Lambert W function.

III. CONCLUSION

We have introduced a simple and efficient analytical model to reproduce the gain behavior of highly-saturated SOAs. This model uses only two parameters and provides a behavior close to the experimental one for high optical-input powers.

REFERENCES

- [1] Y. Qi, W. Zhao, J. Dong, S. Wang, S. Ma, Q. Zhang, and L. Zhang, “Enhancing simulation efficiency in semiconductor optical amplifier (soa) models: A comparative study of first and second order approaches,” pp. 1686–1690, 2024.
- [2] M. J. Connelly, “Wideband Semiconductor Optical Amplifier Steady-State Numerical Model,” *IEEE Journal of Quantum Electronics*, vol. 37, no. 3, pp. 439–447, March 2001.
- [3] P. Morel and A. Sharaiha, “Wideband Time-Domain Transfer Matrix Model Equivalent Circuit for Short Pulse Propagation in Semiconductor Optical Amplifiers,” *IEEE Journal of Quantum Electronics*, vol. 45, no. 2, pp. 103–116, 2 2009.
- [4] A. Ghazisaeidi and L. A. Rusch, “On the efficiency of digital back-propagation for mitigating soa-induced nonlinear impairments,” *Journal of Lightwave Technology*, vol. 29, no. 21, pp. 3331–3339, 2011.
- [5] P. Morel, “Modélisation des amplificateurs optiques à semi-conducteurs : du composant au système,” Ph.D. dissertation, Université de Bretagne occidentale, 2006.
- [6] G. P. Agrawal and N. A. Olsson, “Self-Phase Modulation and Spectral Broadening of Optical Pulses in Semiconductor Laser Amplifiers,” *IEEE Journal of Quantum Electronics*, vol. 25, no. 11, pp. 2297–2306, November 1989.
- [7] R. Corless, G. Gonnet, D. Hare, D. J. Jeffrey, and D. E. Knuth, “On the Lambert W function,” *Advances in Computational Mathematics*, vol. 5, p. 329–359, December 1996.

Realization of high-speed 3D waveguide analysis model via transfer learning based on 2D-FDTD simulation

Gai Ichisawa
Institute of Science Tokyo, Japan
ichisawa.g.b63a@m.isct.ac.jp

Sho Okada
National Institute of Information and
Communications Technology, Japan
okada.s.ah@nict.go.jp

Tomohiro Amemiya
Institute of Science Tokyo, Japan
amemiya.t.e262@m.isct.ac.jp

Abstract—In this study, we realized an optical device analysis program that achieves results equivalent to those of 3D-FDTD with a small amount of computation time and computational resources using transfer learning, and actually applied it to a 1x2 MMI coupler to discuss its usefulness. The proposed model has an R^2 score of 0.901 and an analysis time of about 47.4 μ s per calculation, which is sufficiently fast compared to the 3D-FDTD.

Keywords—FDTD, DNN, Transfer Learning, Side Tuning

I. INTRODUCTION

Optical circuit technology, including silicon photonics, is becoming indispensable for future optoelectronic convergence because it enables high-speed, large-capacity, and low-power data transmission. In this context, the finite difference time domain (FDTD) method is becoming more important for designing various devices in optical circuits. However, a bottleneck in the optimal design of devices using 3D-FDTD is that it requires a large amount of time for analysis (or a large amount of computational resources), even for simple structures.

Against this background, in this study, we realized an optical device analysis program that achieves results equivalent to those of 3D-FDTD with a small amount of computation time and computational resources using transfer learning, and actually applied it to a 1x2 MMI coupler to discuss its usefulness.

II. METHODS OF REALIZING ANALYSIS PROGRAM

When realizing an optical device analysis program that uses deep learning to obtain results equivalent to those of 3D-FDTD, it is necessary to collect a large amount of training data using 3D-FDTD for the target optical device in advance. However, it is clear that this is not realistic in terms of computation time and computational resources.

Therefore, in this study, we introduced a method in which a neural network is roughly trained using a large amount of analysis data with 2D-FDTD, which has a low computational load, and then the network is optimized by transfer learning using a small amount of analysis data with 3D-FDTD. This method is versatile regardless of the type of optical device, and in this study, its effectiveness was verified by creating an analysis program for a 1x2 multi-mode interferometer (MMI) coupler.

III. DATA PREPARATION

As mentioned above, a deep neural network (DNN) analytical model for a 1x2 MMI coupler was created in this study. As shown in Fig. 1, four structural parameters were set as input variables: length L , width W , and output port positions P_{o1} and P_{o2} (-1 for the end of the device, 0 for center, and 1 for the other end of the device), and the output variable was the light intensity from each port.

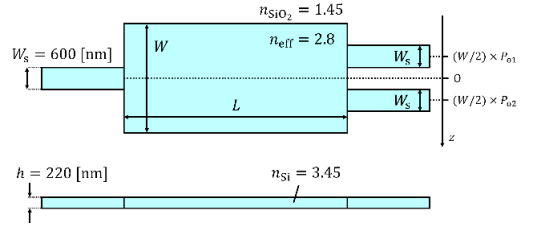


Fig. 1 Structure of MMI applying the proposed analysis method using transfer learning.

Table 1 Structural parameter distribution settings

Parameter	Average	Standard deviation	Range
L	15.5 μ m	4.00 μ m	[3.50, 27.5] μ m
W	3.00 μ m	0.33 μ m	[2.00, 4.00] μ m
P_{o1}, P_{o2}	0	0.33	[-1.0, 1.0]

In this study, we generated 10000 sets of 2D-FDTD data and 400 sets of 3D-FDTD data using *Synopsys RSoft Photonic Device Tools* while randomly varying the input variables to stay within $\pm 3\sigma$ according to the normal distribution in Table 1 (including moderate amounts of structural parameters for devices with high output intensity).

IV. NETWORK DESIGN FOR 2D-FDTD

First, a neural network was trained to predict the intensity of the two output ports of a 1x2 MMI coupler using 1000 sets of 2D-FDTD data. For training, we used 5-fold cross-validation, with the average of the maximum R^2 scores as the evaluation index for the network. Models that were determined to be overlearning by looking at the loss function were excluded from the evaluation.

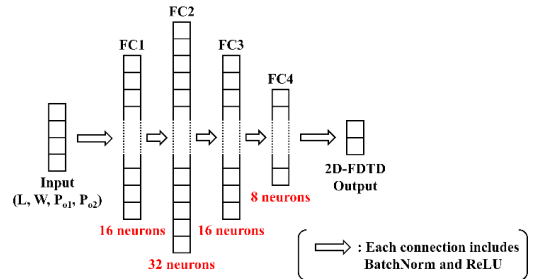


Fig. 2 Network configuration trained with analyzed data from 2D-FDTD.

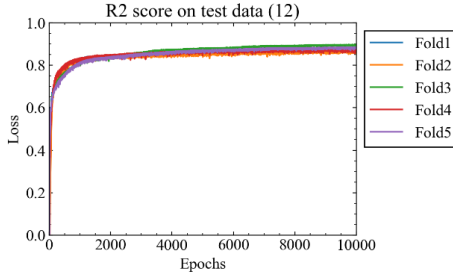


Fig. 3 Score transition of NN shown in Fig. 2.

The optimized network and score transition are shown in Figs. 2 and 3. The optimized DNN was fully connected with 16, 32, 16, and 8 nodes in the hidden layer, where the R2 score was 0.936

V. NETWORK DESIGN FOR 3D-FDTD

Next, based on the network trained with the analysis data from the 2D-FDTD, the network was optimized by transfer learning [1-3] using a small amount of analysis data from the 3D-FDTD. The final DNN analysis model for the 1x2 MMI coupler is shown in Fig. 4. First, the four structural parameters are input to the DNN trained in section IV (Fig. 2) to obtain two feature values. Next, these two feature values and the original four inputs are combined to form a 6-dimensional vector. This vector is input to a small network (2 layers, 8 nodes per layer) to finally obtain the light intensity from each port. After training the small network, the R^2 score was 0.901, as shown in Fig. 5.

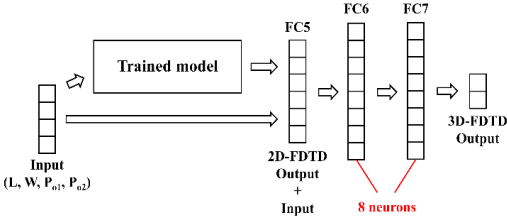


Fig. 4 Transfer learning network configuration trained with analyzed data from 3D-FDTD.

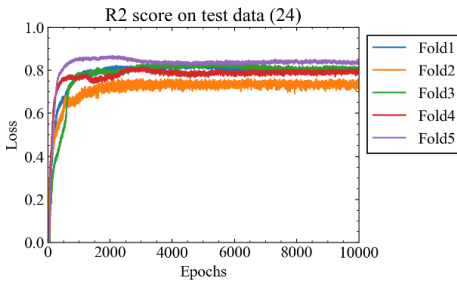


Fig. 5 Score transition of NN shown in Fig. 4.

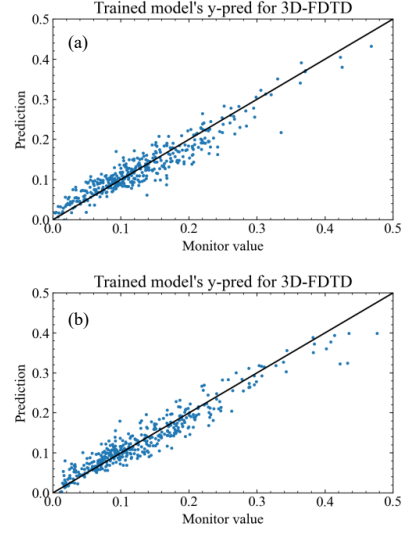


Fig. 6 A plot of the actual 3D-FDTD analysis results and the DNN prediction results obtained in Section V. (a) Output port 1. (b) Output port 2.

Table 2 Average calculation time for each method

Method	Software	Processor	Time
3D-FDTD	Synopsys RSoft Photonic Device Tools	Intel Xeon Gold 6238R	3 h
DNN	Python (PyTorch)	NVIDIA GeForce RTX 3070	47.4 μ s

VI. DNN PERFORMANCE

A plot of the actual 3D-FDTD analysis results and the DNN prediction results obtained in section V is shown in Fig. 6. 10^5 runs of DNN predictions were performed, and all calculations were completed in 4.74 s, for an average analysis time of 47.4 μ s per run. It can be concluded that by using transfer learning, analysis results equivalent to 3D-FDTD could be obtained with less computation time and computational resources.

This method is considered to be versatile because it can be used not only for MMI but also for other optical devices.

ACKNOWLEDGMENT

This work is supported by JSPS KAKENHI (25H00734), JST CREST (JPMJCR24R1), JST ASPIRE (23837157).

REFERENCES

- [1] F. Zhuang, et al., "A Comprehensive Survey on Transfer Learning," in *Proceedings of the IEEE*, vol. 109, no. 1, pp. 43-76, Jan. 2021, doi: 10.1109/JPROC.2020.3004555.
- [2] M. Iman, H. R. Arabnia, and K. Rasheed, "A review of deep transfer learning and recent advancements," *Technologies*, vol. 11, no. 2, p. 40, 2023, doi: 10.3390/technologies11020040.
- [3] J. O. Zhang, A. Sax, J. Malik, L. Guibas, and A. Zamir, "Side-tuning: A baseline for network adaptation via additive side networks," *Computer Vision – ECCV 2020*, pp. 698–714, 2020, doi: 10.1007/978-3-030-58580-8_41.

Instabilities in Pulse Propagation described by Generalized Nonlinear Schrödinger Equations

1st Shalva Amiranashvili

Weierstrass Institute
for Applied Analysis and Stochastics
Berlin, Germany
shalva.amiranashvili@wias-berlin.de

2nd Uwe Bandelow

Weierstrass Institute
for Applied Analysis and Stochastics
Berlin, Germany
uwe.bandelow@wias-berlin.de

3rd Raimondas Čiegis

Vilnius Gediminas Technical University
Vilnius, Lithuania
raimondas.ciegis@vgtu.lt

Abstract—This work investigates instabilities that can occur during pulse propagation along optical fibers. They can have physical origin, as the modulation instability, or being just numerical artefacts. We analyze in particular the numerical stability of operator splitting methods applied to Generalized Nonlinear Schrödinger Equations.

Index Terms—nonlinear fibers; nonlinear Schrödinger equation; modulation instability; splitting methods

I. INTRODUCTION

The propagation of optical pulses along nonlinear and dispersive optical fibers is often described by the generalized nonlinear Schrödinger equation (GNLSE) [1], which we present in the following form

$$i\partial_z\psi + \hat{D}\psi + \gamma|\psi|^2\psi = 0. \quad (1)$$

The GNLSE is suited to describe the evolution of stable pulses such as solitons, but also the modulation instability (MI) which is a fundamental physical phenomenon in the field of nonlinear waves [2]. MI occurs when small spontaneous modulations of initially uniform carrier wave begin to grow, leading to the emergence of various localized structures, such as robust solitary pulses [3] or spontaneous rogue waves [4].

Dispersive effects on wave propagation are governed in the GNLSE by the linear dispersion operator $\hat{D} = \sum_{j=2}^J \frac{\beta_j}{j!} (i\partial_\tau)^j$ and are separated from nonlinear effects, which are governed by the last term in Eq. (1). According to this separation, split-step methods provide an efficient approach for the numerical solution of the GNLSE, because they allow to separating complex problems into simpler, more manageable parts. In fact, in the context of optics, split-step methods are routinely used to study the propagation of pulses in optical networks [5], [6]. However, such methods are explicit and can lead to numerical instabilities, which we investigate. Results previously obtained for multiplicative splitting methods are extended to additive splittings [7]. An estimate of the largest possible integration step is derived and tested. The results are important when many solutions of GNLSE are needed, e.g., in optimization problems or statistical calculations.

We split the GNLSE into linear (A) and nonlinear (B) parts:

$$\partial_z\psi = (B + A)\psi \Rightarrow \psi(z + h) = e^{h(B+A)}\psi(z). \quad (2)$$

The above formal solution can be replaced by its splitting

$$\Psi(z+h) = e^{hB}e^{hA}\Psi(z); \quad e^{h(B+A)} = e^{hB}e^{hA} + O(h^2). \quad (3)$$

$\Psi(z)$ approximates $\psi(z)$ when the integration step $h \rightarrow 0$. The exponential $e^{h(B+A)}$ in Eq. (2) is understood as the propagator.

A. Multiplicative Methods

A multiplicative splitting \mathcal{M} of order p with s stages, which involves $2s$ $a_{1 \leq n \leq s}$ and $b_{1 \leq n \leq s}$, is defined by

$$e^{h(B+A)} = \mathcal{M}(h) + O(h^{p+1}) \quad (4)$$

with $\mathcal{M}(h) = e^{b_s h B} e^{a_s h A} \dots e^{b_1 h B} e^{a_1 h A}$. The splitting coefficients are selected so that the formal Taylor expansions of $\mathcal{M}(h)$ and $e^{h(B+A)}$ coincide as prescribed. The simplest are the Lie–Trotter splitting with $s = p = 1$ and the classical Strang splitting with $s = p = 2$ [8]. Another famous example with $s = p = 4$ is the Suzuki–Yoshida splitting [9], [10]. Equation (4) can be transformed to the equivalent form [10]

$$e^{h(B+A)+\Delta(h)} = e^{b_s h B} e^{a_s h A} \dots e^{b_1 h B} e^{a_1 h A} \quad (5)$$

The leading term in the local error $\Delta(h) = O(h^{p+1})$ consists of commutators of length $p+1$. All commutators with shorter lengths must cancel each other, which gives a system of algebraic equations for the splitting coefficients. When a basis set in the space of commutators is chosen, the local error can be characterized by the ℓ^2 norm of the leading term in $\Delta(h)$,

$$\|\Delta(h)\| = \varkappa \frac{h^{p+1}}{(p+1)!} + O(h^{p+2}), \quad \varkappa = \text{const}. \quad (6)$$

The numerical value of \varkappa is used to compare splittings of the same order to each other, and the final choice of $a_{1 \leq n \leq s}$ and $b_{1 \leq n \leq s}$ is made in favor of the minimal \varkappa .

B. Additive Methods

Additive splitting offers computational advantages, particularly for parallel architectures. If we use multiple splittings of the form (4) and then combine their predictions with appropriate weights, we obtain an additive splitting scheme.

Each multiplicative component of an additive splitting will be referred to as a thread, implying that different threads can be calculated independently on a multi-core machine before

taking their weighted sum to accomplish an integration step. The simplest additive splitting is the second Strang splitting [8]

$$e^{h(B+A)} = \frac{1}{2} (e^{hB} e^{hA} + e^{hA} e^{hB}) + O(h^3). \quad (7)$$

Another example is the splitting with four threads and $p = 3$ derived by Burstein and Mirin [11]. As a third example, we follow the ARBBC splitting [12] with four threads and $p = 4$, which has a 10 times smaller local error parameter $\varkappa = 0.36$, compared to the Suzuki–Yoshida splitting. Both the accuracy and efficiency of the ARBBC splitting have been studied previously [12]. Moreover, Ref. [12] contains a detailed comparison between the aforementioned additive schemes and commonly used multiplicative schemes. However, to the best of our knowledge, little is known about the stability conditions for the additive splittings.

C. Stability Analysis

Both multiplicative and additive splitting methods are explicit schemes, and while they are easy to implement and very fast [13], they can suffer from numerical instabilities. An extension of earlier results on stability to the fourth-order Suzuki–Yoshida splitting was reported in [14], and to an arbitrary multiplicative splitting in [15], again in the GNLSE framework. The extension for the mentioned additive splitting methods are reported in [7]. To assess stability we have derived a *root condition* in [7], requiring eigenvalues of the numerical propagation matrix \mathcal{M} to lie within the unit circle. This condition is sketched in Fig. 1, and it provides the stability domains. For GNLSE this gives the stability criterion for the stepsize h [16]:

$$h \leq \frac{\pi}{\max_{\Omega} |M(\Omega)|}.$$

Here, $M(\Omega)$ is the even part of the dispersion function $D(\Omega)$.

As an example, have tested the correctness of splitting methods with respect to MI. In result, the second Strang splitting [8] fails regardless of step size h . The Burstein and Mirin splitting [11] requires, roughly speaking, a two times smaller integration step than the multiplicative splittings, but can capture the MI. The additive splitting proposed in Ref. [12] can be used with the same integration step as the multiplicative splittings. At least, the stability criterion should be an integral part of any implementation of splitting solvers for GNLSE. This is especially important when the dispersion function and, therefore, the differential operator in GNLSE are approximated by higher-order polynomials. The ARBBC splitting performs comparably to multiplicative schemes even at large h , but is both more accurate and less restrictive.

II. CONCLUSIONS

We have studied restrictions on the numerical integration step h that provide a numerically stable split-step solution of the GNLSE (1). The root condition provides a practical stability check and helps to avoid numerical artifacts. The technique has been applied to the mentioned additive splittings, which are of interest because different threads of such

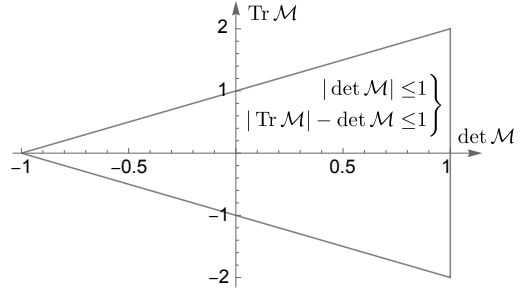


Fig. 1. Stability domain for the propagation matrix \mathcal{M} . If the point $(\det \mathcal{M}, \text{Tr} \mathcal{M})$ is inside the triangle, the eigenvalues of \mathcal{M} are inside the unit circle. This is the root condition. From [7].

splitting schemes can be computed independently on a multi-core machine, and ARBBC is the most reliable scheme.

REFERENCES

- [1] G. P. Agrawal, *Nonlinear Fiber Optics*, Academic, New York, 4 ed., 2007.
- [2] V. E. Zakharov and L. A. Ostrovsky, “Modulation instability: the beginning,” *Physica D: Nonlinear Phenomena* **238**, pp. 540–548, March 2009.
- [3] A. Hasegawa and M. Matsumoto, *Optical Solitons in Fibers*, Springer, 2003.
- [4] M. Erkintalo, K. Hammani, B. Kibler, C. Finot, N. Akhmediev, J. M. Dudley, and G. Genty, “Higher-order modulation instability in nonlinear fiber optics,” *Phys. Rev. Lett.* **107**, p. 253901, Dec 2011.
- [5] S. Musetti, P. Serena, and A. Bononi, “On the accuracy of split-step Fourier simulations for wideband nonlinear optical communications,” *Journal of Lightwave Technology* **36**, pp. 5669–5677, December 2018.
- [6] J. de Negreiros Júnior, D. do Nascimento e Sá Cavalcante, J. de Moraes, L. R. Marcelino, F. de Carvalho Belchior Magalhães, R. R. Barboza, M. de Carvalho, and G. de Freitas Guimarães, “Ultrashort pulses propagation through different approaches of the split-step Fourier method,” *Journal of Mechatronics Engineering*, **1**, pp. 2–11, December 2018.
- [7] S. Amiranashvili, U. Bandelow, and R. Čiegis, “Stability of the Additive Splitting methods for the Generalized Nonlinear Schrödinger Equation,” *Mathematics* **13**(8), p. 1301, 2025.
- [8] G. Strang, “Accurate partial difference methods I: Linear Cauchy problems,” *Arch. Rat. Mech. Anal.* **12**, pp. 392–402, January 1963.
- [9] M. Suzuki, “Fractal decomposition of exponential operators with applications to many-body theories and Monte Carlo simulations,” *Phys. Lett. A* **146**, pp. 319–323, June 1990.
- [10] H. Yoshida, “Construction of higher order symplectic integrators,” *Phys. Lett. A* **150**, pp. 262–268, November 1990.
- [11] S. Z. Burstein and A. A. Mirin, “Third order difference methods for hyperbolic equations,” *J. Comput. Phys.* **5**, pp. 547–571, June 1970.
- [12] S. Amiranashvili, M. Radziunas, U. Bandelow, K. Busch, and R. Čiegis, “Additive splitting methods for parallel solutions of evolution problems,” *Journal of Computational Physics* **436**, pp. 1–14, July 2021.
- [13] M. Lovisetto, D. Clamond, and B. Marcos, “Integrating factor techniques applied to the Schrödinger-like equations. Comparison with Split-Step methods,” *Applied Numerical Mathematics* **197**, pp. 258–271, March 2024.
- [14] J. Yang, *Nonlinear Waves in Integrable and Nonintegrable Systems*, SIAM, 2010.
- [15] S. Amiranashvili and R. Čiegis, “Stability of the higher-order splitting methods for the nonlinear Schrödinger equation with an arbitrary dispersion operator,” *Mathematical Modelling and Analysis* **29**(3), pp. 560–574, 2024.
- [16] F. Severing, U. Bandelow, and S. Amiranashvili, “Spurious four-wave mixing processes in generalized nonlinear schrödinger equations,” *J. Lightwave Technol.* **41**, pp. 5359–5365, August 2023.

Modelling coherent emission in transverse coupled cavity VCSELs

1st Martino D'Alessandro
Politecnico di Torino
Torino, Italy
martino.dalessandro@polito.it

2nd Valerio Torrelli
Politecnico di Torino
Torino, Italy

3th Pierluigi Debernardi
CNR-IEHT
Torino, Italy

4th Alberto Gullino
CNR-IEHT
Torino, Italy

5th Keyvan Azimi Asrari
University of Pavia
Pavia, Italy

6th Markus Lindemann
Ruhr-Universität
Bochum, Germany

7th Thomas de Adelsburg Ettmayer
Ruhr-Universität
Bochum, Germany

8th Guido Giuliani
University of Pavia, Juhlght Srl
Pavia, Italy

9th Alberto Tibaldi
Politecnico di Torino
Torino, Italy

Abstract—Transverse coupled cavity (TCC)-VCSELs are promising candidates for the next generation of high-speed direct modulation devices. We present a comprehensive framework for their investigation based on the dynamical solution of the scalar wave equation and compare it with recent experimental results.

Index Terms—Transverse coupled cavity, VCSELs, coherent emission

I. INTRODUCTION

TCC VCSELs [1] are promising candidates for a number of different applications, such as direct modulation [2], beam steering and terahertz generation [3]. The potential of these devices lies on the presence of two nearly frequency-degenerate (super)-modes [4], which however implies a critical thermal management and impact of technological variations. In this work we present a model based on the dynamical solution of the scalar wave equation. The model naturally handles particular dynamical states for which two modes are coherently phase-locked [2]. Such effects can be observed by adding cross-coupling terms to the standard rate equation model, which are derived from the scalar wave equation [4] and arise from the variations of the refractive index due to gain, self-heating or unwanted variations on the nominal structure.

We consider the structure manufactured in [5], consisting in a standard 850 nm VCSEL with *bow-tie* oxide aperture, comprising two circular cavities of radius $R_{R,L}$, connected by a rectangular region denoted as *bridge*. It is reasonable to assume that, due to the oxidation process, one of the two apertures is slightly bigger than the other ($R_R < R_L$ in this case). We assume that the two cavities are electrically isolated, as done in [6], and that we can pump them separately with currents $I_{R,L}$, respectively. Fig.1 shows a sketch of the oxide aperture together with a cut of the first two optical modes, computed with our in-house VCSEL modal solver. The two modes are nearly degenerate in frequency and threshold gain.

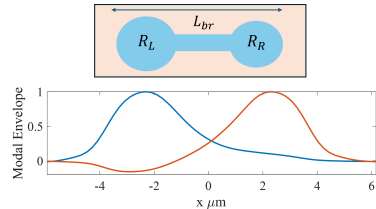


Fig. 1. Sketch of the oxide aperture under investigation together with the first two optical modes. $L_{br} = 4\mu\text{m}$ in this work.

II. THEORY AND RESULTS

By representing the electric field in the quantum well as a sum of the optical modes (*cold-cavity modes*), we obtain a set of dynamical equations for the i -th modal amplitude E_i , reading:

$$\partial_t E_i = (i\omega_i - L_i)E_i + \sum_j k_{ij}E_j, \quad (1)$$

where L_i and ω_i are the i -th modal losses and frequency offset with respect to an arbitrary reference ω_0 , and k_{ij} is given by the following integral on the active region (AR):

$$k_{ij}(t) = \frac{v_g \Gamma_z}{2} \iint_{\text{AR}} \Psi_i^* \Psi_j g(x, y) dx dy, \quad (2)$$

where v_g is the group velocity, Γ_z is the optical confinement factor and $g(x, y)$ is a generalized definition of gain accounting for thermal effects, defined by:

$$g = \underbrace{(1 + i\alpha_h)[G_d(N(x, y) - n_{tr})]}_{\text{carriers}} - \underbrace{i \frac{\Gamma_{th}}{\Gamma_z} \frac{4\pi}{\lambda_0} \frac{dn}{dT} \Delta T(x, y)}_{\text{temperature}} \quad (3)$$

where n_{tr} is the transparency carrier density, G_d is the differential gain, α_h is the linewidth enhancement factor, $\frac{dn}{dT}$ is a

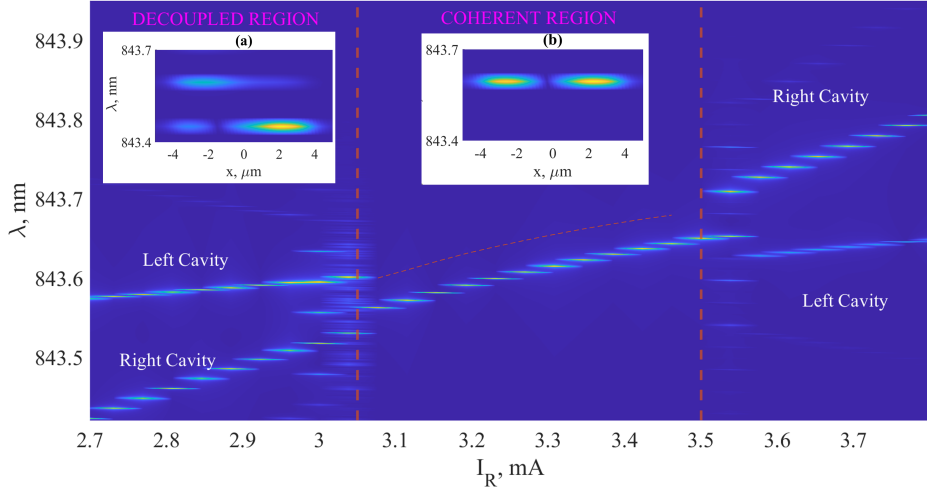


Fig. 2. Simulated optical spectrum for varying I_R for fixed $I_L = 3 \text{ mA}$. The vertical lines denote the boundaries of the coherent region. Insets: wavelength resolved near field for (a) 2.8 mA and (b) 3.2 mA. The dashed line is the emission wavelength of the below-threshold supermode in the coherent range, computed by finding the eigenvalues of the matrix k_{ij} .

phenomenological coefficient describing the variation of the refractive index with respect to the temperature, λ_0 is the reference wavelength associated to ω_0 , Γ_{th} is a phenomenological coefficient to describe the overlap of the standing wave with the longitudinal temperature profile, set to 1 in this work, ΔT is the self-heating temperature variation profile. In this work, we assume ΔT as a superposition of two *gaussians* centered in the two apertures, whose peak values are proportional to the currents $I_{R,L}$, with a coefficient of $7.5 \frac{\text{K}}{\text{mA}}$. Other material parameters can be found in [4]. The model is closed with the self-consistent solution of the carrier diffusion equation by means of a finite-element discretization, as carried out in [2].

We solve the dynamical equations fixing I_L and varying I_R , using the first four modes as basis. Fig. 2 shows the resulting optical spectra. At low I_R , each cavity emits at a distinct wavelength, with a large frequency separation due to the temperature difference between the apertures. As I_R increases and approaches I_L , a coherent regime emerges where both cavities emit at the same frequency, which tends toward the lower-wavelength mode. The plot is asymmetric with respect to $I_R = I_L$, reflecting the structural asymmetry of the device. In particular, the coupling occurs when the smaller cavity is hotter. The two insets display the wavelength-resolved near-field, highlighting the considerations made so far. Given a certain gain and temperature profile, we can interpret as *pumped-cavity* modes the combination of *cold-cavity* modes that diagonalize the matrix k_{ij} , where the imaginary part of the correspondent eigenvalues represents the emission frequency. In this way, we can highlight the presence of a below-threshold

supermode in the coherent range, which is responsible for photon-photon-resonance [4], denoted with the dashed line.

The simulated behaviour aligns well with recent experimental results [7] [6]. Evidence of coherent emission has been also recently observed in [2], showing theoretically and experimentally an enhancement of the bandwidth modulation.

III. ACKNOWLEDGEMENT

Alberto Tibaldi and the members of Ruhr-University and Julight would like to acknowledge the Italian Ministero dell'Università e della Ricerca (MUR) and by the German Bundesministerium für Bildung und Forschung within the EU-ROSTARS project 'COHORT' (E! 6226) for having partially funded this research.

REFERENCES

- [1] H. Dalir, F. Koyama, *Applied Physics Letters* **103**, 091101 (2013).
- [2] M. Lindemann, *et al.*, *Journal of Applied Physics* (submitted) (2025).
- [3] Y. Hu, *et al.*, *Electronics Letters* **61** (2025).
- [4] M. D'Alessandro, *et al.*, *IEEE Photonics Journal* **16**, 1 (2024).
- [5] M. Lindemann, *et al.*, *2023 23rd International Conference on Transparent Optical Networks (ICTON)* (2023).
- [6] W. North, *et al.*, *Journal of Lightwave Technology* **42**, 236 (2024).
- [7] S. T. M. Fryslië, *et al.*, *IEEE Journal of Selected Topics in Quantum Electronics* **23**, 1 (2017).

1D vectorial simulations of anisotropic VCSELs

1st Valerio Torrelli
Politecnico di Torino, CNR-IEIIT
Torino, Italy
valerio.torrelli@polito.it

2nd Martino D'Alessandro
Politecnico di Torino, CNR-IEIIT
Torino, Italy
martino.dalessandro@polito.it

3rd Pierluigi Debernardi
CNR-IEIIT
Torino, Italy
pierluigi.debernardi@cnr.it

Abstract—Recent work has shown that elliptically and circularly polarized vertical-cavity surface-emitting lasers (VCSELs) can be realized by leveraging the interaction between tilted anisotropic layers. To harness this effect for the design of custom-polarized emitters, we present a mathematical framework that enables fast and efficient one-dimensional vectorial simulations of anisotropic VCSELs.

Index Terms—VCSELs, polarization, optical anisotropies

I. INTRODUCTION

Optical anisotropies play a key role in determining the polarization of vertical-cavity surface-emitting lasers (VCSELs), whether they arise from electro- and elasto-optic effects [1], [2] or subwavelength gratings (SWG) [3]. Anisotropies cause dichroism and birefringence, and, when tilted to each other, the supported VCSEL polarizations become elliptical due to a resonator chirality [3], [4]. In this work, we develop a mathematical framework to analyze the polarization of single-mode anisotropic VCSELs, enabling the emission of any custom polarization state.

II. THEORY AND RESULTS

Consider a single-mode VCSEL composed of a stack of anisotropic layers as depicted in Fig. 1. Focusing on a one-dimensional analysis, transverse variations along the (x, y) plane can be neglected, allowing us to focus solely on the longitudinal stack along z . This corresponds to an electric field phasor \mathbf{E} without a z -component. According to [5], \mathbf{E} can be expanded in terms of the modes $\{\mathbf{e}_\mu\}$ supported by a uniform medium with a real scalar dielectric constant ϵ_{ref} (and refractive index r), where μ represents a multi-dimensional label. In this case, $\mu = [i, \alpha]^T$, where $i \in \{x, y\}$ represents the linear polarization either along x or y , while $\alpha \in \{\text{forward (f)}, \text{backward (b)}\}$ indicates the propagation direction. We define $\mathbf{e}_\mu = e_0(\hat{x}\delta_{ix} + \hat{y}\delta_{iy})$, where δ_{ij} is the Kröner delta and e_0 is arbitrary. Two polarization modes are labeled by $\mu = [i, \alpha]$ and $\nu = [i', \alpha']$, and must be normalized so that:

$$\int_{\mathbb{R}^2} \mathbf{e}_\mu \cdot \mathbf{e}_\nu dxdy = \frac{Z_\perp C_\mu}{2s_\mu} \delta_{ii'}, \quad (1)$$

where C_μ is the modal power normalization constant, $s_\mu = \pm 1$ according to α and $Z_\perp = Z_0/r$, Z_0 being the vacuum impedance. The field phasor within the VCSEL can be written as $\mathbf{E}(z) = \sum_\mu a_\mu(z)\mathbf{e}_\mu$, shifting the unknown to the 4 z -dependent expansion coefficients $\{a_\mu\}$.

Each VCSEL layer is described by its thickness t and by its anisotropic dielectric constants ϵ_{XX} and ϵ_{YY} along their principal axes (X, Y) , which can be tilted to our reference system (x, y) by an angle ϕ (top inset of Fig. 1). It is convenient to define the isotropic and anisotropic dielectric

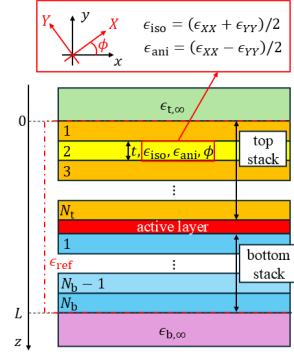


Fig. 1. VCSEL schematic and needed parameters for each layer.

constants ϵ_{iso} and ϵ_{ani} as $(\epsilon_{XX} \pm \epsilon_{YY})/2$, respectively. An isotropic refractive index can be associated to the anisotropic layer as $n_{\text{iso}} = \sqrt{\epsilon_{\text{iso}}/\epsilon_0}$, ϵ_0 being the vacuum dielectric constant.

Expressing $\{a_\mu\}$ as the vector $\mathbf{a} = [a_{xf}, a_{xb}, a_{yf}, a_{yb}]^T$, the transmission matrix of one of the VCSEL layers embedded in the reference medium can be obtained solving the coupled mode equations as $\mathbf{T} = \exp[(\mathbf{B} + \mathbf{K})t]$ [5], \mathbf{B} and \mathbf{K} representing the propagation and coupling matrices. \mathbf{B} is diagonal with $B_{11} = B_{13} = -j\beta_\perp$, $B_{22} = B_{44} = j\beta_\perp$, where j is the imaginary unit, $\beta_\perp = 2\pi r/\lambda$ and λ is the optical wavelength. On the other hand,

$$\mathbf{K} = \frac{j\omega(\epsilon_{\text{iso}} - \epsilon_{\text{ref}})Z_\perp}{2} \begin{bmatrix} -1 & -1 & 0 & 0 \\ 1 & 1 & 0 & 0 \\ 0 & 0 & -1 & -1 \\ 0 & 0 & 1 & 1 \end{bmatrix} + \frac{j\omega\epsilon_{\text{ani}}Z_\perp}{2} \begin{bmatrix} -\cos(2\phi) & -\cos(2\phi) & -\sin(2\phi) & -\sin(2\phi) \\ \cos(2\phi) & \cos(2\phi) & \sin(2\phi) & \sin(2\phi) \\ -\sin(2\phi) & -\sin(2\phi) & \cos(2\phi) & \cos(2\phi) \\ \sin(2\phi) & \sin(2\phi) & -\cos(2\phi) & -\cos(2\phi) \end{bmatrix}, \quad (2)$$

where ω is the optical pulsation. It is useful to define the matrix \mathbf{A} as the first matrix that appears in (2).

According to the sketch in Fig. 1, defining $\mathbf{T}_{i,t}$ and the $\mathbf{T}_{k,b}$ as the transmission matrices of the i -th and k -th layers of the top and bottom stacks, respectively, the transmission matrix of the whole stacks can be obtained as $\mathbf{T}_t = \mathbf{T}_{N_t}\mathbf{T}_{N_t-1}\dots\mathbf{T}_1 = \prod_{i=N_t}^1 \mathbf{T}_{i,t}$ and $\mathbf{T}_b = \prod_{k=N_b}^1 \mathbf{T}_{k,b}$, where N_t and N_b are the number of layers of the top and bottom stacks.

Let us now treat the active layer, considered isotropic, with thickness t_a and a nominal dielectric constant ϵ_a . To support

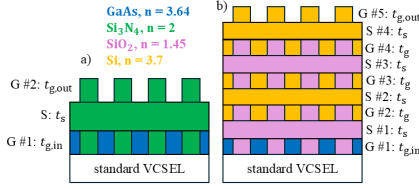


Fig. 2. Structures under investigation. On top of a standard VCSEL epit-structure, we consider 2 (a) or 5 (b) additional SWGs, separated by spacers.

optical modes, its dielectric constant must be modified by a quantity $\Delta\epsilon_a$, whose real part must be zero for cold cavity modes and whose imaginary part is linked to the modal threshold gain and represents an unknown of our problem. The coupling matrix of the active layer can be written as $\mathbf{K}_a = \mathbf{K}_{a,0} + (\Delta\epsilon_a/\epsilon_{\text{ref}})\Delta\mathbf{K}_a$, where $\mathbf{K}_{a,0} = j\omega(\epsilon_a - \epsilon_{\text{ref}})Z_{\perp}\mathbf{A}/2$ and $\Delta\mathbf{K}_a = j\omega\epsilon_{\text{ref}}Z_{\perp}\mathbf{A}/2$. Since $|\Delta\epsilon_a| \ll \epsilon_a$, for thin active layers it is possible to linearize the active transmission matrix as $\mathbf{T}_a = \mathbf{T}_{a,0} + (\Delta\epsilon_a/\epsilon_{\text{ref}})\mathbf{T}_{a,0}\Delta\mathbf{K}_a t_a$, where $\mathbf{T}_{a,0}$ is the transmission matrix of the active layer without any index modification. Using this expression of \mathbf{T}_a , the transmission matrix for the whole VCSEL can be written as:

$$\mathbf{T} = \mathbf{T}_b\mathbf{T}_a\mathbf{T}_t = \mathbf{T}^{(1)} + (\Delta\epsilon_a/\epsilon_{\text{ref}})\mathbf{T}^{(2)}. \quad (3)$$

Finally, splitting the vector $\mathbf{a} \in \mathbb{C}^4$ into its forward and backward components \mathbf{a}_f and $\mathbf{a}_b \in \mathbb{C}^2$, accounting for the fact that within the interval $(0, L)$ all layers are embedded in the reference medium and evaluating the reflection coefficients from the reference medium to the boundary semi-infinite media at $z = 0$ (Γ_{top}) and $z = L$ (Γ_{bottom}), we end up with the following relationships: $\mathbf{a}_f(L^-) = \mathbf{T}_{ff}\mathbf{a}_f(0^+) + \mathbf{T}_{fb}\mathbf{a}_b(0^+)$, $\mathbf{a}_b(L^-) = \mathbf{T}_{bf}\mathbf{a}_f(0^+) + \mathbf{T}_{bb}\mathbf{a}_b(0^+)$, $\mathbf{a}_f(0^+) = \Gamma_{\text{top}}\mathbf{a}_b(0^+)$ and $\mathbf{a}_b(L^-) = \Gamma_{\text{bottom}}\mathbf{a}_f(L^-)$. Solving for $\mathbf{a}_b(0^+)$ and splitting all the components of the transmission matrices according to (3), we end up with the following 2×2 generalized eigenvalue problem:

$$\gamma \mathbf{N}^{(1)} \mathbf{a}_b(0^+) = \mathbf{N}^{(2)} \mathbf{a}_b(0^+), \quad (4)$$

where $\gamma = -\epsilon_{\text{ref}}/\Delta\epsilon_a$ and $\mathbf{N}^{(1,2)} = \mathbf{T}_{bf}^{(1,2)}\Gamma_{\text{top}} + \mathbf{T}_{bb}^{(1,2)} - \Gamma_{\text{bottom}}\mathbf{T}_{ff}^{(1,2)}\Gamma_{\text{top}} - \Gamma_{\text{bottom}}\mathbf{T}_{fb}^{(1,2)}$. By determining the wavelengths for which $\Re\{\gamma\} = 0$, one finds the emission wavelength λ_e of the two supported modes. At λ_e , $\Im\{\gamma\}$ can be used to evaluate the corresponding modal threshold gain g_{th} . The corresponding two eigenvectors $\mathbf{a}_b(0^+)$, defined up to a multiplicative constant, represent the near-field (NF) exiting the device since $\mathbf{a}_b(0^-) \propto \mathbf{a}_b(0^+)$, i.e., $\mathbf{a}_{\text{NF}} = [0, a_{xb}(0^+), 0, a_{yb}(0^+)]^T \in \mathbb{C}^4$. The latter can be transmitted from 0^- to 0^+ using the transmission coefficient from the top semi-infinite medium to the reference medium, then it can be propagated using the transmission matrices up to any section z of the VCSEL. This allows the evaluation of the standing wave as $\text{SW}(z) = |\mathcal{E}_x(z)|^2 + |\mathcal{E}_y(z)|^2$, where $\mathcal{E}_x(z) = a_{xf}(z) + a_{xb}(z)$ (similarly for \mathcal{E}_y), and the Stokes parameters according to [6].

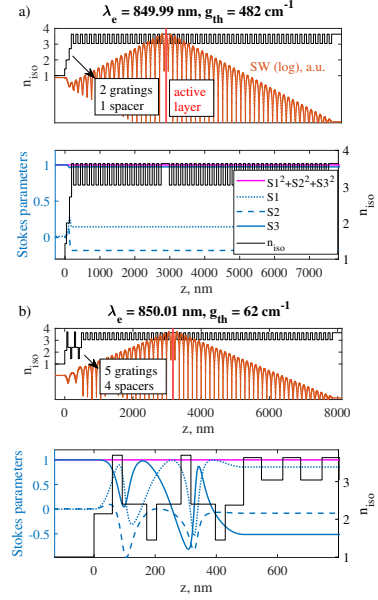


Fig. 3. Refractive index (n_{iso}), emission wavelength, threshold gain, SW and Stokes parameters of the lasing mode supported by structures (a) and (b).

This model is applied to the structures in Fig. 2, optimized for the emission of circularly polarized light. In structure (a), on top of an 850 nm VCSEL structure, we consider two SWGs of thicknesses $t_{g,\text{in}} = 60$ nm and $t_{g,\text{out}} = 41$ nm, tilted by 45° and separated by a spacer of thickness $t_s = 87$ nm. In structure (b), 5 gratings and 4 spacers are considered with parameters $t_s = 32$ nm, $t_{g,\text{in}} = t_{g,\text{out}} = 80$ nm, $t_g = 80$ nm. All gratings from the second on are tilted to the first one with an angle increasing in steps of $\Delta\phi = 3.8^\circ$. All gratings are treated as homogeneous anisotropic media using the Born-Wolf formulae with a 50% filling factor [6]. Fig. 3 reports λ_e , g_{th} and the Stokes parameters of the lasing mode of both structures, showcasing how this model can be used for polarization engineering in any section of the VCSEL.

REFERENCES

- [1] T. Pusch, *et al.*, *Semiconductor Lasers and Laser Dynamics VII* (SPIE, 2016), vol. 9892, pp. 338–343.
- [2] T. Pusch, *et al.*, *Spintronics XIII*, H.-J. M. Drouhin, J.-E. Wegrowe, M. Razeghi, eds., International Society for Optics and Photonics (SPIE, 2020), vol. 11470, p. 114702K.
- [3] V. Torrelli, *et al.*, *Opt. Lett.* **50**, 3082 (2025).
- [4] M. Zimmer, M. Birkhold, M. Jetter, P. Michler, *Vertical-Cavity Surface-Emitting Lasers XXVIII*, C. Lei, K. D. Choquette, eds., International Society for Optics and Photonics (SPIE, 2024), vol. PC12904, p. PC1290402.
- [5] G. P. Bava, P. Debernardi, L. Fratta, *Phys. Rev. A* **63**, 23816 (2001).
- [6] V. Torrelli, M. D'Alessandro, W. Elsäfer, P. Debernardi, *Opt. Lett.* **49**, 3773 (2024).

VCSEL thermal sources: a physics-based simulation approach

1st Alberto Gullino
Consiglio Nazionale Ricerche (CNR) - IEIIT
Torino, Italy
alberto.gullino@cnr.it

2nd Martino D'Alessandro
Politecnico di Torino - DET
Torino, Italy
martino.dalessandro@polito.it

3rd Valerio Torrelli
Politecnico di Torino - DET
Torino, Italy
valerio.torrelli@polito.it

4th Alberto Tibaldi
Politecnico di Torino - DET
Torino, Italy
alberto.tibaldi@polito.it

5th Francesco Bertazzi
Politecnico di Torino - DET
Torino, Italy
francesco.bertazzi@polito.it

6th Pierluigi Debernardi
Consiglio Nazionale Ricerche (CNR) - IEIIT
Torino, Italy
pierluigi.debernardi@cnr.it

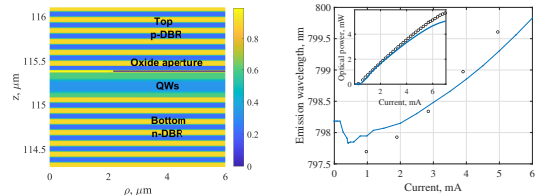
Abstract—Fully-comprehensive physics-based simulations of vertical-cavity surface-emitting lasers (VCSELs) must account for the coupled electrical, optical and thermal problems. While electrical and optical solvers form the foundation of cold-cavity VCSELs modeling, self-heating has the strongest impact during the device operation. In this work, we present the capability of our in-house solver VENUS to model the wavelength red-shift induced by temperature variations and show the spatial distribution of the primary thermal sources: Joule effect, free-carrier absorption, non-radiative recombinations and quantum-well capture. The spatial mapping of each source might allow to limit the impact of self-heating on the performance.

Index Terms—VCSEL, Heat equation, Physics-based

I. INTRODUCTION

Vertical-cavity surface-emitting lasers (VCSELs) serve as optical sources across a diverse set of applications, owing to their well-established advantages. High modulation bandwidth and circular beam profile pushed VCSELs adoption in short-reach, high-speed optical interconnects, particularly within data center environments [1]. Other applications ranging from gas sensing and atomic pumping to optical coherence tomography (OCT) for diagnostic imaging offer further lines of development for alternative applications. In these contexts, the output power of VCSELs is typically constrained by the limited size of their active region. Over the past decade, the need of a single-mode, narrow linewidth and large power coming from LiDARs (Light Detection And Ranging) technologies is pushing for novel design of VCSELs [2]. An instance is represented by multijunction VCSELs, that adopt tunnel junctions to cascade more active stages and enhance internal quantum efficiency and output power.

A common challenge for VCSELs regards self-heating, especially in continuous wave regime. Its primary evidence is the reduction of output power at the so called rollover current, related to the thermally induced gain peak shift, stronger leakage current and non-radiative recombination processes. Additionally, the thermally induced variation of the refractive index across the device shifts the emission wavelength towards



(a) Molar fraction in the cavity proximi- (b) Wavelength red-shift vs bias current
ty. I . Inset: LI curve.

Fig. 1: (a) 2D molar fraction of the VCSEL under analysis and (b) validation of VENUS (solid curve) against experimental results (circles).

red ($0.06 - 0.1 \text{ nm K}^{-1}$) and increases the spatial confinement of the modes (thermal lensing), possibly hindering beam quality and modal purity. A proper heat management should rely on a thermal-aware design of VCSELs, as their capillary diffusion in different markets requires a well rounded understanding of every aspect of their operation to develop high-performance devices.

II. RESULTS AND OUTLOOKS

To date, no experimental technique – whether destructive or non-destructive – possesses the capability of resolving the spatial distribution of self-heating within VCSELs. Experimentally, the sole accessible observable related to the temperature variation is the emission wavelength red-shift. This spectral measurement provides just an indirect glimpse, reflecting the averaged thermally induced modulation of the refractive index across the device.

Our in-house VCSEL static solver VENUS is capable of extracting and reproducing such experimental evidence for axisymmetric structures [3]. An example is reported in Fig. 1, where a standard industry-level oxide-confined ($\rho_{ox} = 2 \mu\text{m}$) *pin* AlGaAs VCSEL with GaAs quantum wells (QWs) emitting at 795 nm (see refractive index profile in Fig. 1a) is simulated. In Fig. 1b, the agreement with experimental emission wavelength and output power (LI) as a function

TABLE I: Thermal conductivity values adopted in VENUS for different sections of the investigated VCSEL [5].

VCSEL region	κ (Wm ⁻¹ K ⁻¹)
Substrate	46
DBRs, active region, mesa (transv.)	15
DBRs, active region, mesa (long.)	12
Passivation	0.5

of current ensures that VENUS is estimating properly self-heating, adopting $dn/dT = 2.35 \cdot 10^{-4}$ K⁻¹.

All the solver details are not reported here, beside the static heat equation solved adopting the mortar element method [4] to compute the spatially-distributed temperature T variation from the heat sink [5], accounted imposing a homogeneous Dirichlet condition at the substrate:

$$\nabla \cdot (\kappa \nabla T) = - \underbrace{\left(\frac{J_n^2}{\sigma_n} + \frac{J_p^2}{\sigma_p} \right)}_{\text{Joule}} - \underbrace{\frac{dS_z(z)}{dz} \cdot P_{st} \cdot |\varepsilon(\rho)|^2}_{\text{FCA}} - \underbrace{\left(qR_{nr}^{3D}(E_{fn} - E_{fp}) - (qC_{cap}^{3D}(E_{fn} - E_{fp}) - R_{st}^{2D}\hbar\omega) \right)}_{\text{NR recomb. capt./esc.}} \quad (1)$$

Here, κ denotes the non-linear thermal conductivity, whose values are reported in Table I. On the right hand side of (1), the expression for every thermal source is discussed afterwards. Each term is spatially dependent and comes from electrical (drift-diffusion, DD) and optical (electromagnetic) solvers.

In this way, VENUS locates the contribution from each thermal source in every point of the VCSEL mesh. In Fig. 2, we report their shape at a bias current of 5 mA. In Fig. 2a, the maximum temperature variations are reported as functions of current $\Delta T(I)$. The vertical line denotes 5 mA, and the inset shows the corresponding temperature longitudinal profile in the central section of the device.

The microscopic Ohm's law describes the Joule effect. It contains the squared current densities $J_{n,p}$ divided by the electrical conductivities $\sigma_{n,p}$. This explains the parabolic trend of $\Delta T_{Joule}(I)$, in blue in Fig. 2a. From Fig. 2c, the peak values arise at the oxide edge, where current crowding effect is relevant. The fringes stem from the DBRs heterointerfaces.

The free-carrier absorption (FCA) term contains the longitudinal derivative of the Poynting vector $S_z(z)$ – capturing the layer-by-layer absorption and the optical standing wave (SW) pattern, the output optical power P_{st} (explaining the linear $\Delta T_{FCA}(I)$, in red in Fig. 2a) and the emitted mode radial field shape $\varepsilon(\rho)$. In Fig. 2d, the fringes reflect the SW pattern, while the strong peak at the output facet comes from the highly absorptive GaAs contact layer.

The non-radiative (NR) recombination processes heating is modeled by multiplying Auger and SRH rates R_{nr}^{3D} by the elementary charge q and the quasi-Fermi level difference $E_{fn} - E_{fp}$. From Fig. 2a, their impact on the overall heating is very limited, and spatially located in the active region (Fig. 2e).

QW carrier capture is treated similarly to NR recombination. The capture rate C_{cap}^{3D} is responsible of filling QW states, acting as a quantum-correction to the bulk DD [3]. Most

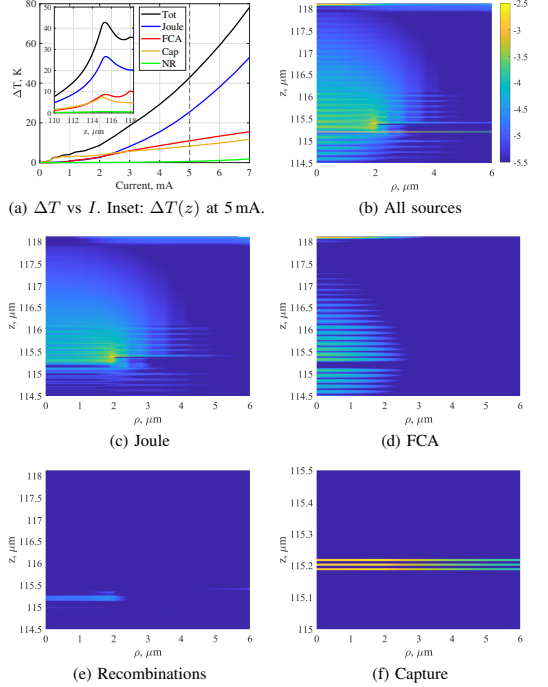


Fig. 2: (a) Temperature variation ΔT vs current I . (b–f) Thermal sources (log. scale) extracted at 5 mA, from the n-DBR pairs next to the cavity up to the output facet (on top). The 2D maps share the same color scale.

captured carriers contribute to the stimulated emission at energy $\hbar\omega$, that is treated as a 2D recombination (R_{st}^{2D}). The net difference between these two terms models the capture heating, localized in the QW nodes (Fig. 2f). Its impact on the overall $\Delta T(I)$ in Fig. 2a, in yellow, quickly increases up to threshold ($I_{th} = 0.5$ mA). After I_{th} , QW populations should remain clamped, as they are balanced with the stimulated emission. Nevertheless, temperature-induced cavity losses demand higher QW carrier densities.

The strength of our thermal model is the possibility of describing each heating source separately. The evaluation of each spatial and current-dependent signature unlocks thermal-aware novel design for high temperature operations.

REFERENCES

- [1] N. N. Ledentsov, *et al.*, “High speed vcsel technology and applications,” *J. Lightwave Technol.*, vol. 40, no. 6, pp. 1749–1763, 2022.
- [2] I. Kim, *et al.*, “Nanophotonics for light detection and ranging technology,” *Nature Nanotechnol.*, vol. 16, no. 5, pp. 508–524, 2021.
- [3] A. Tibaldi, *et al.*, “VENUS: a Vertical-cavity surface-emitting laser Electro-opto-thermal Numerical Simulator,” *IEEE J. Select. Topics Quantum Electron.*, vol. 25, no. 6, p. 1500212, Nov/Dec. 2019.
- [4] A. Tibaldi, *et al.*, “Skew incidence plane-wave scattering from 2-D dielectric periodic structures: analysis by the mortar-element method,” *IEEE Trans. Microwave Theory Tech.*, vol. 63, no. 1, pp. 11–19, 2015.
- [5] P. Debernardi, *et al.*, “Probing thermal effects in VCSELs by experiment-driven multiphysics modeling,” *IEEE J. Select. Topics Quantum Electron.*, vol. 25, no. 6, p. 1700914, Nov/Dec. 2019.

Comparative Study of Nano-Cylindrical Waveguide and Buried-SiO₂ Apertures in Blue InGaN VCSELs

Lakshminarayan Sharma, Lars Persson, Joachim Ciers, and Åsa Haglund
*Department of Microtechnology and Nanoscience
 Chalmers University of Technology,
 41296 Gothenburg, Sweden
 sharmal@chalmers.se*

Abstract—We study transverse mode control in InGaN-based blue vertical-cavity surface-emitting lasers (VCSELs) by investigating the most common index-guiding structure which is an etched nano-cylinder with and without a refill of SiO₂. Using 2–8 μm wide aperture diameters, we evaluate key performance metrics—threshold material gain (g_{th}) and modal discrimination. The etched aperture with a 5 nm etch depth exhibited the lowest threshold material gain among the designs studied. Notably, this configuration showed the smallest increase in threshold material gain when the aperture diameter was reduced from 8 μm to 2 μm . Furthermore, when decreasing the aperture from 8 μm to 4 μm , the g_{th} for the fundamental LP₀₁ mode increased by just 95 cm^{-1} , while still achieving a high modal discrimination of 395 cm^{-1} . These results highlight the ability of the etched aperture to maintain low loss and strong mode selectivity over a practical range of aperture sizes.

I. INTRODUCTION

A truly single-mode VCSEL operates only in the fundamental mode, producing a near-Gaussian beam with superior spectral purity, and low divergence. These properties are critical for various applications such as underwater optical wireless communication, smart glasses, adaptive laser headlights, and atomic clocks.

Lateral optical and current confinement have been achieved through various aperture design approaches in InGaN VCSELs. Such as silicon diffusion [1], air-gap aperture formed by photoelectrochemical etching [2], buried SiO₂ layer [3], and etched-passivated nano-cylindrical aperture [4].

Kuramoto et al. [4] and Terao et al. [5] have experimentally demonstrated single-mode operation in blue-emitting VCSELs using nano-cylindrical apertures with diameters of 3.3 μm and 4 μm , respectively. These results underscore the effectiveness of the nano-cylindrical design in promoting single-mode operation while maintaining a relatively simple and fabrication-friendly structure.

In this paper, we simulated the threshold material gain and modal discrimination of blue InGaN VCSELs having two aperture designs for lateral index guiding; an etched nano-cylinder with and without a refill of SiO₂. The etched aperture had an etch depth of 5 or 10 nm and the SiO₂ refilled had an etch depth of 20 nm that was filled up with 20 nm of SiO₂.

This project has received funding from the European Innovation Council (EIC) under grant agreement 101130710 funded by the European Union.

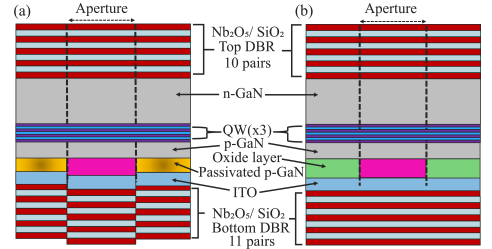


Fig. 1. Schematic of the the simulated VCSEL structure (a) with a passivated nano-cylindrical waveguide aperture and (b) with a buried SiO₂ aperture.

The studied aperture diameters were 2 μm , 4 μm , 6 μm , and 8 μm .

II. DEVICE SIMULATION DESIGN AND PARAMETERS

The VCSEL structure was simulated in Comsol multi-physics, using the finite element eigenfrequency solver. The schematic of the two aperture designs is shown in Figure 1. The VCSEL structure consists of a 10 λ cavity sandwiched in between 10 top and 11 bottom distributed Bragg reflectors (DBRs) of SiO₂ and Nb₂O₅. The DBR pairs were assumed to have zero absorption loss whereas the absorption coefficient for the quantum well barrier was 3 cm^{-1} , GaN 1 cm^{-1} , p-GaN 75 cm^{-1} and ITO 1000 cm^{-1} .

III. RESULTS AND DISCUSSION

The modal discrimination was calculated as the difference in the threshold material gain (g_{th}) for the fundamental mode (LP₀₁) and the next higher order modes (LP₁₁ or LP₀₂). Figure 2 shows the variation in g_{th} for LP₀₁ as a function of the aperture diameter. As expected, g_{th} increases with decreasing aperture size due to increased diffraction loss, especially for aperture diameters below 4 μm . The effective index difference [6] (Δn_{eff}) between the central aperture region and the periphery region as shown in Figure 1 is 6.11×10^{-3} for a 5 nm etch, 12.27×10^{-3} for 10 nm etch and 8.16×10^{-3} for a 20 nm etched structure filled up with SiO₂. A larger Δn_{eff} leads to an enhancement in the mode confinement, but at the expense of an increase in the diffraction losses. The 5 nm

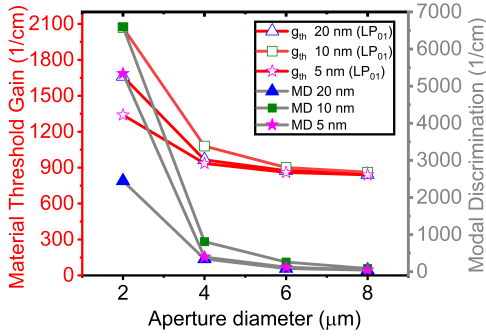


Fig. 2. Simulated impact of the aperture diameter on threshold material gain (g_{th}) for LP₀₁ in red and modal discrimination in gray for 20 nm buried SiO₂ aperture and nano-cylindrical aperture with 10 nm and 5 nm etch depth.

nano-cylindrical waveguide, with the smallest Δn_{eff} , shows the lowest g_{th} , while the 10 nm design, with the largest Δn_{eff} , exhibits the highest g_{th} across all aperture sizes. Figure 2 also presents the corresponding modal discrimination values for each structure as a function of the aperture diameter. The 5 nm etched nano-cylindrical waveguide design exhibited superior modal discrimination, particularly for smaller aperture diameters. For an aperture diameter of 2 μm , the 5 nm nano-cylindrical waveguide structure showed a modal discrimination of 5340 cm^{-1} and g_{th} of 1340 cm^{-1} , while the 20 nm SiO₂ buried structure showed values of 2448 cm^{-1} and 1661 cm^{-1} . The high modal discrimination reflects strong lateral confinement, which suppresses higher-order modes but also increases diffraction losses, raising the threshold gain. A 4 μm aperture diameter device with 5 nm etch shows a good trade-off between high modal discrimination (395 cm^{-1}) and low threshold material gain (935 cm^{-1}). The 20 nm SiO₂ configuration was equally good in terms of single-mode performance with a threshold material gain of 965 cm^{-1} and modal discrimination of 345 cm^{-1} .

Figure 3 presents a tolerance analysis for the 4 μm aperture case reflecting realistic fabrication deviations. The calculated g_{th} remained relatively stable, with values of 920 cm^{-1} for a 4 nm etch depth and 956 cm^{-1} for 6 nm. The corresponding modal discrimination values were 339 cm^{-1} for a 4 nm etch depth and 473 cm^{-1} for 6 nm - sufficient to favor LP₀₁ over higher order modes and maintain single mode operation.

The g_{th} values for the constant 20 nm p-GaN etch with deposited SiO₂ thickness equal to 19 nm is 952 cm^{-1} and for 21 nm is 986 cm^{-1} . The corresponding modal discrimination values were 376 cm^{-1} for a 19 nm SiO₂ deposition and 333 cm^{-1} for 21 nm. Whereas for the constant 20 nm SiO₂ deposition the calculated g_{th} values were 979 cm^{-1} for 19 nm nm p-GaN etch and 962 cm^{-1} for 21 nm. The modal discrimination for this case was 310 cm^{-1} for 19 nm p-GaN etch and 405 cm^{-1} for 21 nm. For the nano-cylindrical apertures, varying the p-GaN etch depth results in centrally

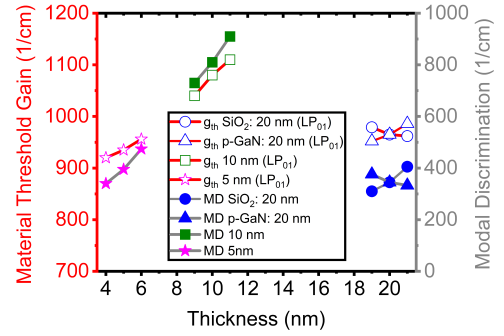


Fig. 3. Thickness vs. threshold material gain (g_{th} ; left Y-axis) and modal discrimination (right Y-axis) for 4 μm aperture structures, highlighting tolerance to fabrication variations. Etch depth variations of ± 1 nm were applied to the nano-cylindrical aperture with 5 nm and 10 nm etched p-GaN. For the buried-SiO₂ structure two cases were considered: (1) variation of the deposited SiO₂ thickness by ± 1 nm with a fixed 20 nm p-GaN etch depth, and (2) variation of the p-GaN etch depth by ± 1 nm while keeping the SiO₂ thickness constant at 20 nm.

elevated structures in all cases. And both g_{th} and the modal discrimination increase with increasing height of this central elevation. However, for the buried-SiO₂ structure, changing either the etched p-GaN or deposited SiO₂ thickness while keeping the other constant leads to both centrally elevated and peripherally elevated structures. We saw that the centrally elevated structure has the lower g_{th} values of the two. Thus, both the 5 nm nano-cylindrical design and the centrally elevated buried-SiO₂ design demonstrates strong modal selectivity, but the latter requires an additional fabrication step.

CONCLUSION

In summary, we performed simulations of InGaN-based blue VCSELs with varying aperture diameters, investigating two transverse index guiding schemes. Our results, together with those from [4, 5] suggest that a modal discrimination value in the range of 300-350 cm^{-1} is a practical benchmark for effective suppression of higher-order transverse modes. This guideline is useful for the design of mode-filtering structures such as surface reliefs, metasurfaces, or tapered oxide apertures. It is important to note that our study is based solely on optical simulations of a cold cavity. For a complete evaluation of VCSEL performance, future work should incorporate coupled optical, electrical, and thermal modeling to account for the full complexity of the device behavior.

REFERENCES

- [1] Yeh et al., Appl. Phys. Lett, 109, 241103 (2016).
- [2] Leonard et al., Appl. Phys. Lett, 108, 031111 (2016).
- [3] Kuramoto et al., Appl. Phys. Express, 12, 091004 (2019).
- [4] Kuramoto et al., Appl. Phys. Express, 13, 082005 (2020).
- [5] Terao et al., Proc. Of SPIE Vol. 11686 (2021).
- [6] G. R. Hadley, Opt. Lett. 20, 1483 (1995).